

**STRUCTURAL HEALTH MONITORING AND FINITE ELEMENT  
MODELING OF THE GALENA CREEK BRIDGE**

A Dissertation  
Presented to  
The Academic Faculty

by

Hamza Aslam

In Partial Fulfillment  
of the Requirements for the Degree  
Master of Science in the  
School of Civil and Environmental Engineering

Georgia Institute of Technology  
December 2021

# **STRUCTURAL HEALTH MONITORING AND FINITE ELEMENT MODELING OF THE GALENA CREEK BRIDGE**

Approved by:

Dr. Ryan Sherman, Advisor  
School of Civil and Environmental Engineering  
*Georgia Institute of Technology*

Dr. Lauren Stewart  
School of Civil and Environmental Engineering  
*Georgia Institute of Technology*

Dr. Donald White  
School of Civil and Environmental Engineering  
*Georgia Institute of Technology*

Date Approved: November 23, 2021

## **ACKNOWLEDGEMENTS**

My growth and success, in both my professional and personal life, would not have been possible without the patience, support, and kindness of my friends and family. I would like to extend my thanks to Dr. Jee Woong (Jay) Park and Dr. Erol Kalkan for their unwavering support and dedication to the project despite a global pandemic. I would also like to acknowledge Sayan Sakhakarmi and Cristian Arteaga from University of Nevada – Las Vegas, as well as the team from the Nevada Department of Transportation, for their help during the instrumentation installation. Most of all I would like to thank my advisor, Dr. Ryan Sherman, for his support and guidance through each challenge.

# TABLE OF CONTENTS

<b>Acknowledgements</b>	<b>iv</b>
<b>List of Figures</b>	<b>viii</b>
<b>Abstract</b>	<b>xiii</b>
<b>CHAPTER 1. Introduction</b>	<b>1</b>
<b>1.1 Background Information</b>	<b>1</b>
<b>1.2 Problem Statement</b>	<b>2</b>
<b>CHAPTER 2. Literature Review</b>	<b>4</b>
<b>2.1 Concrete Bridge Behavior</b>	<b>4</b>
2.1.1 Prestressed Concrete Structures	4
2.1.2 Seismic Behavior of Concrete Structures	5
2.1.3 Barrier Rail Influence on Structure Behavior	8
<b>2.2 Structural Health Monitoring</b>	<b>12</b>
2.2.1 Instrumentation: Accelerometers	13
2.2.2 Applications of Accelerometers in Structural Health Monitoring	15
<b>2.3 Finite Element Analysis</b>	<b>21</b>
2.3.1 Applications of Finite Element Analysis in Structural Engineering	21
<b>CHAPTER 3. Galena Creek Bridge Background</b>	<b>25</b>
<b>3.1 Description of the Galena Creek Bridge</b>	<b>25</b>
3.1.1 Materials	28
3.1.2 Superstructure	28
3.1.3 Substructure	32
3.1.4 Bearings	33
<b>3.2 Previous Galena Creek Bridge Research</b>	<b>34</b>
3.2.1 Taylor & Sanders, 2008	34
3.2.2 Carr & Sanders, 2013	35
3.2.3 Falkensammer, 2018	37
<b>3.3 Nevada Department of Transportation Reports</b>	<b>39</b>
3.3.1 Bridge Inspection Report, 2018	39
3.3.2 Load Rating Report, 09/13/2016	40
<b>CHAPTER 4. Structural Health Monitoring System</b>	<b>42</b>
<b>4.1 Introduction</b>	<b>42</b>
<b>4.2 Primary Seismic System</b>	<b>45</b>
4.2.1 Accelerometers	45
4.2.2 Sensor Installation and Wiring	49
<b>4.3 Secondary Exploratory System</b>	<b>53</b>
4.3.1 Displacement sensors	53
4.3.2 Tilt Meter	56
4.3.3 Temperature gauges	57



4.3.4	Wind Sensor	58
<b>4.4</b>	<b>Data Recorders</b>	<b>59</b>
<b>4.5</b>	<b>Free-field Station</b>	<b>61</b>
<b>CHAPTER 5.</b>	<b>Developing the Control Model</b>	<b>63</b>
<b>5.1</b>	<b>CSiBridge Background Information</b>	<b>63</b>
<b>5.2</b>	<b>Layout Tab</b>	<b>64</b>
<b>5.3</b>	<b>Components Tab</b>	<b>66</b>
5.3.1	Materials	67
5.3.2	Frame Properties	68
5.3.3	Link Properties	70
5.3.4	Deck Sections	71
5.3.5	Diaphragms	73
5.3.6	Parametric Variations	75
5.3.7	Bearings	77
5.3.8	Foundations	78
5.3.9	Abutments	78
5.3.10	Bents	79
<b>5.4</b>	<b>Loads Tab</b>	<b>80</b>
<b>5.5</b>	<b>Bridge Tab</b>	<b>81</b>
5.5.1	Bridge Object Data	81
5.5.2	Spans	82
5.5.3	Abutments	84
5.5.4	Bents	85
5.5.5	Hinges	86
5.5.6	Diaphragms	87
5.5.7	Prestressing Tendons	87
5.5.8	Update	90
<b>5.6</b>	<b>Advanced Tab</b>	<b>91</b>
<b>5.7</b>	<b>Analysis Tab</b>	<b>96</b>
5.7.1	Introduction	96
5.7.2	Dead Load Analysis	96
5.7.3	Modal Analysis	97
5.7.4	Time-history Analysis	99
<b>CHAPTER 6.</b>	<b>Parametric Modeling</b>	<b>101</b>
<b>6.1</b>	<b>Superstructure Material</b>	<b>103</b>
6.1.1	Modal Analysis – Superstructure Material	105
6.1.2	Time History Analysis – Superstructure Material	107
<b>6.2</b>	<b>Structural Damping</b>	<b>111</b>
6.2.1	Modal Analysis – Structural Damping	113
6.2.2	Time-history Analysis – Structural Damping	113
<b>6.3</b>	<b>Elastomeric Bearing Stiffness</b>	<b>116</b>
6.3.1	Modal Analysis – Elastomeric Bearing Stiffness	120
6.3.2	Time-history Analysis – Elastomeric Bearing Stiffness	124
<b>6.4</b>	<b>Effective Moment of Inertia of Substructure</b>	<b>127</b>
6.4.1	Modal Analysis – Effective Column Moment of Inertia	128

6.4.2	Time-history Analysis – Effective Column Moment of Inertia	131
<b>6.5</b>	<b>Link Slab</b>	<b>135</b>
6.5.1	Modal Analysis – Link Slab	137
6.5.2	Time-history Analysis – Link Slab	138
<b>6.6</b>	<b>Superstructure Modeling Approach</b>	<b>142</b>
6.6.1	Modal Analysis	144
6.6.2	Time-History Analysis	147
<b>6.7</b>	<b>Barrier Rail Modeling</b>	<b>153</b>
6.7.1	Modal Analysis – Barrier Rail Modelled as Frame Elements	155
6.7.2	Time-history Analysis – Barrier Rail Modelled using Frame Elements	157
<b>CHAPTER 7.</b>	<b>Refined Final Model</b>	<b>164</b>
<b>7.1</b>	<b>Trivial Solutions</b>	<b>164</b>
<b>7.2</b>	<b>Structural Damping</b>	<b>166</b>
<b>7.3</b>	<b>Effective Moment of Inertia of Substructure Elements</b>	<b>167</b>
<b>7.4</b>	<b>Material Stiffness</b>	<b>168</b>
<b>7.5</b>	<b>Final Proposed Modal Analysis</b>	<b>169</b>
<b>7.6</b>	<b>Final Proposed Model Time-History Analysis</b>	<b>172</b>
<b>CHAPTER 8.</b>	<b>Conclusions and Future Work</b>	<b>177</b>
<b>8.1</b>	<b>Conclusions</b>	<b>177</b>
<b>8.2</b>	<b>Proposal for Future Work</b>	<b>178</b>
8.2.1	Verification of Structural Health Monitoring Systems	178
8.2.2	CSiBridge Finite Element Model	179
<b>APPENDIX A</b>		<b>182</b>
<b>APPENDIX B</b>		<b>190</b>
<b>BIBLIOGRAPHY</b>		<b>219</b>

## LIST OF FIGURES

Figure 1.1: Elevation view of the Galena Creek Bridge .....	1
Figure 2.1: Basic piezoelectric accelerometer schematic .....	14
Figure 2.2: Basic capacitance accelerometer schematic .....	15
Figure 2.3: Single story frame used for cyclical testing (m).....	17
Figure 2.4: Elevation view of accelerometer placement.....	18
Figure 2.5: Plan view of bridge deck accelerometer placement .....	19
Figure 3.1: Galena Creek Bridge location on I-580 south of Reno, NV (Google, 2021). 26	
Figure 3.2: Plan view of east face of Galena Creek Bridge northbound structure .....	27
Figure 3.3: Typical cross section of the two-cell superstructure (m) .....	29
Figure 3.4: Hinge diaphragm elevation view (m).....	30
Figure 3.5: North fillet diaphragm at Span 3 of northbound structure .....	31
Figure 3.6: The superstructure (blue) and substructure (orange) accelerometer placement .....	36
Figure 4.1: Primary seismic SHM system uniaxial accelerometer locations on the Galena Creek Bridge .....	43
Figure 4.2: Secondary exploratory SHM system sensor locations on the Galena Creek Bridge.....	44
Figure 4.3: Utility shed located south of the southbound structure .....	45
Figure 4.4: Kinemetrics ES-U2 accelerometer .....	46
Figure 4.5: Aluminum plate for mounting accelerometers.....	50
Figure 4.6: Example of plate with three sensors at bottom of Pier 4.....	50
Figure 4.7: PVC conduits along the face of Abutment 1 .....	51
Figure 4.8: PVC conduit extruding through the bottom slab near Abutment 1 .....	51
Figure 4.9: Typical cables running along the east girder of the superstructure.....	52
Figure 4.10: Typical connection between primary cables (red) to sensor cables (white) via terminal block .....	52
Figure 4.11: UniMeasure HX-P510 Series Linear Potentiometer .....	54
Figure 4.12: Potentiometer located at west edge of Abutment 1 of northbound structure .....	55
Figure 4.13: Potentiometer installed at west face of Hinge 1 .....	55
Figure 4.14: Rieker Flex Series H6 biaxial inclinometer installed a south face of pier diaphragm at Pier 2 .....	56
Figure 4.15: R.M. Young 41342 temperature probe located in Galena Creek Bridge .....	57
Figure 4.16: R.M. Young 86000 ultrasonic anemometer installed at utility shed .....	59
Figure 4.17: Kinemetrics Obsidian 12X (top) and 36X (bottom) data recorders with cables.....	60
Figure 4.18: Bullet III GPS antennas.....	61
Figure 4.19: Kinemetrics ETNA 2 accelerograph and protective case.....	62
Figure 5.1: Preliminary control model.....	63
Figure 5.2: Horizontal curvature of span 1 (southbound superstructure) .....	65
Figure 5.3: Example layout line input for CSiBridge (southbound superstructure) .....	66
Figure 5.4: Example of sections found in the CSiBridge Components Tab .....	67
Figure 5.5: Example solid rectangular section input for arch diagram.....	69
Figure 5.6: Example Section Designer tool for typical arch frame .....	70
Figure 5.7: Typical box girder cross section (m).....	71

Figure 5.8: CSiBridge template for box girder inputs .....	71
Figure 5.9: Elevation view of Hinge 1 (m) .....	74
Figure 5.10: Bottom slab thickness variation legend .....	75
Figure 5.11: Box girder variation at intersection of superstructure and arch (m) .....	76
Figure 5.12: Example of linear variation input in CSiBridge (Span 5) .....	76
Figure 5.13: Loads Tab as seen in CSiBridge .....	80
Figure 5.14: Example of superstructure span variations in CSiBridge .....	83
Figure 5.15: Example of deck section variation in CsiBridge .....	83
Figure 5.16: Typical CSiBridge input for abutments .....	85
Figure 5.17: Typical CSiBridge input of bent information .....	86
Figure 5.18 – Typical CSiBridge prestressing input .....	89
Figure 5.19: Example of CSiBridge tendon parabolic path .....	90
Figure 5.20: Example of updating bridge object model in CSiBridge .....	91
Figure 5.21: Arch modeled as frame elements in CSiBridge with segment labels .....	92
Figure 5.22: Extrude view of CSiBridge model at base of column and pier .....	94
Figure 5.23: Elevation view of the links connecting the arch and box girder in CSiBridge .....	94
Figure 5.24: Defining the Mass Source for CSiBridge .....	95
Figure 5.25: CSiBridge input for Dead Load Case .....	97
Figure 5.26: CSiBridge input for modal analysis case .....	98
Figure 5.27: Modal analysis results of control model .....	98
Figure 5.28: Example of an imported ground motion from text file in CSiBridge .....	99
Figure 5.29: CSiBridge input for time-history load case simulating an earthquake .....	100
Figure 6.1: Typical use of 40 MPa concrete over Piers 2 and 3 (m) .....	104
Figure 6.2: Cross section of strengthened areas of box girder .....	105
Figure 6.3: Envelope of transverse displacement of northbound superstructure for superstructure material stiffness variants .....	109
Figure 6.4: Maximum longitudinal stresses in superstructure for superstructure material stiffness variants .....	110
Figure 6.5: Envelope of transverse displacement of superstructure from damping analyses .....	114
Figure 6.6: Maximum superstructure stresses from damping analyses .....	115
Figure 6.7: Allowable degrees of freedom (left) of the bearing pads relative to CSiBridge global axes .....	117
Figure 6.8: Upper limit abutment bearing stiffness input for CSiBridge ( $G = 1.38$ MPa) .....	119
Figure 6.9: Upper limit hinge bearing stiffness input for CSiBridge ( $G = 1.38$ MPa) ...	119
Figure 6.10: Maximum longitudinal displacement of superstructures from bearing analyses .....	126
Figure 6.11: Example of MOI reduction factor applied in CSiBridge .....	128
Figure 6.12: Maximum transverse displacement of superstructures for substructure effective MOI analyses .....	133
Figure 6.13: Maximum transverse displacement at midspan of Span 3 .....	134
Figure 6.14: Northbound (white) and southbound (pink) superstructures highlighted by color .....	136

Figure 6.15: Single shell element (teal) connecting northbound (white) and southbound (pink) structures .....	137
Figure 6.16: Maximum transverse displacement of superstructures for link slab analyses .....	140
Figure 6.17: Maximum superstructures stresses for link slab analyses .....	141
Figure 6.18: Example of frame spine model using rigid links that extend to link slab shell .....	143
Figure 6.19: Frame spine superstructure model to replicate the 2013 UNR SAP2000 model.....	143
Figure 6.20: Envelope of longitudinal displacement of superstructures for shell vs solid superstructure analyses (X-axis) .....	149
Figure 6.21: Envelope of transverse displacement of superstructures for shell vs solid superstructure analyses (Y-axis) .....	150
Figure 6.22: Envelope of vertical displacement of superstructures for shell vs solid superstructure analyses (Z-axis) .....	151
Figure 6.23: Superstructure of control model made up of shell elements .....	152
Figure 6.24: Barrier rail frame elements drawn along deck edges .....	153
Figure 6.25: Barrier rail cross section defined using section designer in CSiBridge .....	155
Figure 6.26: Envelope of maximum vertical displacement of superstructures for parapet analyses .....	159
Figure 6.27: Envelope maximum transverse displacement of superstructures for parapet analyses .....	160
Figure 6.28: Envelope maximum longitudinal displacement of superstructures for parapet analyses .....	161
Figure 6.29: Envelope maximum stresses in superstructure for parapet analyses.....	162
Figure 7.1: Envelope of vertical displacements of northbound superstructure for control vs final models .....	174
Figure 7.2: Envelope of transverse displacement of northbound superstructure for control vs final models .....	175
Figure 7.3: Envelope of longitudinal displacement of northbound superstructure for control vs final models.....	176

## LIST OF TABLES

Table 3.1: Concrete classification assignments .....	28
Table 3.2: Prestressing details.....	30
Table 3.3: Diaphragm thicknesses .....	31
Table 3.4: Column heights.....	33
Table 3.5: Inventory Vehicle Load Rating Results.....	41
Table 3.6: Operating Vehicle Load Rating Results .....	41
Table 4.1: Accelerometer location and orientation.....	48
Table 5.1: Inputs for box girder definition for CSiBridge (m) .....	72
Table 5.2: Diaphragm thicknesses .....	74
Table 5.3: Bottom slab thickness variation values.....	75
Table 5.4: Calculated stiffness values for elastomeric bearings .....	77
Table 5.5: Column heights.....	79
Table 5.6: Galena Creek Bridge span lengths and station locations.....	82
Table 5.7: Bent elevation values along global z-axis .....	86
Table 5.8: Diaphragm locations.....	87
Table 5.9: Prestressing strand data.....	90
Table 5.10: Segment end node offset for modeling arch .....	93
Table 6.1: List of parameters and respective variations .....	102
Table 6.2: Top five modes in the longitudinal direction (X-axis) .....	106
Table 6.3: Top five modes in the transverse direction (Y-axis) .....	106
Table 6.4: Top five modes in the vertical direction (Z-axis) .....	107
Table 6.5: Comparison of top longitudinal modes for bearing stiffness variations (X-axis) .....	121
Table 6.6: Comparison of top transverse modes for bearing stiffness variations (Y-axis) .....	122
Table 6.7: Comparison of top vertical modes for bearing stiffness variations (Z-axis) .	123
Table 6.8: Comparison of top longitudinal modes for MOI variant models .....	129
Table 6.9: Comparison of top transverse modes for MOI variant models.....	130
Table 6.10: Comparison of top vertical modes for MOI variant models.....	131
Table 6.11: Top five modes in the longitudinal direction (X-axis) .....	137
Table 6.12: Top five modes in the transverse direction (Y-axis) .....	138
Table 6.13: Top five modes in the vertical direction (Z-axis) .....	138
Table 6.14: Comparison of top long. modes for superstructure modeling analyses (X-axis).....	145
Table 6.15: Comparison of top transverse modes for shell vs frame superstructure (Y-axis).....	145
Table 6.16: Comparison of top vertical modes for shell vs frame superstructure (Z-axis) .....	146
Table 6.17: Comparison of top transverse modes between 2013 SAP2000 model vs spine frame .....	147
Table 6.18: Comparison of top longitudinal modes for control vs frame barrier rail (X-axis).....	156

Table 6.19: Comparison of top transverse modes for control vs frame barrier rail (Y-axis)	156
Table 6.20: Comparison of top vertical modes for control vs frame barrier rail (Z-axis)	157
Table 7.1: Final model concrete material propeties	169
Table 7.2: Comparison of top longitudinal modes for control vs final model (X-axis)	170
Table 7.3: Comparison of top transverse modes for control vs final model (Y-axis) ....	170
Table 7.4: Comparison of top vertical modes for control vs final model (Z-axis) .....	171
Table 7.5: Comparison of top transverse modes for Carr & Sanders vs final model (Y-axis).....	172
Table 8.1: Final model node numbers corresponding with sensor locations .....	180

## SUMMARY

Structural health monitoring (SHM) provides numerous benefits when assessing the condition of a structure for long-term degradation or response to an extreme event. The Nevada Department of Transportation (NDOT) was interested in exploring SHM as an asset monitoring tool for their inventory. As such, the objectives of the current study were to develop and implement two SHM systems for the Galena Creek Bridge, located along I-580 and U.S. Route 395 between Reno and Carson City, NV. Completed in 2012, the Galena Creek Bridge is the largest concrete cathedral arch bridge in the world. The bridge is a twin 526.2-meter long, seven-span, two-cell reinforced concrete box girder structure. The two SHM systems consisted of a primary seismic system and a secondary exploratory system. Both systems were installed on the northbound structure to measure the structural response to seismic activity as well as to routine traffic, thermal expansion and contraction, and wind events. The seismic system consisted of 33 accelerometers and a seismograph, while the exploratory system included temperature, wind, displacement, and tilt sensors. The system software was designed to send real-time notifications to proper authorities on the condition of the bridge following a predefined trigger event.

To compliment the SHM systems, a detailed finite element model was developed in CSiBridge to improve the understanding of the Galena Creek Bridge structural response. A parametric study examined how a range of variables influenced the dynamic properties of the structure. Static dead load, modal, and time-history analyses were performed to provide insights on the influence of each parameter. Recommendations are provided to enable future model calibration to the field-measured data from the SHM systems.



# CHAPTER 1. INTRODUCTION

## 1.1 Background Information

The Galena Creek Bridge system carries Interstate 580 and U.S. Route 395 over the Galena Creek, between Carson City and Reno, Nevada (NDOT, 2019). The bridge is comprised of two 526.2-meter long, seven-span, two-cell reinforced concrete box girder bridges. Span 3 of the structure has a length of 210 meters and is supported by a reinforced concrete arch, distinguishing the Galena Creek Bridge as the largest cathedral arch bridge in the world (Figure 1.1). Elastomeric bearing hinges located in Span 2 and Span 4 divide the structure into three frames. The northbound and southbound units are connected by a link slab along Frame 2 which provides resistance to lateral loads. The deck of each bridge carries three lanes of traffic and experiences an annual daily traffic (ADT) of 18,000 (NDOT, 2019). Construction of the Galena Creek Bridge was completed in August of 2012 (Carr and Sanders, 2013).



**Figure 1.1: Elevation view of the Galena Creek Bridge**

The Galena Creek Bridge is located within a 1,000 km long geological depression called Walker Lane, which runs along the Nevada-California border (Briggs and Hammond, 2011). Walker Lane is a collection of active faults, a product of interactions between the Pacific and North American tectonic plates. As a result, Walker Lane is subject to frequent, and sometimes severe, seismic activity. Earthquakes, such as the 2019 7.1-magnitude earthquake recorded in Ridgecrest, CA, can pose a significant threat to structures located in the Walker Lane network of faults (Wolterbeek, 2020).

Upon completion of the Galena Creek Bridge, a structural health monitoring (SHM) system was installed by researchers at the University of Nevada at Reno (UNR) to better understand the physical and dynamic properties of the structure (Carr and Sanders, 2013). Accelerometers were located throughout the southbound superstructure and baseline data were collected through a series of field tests. A finite element analysis (FEA) model was made of the Galena Creek Bridge to estimate the individual component forces due to the tests (Carr and Sanders, 2013). The field-measured time-history data served as input for the computational model. The UNR SHM system was initially intended to be a permanent fixture; however, it was abandoned after the completion of the 2013 study.

## **1.2 Problem Statement**

The objective of this research was to enhance the understanding of the behavior of the Galena Creek Bridge through computational modeling and the development and implementation of two new, permanent SHM systems. These systems provide continuous monitoring of the bridge behavior during routine service loads, such as traffic, wind, and

thermal expansion, as well as extreme events, such as seismic events. The project has been divided into three primary objectives:

1. The design and installation of a primary SHM system designed to capture the structural response during seismic loading, consisting of 33 accelerometers and a tri-axial seismograph. The seismic system is similar to a proven system design used by the United States Geological Survey (USGS) to monitor the seismic response of buildings as part of the Strong Motion Project; however, the current project is the first adaptation of the system to a bridge structure.
2. The design and installation of a secondary, exploratory SHM system that aims to extend the capabilities of the proven seismic software to include displacement, tilt, temperature, and wind response using potentiometers, inclinometers, temperature gauges, and anemometers.
3. The development of a FEA model of the Galena Creek Bridge using CSiBridge. A parametric study was conducted to evaluate changes in the structural response relative to a defined set of parameters.

Both SHM systems were programmed with threshold values that trigger alerts to the research team and the Nevada Department of Transportation (NDOT). The notifications include a report on the response and inspection priority. The system has the ability to generate multiple report types based on the recipient, such as inspector, engineer, or seismologist. Ultimately, the goal of NDOT is for the Galena Creek Bridge SHM systems to serve as a catalyst for the implementation of future SHM systems.

## **CHAPTER 2. LITERATURE REVIEW**

### **2.1 Concrete Bridge Behavior**

#### *2.1.1 Prestressed Concrete Structures*

Prestressing is a method which mitigates the inherent shortcomings of concrete members to internal tensile stresses by applying compressive forces along the component (ACI, 2021). Pre-tensioning and post-tensioning are the two primary methods of prestressing concrete (FHWA, 2013). The tensile strength of concrete is approximately 10% of the strength in compression (FHWA, 2013); as such, tensile stresses can easily cause concrete components to crack, potentially exposing the steel reinforcement and compromising the long-term durability. Steel tendons are used to apply internal stresses to an unloaded concrete member thereby reducing the area of tensile stress within the member when subjected to design loads and decreasing the likelihood of cracking and spalling. In addition, prestressing concrete mitigates the deflection of the member under design loads, which has the additional benefit of visual appeal to the consumer or client.

The tendons used in pre-tensioning are applied with a jacking force before the concrete is cast. In contrast, post-tensioning involves applying the jacking force after the concrete has cured to a specified minimum compressive strength. For post-tensioning, concrete is cast around ducts containing steel tendons. The transfer of forces is performed by anchoring the dead end and using a hydraulic jack apply a predetermined stress to the steel tendons. Wedges are then used to secure the tendons of the free end into place.

Losses in the transfer of stresses from the steel to the concrete result from a range of variables: warping of the concrete member, friction between the tendon and duct, duct wobble, and the change in angle between the free end and the anchored end (FHWA, 2016). Losses in force transfer due to wobble and friction are directly proportional to the length of the ducts. Once cast, the tendons used in pre-stressed concrete are fixed.

### *2.1.2 Seismic Behavior of Concrete Structures*

The seismic behavior of reinforced concrete structures present unique challenges to integrity evaluation. Areas of concrete elements subject to tensile stresses are, often by design, prone to cracking. General concrete members are designed for tensile stresses to flow through the reinforcing steel, allowing the structure to function under the design loads. Most modern design codes assume linear-elastic behavior for seismic design (Taylor and Sanders, 2008). In practice, cracking changes the properties of the cross section and, subsequently, the dynamic behavior. The opening and closing of cracks during cyclic loading results in non-linear behavior (Gunes and Gunes, 2021). Additionally, the development of new cracks and the growth of existing cracks during a seismic event further complicates dynamic response.

Examination of concrete bridges in the aftermath of seismic events suggests trends in the damage sustained. On May 12, 2008, the Sichuan Province in China experienced a magnitude 8.0 earthquake followed by several magnitude 6.0 aftershocks. A majority of the \$1 billion in damages to the transportation infrastructure was related to bridges. Following this disaster, researchers from the Beijing University of Technology conducted a survey of 320 major reinforced concrete bridges to quantify the extent of the damage and

the method of failure (Qiang *et al.*, 2009). Of the 320 structures investigated, 14% had severe damaged and could no longer safely carry live loads and 39% exhibited moderate damage that impeded the flow of daily traffic.

Recurring modes of damage documented in the investigation were unseated girders, displaced substructure foundations, and failure of pier columns. The latter of these cases was the most prevalent, with single pier columns displaying the most damage (Qiang *et al.*, 2009). Columns that had sufficient ductility to prevent failure suffered cracks and spalls on all faces exposing the steel reinforcing. Conversely, columns that lacked the ductility required to accommodate excessive deformation developed extreme internal stresses. Failure of reinforced concrete pier columns in both bending and brittle shear were documented.

The basis of the seismic design of concrete columns is the distribution of inelastic behavior to designated regions throughout the structure to prevent collapse (Taylor and Sanders, 2008). Insufficient transverse reinforcement leaves columns vulnerable to shear failure, which is often brittle and results in the loss of axial load carrying capacity (Feng, Kaya and Ventura, 2016). Seismic testing of concrete columns in controlled environments offers valuable insight into the dynamic properties and modes of failure. One example of experimentally evaluating the seismic performance of concrete columns was by applying progressively stronger ground accelerations to a concrete column (Sakai and Unjoh, 2006). The test focused on increasing the magnitude of cyclical loading applied to a reinforced concrete column to observe the progression of damage. The results of the test were indicative of the physical response of bridge piers to extreme earthquakes.

The series of tests conducted by Sakai subjected a 0.6 m diameter circular concrete column of a height of 2.14 m to triaxial accelerations. The sample was composed of 41.7 MPa concrete and 351 MPa deformed bars. The column was reinforced by forty 10 mm diameter longitudinal bars and 6 mm diameter hoops spaced at a 75 mm pitch. The dead load of a superstructure was emulated using a 27,000 kg concrete mass at the top of the column.

The columns were subjected to select accelerations from ground motions recorded during a 1983 earthquake in Nihonkai Chubu, Japan. The first series of tests applied the ground motions at an amplitude of 20% of the recorded ground motion to keep the behavior of the structure within the elastic range. The second series of tests increased the amplitude of the ground motions to 400% of those recorded to observe damages during a nonlinear dynamic response.

The 20% ground motion resulted in a maximum lateral displacement of 7 mm and no permanent deformation. None of the reinforcing steel had yielded and the concrete exhibited several hairline cracks. Conversely, the 400% ground motion resulted in the column experiencing plastic deformation, significant spalling, and a severe decrease in moment capacity; however, it remained vertical and retained axial capacity. The damage was most prevalent along the bottom 0.25 m of the column where the longitudinal rebar had buckled outwards and fractured, resulting in permanent deformation. Once buckling occurred, the flexural capacity of the column decreased by 70% and the column exhibited a permanent story drift of 0.196 m. The transverse reinforcement controlled the failure to buckling due to bending moments despite lateral loads up to 108 kN.

### *2.1.3 Barrier Rail Influence on Structure Behavior*

Barrier rails, also referred to as parapets, are not typically considered as structural elements during design, despite influencing the properties of a bridge. Ignoring the effect of secondary elements, such as barrier rails, provides conservative calculations on the load-bearing capacity of bridge girders, but may not accurately represent the actual in-service structural behavior (Eamon and Nowak, 2002).

To observe the contribution of secondary structural elements, a 2002 study (Eamon and Nowak) used finite element modelling (FEM) software to demonstrate the behavior of a series of simple-span, two-lane, bridges subjected to live loads. A total of 18 bridges were studied of varying span length, girder spacing, and girder type. Spans of 10 m, 30 m, and 50 m were evaluated, while girder spacings were either 2 m, 3 m, or 4 m. Both composite steel girders and prestressed concrete girders were considered. Loading consisted of an AASHTO HS-20 for all analyses. Various combinations of barriers, diaphragms, and three types of sidewalks were studied, cumulating in 240 simulations.

The results of the experiment indicated that the secondary structural elements increased the bridge load bearing capacity. A control bridge without additional secondary elements was dominated by a flexural response of the first interior girder, regardless of girder type. The inclusion of sidewalks and barrier rails to the models decreased the moment distribution factors of all girders under identical loading because the secondary structural elements carried a portion of the load. The exterior girders experienced as much as a 40% decrease in the moment distribution factor. As the girder location approached the centerline of the bridge, the decrease in distribution factor reduced. Specifically, the



inclusion of the barrier rail on both sides of the deck increased the moment capacity of the 10 m long model by a factor of 1.9. The influence of the secondary structural elements decreased as the length of the simple span bridge increased. The 30 m span model increased in moment capacity by 1.3, while the 50 m span model increased by a factor of 1.15.

Studies also considered other parameters to account for differences between the AASHTO predicted structural behavior and actual field test results (Conner and Huo, 2006). ANSYS 6.1 was used to create FEA models of two-span continuous bridges of varying widths and skews to evaluate the influence of barrier rails in areas of negative moment. Each span measured 23.86 m long and was supported by prestressed AASHTO Type III concrete beams spaced at 2.74 m. The relationship between the span length and deck width, also referred to as the aspect ratio, was adjusted by either controlling the number of girders or by varying the deck overhang. Aspect ratios ranged from 0.5 to 2.9. In addition, each bridge was evaluated with a skew of  $0^\circ$  and  $45^\circ$ , resulting in 34 models. The AASHTO HS-20 truck was used to perform the live load analyses.

The study concluded that the addition of barrier rails reduced the distribution factor of the exterior girders by up to 36% and the interior-most girder by up to 13% in both the positive and negative moment regions. The aspect ratio of the structure had a marginal impact on the moment distribution factors. The distribution factors were unaffected by aspect ratios below 1.8. The addition of the  $45^\circ$  skew mitigated the stiffness provided by the barriers by up to 4% with the exterior girders showing the most significant changes.

Evaluation of in-service bridges have also been conducted to quantify the behavior of secondary elements on the global structural response. Researchers from Purdue

University investigated the influence of parapets on live load distribution factors on two bridges with varying geometries in Indiana (Akinci, Liu and Bowman, 2008). The US-52 bridge in Lafayette, IN consists of one concrete span and five continuous steel spans of varying lengths. The I-65 Bridge in Hobart, IN is a single-span steel plate girder bridge with integral abutments. Both bridges had unique girder types, girder spacing, widths, and parapets. The US-52 bridge was retrofitted with an 0.84 m tall parapet in 1989 and the I-65 structure was designed with a 1.17 m tall parapet. Another significant difference was that the I-65 bridge had a structurally-continuous barrier rail while the length of the US-52 bridge required expansion joints in the barrier rail. FEA models were developed in SAP2000. In addition to the HS-20 design truck, superload trucks defined by Indiana and Wisconsin Departments of Transportation were used to produce additional live load conditions. The FEA column design software PCA Column V.2003 was used to calculate the axial and bending moment capacity for each parapet.

The case study of the two Indiana bridges confirmed that the parapet reduced the distribution factors by up to 30%. Discontinuities in the bridge parapet, such as expansion joints, acted as stress concentrations. In areas of positive moment, the parapet discontinuity created a notch effect, intensifying the stresses in the bottom flange of the exterior girder. In areas of negative moment, tensile stresses led to significant cracking in the bridge deck and parapet. The stiffness contribution from a parapet was directly proportional to the stiffness of the standalone parapet, meaning a stiffer parapet attracted higher stresses and increased the capacity of the bridge.

A further investigation on barrier rail stiffness by Eddine, Tarhini and Mabsout, (2020) evaluated span length, girder spacing, barrier stiffness, and railing configurations.

A single-span simply-supported steel girder bridge was modelled using SAP2000. Much of the previous research studying parapet effects on structural behavior assumed barriers on both sides of the bridge deck. To further scrutinize the relationship between the distribution factors and load position, barrier rails were added individually on each side of the deck as well as to both sides simultaneously. The control railing, which had dimensions of 0.2 m x 0.76 m, had a baseline stiffness that served as the standard of comparison for the variant models. The stiffness of the barrier rail in the variant models was controlled by editing the height of the barrier rail between 0.62 m and 1.22 m. Increasing the height of the component increased the stiffness. By editing the height of the barrier rail modeled, the study considered barrier rails with factored stiffnesses of 0.5, 2.0, 3.0, and 4.0. AAHSTO HS-20 design trucks were used to apply live loads for each of the 240 simulations.

The previous studies demonstrate secondary structural elements result in greater load bearing capacity than assumed through traditional calculation methodologies. However, research on the parapet contributions to bridge capacity is a relatively modern field of study and many questions remain unexplored. A recurring theme throughout these studies is that as the complexity of the structure increases, the stiffness contribution from the parapet decreases. This implication leaves room for further examination of barrier stiffness effects on complex structures, such as the Galena Creek Bridge. Specifically, the case study of the two Indiana steel girder bridges provided a foundation upon which to further explore the consequences of discontinuities in parapets for existing bridges.

## 2.2 Structural Health Monitoring

Structural inspections and evaluations are integral in ensuring the longevity of infrastructure. As per the United States Code of Federal Regulations, typical in-service bridges require a routine inspections every 24 months to be performed by a certified engineer (CFR §650, 2021). During routine visual inspections, engineers assess and document damage to the structure and assign numerical values denoting the condition of the bridge based on the standards set by the *AASHTO Manual for Condition Evaluation of Bridges* (AASHTO, 2008, Wang, 2010). The time between routine bridge inspections leaves a 24-month window in which the condition of the bridge can change. This gap in data collection poses a safety liability. An additional consideration of visual inspections is access. Physical access to every bridge component considered is required, sometimes requiring the use of specialized equipment, such as under bridge inspection trucks. SHM systems offer potential solutions to many of these shortcomings.

The purpose of SHM systems is to provide engineers with a reliable and efficient way to assess the integrity of a structure in real-time. For an accelerometer-based SHM system, the dynamic response of a structure is quantified by measuring the global vibration data, also known as its modal parameters (Gunes and Gunes, 2021). The modal parameters of a structure are controlled by physical properties, such as stiffness, damping, and mass. By detecting discrepancies in the modal parameters during or after a seismic event, *in situ* SHM systems can reveal changes to the physical properties due to damage.

Using discrepancies in modal parameters to detect damage has limitations. Factors such as temperature, moisture, live loads, and wind loads can also influence the dynamic

response of a structure. Damage to a structure needs to be sufficient such that the change in modal data is significantly higher than variations due to noise. Conversely, setting the threshold for the change in parameters too high will result in potential damage going unnoticed. Additionally, damage to components that are not crucial to the vibration of the structure could also go undetected.

The primary modal information of any structure are the respective frequencies and mode shapes. Changes in the mode shape curvature, a higher derivative of mode shapes, are more sensitive to changes in physical properties (Gunes and Gunes, 2021). However, both mode shape and mode shape curvature methods of damage detection in structures require significant damage to incite recordable changes in data. Furthermore, accurate feedback requires a SHM network consisting of numerous highly precise sensors across the entire structure. The inefficiency of this approach makes it unsuitable for *in situ* application. A more modern, and reliable, approach to dynamic structural analysis is to identify changes in stiffness and flexibility. Lower frequencies modes are responsive to changes in stiffness and are easier for a SHM system to identify.

### 2.2.1 Instrumentation: Accelerometers

Accelerometers quantify the rate of change in velocity by converting kinetic energy into electric signals (Xu and Xia, 2012). Measured accelerometer data can be used to calculate the dynamic properties of a structure, such as displacements, natural frequencies, damping ratios, mode shapes, and stiffness. Several considerations must be evaluated when selecting and locating accelerometers for a SHM system. Ideal accelerometer placement is at the center of gravity of the desired component. In practice, locating the accelerometer

precisely at the center of gravity of a member is not feasible; therefore, it is commonly assumed that the dynamic behavior of a member from its center of gravity to the surface upon which the sensor is attached is negligible. In addition, the mass of the transducer should be small relative to the object of interest such that it does not interfere with the dynamic response, a rare issue when considering bridge structures.

Piezoelectric and capacitance accelerometers are the two primary types of transducers used in practice and are identified by their method of data collection (Xu and Xia, 2012). The basic piezoelectric accelerometer consists of a damped spring-mass system connected to a piezoceramic or piezoelectric crystal, as demonstrated in Figure 2.1. Piezoelectric materials are transducers which generate an electrical charge upon experiencing internal stresses. The magnitude of the charge is directly proportional to the level of stress experienced by the material. The greater the deformation caused by the mass-spring system, the higher the voltage generated. When the sensor is subject to an acceleration, the mass is displaced and deforms the piezoceramic material. The deformation, and subsequent internal stresses, of piezoceramic material converts the kinetic energy into an electric signal. Piezoelectric accelerometers have long service lifespans, but can be inefficient or inaccurate, at reading low frequencies (generally below 1 Hz).

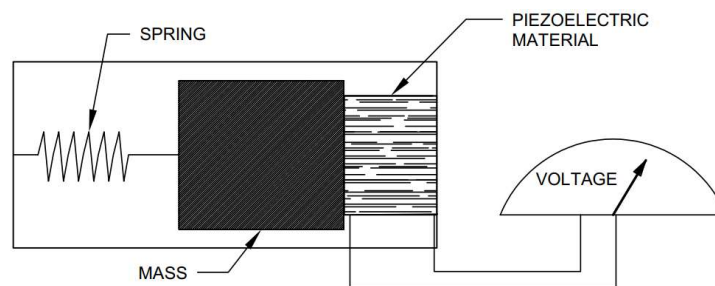


**Figure 2.1: Basic piezoelectric accelerometer schematic**

As with the piezoelectric accelerometer, the capacitance accelerometer is a transducer which quantifies kinetic energy as an electric signal (Xu and Xia, 2012). Capacitance accelerometers contain two plates, known as electrodes, that generate a charge based on the distance between them. One electrode is fixed while the other is attached to an internal mass-spring system, as seen in Figure 2.2. The initial distance between the electrodes under neutral conditions provides a baseline electrical charge. During an acceleration, the sensor displaces the mass-spring plate which, in turn, generates a change in the electrical charge. The variation in charge is used to quantify the acceleration experienced; the more the electrical charge varies, the greater the acceleration. Capacitance accelerometers can read true DC responses (0 Hz) and maintain accuracy through extremely low frequencies, making them optimal for flexible structures that typically exhibit long periods.

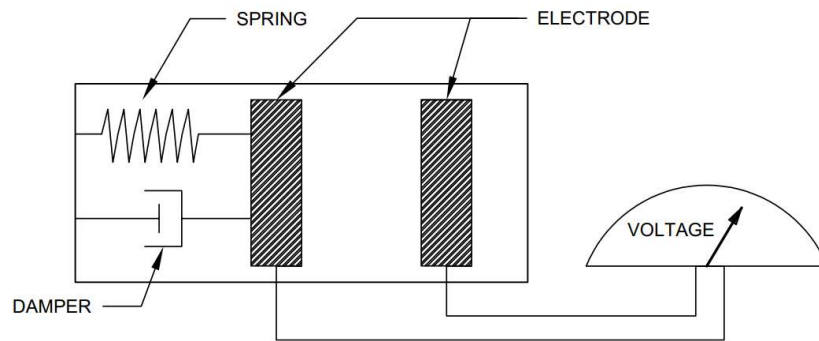


**Figure 2.2: Basic capacitance accelerometer schematic**

### *2.2.2 Applications of Accelerometers in Structural Health Monitoring*

An accelerometer-based SHM system is the optimal choice for a structure subject to seismic activity. The recorded data can be used to determine discrepancies in modal information and identify structural damage. Calculating the modal information and structural integrity of a reinforced concrete structure based solely on the gross cross-

sectional area is not an accurate representation of the actual dynamic behavior (Gunes and Gunes, 2021). Using accelerometers to monitor the changes in seismic response is the most reliable method of damage detection for concrete structures.

Gunes and Gunes (2021) demonstrated an example of accelerometers effectively determining the dynamic properties of concrete frames by subjecting a simple one-story concrete frame supported by two columns to a series of cyclical pushover tests of increasing amplitude. The purpose of the study was to better understand the trends between damage progression versus natural frequency and damping in reinforced concrete frames. Performing this experiment using a single degree of freedom rigid frame reduced the complexity of the analysis. Additionally, the SHM system was used to determine the location and magnitude of the damage sustained.

The single-story test frame used for the experiment was comprised of a 2.0 m long beam supported at each end by two 1.5 m tall columns with fixed bases. All elements were 0.2 m x 0.3 m rectangular cross sections and consisted of 27.5 MPa concrete and 412 MPa reinforcing steel (Figure 2.3). Ten pushover tests had applied story drift amplitudes ranging from 0.25% up to 4.0%. After each pushover test, impact vibration tests were performed, and the free vibration response of the structure was measured. Vibration tests were performed by striking the concrete frame with 5 kN instrumented sledgehammer. Eight uniaxial accelerometers, located along the frame, measured the dynamic response of the frame. An Eigensystem Realization Algorithm was used to calculate the natural frequencies and damping ratios using the measured data. The Damage Location Vector approach estimated the locations where the structural integrity was compromised.



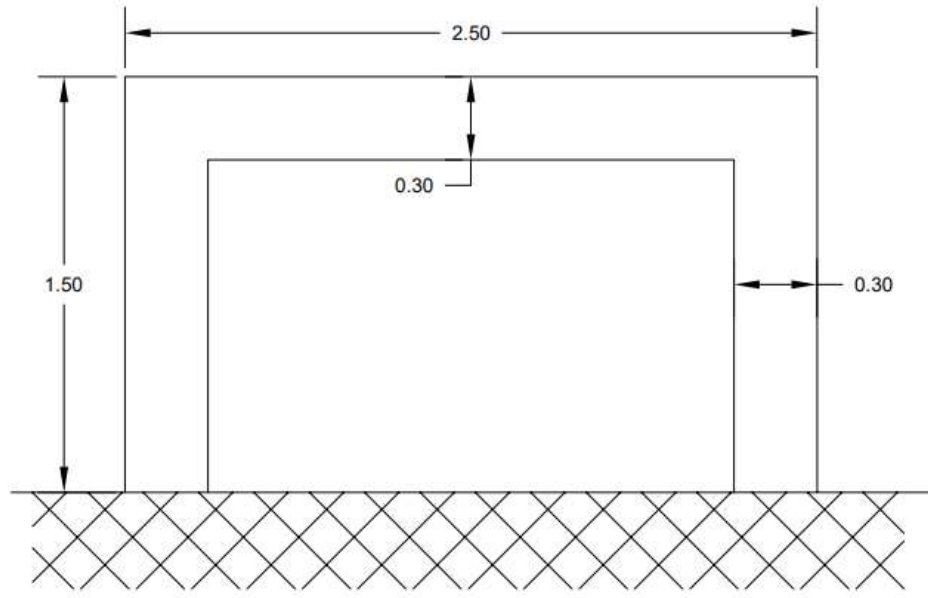


**Figure 2.3: Single story frame used for cyclical testing (m)**

The study was successful in using the accelerometers to interpret changes in the modal properties of the structure as damage progressed. As expected, the moment frame exhibited hairline cracking at the beam-column joints from the first pushover test. As the magnitude of the applied story drift increased, the cracks expanded from the joints and the base of the columns. It was noted that the modal frequencies of the frame decreased sharply with each pushover test. The frequency of mode 1 of the undamaged structure, 40.9 Hz, fell to 13.8 Hz by the conclusion of testing, a change of 65.8%. The damping ratio of the frame varied with each cycle of tests; however, a correlation between damping and damage progression could not be established. It was assumed the opening and closing of cracks during displacement was a major factor in the inconsistent damping ratios. Damage Location Vectors were shown to consistently detect locations where the structural integrity of the frame was compromised. Although this approach to damage detection was not able to accurately quantify the extent of the cracking, it was viable as a means to prioritize areas for visual inspection.

*In situ* applications of accelerometer SHM systems were also proven effective in detecting irregularities in modal properties, as seen in an observational study of several bridges in Tokyo, Japan. Japan lies on the eastern boundary of the Eurasian tectonic plate, making it prone to seismic activity. A research team from the University of Tokyo developed permanent accelerometer-based SHM systems for three bridges in the Tokyo area (Fujino and Siringoringo, 2011). The Rainbow Bridge, Tsurumi Fairway Bridge, and Yokohama Harbor Bridge were designed prior to modern advancements in seismic design codes. The application of SHM systems allowed engineers to evaluate the risk posed to these bridges from ground motions. The structures included suspension and cable stayed bridges that shared a similar framework: three spans supported by towers at each pier. As such, the accelerometer placement for the three bridges followed the same general sensor layout presented in Figure 2.4 and 2.5. Sensors measured acceleration in all three degrees of freedom and were placed at critical locations along the pier columns, tower, and deck.

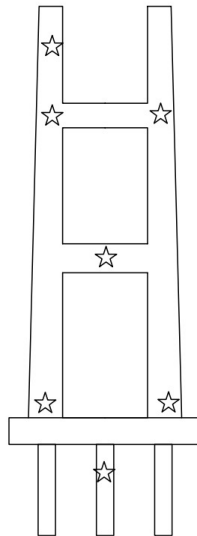


**Figure 2.4: Elevation view of accelerometer placement**

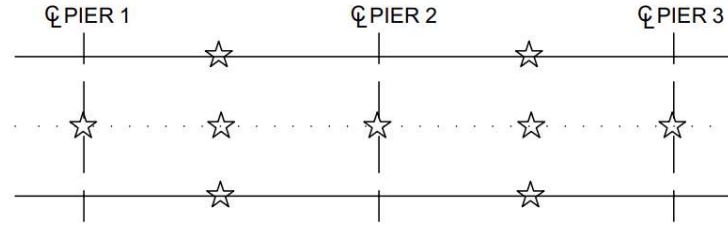


**Figure 2.5: Plan view of bridge deck accelerometer placement**

Of the three structures considered in the study, the Yokohama Harbor Bridge, an 860 m, three-span, cable stayed structure, was unique in its use of link bearing connections between the end piers and girder (Fujino and Siringoringo, 2011). The links were designed to reduce the transfer of forces between the superstructure and substructure, alleviating some of the internal forces in the pier columns. Longitudinal mode shapes, calculated using data collected by the SHM system, revealed discrepancies between the field data and expected performance. The first longitudinal mode demonstrated relatively large displacements, suggesting that a hinge had formed. However, the second longitudinal mode exhibited significantly smaller modal displacements than those predicted. The reason for the discrepancy from the predicted behavior was attributed to the link bearing connections functioning as hinges. This additional unexpected stiffness resulted in greater internal stresses in the columns and increased vulnerability of the superstructure to uplift. Based on the findings, the research team recommended seismic retrofitting by means of externally prestressed cables at the piers.

Accelerometers provide insight on dynamic structural response to all forms of dynamic loadings, not simply seismic events. A survey of structures across Asia considered the Hakucho Bridge, a 720 m long suspension bridge in Muroran, Hokkaido, Japan (Annamdas, Bhalla and Soh, 2017). Vibration from excessive wind conditions posed a

danger to crossing pedestrians and motorcycles. In addition, the wind loading created fatigue conditions similar to those of live loads. Nineteen uniaxial accelerometers were installed along the centerline of the deck across Spans 1 and 2 to measure the transverse excitation. Sensors were spaced evenly at 55 m increments on Span 1 and 30 m increments on Span 2. Baseline data was collected by accelerometers in a series of wind tunnel experiments, revealing a quadratic relationship between wind velocity and bridge damping and stiffness. Using the relationship established, the dynamic behavior captured by the SHM system was used to calculate the physical properties in real time to detect any changes.

Another location that used accelerometers was the Burj Khalifa, located in Abu Dhabi, Dubai. The structure is not located in an area with prolific seismic activity; however, the height of the Burj Khalifa makes the structure susceptible to high wind loads. Standing at 848 m tall, the Burj Khalifa is currently the tallest free-standing structure on the planet. The height of the tower introduced complex structural health concerns and required state-of-the-art structural analysis methodologies. During construction of the Burj Khalifa, researchers from the University of Notre Dame installed a network of accelerometers to measure the sway of the structure as a result of wind loads. In addition, a global positioning system was installed 549 m from the base to measure displacement of the tower from its neutral position. Temperature gauges, humidity sensors, and anemometers document the environmental conditions from a weather station located 495 m from the base.

The initial SHM system was a temporary installation until the completion of the tower, upon which a permanent network was installed. The permanent SHM system expanded capabilities, consisting of a more robust network of accelerometers. Three pairs

of transducers were installed at the foundation level and six pairs at floors 73, 123, 155, 160, Tier 23A, and at the top of the pinnacle. Twenty-three sonimometers, an extremely sensitive and durable anemometer, monitor wind speed and direction at every terrace and setback floor. The SHM system can evaluate the predicted displacement of the tower against the actual displacement recorded by the accelerometers in real time (Annamdas, Bhalla and Soh, 2017).

## **2.3 Finite Element Analysis**

Finite element analysis (FEA) software aids engineers in the design and analysis of structures. Design codes often assume linear-elastic behavior with conservative safety factors to avoid complex non-linear calculations (Taylor and Sanders, 2008). FEA software can be used to make complex design and analyses calculation more accessible, as well as potentially provide more accurate results. FEA simplifies challenging analyses by dividing complex structures and components into smaller subsections, thus resulting in more manageable calculations. FEA software has many functions in structural engineering, including designing new structures, rehabilitating existing structures, and simulating component behavior during failure.

### *2.3.1 Applications of Finite Element Analysis in Structural Engineering*

Using FEA as a load rating tool provides quantifiable data that can be used to assess the condition of structures. A 2010 study assessed the condition of highway bridges throughout Georgia to determine correlations between the condition rating assigned during routine inspections and the actual load capacity calculated by FEM (Wang, 2010). The goal of the study was to propose improvements to the bridge rating system to yield more

consistent and accurate evaluations. The current tolerances permitted by the *AASHTO Manual for Condition Evaluation of Bridges* can lead to the same bridge being assigned inconsistent safety ratings from separate inspections. The four highway bridges selected for the study were meant to represent a majority (up to 77%) of the Georgia Bridge Management System database. The bridges modeled included a straight concrete bridge, a skewed concrete bridge, a prestressed girder bridge, and a steel girder bridge.

The as-inspected bridges were modeled using the commercial FE package ABAQUS. The capacity of the bridges was evaluated using the Georgia Department of Transportation (GDOT) design loads to generate an updated rating factor. The calculated factor was then compared to the respective rating factor assigned during the routine inspection. In all four bridges, the models suggested a higher load capacity than the inspection reports. The study concluded by proposing a refined approach using FEA software to assess the structural health.

As seen in the wake of the 2008 Wenchuan earthquake, seismic events can incapacitate bridges by displacing the substructure footings through dynamic soil movements (Qiang *et al.*, 2009). A similar challenge was observed during the 2016 modeling of the Portage Creek Bridge in Victoria, British Columbia. A SAP2000 model was developed by the British Columbia Ministry of Transportation (MoTI) as part of an effort to rehabilitate and monitor structures vulnerable to seismic conditions (Feng, Kaya and Ventura, 2016). The superstructure and substructure were modeled using traditional frame elements and the concrete deck was input as shell elements. Ground conditions were represented as a link element with user-defined properties. Fixed bearings were modeled

as rigid link elements, while roller bearings were allowed free translation along the longitudinal axis.

The dynamic properties of the Portage Creek Bridge were measured using non-destructive ambient vibration tests and processed using the ARTeMIS software. Calibration of the model was done by manually adjusting the properties of the link elements by trial-and-error until the modal properties in SAP2000 reflected those calculated by ARTeMIS. By increasing the stiffness of the link elements representing roller bearings by more than 100% of the original value, the mode shapes of the model came within a 5.4% tolerance of the mode shapes of the actual bridge.

In addition to being used for design, FEA is one of the most common methods used to determine and simulate modes of failure. In the aftermath of the 2008 Wenchuan earthquake, researchers used the LS-DYNA software to better understand the modes of failure of concrete bridges from seismic loads. The purpose of the study was to verify multiscale FEA modeling as an effective means of failure simulation as well as better understanding the damage inflicted during an earthquake. A multiscale approach observes select locations of the model at both a structural and material level (Hu *et al.*, 2017).

Preliminary tests consisted of creating a solid model and a multiscale model of a simple two-span bridge. Creating the bridge as a solid model offered a more detailed and thorough analysis of the structure at the cost of lower computational efficiency. Comparing variations in analysis results between the two models determined the effectiveness of using a multiscale model. The two models were subjected to modal, quasi-static, and time-history analysis. The results revealed that the multiscale model was marginally stiffer, resulting in

internal forces that were 8.7% greater than those of the solid model. The research team accepted the margin to be within the precision of practical engineering and decided to continue further tests with the simpler multiscale modeling approach.

The second phase of this study was to simulate a four-span reinforced concrete bridge that collapsed during the Wenchuan earthquake using a multiscale model. Sections of the bridge near connections and expansion joints as solid elements, while less vulnerable parts were defined by frame elements. The space for expansion joints was accounted for and frames were connected by solid elements with user-defined properties. Soil conditions were not taken into consideration and ground connections were assumed as fixed. The models were subjected to bi-directional ground accelerations recorded during the 1999 Chi-Chi earthquake.

Similar to the Portage Creek Bridge, the shortest pier was the controlling element. Due to having relatively low ductility, the shortest pier column attracted the largest forces, yielded, and resulted in the subsequent instability and collapse of the remaining structure. Additionally, superstructure collisions between frames at the expansion joints significantly contributed to the forces applied at the pier columns. The study concluded that restrainers and energy dissipation dampers at expansion joints would significantly reduce the load generated by superstructure displacements.



## **CHAPTER 3. GALENA CREEK BRIDGE BACKGROUND**

### **3.1 Description of the Galena Creek Bridge**

The Galena Creek Bridge was constructed in Nevada as part of I-580 Freeway Extension Project to connect Reno and Carson City (Figure 3.1). NDOT designed the Galena Creek Bridge in accordance with AASHTO *Standard Specifications for Highway Bridges, 16th Edition*, including the 2000 interims (NDOT, 2006). Design loads for the bridge included the standard HS-25-44 truck and California P-13 permit vehicle, while the seismic design was based on a 475-year earthquake. The initial design plans consisted of a steel pilot truss arch that would serve as the framework for the cathedral arch; however, disputes between NDOT and the bridge contractor regarding wind loads during construction led to delays in development. Ultimately, the steel pilot truss approach was dismissed in favor of conventional falsework. Construction of the bridge began in 2008 and was completed in 2012.



**Figure 3.1: Galena Creek Bridge location on I-580 south of Reno, NV (Google, 2021)**

The bridge is comprised of two seven-span structures joined by a link slab (Figure 3.2). Hinges in Spans 2 and 4 divide the structure into three frames, each with its own prestressing system. Both the northbound and southbound structures carry three lanes of traffic and experience an average daily traffic of 18,000 vehicles. Each of the 12 piers consists of a single rectangular box column. Span 3 of each structure, measuring 210 m, is supported by a cathedral arch. The bases of the arch and adjacent columns are fixed to a concrete thrust block that is anchored into competent bedrock. The remaining columns are supported by rectangular footings anchored by cast-in-drilled-holes piles of varying depth.

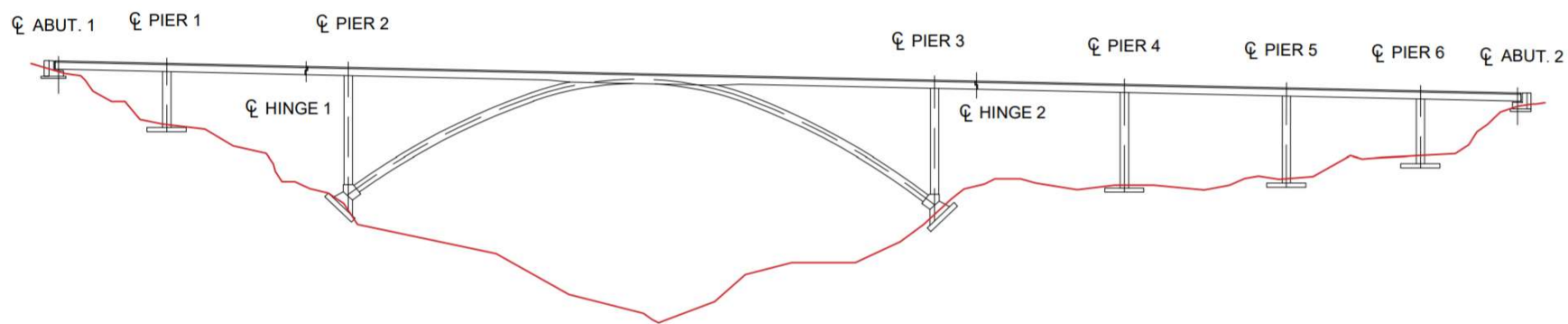


**Figure 3.2: Plan view of east face of Galena Creek Bridge northbound structure**

### 3.1.1 Materials

All reinforcing steel is ASTM A706 Grade 50 and all post-tensioning bars are ASTM A416 Grade 1860 MPa. Eight classifications of concrete, ranging in strength from 25 MPa to 40 MPa, are used for the different components of the Galena Creek Bridge. Table 3.1 details each classification, strength, and application(s).

**Table 3.1: Concrete classification assignments**

<b>NDOT Concrete Classification</b>	<b>Strength (MPa)</b>	<b>Application(s)</b>
AA	28	Abutments, Wingwalls
AA	28	Thrust blocks, Footings
D	25	Cast-in-drilled-hole piles
DA	28	Pier columns
DA	31	Bottom slab, Diaphragms, Girders
DA	40	Bottom slab, Girders, Diaphragms over Pier 2 and 3
EA	31	Approach slab, Barrier rails
EA	31	Top slab, Hinges

### 3.1.2 Superstructure

The superstructure of each bridge consists of a two-cell reinforced concrete box girder that is primarily composed of 31 MPa concrete (Figure 3.3). Additional strength over Piers 2 and 3 is provided by the use of 40 MPa concrete for the bottom slab and girders. The 40 MPa concrete section begins at each hinge and extends 30.6 m towards the arch. The typical box girder section (Figure 3.3) varies at locations along the length of the structure. The thickness of the bottom slab transitions linearly from 200 mm to 600 mm over Piers 2 and 3 and up to 400 mm over Piers 1, 4, 5, and 6. At these locations, the

thickness of the bottom slab extrudes inwards such that the total depth of the girder remains constant.

Span 3 of each bridge is 210 m long and is supported by a cathedral arch. The crown of the arch coincides with the midspan of Span 3. At this location, the arch extrudes 3.55 m into the box girder. A 2.20 m radius fillet melds the intersection of the bottom slab with the arch to minimize the concentration of stresses. The depth of the box girder and the thickness of the bottom slab increase linearly at the junction of the arch and the superstructure. The girder depth increases to 3.56 m and the soffit thickness increases to 0.40 m. Hatches, located at the columns and the arch crown, allow access between the east and west cells of each box.

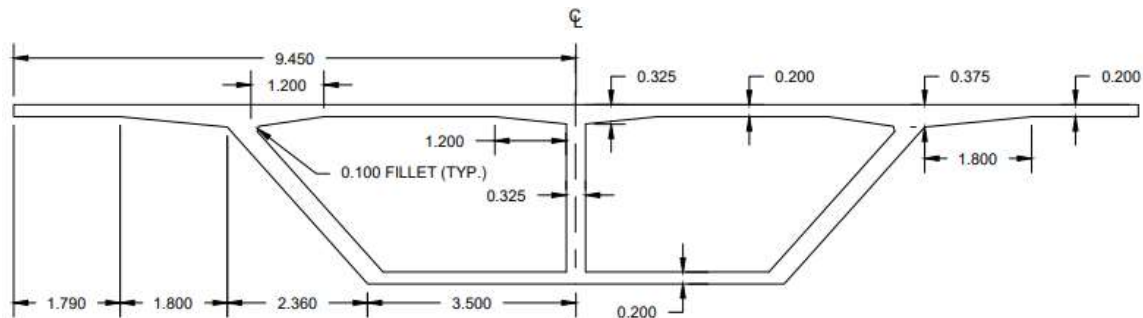


**Figure 3.3: Typical cross section of the two-cell superstructure (m)**

Expansion joint hinges are located 15 m south of Pier 2 and 15 m north of Pier 3, dividing the bridges into three frames. Each hinge consists of an overhang and lower cantilever portion connected by three elastomeric bearing pads (Figure 3.4). The lower cantilevers are elements of Frame 2, and the overhangs are extensions of Frames 1 and 3.

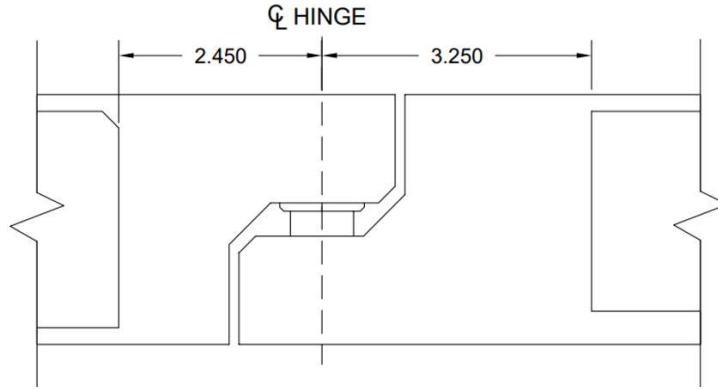


**Figure 3.4: Hinge diaphragm elevation view (m)**

Each frame possesses an internal longitudinal post-tensioning system. Additionally, both expansion joints are reinforced by external post-tensioning. Longitudinal post-tensioning tendons consist of 27 strands with a diameter of 15.24 mm. Internal longitudinal strands are embedded in the web and walls of the box girder. The deck is transversely post-tensioned at the abutments, hinges, and pier caps. Transverse post-tensioning tendons consist of four 15.24 mm strands. Post-tensioning was conducted once the concrete achieved a compressive strength of 24 MPa. The coefficient of friction,  $U$ , was 0.25 for transverse tendons and 0.20 for longitudinal tendons. All tendons are set in 10 mm deep anchors at and have a wobble factor,  $K$ , of 0.00066/m. Table 3.2 provides the tendon quantity, jacking force, and predicted losses for each frame and the deck.

**Table 3.2: Prestressing details**

Location	Number of Tendons	Jacking Force (kN)	Losses (MPa)
Frame 1	9	48,300	179
Frame 2 (Internal)	18	101,300	276
Frame 2 (External)	6	32,600	276
Frame 3	12	64,200	241
Deck (Transverse)	9	812	180

Full height diaphragms of varying thickness (Table 3.3) provide torsional resistance throughout the interior of the box structure (Figure 3.5). Diaphragms are located at the abutments, fillets, arch crown, and midspans. Pier diaphragms coincide with the integral pier columns. Intermediate, fillet, and crown diaphragms provide additional stiffness. Fillet diaphragms mark where the superstructure connects with the arch. A crown diaphragm is located 6.75 m from the crown of the arch on both sides. A single intermediate diaphragm is located close to the midspan of every span, with the exception of Span 3. Span 3 has two intermediate diaphragms located between the fillet diaphragms and the adjacent pier diaphragms.

**Table 3.3: Diaphragm thicknesses**

<b>Diaphragm Type</b>	<b>Thickness (m)</b>
Abutment	1.60
Crown	0.30
Fillet	0.50
Intermediate	0.25
Pier	3.60
Hinge Upper	2.45
Hinge Lower	3.25



**Figure 3.5: North fillet diaphragm at Span 3 of northbound structure**

Additional superstructure elements include the link slab and concrete barrier rails. The 0.20 m thick link slab connects the northbound and southbound structures between the two hinges. The link slab runs the entire length of Frame 2 and is integral with the superstructure. This connection between the twin bridges provides lateral resistance by distributing loads between the two structures. Concrete barrier rails, flush with each end of both decks, were cast after the prestressing was completed. The barrier rail has intermittent expansion joints along the length of the superstructure. Each barrier rail is 1.07 m tall and has a linear weight of 6.503 kN/m.

### *3.1.3 Substructure*

Both the northbound and southbound structures of the Galena Creek Bridge are seven spans and supported by six single-column piers of varying heights (Table 3.4). The hollow rectangular piers have exterior dimensions of 6.0 m x 3.0 m, interior dimensions of 4.0 m x 1.8 m, and 0.15 m chamfers in each corner. The columns are oriented with the 6.0 m face, transverse to the centerline of the bridge, to increase resistance to lateral forces. The cross-sectional dimensions of the columns are uniform while the steel reinforcement varies between the pier columns based on the expected shear and flexural demands (NDOT, 2006). Piers not connected to the cathedral arch sit on 14.0 m x 13.42 m x 2.75 m footings with 12 cast-in-drilled-hole piles having a diameter of 1.22 m. The depth of the piles varies because each was dug to competent bedrock.



**Table 3.4: Column heights**

<b>Pier Number</b>	<b>Northbound Structure (m)</b>	<b>Southbound Structure (m)</b>
1	19.189	16.622
2	38.047	38.049
3	38.769	38.769
4	34.402	19.983
5	31.277	22.158
6	23.935	16.458

The hollow rectangular cathedral arch supporting Span 3 has exterior dimensions of 6.0 m x 3.6 m and interior dimensions of 5.2 m x 2.8 m with 0.35 m chamfers. The interior of the arch is accessed using a manhole from the box girder. Thrust blocks anchor the bases of the arch to the bottom of the columns at Piers 2 and 3. The footings for Piers 2 and 3 have dimensions of 15.65 m x 12.0 m x 2.0 m and 18.05 m x 12.0 m x 2.0 m, respectively. Footings for both piers are angled at 36°52'12" towards the arch and fixed to the bedrock using 12 steel anchors. The thrust blocks of both piers are connected by a 4.0 m x 6.0 m link beam to further resist lateral loads.

#### *3.1.4 Bearings*

Reinforced elastomeric bearing pads are located at the abutments and expansion joints to permit translation of the superstructure. Each of these locations have three bearing pads spaced at 2.88 m, with the middle bearing aligned with the centerline of the superstructure. All bearings are composed of 60 durometer elastomer and reinforced by alternating layers of elastomer with 2.0 mm thick steel plates. The hinge bearings have a

length of 0.71 m, transverse width of 0.76 m, and a height of 0.29 m. The length, width, and height of the abutment bearings are 0.64 m x 0.64 m x 0.12 m, respectively.

### **3.2 Previous Galena Creek Bridge Research**

#### *3.2.1 Taylor & Sanders, 2008*

Taylor and Sanders of the University of Nevada Reno conducted the first research on the Galena Creek Bridge in 2008. The purpose of the first UNR study was to perform a non-linear time-history seismic analysis of the Galena Creek Bridge using SAP2000 v.14 (Taylor and Sanders, 2008). The results of the non-linear analysis were compared to the response spectrum from the original bridge design to better understand the dynamic properties of the structure. The original scope of the study was to install 108 strain gages with thermistors to the steel pilot truss arch to document the response to thermal stimuli during the construction. Due to constructability complications, construction was delayed, and the contractor opted for traditional formwork. The construction monitoring project was retired, and the focus became to better understand the dynamic behavior of the bridge under seismic excitation using a FEM.

The bridge was modeled in SAP2000 using predominantly two-dimensional frame elements. Gap and hook elements were used to simulate the non-linear behavior of the bearings at the hinges and abutments. Elastic-perfectly-plastic non-linear link elements simulated soil conditions. To determine the dynamic response, the model was subjected to time-history accelerations along all three axes. However, one of the challenges faced by the research team was limited ground motion data available for seismic activity in Walker Lane. The model was subjected to seven unique ground motions, as proposed by FEMA,

meant to simulate seismic activity of the area. The ground motions selected ranged from magnitude 6.0 to 7.8. The average response from the seven unique ground motions was used to determine the most likely structural behavior.

Non-linear time-history analysis was shown to be an effective method to observe the seismic response of the structure. The mode of failure for the column and arch members was flexure due to their large unbraced lengths. Moment curvature plots were used to observe plastic hinging behavior of the bridge substructure and Takeda hysteresis models were used to determine the moment-rotation response. A non-linear response spectrum was then calculated by scaling linear-elastic response spectrums based on factors from the Federal Emergency Management Agency (FEMA) 356 design code. Taylor proposed that this more elaborate method of analysis be reserved for complex structures. Simply by applying several modification factors, the elastic response provided reasonable conservative estimates of the behavior from elastic response spectrum analysis.

### *3.2.2 Carr & Sanders, 2013*

During a second study by UNR in 2013, Carr and Sanders used a SHM system in conjunction with an FEM to document the dynamic properties of the completed Galena Creek Bridge (Carr and Sanders, 2013). The SHM system consisted of a series of accelerometers located along the southbound superstructure. Data was collected from a series of field tests to determine the modal properties of the finished structure. A modal analysis was used to establish the accelerometer placement along Frame 2. Four uniaxial sensors and four biaxial sensors were attached to the deck at 30 m intervals. Five triaxial sensors were situated at the bottom and top of the piers adjacent to the arch and the crown

of the arch. The blue stars in Figure 3.6 mark the superstructure sensors and the orange rhombus mark the substructure sensors. A FEM of the Galena Creek Bridge was developed in SAP2000 v14.2.4 and calibrated to simulate the behavior of the structure.

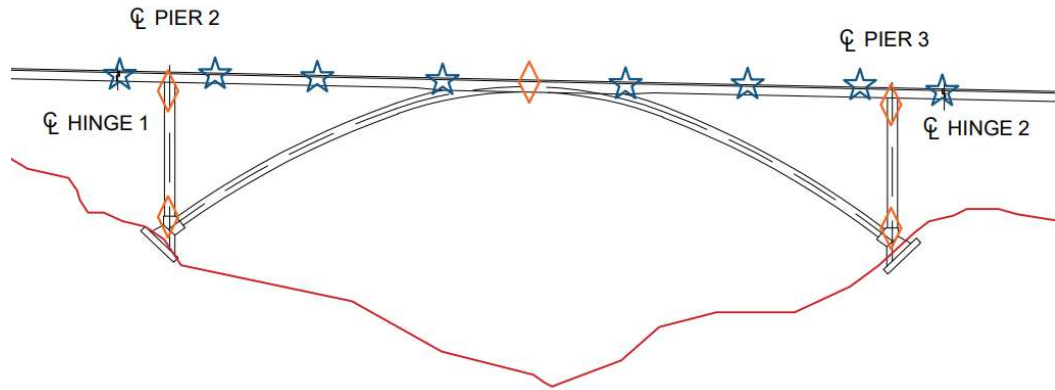


**Figure 3.6: The superstructure (blue) and substructure (orange) accelerometer placement**

Two series of field tests were conducted to test the system: vertical and transverse loadings. For the first set of tests, a Volvo A40F truck crossed the bridge at varying speeds as well as driving over a 0.15 m ramp to measure the bridge response to vertical excitation. The first test had the truck traverse the ramp slowly to simulate a single static point load. Following the static tests, the experiments were conducted with the truck crossing the bridge at constant velocities of 22.4, 33.6, and 55.9 m/s. The second set of tests applied a transverse excitation to the bridge by mounting an eccentric mass shaker to the link slab that connects the northbound and southbound structures. The measured acceleration data from all tests were compared to the behavior of the SAP2000 models.

The SAP2000 model was primarily defined using 2-D frame elements. The expansion joints between the hinges were modeled using link elements that restricted translation in the transverse and vertical directions and limited rotation about the longitudinal axis. The link slab connecting the northbound and southbound structures was

replicated using rigid link and shell elements. Post-tensioning was simulated using external loads applied to the structure. The behavior of the SAP2000 model was limited to fully elastic because of the computational resources associated with a non-linear analysis.

Comparing the frequencies of the primary mode shapes between the FEM and the measured field data revealed that the model typically underpredicted the peak accelerations from the truck experiments. Carr proposed that the discrepancies were a result of difficulties simulating truck loads on the SAP2000 model and predicted that a single degree of freedom system to model the truck loading would produce more accurate results.

### *3.2.3 Falkensammer, 2018*

The primary purpose of the 2018 Galena Creek Bridge study was to finalize the sensor type for the seismic monitoring system, determine sensor locations, and begin development of a FEA model of the structure (Falkensammer, 2018). Further, the study proposed a secondary SHM system to expand the reliability and capabilities of the primary seismic SHM system for additional signal types and load responses. Although the accelerometers had been proven as an effective seismic SHM system through their use in the NSMP, the inclusion of additional sensors would generate a more comprehensive report on the condition of the bridge, providing a more complete SHM test-bed for NDOT.

A major focus of the initial research was the development of a FEA model using CSiBridge. The ultimate purpose of the model was to calibrate it to field measured data. The initial model was defined using the Bridge Wizard tool to expedite the modelling process. Additional modelling considerations, such as the link slab and arch, were incorporated after the Bridge Wizard inputs. The superstructure and link slab were defined

as shell elements, while the pier columns and arches were modelled as frame elements. As with the SAP2000 model from the UNR study, the future wearing surface (FWS) and barrier rail were applied as external loads to the superstructure. To confirm the validity of the initial modelling procedure, the dead load of the structure, as computed in CSiBridge, was compared to hand calculations. The calculated self-weight was 499.0 MN compared to the 502 MN extracted from CSiBridge; a difference of only 0.6%.

The primary mode shapes and modal periods from the CSiBridge analyses were compared to the 2013 UNR model. It was noted that the periods for the primary modes about all three axes were lower than those of the SAP2000 model, suggesting that initial model had an increased stiffness. The boundary conditions of the model were reevaluated to determine the reason for the increased stiffness. It was noted that the shear keys at the abutments restricted transverse displacement but permitted longitudinal translation due to the elastomeric bearings. As such, the abutment restrictions were shifted from fully-fixed bearings to allowing displacement about the longitudinal axes. The bearings connecting the frames were also reconsidered for the final model. The bearing stiffnesses were calculated and assigned to the links connecting the frames to better model the connection between bridge frames. The adjustments had the intended effect of increasing the modal periods throughout, resulting in an average of 6.2% difference between the top transverse modes of the CSiBridge and SAP2000 models. The study concluded by recommending further research to improve the modelling techniques and the understanding of the dynamic properties of the Galena Creek Bridge, leading to the current research.

### **3.3 Nevada Department of Transportation Reports**

#### *3.3.1 Bridge Inspection Report, 2018*

Routine bridge inspections of the Galena Creek Bridge are performed by NDOT personnel every 24 months (CFR §650, 2021). Visual inspections and non-destructive testing are used to evaluate the condition of the bridge elements. Due to the size and location of the bridge, inspections require the use of under bridge inspection units (UBIT), ladders, and rope access climbing methods. The bridge is situated several hundred meters over the Galena Creek; however, the waterway does not impact the footings; as such, degradation measurements are not required. The underground cast-in-place piles were not evaluated during routine inspections. Both the northbound and southbound structures were given a “low risk” rating. Superficial cracking, light efflorescence, minor spalling, and some exposed rebar did not demonstrate notable impact to the structural integrity. The inspection report was reviewed on 08/08/2018 and sealed by an NDOT Professional Engineer on 12/31/2018. Note that although the original bridge design was in metric, inspection reports are documented using imperial (US) units.

The top flange soffit exhibited transverse cracking with efflorescence throughout both bridges. The cracks were generally hairline cracks, expanding up to 3 mm wide. Efflorescence staining was also noted at cracks originating from construction joints. An exposed epoxy coated rebar with minor rusting was noted at the underside of the overhang in Span 2 of the northbound structure. The exterior and interior girders, similarly, had transverse hairline cracking with efflorescence throughout. Diagonal shear cracking up to

1 mm wide was noted at pier and hinge locations. The east exterior girder exhibited more prolific cracking than the west girder, likely due to exposure to ultraviolet light.

Longitudinal cracking was noted throughout the interior of the bridge arches, most notably at the thrust blocks. Arch diaphragms exhibited vertical cracking along the full height of the section. Vertical cracks up to 1 mm wide were noted at the fillet where the arch meets the superstructure. Pier columns showed signs of shrinkage cracking up to 1 mm wide and moderate honeycombing up to 6 mm deep. Hairline cracking was sporadic on both the interior and exterior of the pier columns. Spalls up to 25 mm deep stemmed from construction joints. Piers 5 and 6 had ponding water up to 20.3 cm deep, most likely a result of groundwater infiltration. Both abutments displayed isolated hairline cracks along the backwall and wingwalls. Expansion joints, hinges, and drainpipes accumulated typical debris that did not hinder the intended functions.

Although several sprinkler heads appeared slightly depressed, the ice removal system was not tested. Maintenance to be performed before the next inspection included cleaning the deck drains, cleaning the expansion joints, and replacing the preformed joint filler. The hinge crawl space was also to be cleaned and covered to avoid the buildup of further debris. Further suggested maintenance included replacing the chain link fence situated on the concrete barrier, re-applying a protective coating to the substructure, and patching any spalls.

### *3.3.2 Load Rating Report, 09/13/2016*

A load rating report of the superstructure was performed by NDOT using SAP2000, WinBDS 5.0.3, and PTRater 4.2 based on the 05/22/2014 bridge inspection report. The live



loads used for the analysis were the AASHTO HS20-44 truck and lane loads as well as California permit vehicles P5, P9, and P13. The rating factors for P7 and P11 trucks were interpolated based on the results of the evaluated California permit vehicles. The results of the load rating analysis, as shown in Table 3.5 and 3.6, state that the bridge has sufficient strength to carry the designated live loads. In addition, it should be noted that the mode of failure for each case was flexure.

**Table 3.5: Inventory Vehicle Load Rating Results**

Vehicle	Rating Factor	Method of Failure
HS20-44	1.37	Flexure

**Table 3.6: Operating Vehicle Load Rating Results**

Vehicle	Rating Factor	Method of Failure
HS20-44	2.29	Flexure
P5	2.88	Flexure
P7	2.28	Flexure
P9	1.67	Flexure
P11	1.45	Flexure
P13	1.23	Flexure

## **CHAPTER 4. STRUCTURAL HEALTH MONITORING SYSTEM**

### **4.1 Introduction**

As part of the National Strong Motion Project, the United States Geological Survey (USGS) installed an accelerometer-based SHM system at 28 hospitals and two university campuses to monitor the building response to seismic activity. This proven system was adapted for a bridge application and implemented on the Galena Creek Bridge. A network of uniaxial accelerometers served as the foundation for the primary seismic SHM system. The accelerometers were located throughout the structure, as seen in Figure 4.1, based on modal analyses of the bridge. The selected layout provided a comprehensive image of the dynamic response.

A secondary exploratory SHM system was developed that consisted of four potentiometers, two inclinometers, an anemometer, and two temperature gauges. The sensors were installed on the bridge, as seen in Figure 4.2. The secondary system was designed to be used in conjunction with the accelerometers to provide additional data on the bridge response during seismic events as well as from routine traffic and environmental effects. All sensors for both systems were connected by wires to data recording systems stored inside a de-icing utility shed located adjacent to the bridge (Figure 4.3). The manufacturer specification sheets for the sensors listed in this chapter are available in Appendix B.

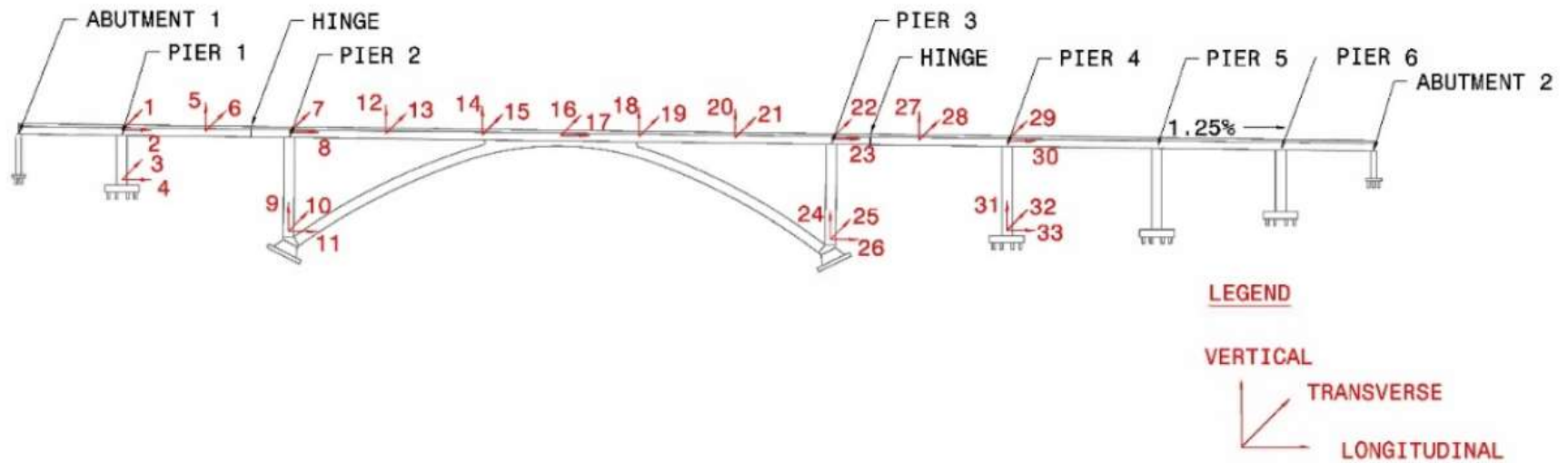
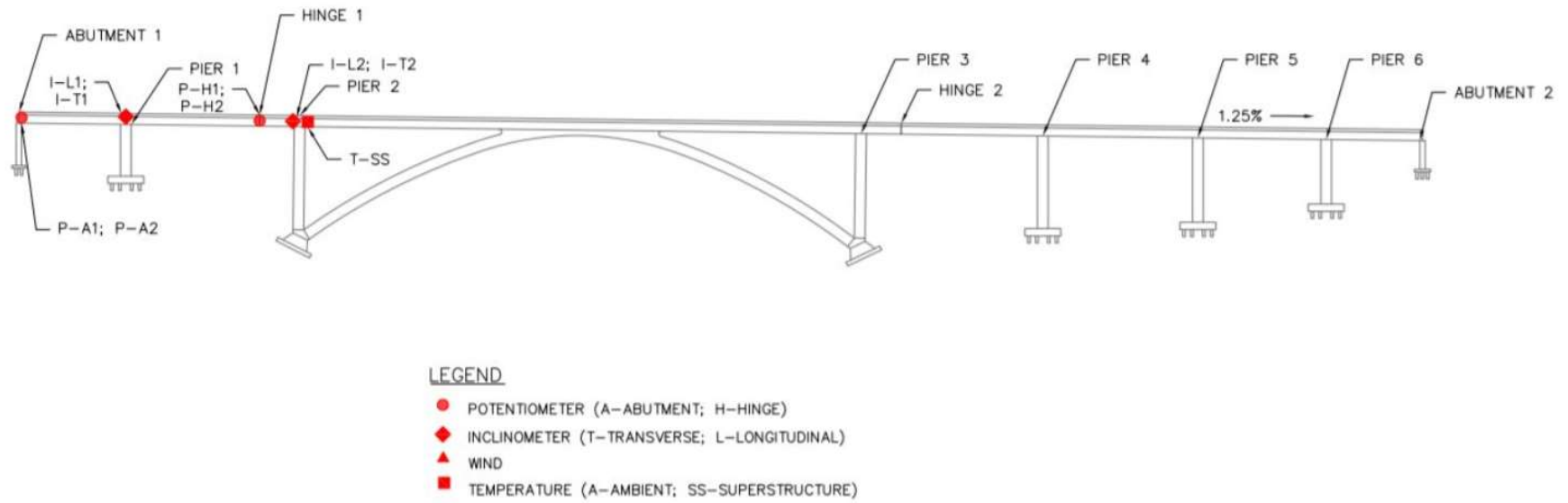


Figure 4.1: Primary seismic SHM system uniaxial accelerometer locations on the Galena Creek Bridge



**Figure 4.2: Secondary exploratory SHM system sensor locations on the Galena Creek Bridge**



**Figure 4.3: Utility shed located south of the southbound structure**

## **4.2 Primary Seismic System**

### *4.2.1 Accelerometers*

The primary network of sensors consisted of 33 Kinometrics EpiSensor ES-U2 uniaxial accelerometers (Kinometrics, 2021). Designed to produce low levels of self-noise, the selected accelerometers are intended for SHM applications. The sensors are capable of recording accelerations between  $\pm 0.25g$  and  $\pm 4.00g$  and vibrations ranging from 1 Hz to 200Hz, providing the option to select the limits. Each sensor measures 55 mm x 65 mm x 97 mm and weighs 0.35 kg (Figure 4.4). The ES-U2 were designed for use in rugged conditions, housed in a watertight enclosure and an operating temperature range between  $-20^{\circ}$  and  $70^{\circ}C$ .



**Figure 4.4: Kinemetrics ES-U2 accelerometer**

Previous Galena Creek Bridge research by UNR utilized uniaxial, biaxial, and triaxial accelerometers (Carr and Sanders, 2013). The exclusive use of uniaxial accelerometers was the optimal choice for this project. Uniaxial sensors are more cost effective than their more complex counterparts. In the case of sensor failure, the cost to replace a single unit is significantly lower for a uniaxial accelerometer. Additionally, failure of a triaxial sensor would result in a complete loss of data from that location. Should a uniaxial accelerometer stop functioning, the other sensor(s) at that location would continue to provide feedback, mitigating potential data loss. Finally, most sensor locations did not require acceleration measurements along all three axes; therefore, use of uniaxial accelerometers resulted in the most efficient and flexible system design.

Accelerometers were located throughout the Galena Creek Bridge to capture critical responses during a seismic event (Table 4.1). The number of sensors and orientation (i.e., longitudinal, transverse, and vertical) at each location were optimized to collect relevant data to inform engineers and inspectors of the bridge condition. Sensors were

typically located at the top and bottom of piers, arch section, and along the length of the superstructure (Figure 4.1).

Longitudinal sensors were located at the top and bottom of Piers 1 through 4 and the crown of the arch. Frame 1 is supported by Pier 1 which has a column height of 19.189 m, marking it as the shortest column of the bridge. As previously discussed, shorter columns often result in high internal stresses and greater accelerations transferred to the superstructure. Conversely, Piers 2 and 3 are the tallest columns of the structure and are expected to experience the largest displacements.

Vertical sensors were located at the bottom of Piers 2 through 4 as well as at the midspan of Spans 1 and 4, arch-superstructure merge, and halfway between the merges and adjacent piers (Figure 4.1). The locations along the superstructure furthest from the substructure components are most prone to vertical displacements. Discrepancies between the sensors at the bottom of the piers and the free-field site may indicate that the substructure foundations have been compromised.

The Galena Creek Bridge is most vulnerable to lateral forces because the structure is the most flexible in the transverse direction. Therefore, transverse sensors were located at every accelerometer location.

**Table 4.1: Accelerometer location and orientation**

Sensor Number	Direction	Location
1	Transverse	Top of Pier 1
2	Longitudinal	
3	Transverse	Bottom of Pier 1
4	Longitudinal	
5	Vertical	Midspan of Span 2
6	Transverse	
7	Transverse	Top of Pier 2
8	Longitudinal	
9	Vertical	Bottom of Pier 2
10	Transverse	
11	Longitudinal	
12	Vertical	Midspan between Pier 2 and south merge
13	Transverse	
14	Vertical	South arch/superstructure merge
15	Transverse	
16	Transverse	Crown of Arch at Span 3
17	Longitudinal	
18	Vertical	North arch/superstructure merge
19	Transverse	
20	Vertical	Midspan between Pier 3 and north merge
21	Transverse	
22	Transverse	Top of Pier 3
23	Longitudinal	
24	Vertical	Bottom of Pier 3
25	Transverse	
26	Longitudinal	
27	Vertical	Midspan of Span 4
28	Transverse	
29	Transverse	Top of Pier 4
30	Longitudinal	
31	Vertical	Bottom of Pier 4
32	Transverse	
33	Longitudinal	



#### *4.2.2 Sensor Installation and Wiring*

Accelerometers were installed at 15 locations along the northbound structure. A 30.5 cm x 30.5 cm x 0.7 cm anodized aluminum plate was fabricated for each of the 15 locations (Figure 4.5). Up to three sensors could be attached to each plate to measure acceleration in all three axes (Figure 4.6). The plates were attached to the interior walls of the structure using concrete anchor screws. The concrete surface was not smooth; therefore, the plate provided a flat surface to mount the accelerometers. In addition, the plate was designed with slotted holes to facilitate leveling to ensure the sensors were accurately aligned in each direction. Each accelerometer was then be mounted to the plate in the desired orientation using hex nut screws. The final step was leveling all sensors to ensure accurate measurements.

The sensors were connected to the data recorder by 15 primary cables (i.e., one to each sensor location throughout the bridge). The cables were routed through PVC conduits that extend from the north wall of the utility shed, along the wingwall and face of Abutment 1 (Figure 4.7), and through the bottom slab of Span 1 (Figure 4.8). The cables were suspended along the length of the structure on L-shaped brackets mounted to the east girder of the box, until the desired sensor location (Figure 4.9). Terminal blocks were used to connect each accelerometer to the primary cable (Figure 4.10). Each primary cable contained wires to connect up to three sensors using the terminal block, although not all sensor locations (Figure 4.1) required three accelerometers.



**Figure 4.5: Aluminum plate for mounting accelerometers**

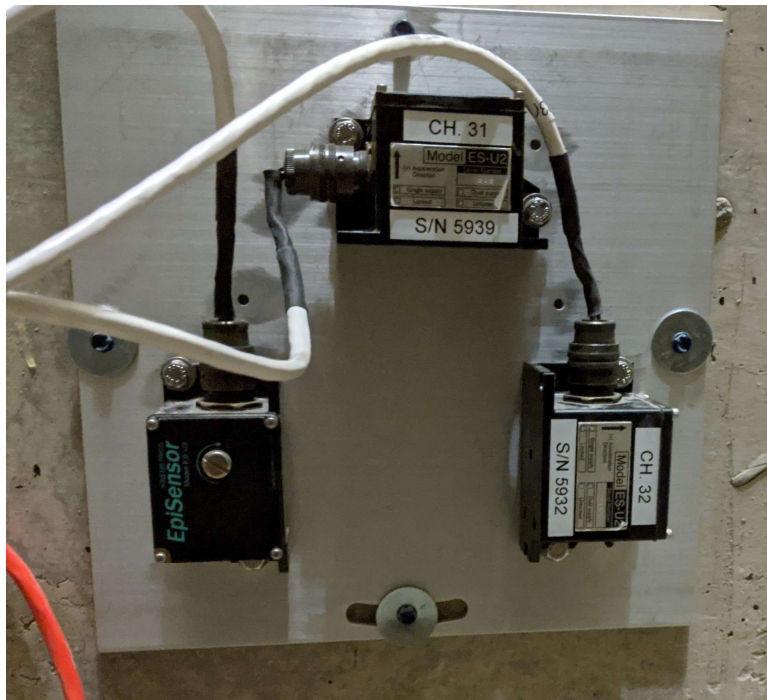


**Figure 4.6: Example of plate with three sensors at bottom of Pier 4**



**Figure 4.7: PVC conduits along the face of Abutment 1**



**Figure 4.8: PVC conduit extruding through the bottom slab near Abutment 1**



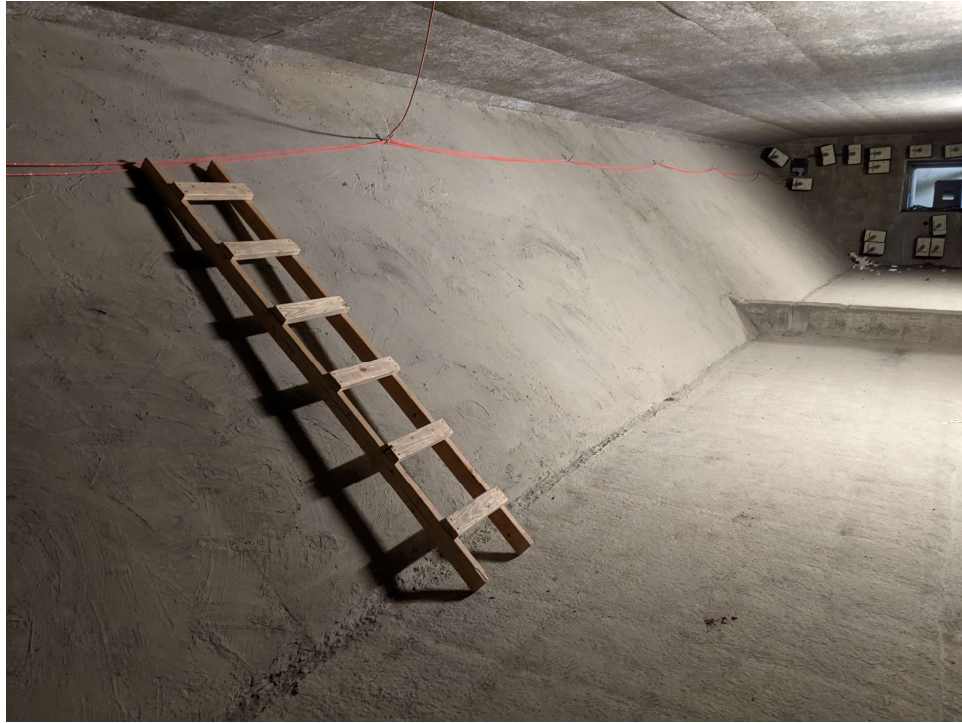


**Figure 4.9: Typical cables running along the east girder of the superstructure**

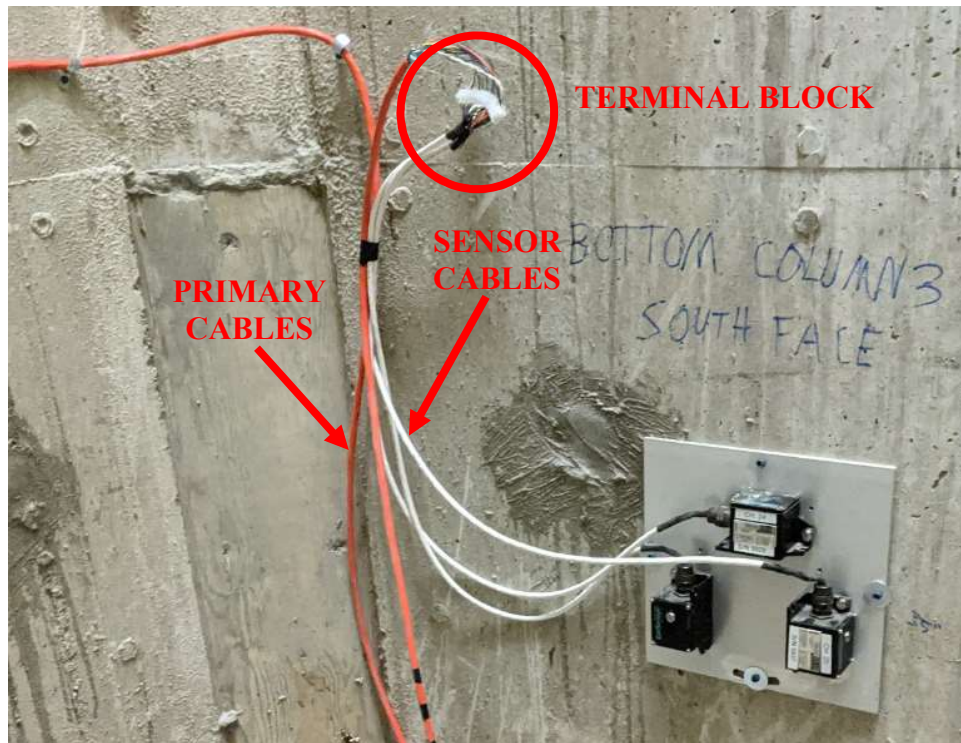


**Figure 4.10: Typical connection between primary and sensor cables via terminal block**

### 4.3 Secondary Exploratory System

The USGS installed seismic SHM systems at 28 hospitals and two universities as part of the National Strong Motion Project, successfully demonstrating accelerometer-based SHM systems. Development of a secondary exploratory SHM system further expanded the scope of the primary SHM system by adding additional sensor types to measure additional responses. The secondary system consists of displacement, tilt, temperature, and wind sensors.

#### 4.3.1 *Displacement sensors*

UniMeasure HX-P510 string potentiometers (Figure 4.11) were installed on the Galena Creek Bridge to observe longitudinal displacement between the Frame 1 superstructure and adjacent components during both seismic activity and routine thermal expansion and contraction (UniMeasure, 2021). Monitoring the expansion joints reveals if the bearings at the hinges and abutments are functioning as intended. The displacement sensor dimensions and weight are 120 mm x 74 mm x 74 mm and 900 g, respectively. Each sensor contains a 0.4 mm diameter string that extends along a single axis up to 2.0 m. The transducer records variations in the extension and retraction of the string with a typical margin of error of  $\pm 0.3\%$ . The HX-series are designed for rugged, field environments. The sensors are made to function within  $-40^{\circ}$  and  $85^{\circ}\text{C}$  and are resistant to water and corrosion.



**Figure 4.11: UniMeasure HX-P510 Series Linear Potentiometer**

A pair of displacement sensors were attached the face of Abutment 1 to measure the longitudinal displacement of Frame 1 relative to Abutment 1, as seen in Figure 4.12. The sensors were mounted on the face of the abutment at each side of the bottom slab of the box girder. They were oriented such that the string lay parallel to the superstructure, approximately 20 cm below the bottom slab. The potentiometer string was attached to a custom mounting bracket that was installed on the underside of the bottom slab of the bridge.



**Figure 4.12: Potentiometer located at west edge of Abutment 1 of northbound structure**

The second pair of potentiometers were installed at Hinge 1 to monitor the expansion joint and relative movement between Frames 1 and 2. The sensors also provided data regarding the bearing function (Figure 4.13). The first sensor was attached to the east wall of the east cell, while the second sensor was mirrored on the west wall of the west cell. Displacement discrepancies between the potentiometers at each pair indicate irregularities of the structure expansion as related to twist.

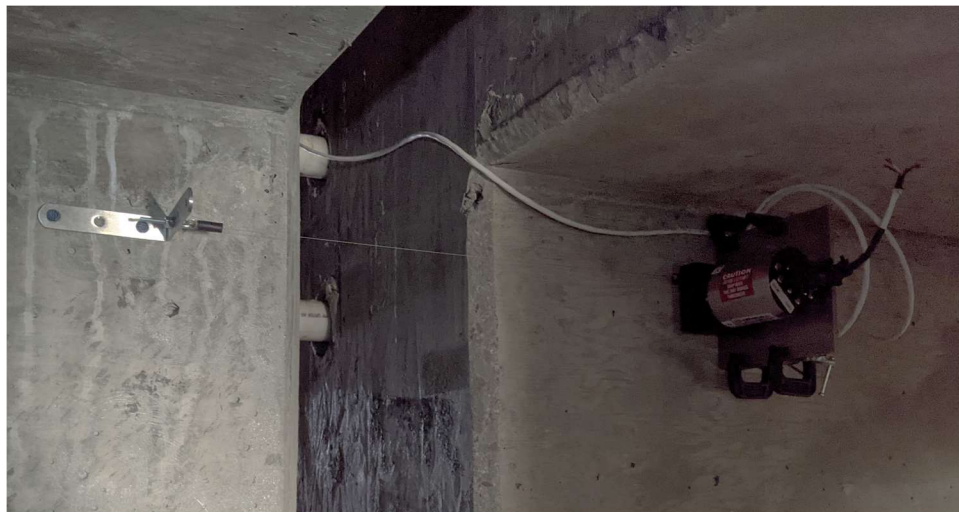


**Figure 4.13: Example of potentiometer installed at Hinge 1**



#### 4.3.2 Tilt Meter

Reiker Flex Series H6 inclinometers were used to observe rotation at the top of Piers 1 and 2. The biaxial sensors can detect changes in angle up to  $\pm 180^\circ$  about two axes in  $0.05^\circ$  increments with a margin of error up to  $0.2^\circ$ . The inclinometers are designed for field-environments, with a temperature range between  $-40^\circ$  and  $85^\circ\text{C}$  and waterproof housing. The sensor measures 110 mm x 82.8 mm x 45.7 mm and weighs 525 g (Reiker, 2021).



**Figure 4.14: Reiker Flex Series H6 biaxial inclinometer installed a south face of pier diaphragm at Pier 2**

The tilt meters were installed at the south face of the pier diaphragms at Piers 1 and 2 oriented along the vertical and transverse axes of the bridge. The data collected by the primary system reveals variations in acceleration and displacement between the top and



bottom of the columns. The inclusion of inclinometers provides a better representation of column behavior by recording changes in tilt to indicate warping of the columns and superstructure. Inclinometers can also indicate disturbances in the superstructure in the case of foundation displacement due to settlement as well as column tilt due thermal expansion and contraction of the superstructure.

#### *4.3.3 Temperature gauges*

An R.M. Young Model 41342 Temperature Probe was mounted to record ambient temperature outside the shed. A second probe was located inside the bridge. The sensors were installed with multi-plate, aspirated radiation shields which protected the sensor from solar and environmental damage. The temperature gauges had an effective range of  $\pm 50^{\circ}\text{C}$  with an accuracy of  $\pm 0.3^{\circ}\text{C}$ . Temperature measurements are used to correlate between the environmental conditions and the longitudinal displacements of the bridge (Young, 2021).



**Figure 4.15: R.M. Young 41342 temperature probe located in Galena Creek Bridge**

The sensor located inside the bridge was installed on the east face of the web, roughly 2 m north of the intermediate diaphragm of Span 1. Note that the probe measures

the temperature of the surrounding air. Due to the insulation provided by the exterior concrete walls of the box, it is assumed that there is a negligible temperature difference between the air temperature inside the bridge and the concrete superstructure. The second sensor was installed on a mounting bracket on the west wall of the shed (Figure 4.3). The sensor was located 1 m above the roof of the shed to mitigate influence from radiation off solid objects.

#### *4.3.4 Wind Sensor*

An R.M. Young 86000 Ultrasonic Anemometer, developed by Meteorological Instruments, was used to record the magnitude and direction of wind. The sensor transmits and records feedback from ultrasonic pulses emitted by three nodes, thereby accurately measuring wind speed without moving mechanical parts. The elimination of moving components greatly improves the reliability and durability of the anemometer. The wind speed measurement range is between 0 m/s to 75 m/s with changes in velocity in 0.01 m/s increments. The sensor can detect wind direction about the plane perpendicular to the axis about which it is mounted. The wind direction feedback is provided in up to  $0.1^\circ$  and is guaranteed accurate within  $\pm 2^\circ$ . The sensor measures 29 cm in height and 11 cm in diameter (Young, 2021). The anemometer was installed on a bracket to the exterior of the shed. To provide the sensor with unobstructed data, the bracket extrudes 1.5 m above the roof of the shed, as seen in Figure 4.3 and Figure 4.16. While it is unlikely that wind conditions would have a significant impact on the health of the structure or the dynamic behavior, the addition of the anemometer demonstrates the effective integration of this sensor into the global SHM system.



**Figure 4.16: R.M. Young 86000 ultrasonic anemometer installed at utility shed**

#### **4.4 Data Recorders**

Both the seismic and secondary SHM systems had individual data recorders located in the utility shed. The primary SHM system utilized a Kinometrics Obsidian 36X data recorder, while the secondary sensors employed a Kinometrics Obsidian 12X data recorder (Figure 4.17). The Obsidian 36X system has a 36-channel capacity, 33 of which are used for the primary seismic monitoring system. The Obsidian 12X system has a 12-channel capacity that was fully utilized for the secondary sensors. The Kinometrics Obsidian hardware was developed for seismic SHM. The hardware was chosen for its capacity to process significant influx and deliver outputs to analysis software. Each unit is preset with several default formats upon which to record and display data. The data recorders are resistant to water and fully operational between temperatures of -20° and 70° C.

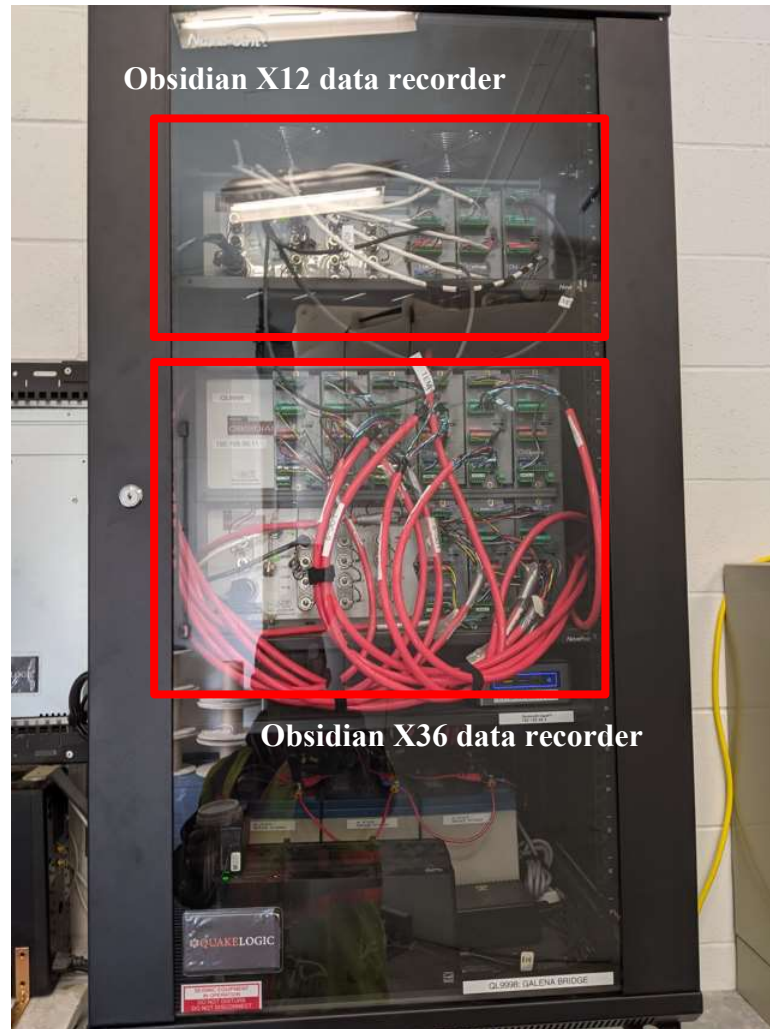


**Figure 4.17: Kinometrics Obsidian 12X (top) and 36X (bottom) data recorders with cables**

Each data recorder is capable of wireless communication through a USB-based Wi-Fi connection. Both data recording systems were wired to separate Bullet III GPS antennas that were mounted on the exterior of the north wall of the utility shed (Figure 4.18). The head of the antenna was 77.5 mm in diameter and measured 66.2 mm tall.



**Figure 4.18: Bullet III GPS antennas**

#### **4.5 Free-field Station**

A Kinemetrics ETNA 2 accelerograph was used as a free-field station to record the local ground motions due to seismic activity. The ETNA 2 casing holds a triaxial accelerometer and internal data recording system. The accelerograph is capable of recording ground motions of up to  $\pm 4g$ ; the range is selectable by the user. A built-in GPS allows the system to note the orientation of the ground motions without the need of additional sensors. The internal data recording system has a capacity of 32 GB. The system is compatible with a USB-based Wi-Fi connection or cellular modem. The ETNA 2 measures 15 cm x 15 cm x 7.5 cm, weighs 1.5 kg, and is operational between temperatures of  $-20^{\circ}$  and  $70^{\circ}$  C. The unit is mounted to the wall of the utility shed and enclosed in a protective case as seen in Figure 4.19.



**Figure 4.19: Kinematics ETNA 2 accelerograph and protective case**

## CHAPTER 5. DEVELOPING THE CONTROL MODEL

### 5.1 CSiBridge Background Information

Computers and Structures, Inc. (CSI) is a California-based software company that produces structural and earthquake engineering software. Their flagship finite element analysis (FEA) software, SAP2000, accommodates a wide range of structural engineering applications, from bridges and buildings to dams and communication towers. The versatility of SAP2000 is due, in part, to the array of tools offered to model structures. Link, shell, frame, and user-defined elements can be assembled in countless ways to suit general structural engineering needs. Although SAP2000 is a capable FEA modeling software for bridge engineering, CSI offers CSiBridge as a more specialized instrument for bridge applications. CSiBridge includes features such as prestressing, hinge and bearing properties, vehicular live loads, and staged construction analysis, thereby making it a suitable choice for the Galena Creek Bridge analysis. Figure 5.1 is an example of the preliminary control model of the Galena Creek Bridge created in CSiBridge v22.1.0.

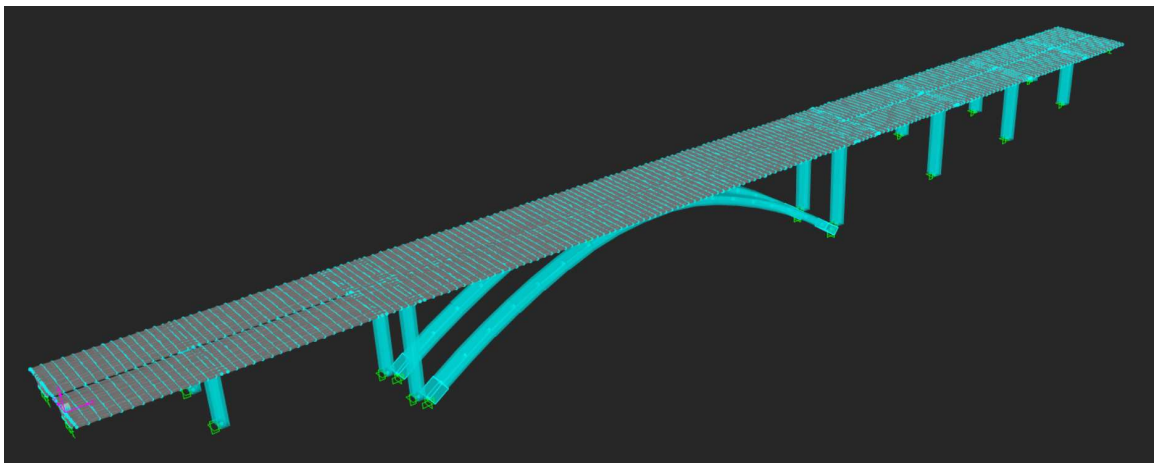


Figure 5.1: Preliminary control model

The following sections provide a detailed description of the development of the Galena Creek Bridge control model. Each section is written in the form of a modeling guide to allow future readers the ability to follow the development process and recreate the model. CSiBridge includes a “Bridge Wizard” feature to guide the user through each input required to create a functional bridge model. The feature can provide time savings, especially for routine structures. However, the Bridge Wizard was not employed to model the Galena Creek Bridge due to the structure complexity. A manual approach was selected to enable a better understanding of how input parameters influenced the model response and resulting output. Furthermore, the selected approach more readily facilitated model refinements as field-measured data was collected and used to refine the initial model.

## **5.2 Layout Tab**

The Layout Tab is where the global coordinate system is defined, thereby setting the basic orientation of the bridge. The global x-axis was in the longitudinal direction, the y-axis denotes the transverse direction, and the z-axis represents the vertical direction. CSiBridge utilizes a user-defined layout line as the template upon which the bridge is modeled. For live load analyses, vehicle lanes can also be defined in the Layout Tab which are then applied as two-dimensional surfaces along the top slab of the bridge.

The primary units for force, length, and temperature are defined in the Layout Tab. The Galena Creek Bridge was designed using the metric system; therefore, the model employed units of kilonewtons (kN) for force, meters (m) for length, and Celsius (°C) for temperature.



The first step of the modeling procedure was to define layout lines which serve as the reference upon which the structure is built. For the Galena Creek Bridge, layout lines for both the northbound and southbound structures had an initial bearing of N90E, an initial grade of -1.25% in the longitudinal direction, and an end station of 525 m. Span 1 of the southbound bridge was built on a horizontal curve with a 730 m radius (Figure 5.2). The radius was assumed to be sufficiently large such that it could be ignored for the modeling process; as such, the layout lines for both structures were modeled as completely straight. The centerlines of the northbound and southbound structures are 20.92 m apart for the entire length of the bridge, with the exception of the horizontal curve at Span 1. As such, initial stations for the northbound and southbound structures were defined as (0,0,0) and (0,20.92,0), respectively. Figure 5.3 is an example of the layout line inputs for the southbound bridge. Lanes were not defined during this part of the modeling procedure because live loads were assumed to have a negligible impact on the seismic response of the bridge; however, lane assignments could be added in the future to evaluate the response of routine traffic loading.

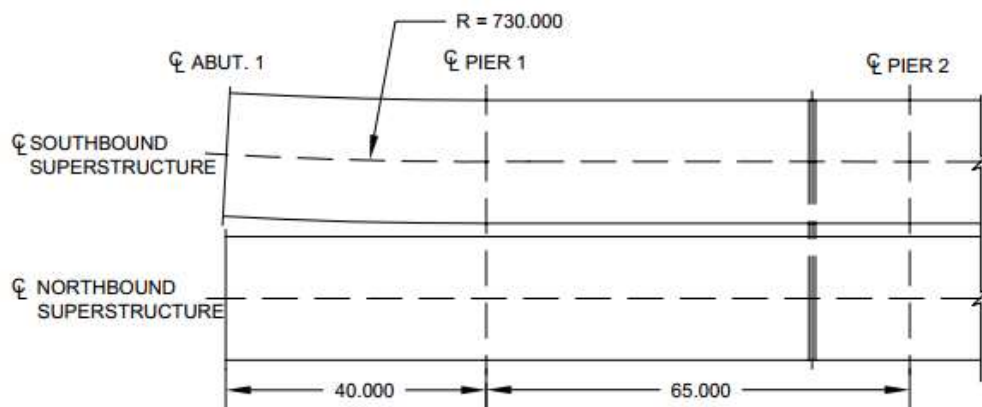


**Figure 5.2: Horizontal curvature of span 1 (southbound superstructure)**

**Bridge Layout Line Data**

Bridge Layout Line Name: SB Layout Line

Coordinate System: GLOBAL

Shift Layout Line: Modify Layout Line Stations...

Units: KN, m, C

Coordinates of Initial Station

Global X: 0.

Global Y: 20.92

Global Z: 0.

Initial and End Station Data

Initial Station (m): 0.

Initial Bearing: N900000E

Initial Grade in Percent: -1.25

End Station (m): 525.

Horizontal Layout Data

Define Horizontal Layout Data... Quick Start...

Define Layout Data

Define Vertical Layout Data... Quick Start...

Plan View (X-Y Projection)

Station: 0.

Bearing: 0.

Radius: 0.

Grade: 0.

X: 229.8864

Y: 288.8409

Z: 0.

Refresh Plot

OK Cancel

**Figure 5.3: Example layout line input for CSiBridge (southbound superstructure)**

### 5.3 Components Tab

Individual structural components behave in tandem, thereby creating the system-level response. The Components Tab in CSiBridge is used to define initial pieces, such as materials, member cross sections, and hinge properties, before being assigned to the global bridge object. The various definitions are organized into three sections and further divided by drop down menus (Figure 5.4). Each menu applicable to the Galena Creek Bridge is discussed in the following subsections. The subsections are organized in the order that they are presented to the user in CSiBridge when inputting initial structure definitions.

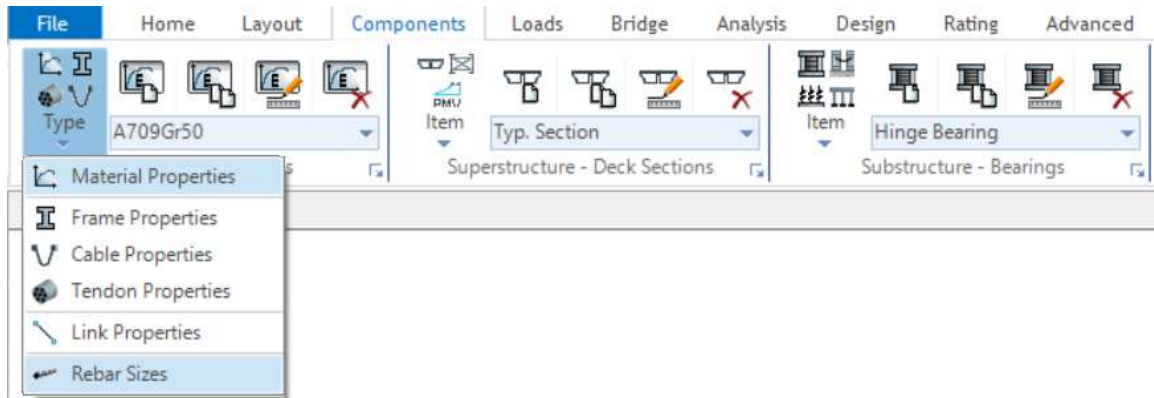


**Figure 5.4: Example of sections found in the CSiBridge Components Tab**

### 5.3.1 Materials

Several concrete compressive strengths were used throughout the Galena Creek Bridge, as denoted in the design plans on sheet BG-228. Concrete strengths of 28 MPa, 31 MPa, and 35 MPa were defined for the model. The density for all concrete was defined as 23.56 KN/m<sup>3</sup> (150 lbf/ft<sup>3</sup>), while the modulus of elasticity was calculated using Equation 5.1 from ACI 318-21M Equation 19.2.2.1.b, where  $f'_c$  is in MPa (ACI, 2021).

Some elements of the Galena Creek Bridge were built using a combination of concrete strengths. Specifically, 40 MPa concrete was used in Frame 2 for the bottom slab and webs of the box girder over Piers 2 and 3, while 31 MPa concrete was used for the top slab and pier diaphragms. CSiBridge does not permit multiple material properties to be assigned to a single superstructure cross section, nor does it allow material properties to vary along the span. Thus, it was conservatively assumed that the superstructure consisted of 31 MPa concrete throughout. As demonstrated by Equation 5.1, the elastic modulus of concrete is a function of the compressive strength, thereby influencing the stiffness and dynamic properties.

$$E_c = 4,700 \times \sqrt{f'_c}$$

**Equation 5.1: Modulus of elasticity of concrete (ACI, 2021)**

The Galena Creek Bridge used A706 Grade 50 steel for the traditional reinforcing bars. While CSiBridge can include reinforcing steel in models, the reinforcing was omitted because it did not influence on the modal properties or dynamic behavior of the structure. Prestressing tendons for the Galena Creek Bridge were A416 Grade 270 steel with a coefficient of friction of 0.2 and a wobble factor of 0.00066/m. The jacking force and projected losses for each set of prestressing tendons are displayed in Table 5.9. Note that the prestressing information was not input during the Components Tab portion of the modeling procedure, rather it was later included when defining the bridge object spans.

### 5.3.2 *Frame Properties*

Two methods were used to define frame sections. Solid members, such as the link beam and arch diaphragm, were defined using the conventional option of generating a new rectangular concrete section (Figure 5.5). The required input included the member depth, width, and material. Reinforcement details and material property modifiers, while not required, could be included when defining the section. The link beams and arch diaphragms had dimensions of 6.0 m x 4.0 m and 6.0 m x 3.6 m, respectively. The material for the arch diaphragm was 35 MPa concrete and the material for the link beam was 28 MPa concrete.

**Rectangular Section**

Section Name:

Section Notes:

Display Color:

**Dimensions**

Depth (t3):

Width (t2):

**Material**

+  ▼

**Property Modifiers**

**Properties**

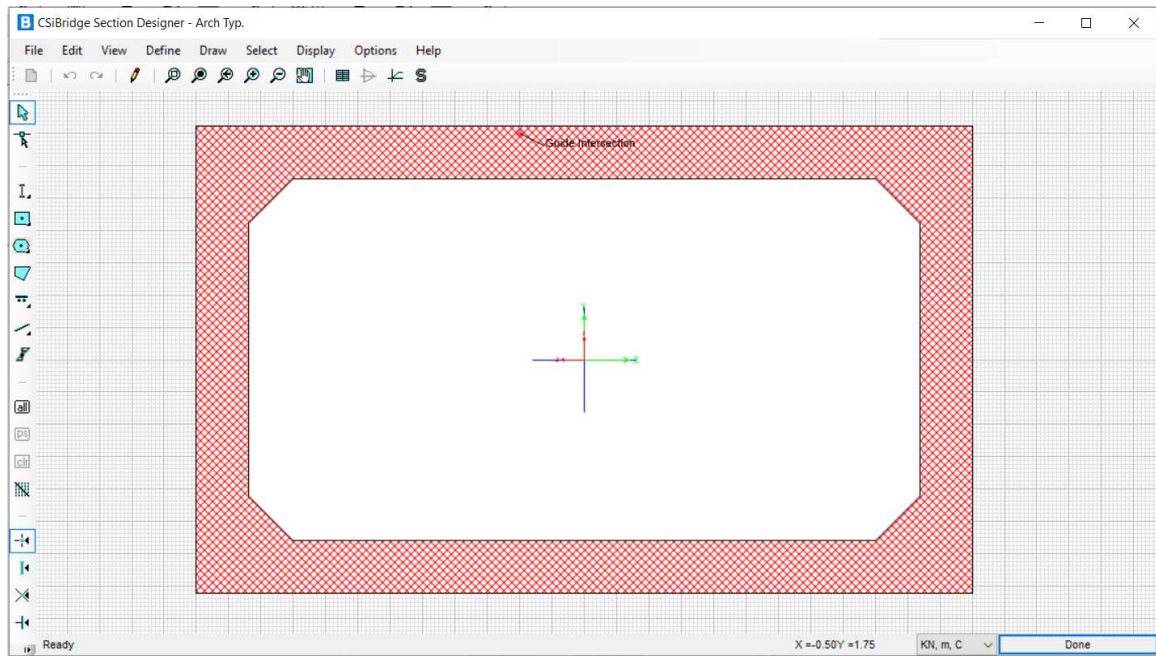
**Section**

Diagram showing a rectangular section on a grid with dimensions 2 and 3 indicated.

**Figure 5.5: Example solid rectangular section input for arch diagram**

The second approach was to create a unique section using the Section Designer tool (Figure 5.6). The self-weight of the Galena Creek Bridge was manually calculated to verify the total dead load. The hollow pier and arch sections were defined using Section Designer. The perimeters of the pier column and arch sections were drawn using the “draw solid shape” tool, while the interior perimeters were created with the “draw polygon shape” tool. The “resaper” tool was used to define the coordinates for the interior perimeter to incorporate the interior chamfers. Changing the material property of the interior shape to “OPENING” generated the box section void. The outside perimeter was drawn using the “draw solid shape” tool and was assigned the material property of the section.

The material for the arch was 35 MPa concrete and the material for the pier column was 28 MPa concrete. The typical pier column had exterior dimensions of 6.0 m x 3.0 m, interior dimensions of 4.0 m x 1.8 m, and interior chamfers of 0.15 m. The typical arch cross section had exterior dimensions of 6.0 m x 3.6 m, interior dimensions of 5.2 m x 2.8 m, and interior chamfers of 0.15 m.



**Figure 5.6: Example Section Designer tool for typical arch frame**

### 5.3.3 Link Properties

Link objects are one-dimensional elements which can be assign specialized properties, such as simulating linear, nonlinear, and even frequency-dependent behavior. Link elements provided a means to connect sections of the Galena Creek Bridge that were difficult to model using frame or shell elements; namely, the fillet merge between the superstructure and the arch. The link elements provided a rigid connection between the two joints without adding additional dead load found in frame elements. The ends were defined

#### 5.3.4 Deck Sections

Technical drawing of a cross-section of a reinforced concrete beam. The drawing shows dimensions for the beam's width, height, and reinforcement. Key dimensions include a total width of 9.450, a central crack width of 0.325, and a bottom reinforcement bar diameter of 0.200. A note indicates a "0.100 FILLET (TYP.)" at the bottom corner. The drawing is labeled "Q" at the top center.

71

**Table 5.1: Inputs for box girder definition for CSiBridge (m)**

Number of Interior Girders	1
Total Width	18.9
Total Depth	3
Left Exterior Girder Bottom Offset (L3)	2.36
Right Exterior Girder Bottom Offset (L4)	2.36
<b>Slab and Girder Thickness</b>	
Top Slab Thickness (t1)	0.2
Bottom Slab Thickness (t2)	0.2
Exterior Girder Thickness (t3)	0.325
Interior Girder Thickness (t4)	0.325
<b>Fillet Horizontal Dimension Data</b>	
f1 Horizontal Dimension	1.8
f2 Horizontal Dimension	1.8
f3 Horizontal Dimension	0.1
f4 Horizontal Dimension	1.2
f5 Horizontal Dimension	1.2
f6 Horizontal Dimension	0
f7 Horizontal Dimension	0
f8 Horizontal Dimension	0
<b>Fillet Vertical Dimension Data</b>	
f1 Vertical Dimension	0.175
f2 Vertical Dimension	0.175
f3 Vertical Dimension	0.1
f4 Vertical Dimension	0.175
f5 Vertical Dimension	0.125
f6 Vertical Dimension	0
f7 Vertical Dimension	0
f8 Vertical Dimension	0
<b>Left Overhang Data</b>	
Left Overhang Length (L1)	3.59
Left Overhang Outer Thickness (t5)	0.2
<b>Right Overhang Data</b>	
Right Overhang Length (L2)	3.59
Right Overhang Outer Thickness (t6)	0.2



The weight of the future wearing surface and barrier rails were manually calculated and applied as an area load and line load, respectively, in the Deck Section Definition. The barrier rail line load was calculated as 6.50 kN/m by multiplying the density of concrete (23.56 kN/m<sup>3</sup>) by the barrier cross-sectional area (0.28 m<sup>2</sup>). The FWS area load of 1.80 kN/m<sup>2</sup> was calculated by assuming an average thickness of 76 mm and a wearing surface density of 23.56 kN/m<sup>3</sup>. The 2.0% transverse superelevation was assumed to have a negligible impact on the stiffness of the bridge and was not included in the inputs. The bottom slab of the superstructure increases in thickness over the piers. The depth of the girder increases between the fillet diaphragms where the arch meets the superstructure. These variations in deck geometry along the length of the bridge are addressed in the upcoming Parametric Variations section.

#### *5.3.5 Diaphragms*

Interior diaphragms of varying thicknesses were located throughout the superstructure (Table 5.2). Abutment diaphragms are flush with the ends of the superstructure at Spans 1 and 7. An intermediate diaphragm is located near the midspan of all spans, with the exception of Span 3. Span 3 contains two intermediate diaphragms located 40 m from each pier, providing support between the piers and the crown of the arch. The fillets that merge the arch and box girder are marked by a fillet diaphragm and the crown of the arch has two crown diaphragms spaced 13.5 m apart. All diaphragms were modeled using the 31 MPa concrete material used for the superstructure and considered to be solid along the full depth of the girder, regardless of the access holes.

**Table 5.2: Diaphragm thicknesses**

Diaphragm Type	Thickness (m)	Bridge Sheet
Abutment	1.60	BG-209
Crown	0.30	BG-161
Fillet	0.50	BG-187
Intermediate	0.25	BG-187
Pier	3.60	BG-98
Hinge Upper	2.45	BG-217
Hinge Lower	3.25	BG-212

Hinges, located in Spans 2 and 4, divide the Galena Creek Bridge into three frames. The hinges consist of an overhang and suspended cantilever connected by an elastomeric bearing. The hinge was modeled as a single point at the centerline of the elastomeric bearing, 15 m from the centerline of the nearest pier. The diaphragm thicknesses for each portion of the hinge were measured from the centerline of the bearing to the face of the diaphragm (Figure 5.9).

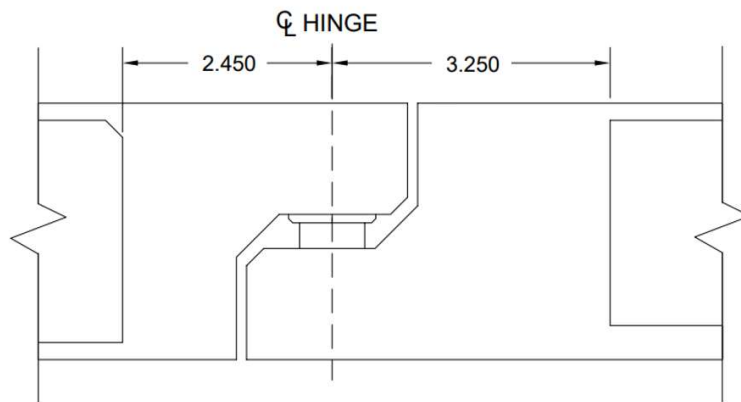


**Figure 5.9: Elevation view of Hinge 1 (m)**

### 5.3.6 Parametric Variations

The bottom slab thickness increases linearly over the piers and between the fillet diaphragms, where the superstructure connects to the arch. The bottom slab extrudes inwards at the piers so that the total girder depth does not change. The bottom slab variations are defined in Figure 5.10 and Table 5.3. The bottom slab thickness was assumed uniform along the 1.8 m depth of the pier diaphragms.

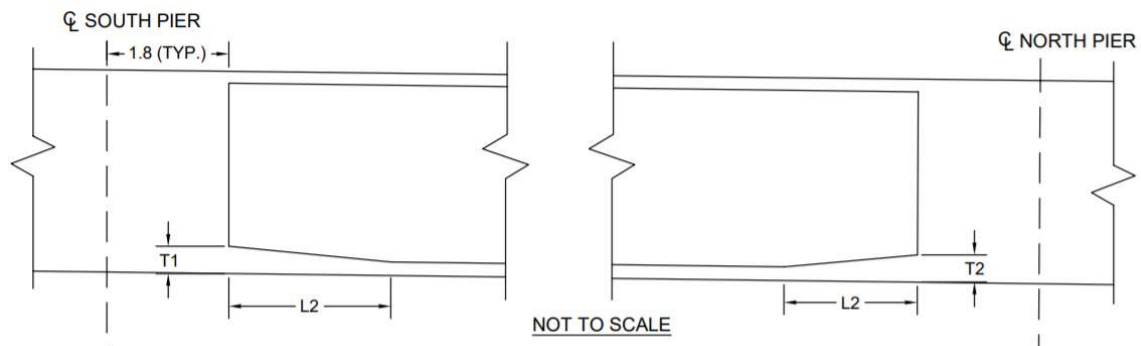


**Figure 5.10: Bottom slab thickness variation legend**

**Table 5.3: Bottom slab thickness variation values**

Span Number	T1 (mm)	L1 (m)	T2 (mm)	L2 (m)
1	200	N/A	400	2.5
2	400	5.0	600	15.0
3	600	6.0	400	13.2
4	600	13.2	400	5.0
5	400	4.0	400	4.0
6	400	3.0	400	3.0
7	400	2.0	200	N/A

The girder depth increases from 3.0 m to 3.6 m over 8.0 m between the fillet diaphragms in Span 3 (Figure 5.11). Changes in the deck section were defined in CSiBridge for individual spans. The length of the variations was in relation to the start of the respective

span, as seen in Figure 5.12. Span 3 required two separate parametric variations to denote the soffit thickness increase as well as the girder depth change.

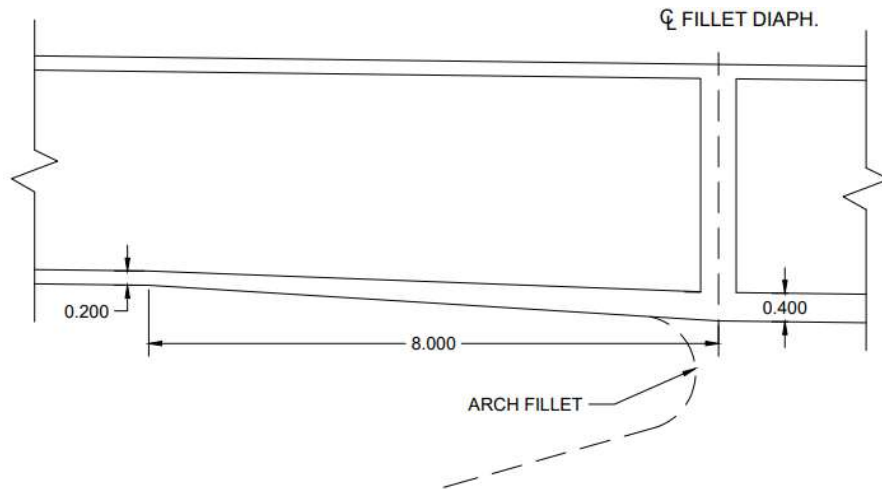


**Figure 5.11: Box girder variation at intersection of superstructure and arch (m)**

**B Variation Definition**

Variation Name:  Units:

**Variation Definition**

Point ID	Segment Type and Point Type Segment Is From Point(n - 1) to Point(n)	Distance m	Dim. Change m	Slope m / m
1	Start of Variation	0.	0.2	
2	Linear	1.8	0.2	
3	Linear	5.8	0.	
4	Linear	52.2	0.	
5	Linear	56.2	0.2	
6	Linear to End of Variation	58.	0.2	

**Variation Sketch** ☐ Use Equal Horizontal And Vertical Scales In Sketch

Dimension Change Sign:

Distance:  Dim. Change:  Slope:

**Figure 5.12: Example of linear variation input in CSiBridge (Span 5)**

### 5.3.7 Bearings

A set of three elastomeric bearings are located at each abutment and hinge of the Galena Creek Bridge. Elastomeric bearings were independently defined for the abutment and hinge (Table 5.4). It was assumed the elastomeric bearings were under large compressive forces; as such, rotation about the longitudinal and transverse axes as well as the translation along the z-axis were negligible. The lateral, vertical, and rotational stiffness properties were calculated as a function of the bearing dimensions using Equations 5.2 – 5.4, respectively (Akogul and Celik, 2008). Bearing dimensions were presented in sheets BG-238 and BG-239 of the design plans.

$$K_H: \frac{G * A}{H_r}$$

**Equation 5.2: Elastomeric bearing lateral stiffness**

$$K_V: \frac{E * A}{H_r}$$

**Equation 5.3: Elastomeric bearing vertical stiffness**

$$K_\theta: \frac{E * I}{H_r}$$

**Equation 5.4: Elastomeric bearing rotational stiffness**

**Table 5.4: Calculated stiffness values for elastomeric bearings**

<b>Bearing Location</b>	<b><math>K_H</math> (kN/m)</b>	<b><math>K_V</math> (kN/m)</b>	<b><math>K_\theta</math> (kN×m)</b>
Abutment	4,215	17,500	597.2
Hinge	2,208	9,167	385.1

Bearing property definitions were also required when defining the substructure to superstructure connection. The concrete columns of the Galena Creek Bridge extrude into the girder and act as diaphragms; therefore, it was assumed that the connection between the column and superstructure was rigid. A fully-fixed mock bearing was defined to reflect the integral connection between the piers and the superstructure.

#### *5.3.8 Foundations*

Foundations for the Galena Creek Bridge include footings anchored by cast-in-place piles and thrust blocks anchored by steel tiedowns. The footings, located at the base of piers 1, 4, 5, and 6, are each rooted by 12 cast-in-drilled-hole piles. The 1.22 m diameter holes were drilled to bedrock, ranging from 6.1 m to 15.1 m deep. The thrust blocks for Piers 2 and 3 are cast directly into the rock face of the slope below the structure. The base of each thrust block is anchored to the bedrock using 12 tiedowns. Due to the robust connection between the footings and bedrock, it was assumed that the footings were fixed with the ground and not modeled. Fully-fixed foundation springs were assigned at the base of each pier column to represent this assumption.

#### *5.3.9 Abutments*

The abutments at the end of the Galena Creek Bridge are perpendicular to the centerline of the bridge. The superstructure of the Galena Creek Bridge rests on elastomeric bearings at the abutments with shear keys restricting translation in the transverse direction. As there are no unique defining properties of the abutments that would influence the dynamic properties of the FEA model, only a single typical abutment was defined. The typical abutment was connected to the bottom of the girder as opposed to being integral,

thereby simulating the behavior of the elastomeric bearing pads. The abutments are assigned to the bridge objects later in the modeling procedure.

#### 5.3.10 Bents

The superstructure of the Galena Creek Bridge is supported by 12 pier columns of varying heights. The columns extend into the structure and act as pier diaphragms. The rectangular columns are oriented to resist transverse bending. Column heights were determined by calculating the difference in elevation between the bottom of the superstructure and the top of the footing at the centerline of each pier (Table 3.4). The heights for the northbound and southbound superstructure varied due to local topography, with the northbound structure typically having longer heights. The boundary conditions at both the base and top of the column were defined as fully fixed. The top of each pier column of the Galena Creek Bridge includes a bent; however, a cap beam section was not explicitly modeled because the columns extend into the superstructure, forming a direct connection. This connection was modeled as fully integral with the box girder.

**Table 5.5: Column heights**

<b>Pier Number</b>	<b>Northbound Structure (m)</b>	<b>Southbound Structure (m)</b>
1	19.189	16.622
2	38.047	38.049
3	38.769	38.769
4	34.402	19.983
5	31.277	22.158
6	23.935	16.458

## 5.4 Loads Tab

The Loads Tab is used to define the various forces and conditions that is applied to the structure during analyses (Figure 5.13). Live load vehicles, time-history loadings, and response spectrum are some of the loads that can be defined. Vehicle lanes and truck live loads were not defined because routine traffic live loads were assumed to have a negligible impact on the dynamic response of the Galena Creek Bridge.

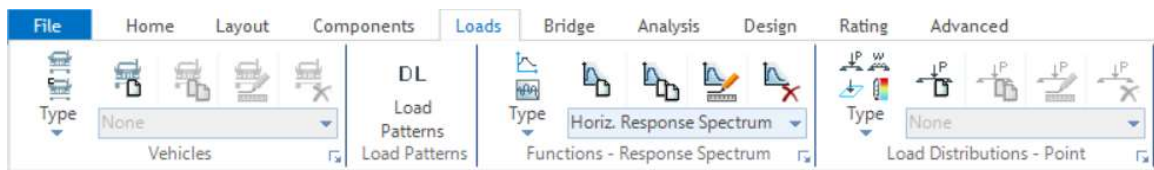


**Figure 5.13: Loads Tab as seen in CSiBridge**

Ground motion accelerations were input as time-history loads to CSiBridge by importing two-column .txt files. The left column of the text is the time, in seconds, for each set of data. The right column of text denotes the excitation at the adjacent timestamp. The excitation can be in the form of either a force or an acceleration as long as the units are consistent throughout. Importing time-history data using this method only notes the numerical values for the applied accelerations; units are not assigned until defining the load combinations under the Analysis Tab. The primary models were created prior to the complete installation of the SHM system; therefore, the dynamic response of the models was preliminarily evaluated using ground motion accelerations recorded during a magnitude 6.9 earthquake that occurred in El Centro, California in 1940. High intensity ground motions were selected to emulate an extreme event experienced by structures near the area of the Galena Creek Bridge. Ground accelerations in the north-south (global X-axis), east-west (global Y-axis), and vertical (global Z-axis) directions were imported.



It should be noted that the barrier rail and FWS loads were input during the deck section definition. Reviewing the “Loads Distribution” dropdown menu revealed the line loads and area loads for the barrier and FWS, respectively, were automatically populated. The autogenerated inputs were dictated by the deck section values. Manual edits to the auto filled values are reverted when updating the model. This is only applicable to barrier rail and FWS loads, and by proxy, the sidewalk load. CSiBridge does not automatically edit values for additional point, line, or area loads applied outside of the deck definition.

## **5.5 Bridge Tab**

CSiBridge refers to the FEA model under consideration as the “bridge object.” The Bridge Tab provides a platform to assign the components defined into a bridge object to be used for analyses. The primary difference between the northbound and southbound bridges was the height of the columns. For modeling efficiency and accuracy, a single superstructure model (i.e., northbound) was generated and copied about the southbound layout line. The southbound structure was then modified by assigning the appropriate pier definitions.

### *5.5.1 Bridge Object Data*

The first step of modeling the bridge object is to define the spans within the length of the structure. Spans can be defined either by station length or span length, which are demonstrated in Table 5.6. As there is no definitive advantage of one method over the other, the spans were input using span length. The spans of the Galena Creek Bridge are defined from south to north; Station 0 coincides with the centerline of the south abutment.

**Table 5.6: Galena Creek Bridge span lengths and station locations**

	Span 1	Span 2	Span 3	Span 4	Span 5	Span 6	Span 7
Span Length (m)	40	65	210	68	58	48	36
Start Station (m)	0	40	105	315	383	441	489
End Station (m)	40	105	315	383	441	489	525

### 5.5.2 *Spans*

The purpose of the “Spans” definition is to input any parametric variations of the superstructure along a span. The linear variations, previously defined in the Components Tab, are applied to the bottom slab thickness, as demonstrated in Figure 5.14. Superstructure variations were assigned to the respective spans, with Span 3 requiring two inputs for the bottom slab and box girder depth. “The Show Section Variation” option was used to visually confirm the correct superstructure variations were assigned at locations with geometric changes (Figure 5.15).

**B Bridge Section Variation Definition**

Bridge Object Name: NB Structure  
Span Label: Span 3  
Base Bridge Section Property: Typ. Section

Bridge Section Variation Is Defined By:  
☒ User Definition Define/Show Variations...  
☐ Reference to Another Span

Display Section  
Show Base Section...  
Show Section Variation...

User Defined Variation For Concrete Box Girder - Sloped  
☒ Distance Measured from Start of Span ☐ Distance Measured from Start Abutment

Parameter	Variation
<b>General Data</b>	
Total Width	Constant
Total Depth	Span 3 Depth Change
Left Exterior Girder Bottom Offset (L3)	Constant Girder Slope
Right Exterior Girder Bottom Offset (L4)	Constant Girder Slope
<b>Slab and Girder Thickness</b>	
Top Slab Thickness (t1)	Constant
Bottom Slab Thickness (t2)	Span 3 Bot. Slab Var. ▾
Exterior Girder Thickness (t3)	Constant
Interior Girder Thickness (t4)	Constant
<b>Fillet Horizontal Dimension Data</b>	
f1 Horizontal Dimension	Constant
f2 Horizontal Dimension	Constant
f3 Horizontal Dimension	Constant

OK Cancel

Figure 5.14: Example of superstructure span variations in CSiBridge

**B Bridge Object Display**

File

Bridge Section

Distance Along Span, m: 100.002  
Total Span Length = 210. m Refresh View

Bridge Object Name and Span  
NB Structure  
Span: SPAN3

Properties  
Show Section Properties  
Units: KN, m, C ▾

Options  
☒ Show Dots At Points  
☐ Display Point Labels  
☐ Disable Corner Point Snap

Mouse Pointer Coordinates  
X Coord: 19.6301  
Y Coord: 3.3171

OK Cancel

Figure 5.15: Example of deck section variation in CsiBridge

### 5.5.3 *Abutments*

The abutments followed the same numbering system as the spans: the south supports were Abutment 1, and the north supports were labeled as Abutment 2. Abutment diaphragms were denoted as flush with the end of the superstructure. The superstructure was supported at each abutment by three bearings centered about the layout line with a uniform spacing of 2.88 m. As stiffness values were assigned in the Bearing definition, no additional restrainer properties were attached to the bearings when defining the abutments. The 0.15 m joint between the superstructure and abutment seat is connected by a reinforced elastomeric bearing. This was modeled in CSiBridge by locating the abutment and bearings 0.15 m and 0.075 m below the bottom of superstructure, respectively. CSiBridge uses elevation values for the substructure with respect to the global coordinate system; therefore, the elevations had to consider the 1.25% longitudinal grade. Abutment and bearing elevations for the start abutment were -3.15 m and -3.08 m and the elevations at the end abutment were -9.86 m and -9.71 m, respectively.

**Figure 5.16: Typical CSiBridge input for abutments**

#### 5.5.4 Bents

The pier column information, previously defined in the Components Tab, was assigned at the ends of Span 1 – 6. Pier diaphragms were assigned at each bent location as well as the “mock” fixed bearing. Like the end abutment, the elevation values were based off the global z-axis (Table 5.7). Values were calculated based on the station location, accounting for the -1.25% longitudinal grade. Bent elevations were input as flush with the bottom of the 3 m deep box girder (Figure 5.17).

**Figure 5.17: Typical CSiBridge input of bent information**

**Table 5.7: Bent elevation values along global z-axis**

	Pier 1	Pier 2	Pier 3	Pier 4	Pier 5	Pier 6
Bent Elevation (m)	-3.5	-4.3125	-6.9375	-7.7875	-8.5125	-9.1125

### 5.5.5 Hinges

Hinges divide the structure into three frames, defined based on the distance from the start of their respective span: Hinge 1 is 50 m from the start of Span 2 and Hinge 2 is 15 m from the start of Span 4. The hinges were assumed to be at half the depth of the girder (1.5 m) with global elevations of -2.63 m and -5.63 m for Hinges 1 and 2, respectively. Each hinge consists of an upper and lower cantilever connected by three elastomeric bearings (Figure 5.9). The lower cantilever portions of the hinges are attached to Frame 2.

The overhang cantilever portions are parts of Frames 1 and 3. These considerations were incorporated when assigning diaphragm definitions to either side of the hinge.

#### 5.5.6 Diaphragms

Only the intermediate, fillet, and crown diaphragms were explicitly modeled. Diaphragms at the abutments, piers, and hinges were assigned during the definition of each respective component. Diaphragm locations were assigned from the start of each span, as shown in Table 5.8.

**Table 5.8: Diaphragm locations**

Location	Diaphragm Type	Distance from Start of Span (m)
Span 1	Intermediate	17.60
Span 2	Intermediate	29.00
Span 3	Intermediate	40.00
	Fillet	74.25
	Crown	98.40
	Crown	111.90
	Fillet	135.75
	Intermediate	170.00
Span 4	Intermediate	36.60
Span 5	Intermediate	29.00
Span 6	Intermediate	24.20
Span 7	Intermediate	21.00

#### 5.5.7 Prestressing Tendons

Five sets of prestressing tendons were used to counter tensile stresses in the structure, as detailed in Table 5.9. All three frames has an internal prestressing system anchored at either the hinge diaphragm or abutment diaphragm. Additionally, Frame 2 also has external

prestressing tendons at the hinge diaphragms. The effect of prestressing was assigned to the model as a force. The A416 Grade 270 steel used for the tendons was a preset material option from CSiBridge. The center of gravity of the prestressing force follows a series of parabolic curves, as denoted on sheet BG-225 of the bridge design plans. An example of a typical input for prestressing data in the model is demonstrated in Figure 5.18.

Modeling the tendons in CSiBridge was done by defining a series of nodes that follow the path of the prestressing force. Once the initial starting station was assigned, nodes alternated between “Parabola Intermediate Point” and “Parabola End Point” to define the path of the strand center of gravity. Peaks and valleys marked intermediate points, while inflection points marked parabola end nodes (Figure 5.19). The vertical offset input for each node was based on the local axis of the layout line as opposed to the global axis; therefore, the -1.25% longitudinal grade was not considered when assigning the tendon locations.

The transverse location of the prestressing force can be edited in CSiBridge. It was assumed that adjusting the horizontal layout of the strands did not have an impact on the dynamic properties of the model and, thus, no modifications were performed. Similarly, transverse prestressing in the integral deck over each pier was assumed to have a negligible effect on structural behavior and was not included in the bridge model.



**Figure 5.18 – Typical CSiBridge prestressing input**

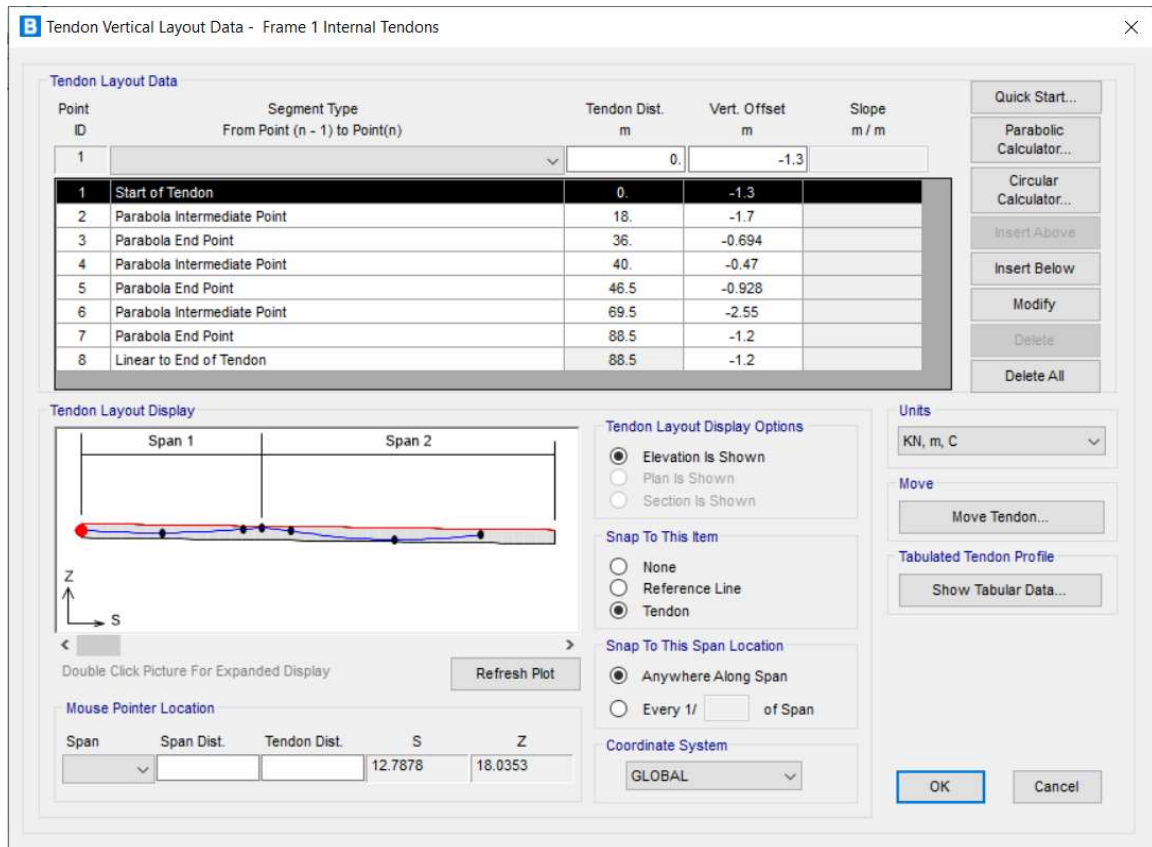


**Figure 5.19: Example of CSiBridge tendon parabolic path**

**Table 5.9: Prestressing strand data**

Location	Number of Tendons	Strands per Tendon	Jacking Force (kN)	Losses (MPa)
Frame 1	9	27	48,300	179
Frame 2 (Int.)	18	27	101,300	276
Frame 2 (Ext.)	6	27	32,600	276
Frame 3	12	27	64,200	241
Deck (Trans.)	9	4	812	180

### 5.5.8 Update

Inputting components into a bridge object model does not automatically incorporate the changes. The Update feature refreshes the model and incorporates changes made to the selected bridge object. This feature is intended to reduce loading times and improve

processing speed by allowing the user to dictate the refresh rate of any changes made to the bridge object. It should be noted that the Update feature only incorporates edits made to the bridge object model components and does not refresh additional modeling performed using the tools in the Advanced Tab.

The Update feature offers the option to model the superstructure as either as frame, shell, or solid elements. The northbound and southbound structures of the Galena Creek Bridge were updated individually as Area Object Models to model the superstructure as a collection of 3D shell elements, as seen in Figure 5.20. Although modeling the structure as a solid object may better simulate the physical behavior than a shell model, the additional computational time did not warrant the relatively minor change in analysis results.

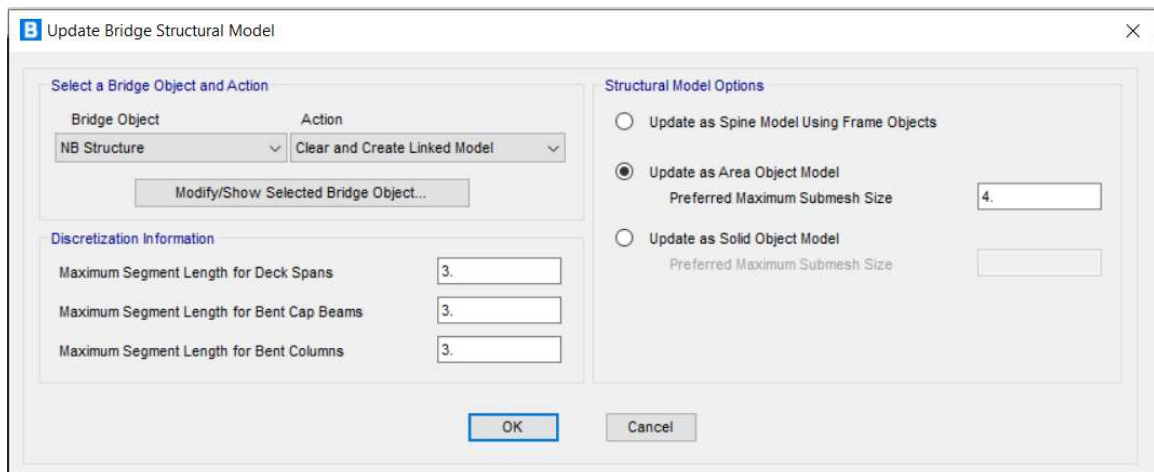


**Figure 5.20: Example of updating bridge object model in CSiBridge**

## **5.6 Advanced Tab**

The Advanced Tab provides an array of tools to add or edit properties not defined by the presets available in the Components Tab. The arch of the Galena Creek Bridge was modeled as a series of 19 frame elements following the segment geometry defined on

sheets BG-10 and BG-142 of the design plans, as seen in Figure 5.21 (NDOT, 2006). The segments are labeled from south to north, starting with Segment 0. Segments north of the crown of the arch, Segment 9, continue in descending order with the additional suffix of “A” (Figure 5.21). In the model, 19 segment ends were defined by generating nodes offset along the global x and z-axis, as shown in Table 5.10. After the template for the arch had been positioned, the joints were connected using frame elements. All of the frame elements are box sections, with the exception of Segments 0 and 0A which are solid shapes to denote the arch diaphragm (Figure 5.22).

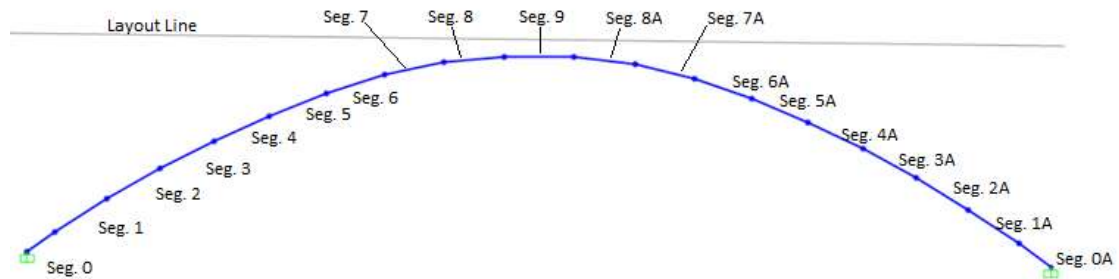


**Figure 5.21: Arch modeled as frame elements in CSiBridge with segment labels**

**Table 5.10: Segment end node offset for modeling arch**

<b>Segment Number</b>	<b>X-axis offset (m)</b>	<b>Z-axis offset (m)</b>
0	5.539	3.829
1	10.203	6.502
2	10.507	6.000
3	10.784	5.485
4	11.037	4.957
5	11.263	4.416
6	11.517	3.695
7	11.838	2.480
8	12.033	1.212
9	13.814	-0.183
8A	11.997	-1.532
7A	11.767	-2.794
6A	11.416	-4.000
5A	11.142	-4.715
4A	10.901	-5.248
3A	10.635	-5.770
2A	10.342	-6.277
1A	10.027	-6.771
0A	6.313	-4.639

As was the case for Piers 2 and 3, the arch was assumed to be fully-fixed at the connection to the thrust block. The rectangular box section of the Galena Creek Bridge arch is oriented to provide lateral resistance. To verify that the frame elements were correctly oriented, the arch was observed from several angles using a 3D view of the extruded members (Figure 5.22). Each frame element was visually inspected to confirm that the longer face of the rectangular section was oriented along the global y-axis.

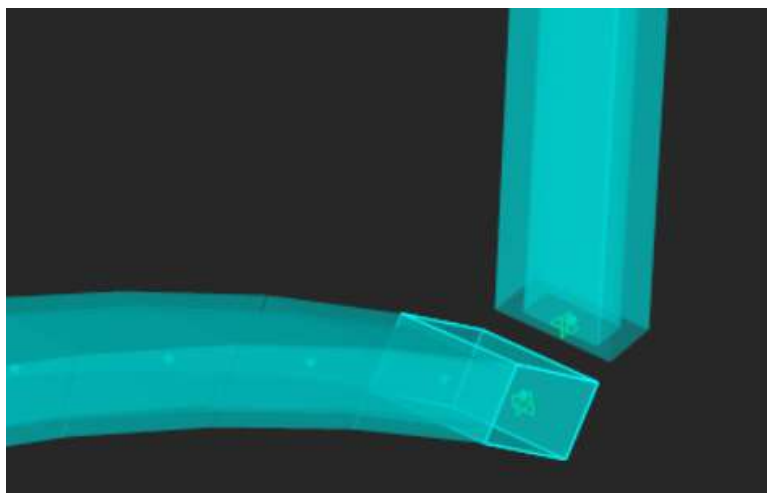


**Figure 5.22: Extrude view of CSiBridge model at base of column and pier**

The arch crown extends into the superstructure where the superstructure box girder increases in depth. CSiBridge does not have a function to join components in this manner; therefore, the merge was modeled by connecting rigid link elements from the bottom of the box girder to nodes along the arch frame elements. Figure 5.23 shows the elevation view of the arch crown where the two components merge. The three middle link elements connecting the arch to the bottom of the superstructure are not explicitly visible in the figure because they are relatively small compared to the scale of the image. The exterior-most link elements extend down from the fillet diaphragms to the arch. Modeling additional link elements had a negligible impact on the response of the structure. Increasing the number of link elements to 13 decreased modal participation factors by less than 0.2% and transverse displacement less than 0.7 mm.

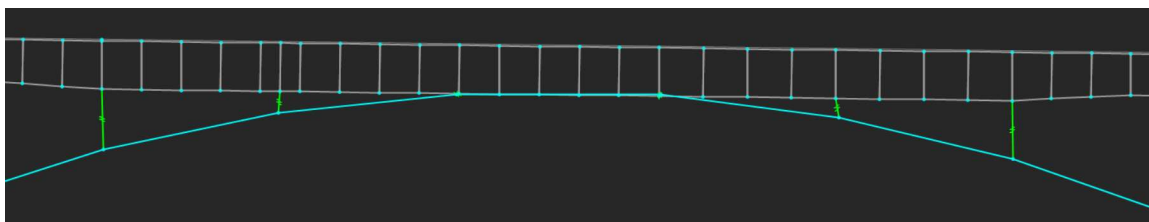


**Figure 5.23: Elevation view of the links connecting the arch and box girder in CSiBridge**

The final step before running an analysis was to define the Mass Source. The mass source specifies the elements and loads considered as a mass for modal analyses. As the linear time-history analyses use the modal results to calculate dynamic response, accurately defining the mass source is critical to achieving accurate results. The default setting for the mass source only considers the self-weight of elements. The FWS area and barrier rail load patterns were included as masses, demonstrated in Figure 5.24, to better represent the actual mass of the bridge when performing analyses.

**Mass Source Data**

Mass Source Name:

**Mass Source**

- ☒ Element Self Mass and Additional Mass
- ☒ Specified Load Patterns

**Mass Multipliers for Load Patterns**

Load Pattern	Multiplier
Future WS	1.
Future WS	1.
Barrier	1.

Buttons: Add, Modify, Delete, OK, Cancel

**Figure 5.24: Defining the Mass Source for CSiBridge**

## 5.7 Analysis Tab

### 5.7.1 Introduction

The results from three load cases were considered when developing the CSiBridge model. All model variants, including the control model, were subjected to a dead load, modal, and time-history analysis. The dead load case was a basic method to confirm consistency between the models. Although many factors influence the modal properties of the FEM, the gravity loads from the structure remained constant. Excessive variations in the dead load implied a flaw in the modeling process, aiding in debugging the model and identifying errors. Modal analysis provides the dynamic properties of the bridge, based on the physical properties and layout of the structure. Comparing changes, such as modal periods and participation ratios, revealed how variations to the model influence the physical properties and subsequent dynamic behavior. The linear time-history analysis, simulating an earthquake, shows the accelerations, displacements, and stresses experienced by the structure during an extreme event, providing a brief window into the physical response of the bridge as it is subjected to ground motions.

### 5.7.2 Dead Load Analysis

CSiBridge determines the self-weight of the structure by taking the sum of the vertical forces at all the base nodes. The dead load combination included the physical self-weight of the modeling elements, barrier rail line loads, and FWS area loads (Figure 5.25). Manual calculations for the structure dead load can be found in the Appendix A.



**Load Case Data - Linear Static**

Load Case Name:  Set Def Name Modify/Show...

Load Case Type: Static Design...

Stiffness to Use:  
☒ Zero Initial Conditions - Unstressed State  
☐ Stiffness at End of Nonlinear Case

Important Note: Loads from the Nonlinear Case are NOT included in the current case

Analysis Type:  
☒ Linear  
☐ Nonlinear

Mass Source:

Load Type	Load Name	Scale Factor
Load Pattern	DEAD	1.
Load Pattern	Barrier	1.
Load Pattern	Future WS	1.

Add Modify Delete

OK Cancel

**Figure 5.25: CSiBridge input for Dead Load Case**

The dead load of the structure calculated by CSiBridge was 504.2 MN. Manual calculations determined the self-weight of the Galena Creek Bridge to be 505.9 MN, a difference of 0.34%. Previous research of the Galena Creek Bridge calculated the self-weight of the structure as 499.0 MN, which yields a difference of 0.99%. The difference between both calculated values of the self-weight and the CSiBridge dead load are less than 1.0%; therefore, it is likely that all the component inputs for the Galena Creek Bridge object had been modeled sufficiently.

### 5.7.3 Modal Analysis

The modal response of a structure is a function of the physical properties. After a modal analysis, CSiBridge provides information on modal periods, frequencies, participation factors, and more. Changes to these parameters reveal how modifying independent variables of the model influences the physical and modal properties. Furthermore, comparing the results of the control model to previous research served as a

benchmark for dynamic properties. Due to the computational efficiency of using a shell bridge object to conduct the modal analysis, up to 100 modes were reported (Figure 5.26).

The initial results of the modal analysis are demonstrated in Figure 5.27.

Figure 5.26: CSiBridge input for modal analysis case

	OutputCase	StepType Text	StepNum Unitless	Period Sec	UX Unitless	UY Unitless	UZ Unitless	SumUX Unitless	SumUY Unitless	SumUZ Unitless	RX Unitless
▶	MODAL	Mode	1	1.739789	3.757E-07	0.52418	9.697E-08	3.757E-07	0.52418	9.697E-08	0.05456
	MODAL	Mode	2	1.342364	0.12342	3.581E-08	5.607E-05	0.12342	0.52418	5.616E-05	3.713E-09
	MODAL	Mode	3	1.214145	7.518E-06	0.00575	1.143E-07	0.12343	0.52993	5.628E-05	0.00015
	MODAL	Mode	4	1.027973	5.757E-06	0.03387	2.211E-08	0.12343	0.5638	5.63E-05	0.00996
	MODAL	Mode	5	0.978535	0.15056	1.183E-07	5.633E-05	0.274	0.5638	0.00011	3.872E-05
	MODAL	Mode	6	0.788076	2.346E-05	0.03675	1.722E-06	0.27402	0.60055	0.00011	0.02237
	MODAL	Mode	7	0.761587	0.06197	0.00047	0.00212	0.33598	0.60102	0.00223	0.00037
	MODAL	Mode	8	0.743692	0.00108	0.00047	0.00011	0.33706	0.60149	0.00234	0.005
	MODAL	Mode	9	0.717267	0.00014	0.0424	0.00145	0.33721	0.6439	0.00379	0.00015
	MODAL	Mode	10	0.711639	0.00121	0.00051	0.06836	0.33842	0.64441	0.07215	8.301E-05
	MODAL	Mode	11	0.69448	0.00039	0.02225	3.184E-06	0.33881	0.66666	0.07216	0.02321
	MODAL	Mode	12	0.669667	0.09256	2.602E-05	0.0202	0.43137	0.66669	0.09235	0.00373
	MODAL	Mode	13	0.657849	0.01171	0.00728	0.0035	0.44308	0.67397	0.09586	0.01805
	MODAL	Mode	14	0.635307	0.01183	0.00017	0.00576	0.45491	0.67414	0.10162	0.03364
	MODAL	Mode	15	0.621209	0.09588	0.00042	0.02641	0.55079	0.67455	0.12802	0.00818

Figure 5.27: Modal analysis results of control model

#### 5.7.4 Time-history Analysis

To evaluate the dynamic response of the CSiBridge model, it was subjected to ground motion accelerations along all three degrees of freedom. Ground motions of the 1940 magnitude 6.9 El Centro earthquake were selected to represent extreme condition for the Galena Creek Bridge. Ground motions along the longitudinal, vertical, and transverse axes were imported in the form of two-column .txt files. The left column of the file is the timestamp (sec) of the datapoint and the right column is the corresponding acceleration (g). The imported .txt file is conveyed as a function graph, as seen in Figure 5.28.

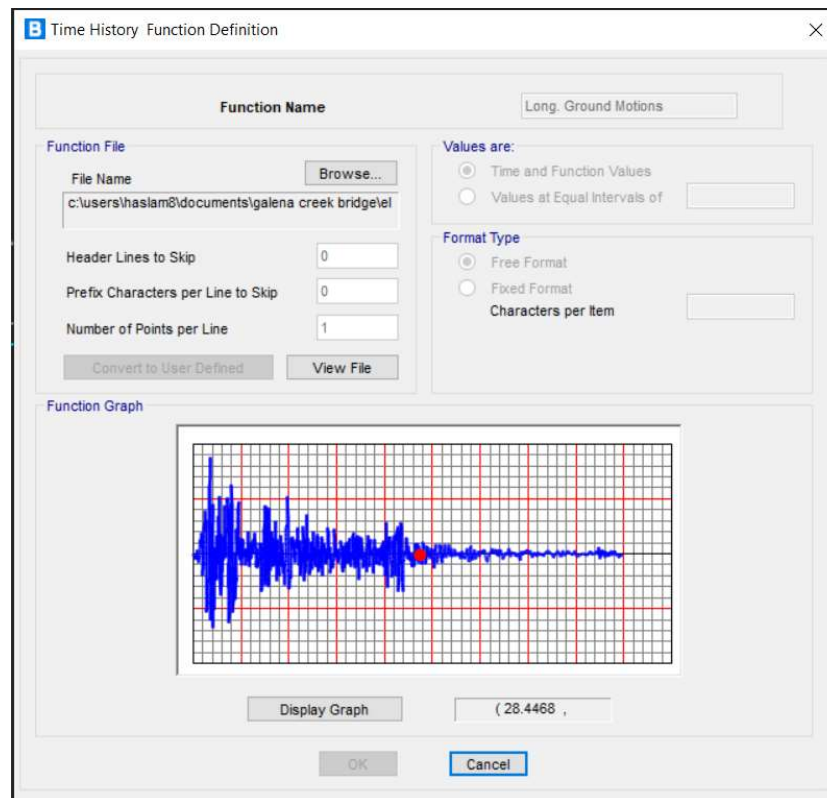


Figure 5.28: Example of an imported ground motion from text file in CSiBridge

The base unit for distance used for the CSiBridge model was meters; therefore, the ground motions were subject to a scale factor of 9.81 to convert from gravitation acceleration to  $\text{m/s}^2$  (Figure 5.29). Previous research on the Galena Creek Bridge

emphasized the significance of using appropriate ground motions, specifically those reflective of the structure geographical location (Taylor and Sanders, 2008). While the sample ground motions used for the preliminary analyses are not directly from Walker Lane, they aid in understanding the bridge response to extreme events. Additional information from the SHM system is needed to further refine the model to reflect the physical behavior.

**Load Case Data - Linear Modal History**

**Load Case Name:** Linear Earthquake Analysis **Set Def Name** **Notes:** Modify/Show...

**Load Case Type:** Time History **Design...**

**Initial Conditions:**  
☒ Zero Initial Conditions - Start from Unstressed State  
☐ Continue from State at End of Modal History  
 Important Note: Loads from this previous case are included in the current case

**Modal Load Case:**  
 Use Modes from Case **MODAL**

**Loads Applied:**

Load Type	Load Name	Function	Scale Factor
Accel	U1	Long. Groun	9.81
Accel	U2	Trans. Ground M	9.81
Accel	U3	Vert. Ground Mo	9.81

☐ Show Advanced Load Parameters

**Time Step Data:**  
 Number of Output Time Steps: 18001  
 Output Time Step Size: 5.000E-03

**Other Parameters:**  
 Modal Damping: None **Modify/Show...**

**Analysis Type:** ☒ Linear ☐ Nonlinear  
**History Type:** ☒ Transient ☐ Periodic  
**Solution Type:** ☒ Modal ☐ Direct Integration ☐ Frequency Domain  
**Mass Source:** Previous (MSSSRC1)

**OK** **Cancel**

**Figure 5.29: CSiBridge input for time-history load case simulating an earthquake**

## **CHAPTER 6. PARAMETRIC MODELING**

A parametric analysis was conducted to understand the behavior of the Galena Creek Bridge to variations in select parameters that are believed to influence the dynamic response. This investigation evaluated seven parameters (Table 6.1): superstructure material, material damping, elastomeric bearing stiffness, column effective moment of inertia, superstructure modeling method, link slab modeling method, and barrier rail modeling technique. Each parameter was further defined by a range of variables used to assess the influence of the given parameter. In total, 23 analyses were conducted as part of the study and a final recommended model is detailed in Chapter 7. Ultimately, the results of the parametric study will be used to validate the final model with the field-measured data from the SHM system and will be used to make any necessary model refinements.

**Table 6.1: List of parameters and respective variations**

Parameter	Superstructure Material (MPa)	Material Damping (%)	Elastomeric Bearing Stiffness, $G$ (MPa)	Column Effective Moment of Inertia, $E$	Superstructure Modeling Method	Link Slab Modeling Method	Barrier Rail Modeling Technique
Control	31	2	Pinned	$1.00I_g$	Shell	6 m max.	Line Load
Variations	36	5	0.9	$0.95I_g$	Frame Spine	3 m max.	Frame
	40	7	1.38	$0.90I_g$	Solid	12 m max.	
			Fixed	$0.85I_g$			
				$0.80I_g$			
				$0.75I_g$			
				$0.70I_g$			
				$0.65I_g$			
				$0.60I_g$			
				$0.55I_g$			
				$0.50I_g$			

Dead load, modal, and time-history analyses were performed on each model variant to assess changes in the structural response. Initially, the dead load analysis was used to verify that any modifications to the control model did not result in anomalous variations. Consistency of the calculated weight served as a preliminary quality control check before the results from either the modal analysis or the time-history analysis were considered. Following the dead load verification, a modal analysis was conducted to determine the natural frequencies. The top five modes about all three degrees of freedom, in terms of participation factor, were recorded and used during the subsequent analyses. Finally, a time-history analysis of each model was performed, applying the ground motion accelerations from the magnitude 6.9 El Centro earthquake. The accelerations, which were 53 seconds in duration in increments of 0.02 seconds, were applied along all three degrees of freedom. The selected seismic event was intended to represent an extreme loading case for the Galena Creek Bridge. The resulting response of both the superstructure and substructure elements were considered. Variations in displacement and internal stresses provided feedback on how each parametric variation influenced dynamic behavior.

## **6.1 Superstructure Material**

A range of concrete strengths were used for the construction of the Galena Creek Bridge, as discussed in Section 0. Most components, such as the arch and the pier columns, were comprised of a single type of concrete. However, the box girder superstructure was primarily 31 MPa concrete with some sections constructed of 40 MPa concrete. Higher strength concrete were used in areas where additional strength and stiffness were required: bottom slab, web, and exterior girders of the box girder over Piers 2 and 3. The higher strength area extends 13.05 m from the from the centerline of the pier to the hinge

diaphragm, and 16.0 meters toward the center of the arch, demonstrated by Figure 6.1. CSiBridge does not permit the user to incorporate material changes to the superstructure along the length of the bridge, nor does it provide a means to compose a composite box girder from multiple materials. As demonstrated in Equation 5.1, the Modulus of Elasticity of the concrete is calculated as a function of the compressive strength. Therefore, defining the superstructure of the control model as 31 MPa concrete would likely result in a more flexible response than the actual bridge due to the reduced stiffness.

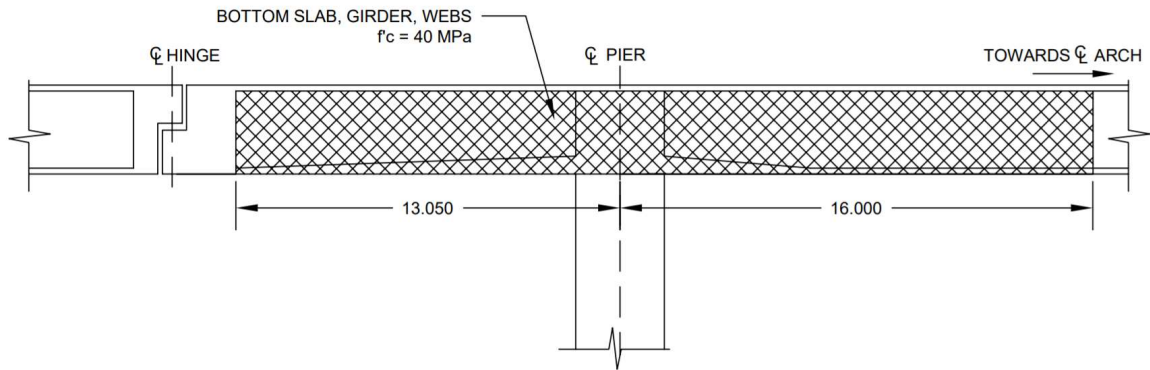


**Figure 6.1: Typical use of 40 MPa concrete over Piers 2 and 3 (m)**

Two model variants were created to account for the additional superstructure stiffness at these locations. The variants considered higher strength concrete for the superstructure over the entirety of Spans 2 – 4. The first variant used a weighted average approach to determine the superstructure material strength. The deck, 31 MPa material, has a cross-sectional area of 3.78 m<sup>2</sup>. The remaining box girder, including the bottom slab, web, and girders, was comprised of 40 MPa concrete and has a cross section of 4.73 m<sup>2</sup> (Figure 6.2). The weighted average approach approximates the material strength of the composite sections as 36 MPa. The second variant, considered an overstrength model, applied 40 MPa concrete to the entirety of Spans 2 – 4. The overstrength approach was



intended to serve as an upper limit on the response due to increased stiffness between the design and as-built concrete strengths.

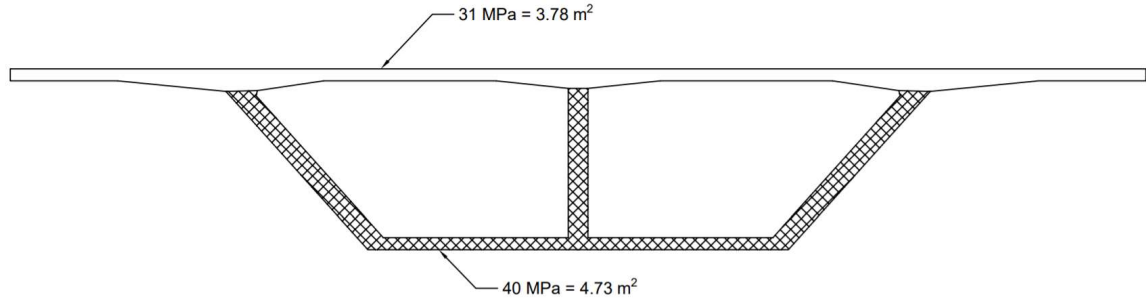


**Figure 6.2: Cross section of strengthened areas of box girder**

#### 6.1.1 Modal Analysis – Superstructure Material

It was expected that increasing the compressive strength, and subsequently  $E$ , would yield an increase in structure stiffness. This expectation was confirmed by the result of the modal and time-history analyses.

Table 6.4 provides a side-by-side comparison of the resulting periods and modal participation factors for the top five modes about all three degrees of freedom. The variant models composed of higher strength concrete demonstrated increased participation ratios and frequencies across most modes in the vertical and transverse directions. Mode 1, the primary transverse mode, was an outlier as the participation factor increased marginally from 55.0% to 55.6%, while the modal period decreased.

In contrast, the 36 MPa and 40 MPa models demonstrated higher modal participation factors about the longitudinal direction. The stiffer superstructures resisted deflections about the vertical and transverse axes. However, the increase in stiffness also attracted larger stresses which were transferred to the substructure components. The

rectangular box columns and arches are oriented to resist transverse loading; as such, the additional stresses carried by the substructure resulted in increased displacement about the column weak axis (i.e., longitudinal direction).

**Table 6.2: Top five modes in the longitudinal direction (X-axis)**

31 MPa Superstructure (Control Model)			36 MPa Superstructure				40 MPa Superstructure			
Mode	Period, $T_{control}$ (s)	Modal Part. Factor (%)	Mode	Period, $T$ (s)	Modal Part. Factor (%)	$T/T_{control}$	Mode	Period, $T$ (s)	Modal Part. Factor (%)	$T/T_{control}$
2	1.342	12.3	2	1.318	12.4	0.982	2	1.305	12.5	0.972
4	0.976	15.1	4	0.976	11.0	1.000	4	0.975	15.1	0.999
9	0.671	9.2	9	0.661	12.4	0.985	9	0.655	11.9	0.976
11	0.627	9.8	11	0.619	16.8	0.987	11	0.613	9.0	0.978
39	0.284	9.3	40	0.279	16.8	0.982	40	0.277	17.1	0.975

**Table 6.3: Top five modes in the transverse direction (Y-axis)**

31 MPa Superstructure (Control Model)			36 MPa Superstructure				40 MPa Superstructure			
Mode	Period, $T_{control}$ (s)	Modal Part. Factor (%)	Mode	Period, $T$ (s)	Modal Part. Factor (%)	$T/T_{control}$	Mode	Period, $T$ (s)	Modal Part. Factor (%)	$T/T_{control}$
1	1.688	55.0	1	1.669	55.4	0.989	1	1.657	55.6	0.982
5	0.819	9.5	5	0.815	9.2	0.995	5	0.812	9.0	0.991
17	0.513	7.0	17	0.511	6.6	0.997	17	0.509	4.0	0.993
24	0.386	1.9	25	0.377	1.5	0.976	16	0.515	3.7	1.333
51	0.240	1.2	36	0.3	1.2	1.250	25	0.373	1.9	1.554

**Table 6.4: Top five modes in the vertical direction (Z-axis)**

31 MPa Superstructure (Control Model)			36 MPa Superstructure				40 MPa Superstructure			
Mode	Period, $T_{control}$ (s)	Modal Part. Factor (%)	Mode	Period, $T$ (s)	Modal Part. Factor (%)	$T/T_{control}$	Mode	Period, $T$ (s)	Modal Part. Factor (%)	$T/T_{control}$
7	0.713	5.8%	7	0.699	5.2%	0.981	7	0.691	4.9%	0.970
15	0.560	3.9%	18	0.495	4.0%	0.884	18	0.488	3.6%	0.871
18	0.506	4.1%	20	0.457	3.9%	0.904	20	0.449	3.8%	0.888
20	0.469	3.9%	21	0.448	3.8%	0.954	21	0.44	4.1%	0.937
44	0.263	6.1%	44	0.257	4.4%	0.976	43	0.254	4.7%	0.965

### 6.1.2 Time History Analysis – Superstructure Material

Displacements and internal stresses were both considered when examining the results of the time-history analysis from the El Centro earthquake ground motions. The data collected were evaluated using an envelope approach. The envelope approach considers the status of the bridge at every step of the time-history analysis and consolidates the most extreme response at each location along the length of the structure. Figure 6.3 displays the maximum absolute displacements of the superstructure in the transverse direction for the control model (31 MPa) in contrast to the 40 MPa superstructure model. The length along the structure (y-axis in the graph) is measured from Abutment 1 to Abutment 2. Figure 6.4 displays extreme longitudinal stresses experienced along the length of the superstructure.

As seen in Figure 6.3, the 40 MPa superstructure demonstrated a reduced curvature of deformation along Spans 2 – 4, suggesting that the spans modeled using stiffer materials had reduced second-order effects. As a result, other sections of the superstructure

experience increased first-order deformations. This phenomenon is best observed along the negative displacements of Spans 5 – 7 in Figure 6.3. As expected, the stiffer superstructure resulted in larger internal stresses. The midspan of Span 2 and adjacent half of Span 3 both showed up to a 26.7% increase in stress, supporting the data shown in Figure 6.3 (i.e., the internal stresses increase as the superstructure resists second-order deformations).

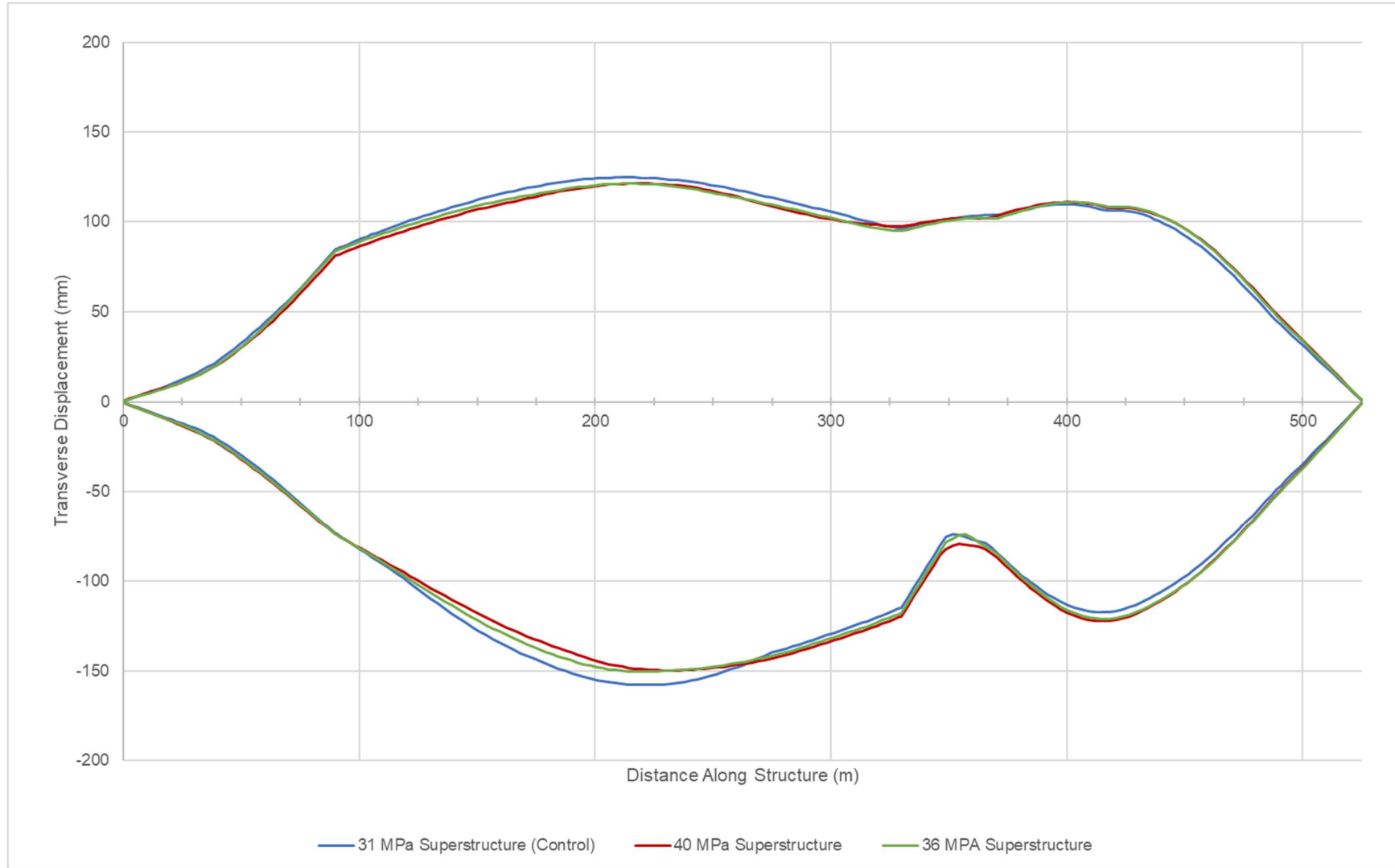


**Figure 6.3: Envelope of transverse displacement of northbound superstructure for superstructure material stiffness variants**

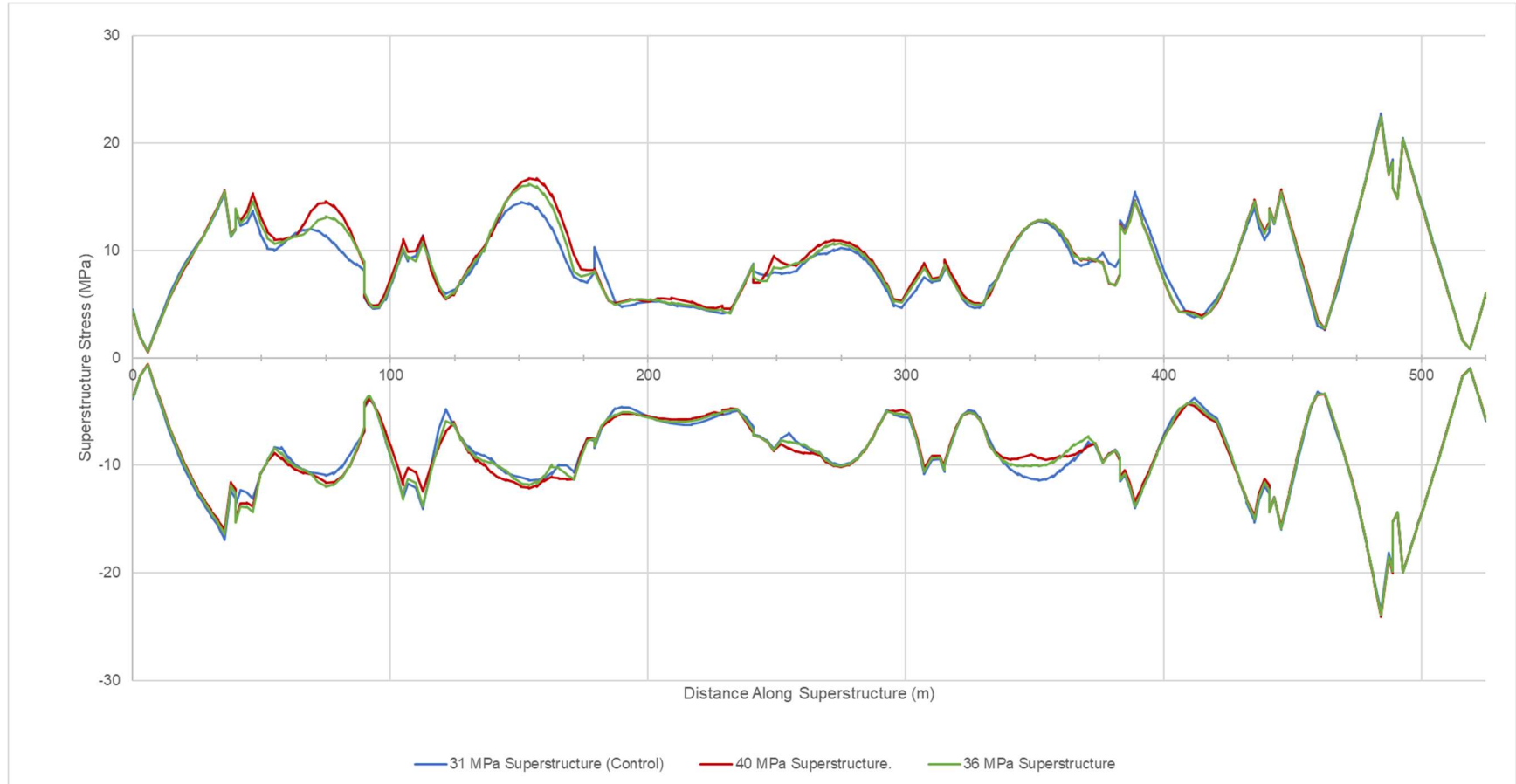


**Figure 6.4: Maximum longitudinal stresses in superstructure for superstructure material stiffness variants**

The evaluation of superstructure material stiffness has several limitations that must be considered. As previously mentioned, the material change was applied to the full length of Spans 2 – 4 due to modeling limitations of CSiBridge. In reality, only portions of the box girder over select areas of Piers 2 and 3 were comprised of higher strength concrete. As a result, it is likely that the changes in second-order effects between model variants were more dramatic than those exhibited by the existing structure. Future research into the stiffened superstructure sections could consider assigning property modifiers to the designated areas using tools in the Advanced Tab of CSiBridge.

As previously mentioned, the material strengths specified in the design plans are minimum requirements. Therefore, it is likely that the actual concrete strength and stiffness of the Galena Creek Bridge is higher than the control model. This same logic would apply to all concrete components of the entire bridge (i.e., not solely the superstructure sections that use 40 MPa concrete). The accuracy of the model could be further improved by examining cylinder test results sampled from the concrete used during construction; however, an average value would need to be employed for the composite superstructure sections. Determining the actual effective strength of the concrete may improve the calibration of the model to the existing structure.

## **6.2 Structural Damping**

Damping is a structural property which quantifies the dissipation of kinetic energy (Chopra, 2012). A structure swaying in free vibration with no material damping would oscillate with the same amplitude and frequency indefinitely. The amplitude of vibration is reduced over time as a function of damping. In a 2013 study, the Galena Creek Bridge

was subject to vertical and lateral excitation to determine baseline values for the physical properties (Carr and Sanders, 2013). A vertical excitation was induced by driving a 16,400 kg truck off of a 0.15 m tall ramp, while lateral excitation was induced using an eccentric mass shaker mounted to the link slab.

The damping values from the vertical loading experiments ranged from 1.3% to 2.2%, with an average of 1.85%. The bridge reliably demonstrated an average damping of 3.0% during the higher frequencies generated by the mass shaker. These results are consistent with the 2% – 3% damping typical for reinforced concrete structures with negligible cracking (Chopra, 2012). The most recent bridge inspection noted cracking throughout the columns and arches up to 0.8 mm wide and minor spalls up to 12.7 mm deep (NDOT, 2018). The damage recorded from this bridge inspection was assumed to have an insignificant impact on the modal properties of the Galena Creek Bridge. Based on the results of the field tests and the corroborating values from established sources, the initial material damping for the concrete definitions in CSiBridge were set as 2.0%.

To evaluate the influence of the structure damping ratio on the response of the model to ground motions, two additional model variants were created. Reinforced concrete exhibiting minor hairline cracking developed throughout the service life is typically representative of 5% damping (Chopra, 2012). Conversely, material damping of 7% is more indicative of concrete members that display significant cracking that occurs before the yielding of the reinforcing steel. For each case, the damping ratio of interest was assigned to every type of concrete definition in that model.



### *6.2.1 Modal Analysis – Structural Damping*

All CSiBridge models were considered to be classically damped systems where the modal properties are not dependent on the damping ratio, and the modes for an undamped model would be the same as those of a model with any material damping value. As such, the modal information for this series of tests is identical with those of the control model and modal analyses were not performed for this variable.

### *6.2.2 Time-history Analysis – Structural Damping*

Comparing the transverse displacements between the models in Figure 6.5 shows consistent and expected patterns; specifically, as the damping value increases the displacement of the superstructure decreases. At the crown of the arch, the control model has a maximum transverse displacement of 15.7 cm. The 5% damping model exhibits a 10.1% decrease in displacement (14.0 cm) at the same location. The crown of the arch of the 7% damping model only displaces 13.4 cm, a 14.7% decrease from the control model. Further, the limited data suggests that continual increases in material damping yields diminishing changes in the displacement of the superstructure.

Similarly, increasing the damping reduces the internal stresses of the superstructure, with the same pattern of diminishing returns observed. Figure 6.6 reveals that increasing the damping from 2% to 5% reduced the stresses up to 19.8%. However, the plots for 5% and 7% damping are nearly congruent. Although the 7% damping model displayed reduced stresses across the entire length of the bridge, the superstructure only noted an average decrease of 0.8 MPa. In contrast, the 5% damping model experienced an average reduction of 2.0 MPa compared to the 2% damping control model.

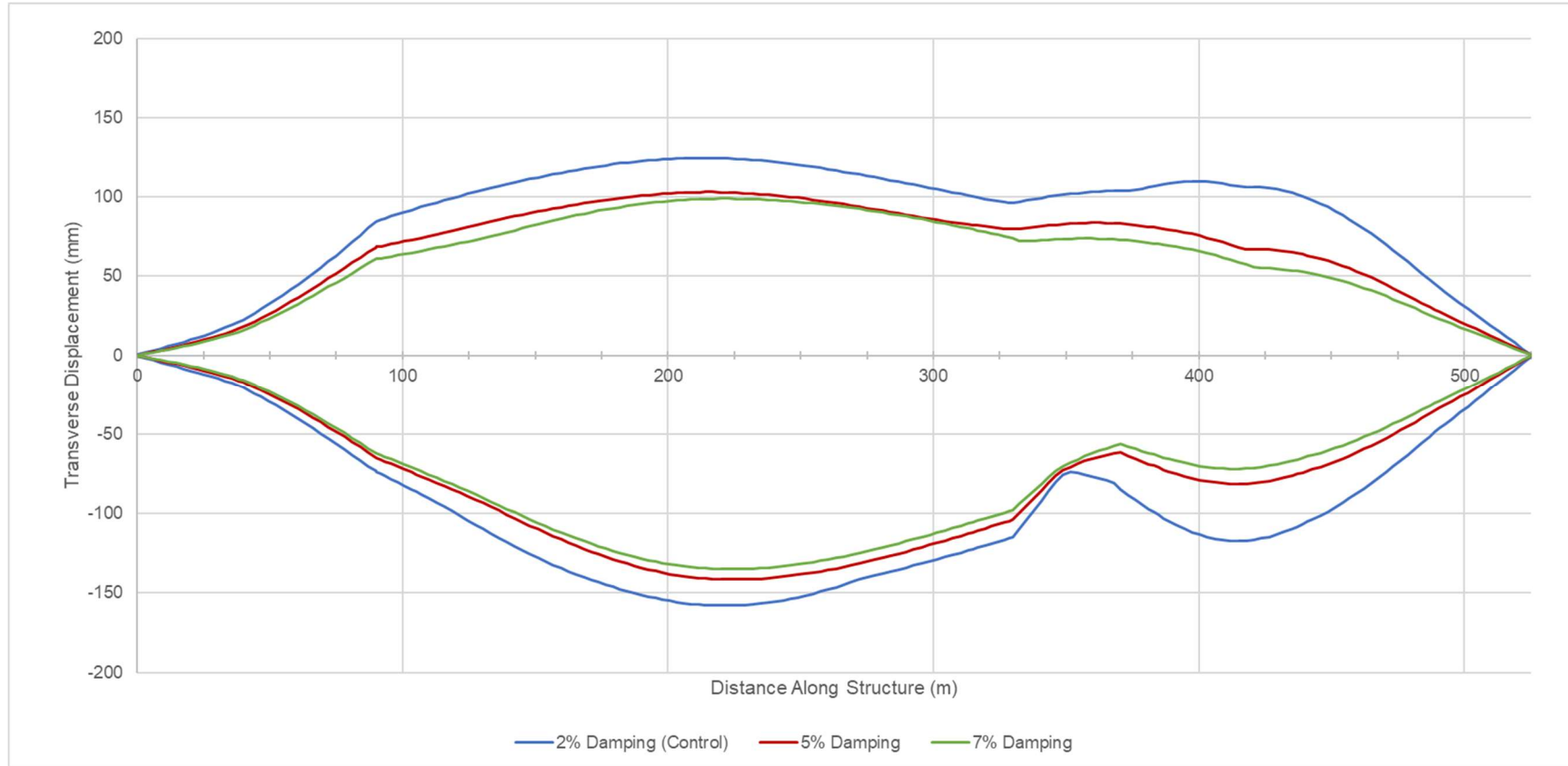


**Figure 6.5: Envelope of transverse displacement of superstructure from damping analyses**

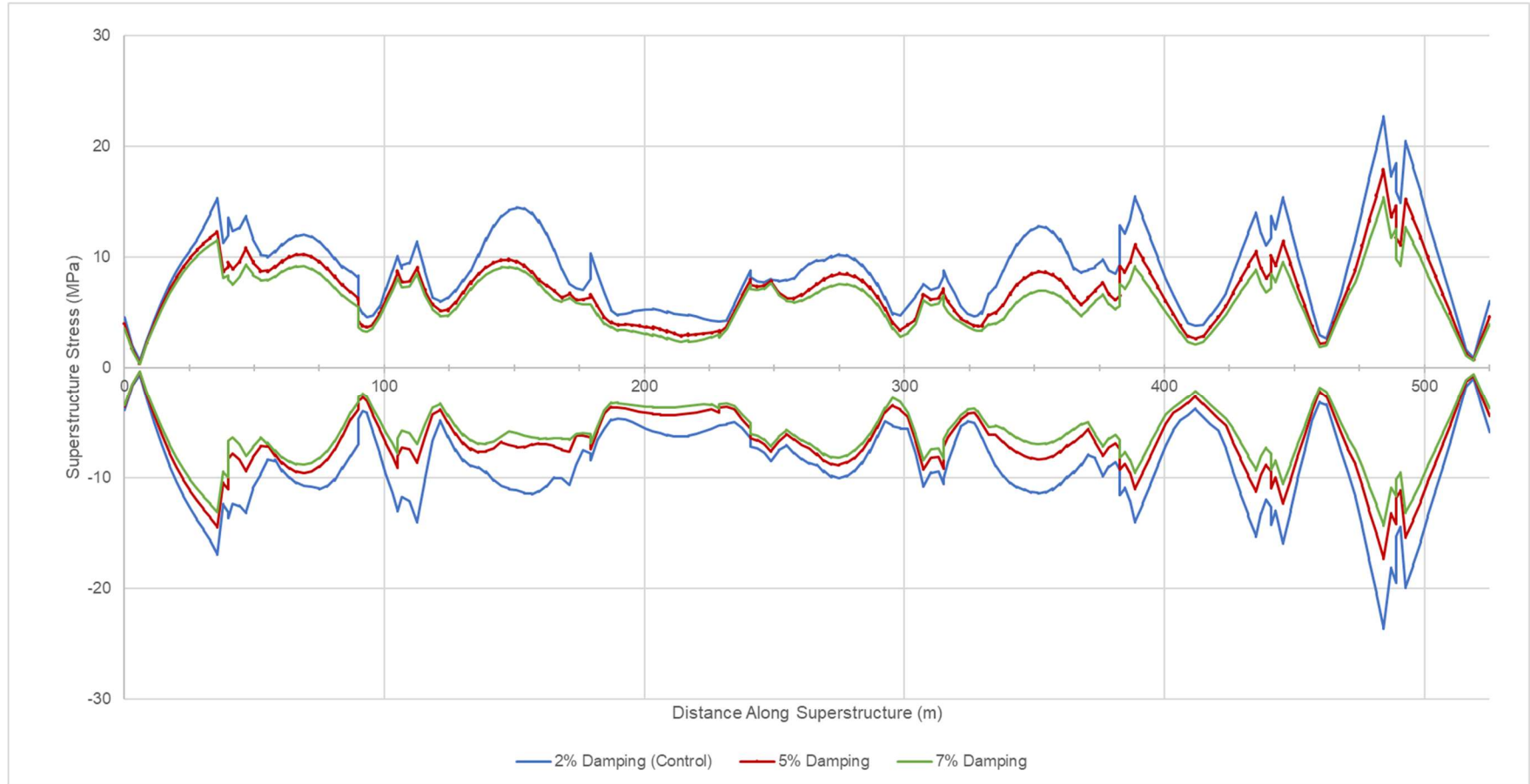


**Figure 6.6: Maximum superstructure stresses from damping analyses**

The results from the time-history analyses show that damping has a significant influence on the displacement and stresses experienced by the structure. Verification of the current damping of the Galena Creek Bridge would be conducted by comparing the dynamic response of the structure to the FEM. The damping of concrete structures is directly dependent on the structural integrity of the concrete; therefore, as cracks initiate and propagate in bridge components, the material damping value changes as well. This parametric evaluation assumed the same material damping throughout all concrete components of the model. As the Galena Creek Bridge continues to develop cracking throughout the service life, appropriate damping ratios would need to be applied to deteriorating components to continuously reflect the true behavior.

### **6.3 Elastomeric Bearing Stiffness**

The elastomeric bearings of the Galena Creek Bridge permit mild translation and rotation of the superstructure at the expansion joints and abutments. These components can be effective in reducing the stresses within the superstructure by allowing limited and controlled deflection. Properly replicating bearing behavior in CSiBridge is key to simulating the interactions between the frames of the existing structure.

CSiBridge has bearing stiffness inputs for both translation and rotation about the three degrees of freedom in the bearing definition. Restrainer properties can also be attached to bearings as a means to add advanced properties, such as limitations on allowable rotation and translation. Although both methods of assigning physical properties to bearings in CSiBridge are viable, the calculated stiffness values were input in the initial bearing definitions to simplify the editing procedure and to facilitate model updates.

Typically, restrainer properties would be used to model complex elements, such as seismic retrofitting steel cables. The most recent bridge inspection performed by NDOT did not note excessive or unusual displacements at the abutments and hinges (NDOT, 2018). As such, additional restrainer inputs were not deemed necessary.

CSiBridge requires the user to explicitly define the number of bearings used when defining the substructure elements, such as the abutments or bents. However, the input for hinges only permits a single bearing component to be assigned. The orientation of the bearings at the hinges are congruent; therefore, it was assumed that the three bearings at the hinges behaved in tandem. The physical properties of the single hinge bearing defined in CSiBridge were the summation of the stiffnesses of the three elastomeric bearings in the actual structure. Figure 6.7 demonstrates the allowable rotations and translations assigned to the bearing definitions with respect to the global axes definition in CSiBridge. The idealized models of reinforced elastomeric bearings conservatively assumed no rotation about the longitudinal or transverse axis.

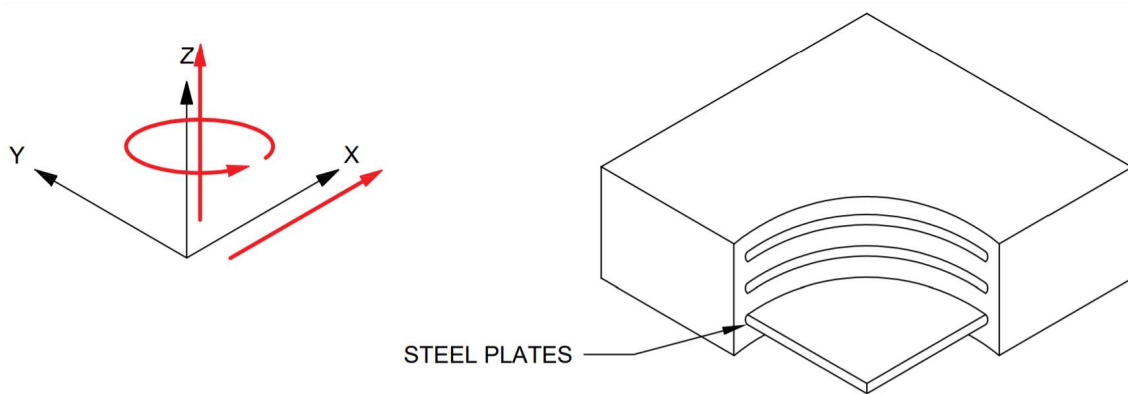


**Figure 6.7: Allowable degrees of freedom (left) of the bearing pads relative to CSiBridge global axes**

Equations 5.2 – 5.4 were used to calculate the stiffness of the bearing pads (Akogul, 2008). Table 14.7.6.2-1 of the AASHTO LRFD Specifications suggests the allowable shear modulus ( $G$ ) range for 60 durometer elastomers is from 0.90 MPa to 1.38 MPa at 22.8° C (AASHTO, 2021). The control model assumed  $G = 0.90$  MPa to allow the initial structure to have decreased stiffness. Evaluation of bearing stiffness involved assigning the maximum recommended shear modulus ( $G = 1.38$  MPa). This approach was used to determine the probable range that the bearing stiffnesses would influence the dynamic properties of the FEM. The calculated values for the hinge and abutment bearings using  $G = 1.38$  MPa are displayed in Figure 6.8 and Figure 6.9.

Two additional bearing conditions were considered to suggest the probable limit of influence that bearings have on the dynamic properties of the structure. Removing the stiffness values would assume that the bearings allowed free translation and rotation about the desired degrees of freedom. This modeling condition would result in a decrease in stiffness and likely increase in displacements. Conversely, modeling all bearings as fully fixed would simulate the maximum stiffness bearing conditions would produce.

**Bridge Bearing Data**

**Bridge Bearing Name** Abutment Bearing **Units** KN, m, C

**Bridge Bearing Is Defined By:**

☐ Link/Support Property ☐ User Definition

**User Bearing Properties**

DOF/Direction	Release Type	Stiffness
Translation Vertical (U1)	Partial Fixity	3451091.
Translation Normal to Layout Line (U2)	Fixed	
Translation Along Layout Line (U3)	Partial Fixity	5483.675
Rotation About Vertical (R1)	Partial Fixity	748.704
Rotation About Normal to Layout Line (R2)	Fixed	
Rotation About Layout Line (R3)	Fixed	

OK Cancel

Figure 6.8: Upper limit abutment bearing stiffness input for CSiBridge ( $G = 1.38$  MPa)

**Bridge Bearing Data**

**Bridge Bearing Name** Hinge Bearing **Units** KN, m, C

**Bridge Bearing Is Defined By:**

☐ Link/Support Property ☐ User Definition

**User Bearing Properties**

DOF/Direction	Release Type	Stiffness
Translation Vertical (U1)	Partial Fixity	7441561.
Translation Normal to Layout Line (U2)	Fixed	
Translation Along Layout Line (U3)	Partial Fixity	8618.713
Rotation About Vertical (R1)	Partial Fixity	1659.39
Rotation About Normal to Layout Line (R2)	Fixed	
Rotation About Layout Line (R3)	Fixed	

OK Cancel

Figure 6.9: Upper limit hinge bearing stiffness input for CSiBridge ( $G = 1.38$  MPa)

### *6.3.1 Modal Analysis – Elastomeric Bearing Stiffness*

Increasing the shear modulus of the elastomers from 0.90 MPa to 1.38 MPa marginally increased the stiffness of the structure. Although Table 6.6 shows that there were no noticeable changes to the transverse modes, the longitudinal modes demonstrated the greatest dependence on this parameter. The bearings at both the hinges and abutments were restricted in the transverse direction by shear keys; as such, increasing the bearing stiffness resulted in the frequencies of the top transverse modes changing less than 1.0%. Likewise, the top vertical modes experienced inconsequential changes (under 0.5%). The high vertical stiffness of the elastomer resulted in the bearings acting similar to being fully constrained in translation along the vertical axis. In contrast, the top longitudinal modes experienced period and participation factor reductions of up to 2.7% and 14.3%, respectively (Table 6.5).

The fully fixed bearing variant restricted translation and rotation about all three degrees of freedom. As expected, the periods for most modes decreased to reflect the increased stiffness of the model. Note that several of the top transverse modes demonstrated significant increase in periods, likely a result of restricting rotation about the vertical axis. Conversely, 14 of the 15 modes observed of the free bearing model showed an incremental increase in periods. It should be noted that Table 6.7 reveals the change in vertical modes was almost negligible, with the average increase being less than 0.2%. This further confirms that the high calculated vertical stiffness of the elastomeric bearings acts similar to a bearing that completely restricts vertical translation.



**Table 6.5: Comparison of top longitudinal modes for bearing stiffness variations (X-axis)**

<b>G = 0.90 MPa Bearings (Control Model)</b>			<b>G = 1.38 MPa Bearings</b>				<b>Fully Fixed Bearings</b>				<b>Free Bearings</b>			
<b>Mode</b>	<b>Period, <math>T_{control}</math> (s)</b>	<b>Modal Part. Factor (%)</b>	<b>Mode</b>	<b>Period, <math>T</math> (s)</b>	<b>Modal Part. Factor (%)</b>	<b><math>T/T_{control}</math></b>	<b>Mode</b>	<b>Period, <math>T</math> (s)</b>	<b>Modal Part. Factor (%)</b>	<b><math>T/T_{control}</math></b>	<b>Mode</b>	<b>Period, <math>T</math> (s)</b>	<b>Modal Part. Factor (%)</b>	<b><math>T/T_{control}</math></b>
2	1.342	12.3	2	1.332	13.0	0.992	3	0.919	5.4	0.685	2	1.366	10.8	1.017
4	0.976	15.1	4	0.952	14.9	0.975	11	0.550	3.3	0.564	4	1.027	15.6	1.052
9	0.671	9.2	9	0.666	8.5	0.993	17	0.454	11.1	0.677	9	0.684	9.7	1.019
11	0.627	9.8	11	0.623	9.9	0.994	36	0.277	27.1	0.442	11	0.633	9.4	1.011
39	0.284	9.3	40	0.283	10.6	0.996	37	0.272	14.2	0.957	39	0.285	15.7	1.002

**Table 6.6: Comparison of top transverse modes for bearing stiffness variations (Y-axis)**

<b>G = 0.90 MPa Bearings (Control Model)</b>			<b>G = 1.38 MPa Bearings</b>				<b>Fully Fixed Bearings</b>				<b>Free Bearings</b>			
<b>Mode</b>	<b>Period, <math>T_{control}</math> (s)</b>	<b>Modal Part. Factor (%)</b>	<b>Mode</b>	<b>Period, <math>T</math> (s)</b>	<b>Modal Part. Factor (%)</b>	<b><math>T/T_{control}</math></b>	<b>Mode</b>	<b>Period, <math>T</math> (s)</b>	<b>Modal Part. Factor (%)</b>	<b><math>T/T_{control}</math></b>	<b>Mode</b>	<b>Period, <math>T</math> (s)</b>	<b>Modal Part. Factor (%)</b>	<b><math>T/T_{control}</math></b>
1	1.688	55.0	1	1.688	55.0	1.000	1	1.595	56.2	0.945	1	1.689	55.0	1.000
5	0.819	9.5	5	0.819	9.5	1.000	4	0.731	7.8	0.893	5	0.819	9.5	1.000
17	0.513	7.0	17	0.513	7.1	1.000	13	0.500	2.7	0.976	17	0.513	7.0	1.000
24	0.386	1.9	24	0.386	1.9	1.000	15	0.482	1.4	1.249	24	0.386	1.9	1.000
51	0.240	1.2	50	0.240	1.2	1.000	20	0.382	2.3	1.594	50	0.240	1.2	0.998

**Table 6.7: Comparison of top vertical modes for bearing stiffness variations (Z-axis)**

<b>G = 0.90 MPa Bearings (Control Model)</b>			<b>G = 1.38 MPa Bearings</b>				<b>Fully Fixed Bearings</b>				<b>Free Bearings</b>			
<b>Mode</b>	<b>Period, <math>T_{control}</math> (s)</b>	<b>Modal Part. Factor (%)</b>	<b>Mode</b>	<b>Period, <math>T</math> (s)</b>	<b>Modal Part. Factor (%)</b>	<b><math>T/T_{control}</math></b>	<b>Mode</b>	<b>Period, <math>T</math> (s)</b>	<b>Modal Part. Factor (%)</b>	<b><math>T/T_{control}</math></b>	<b>Mode</b>	<b>Period, <math>T</math> (s)</b>	<b>Modal Part. Factor (%)</b>	<b><math>T/T_{control}</math></b>
7	0.713	5.8	8	0.704	3.2	0.988	5	0.708	9.7	0.994	7	0.720	4.2	1.010
15	0.560	3.9	18	0.505	3.9	0.902	10	0.565	8.8	1.009	15	0.561	4.8	1.001
18	0.506	4.1	20	0.469	4.0	0.927	13	0.500	5.5	0.990	18	0.506	4.3	1.000
20	0.469	3.9	21	0.458	3.4	0.976	14	0.499	8.1	1.062	20	0.469	4.0	1.000
44	0.263	6.1	44	0.263	6.3	1.000	39	0.262	5.9	0.996	44	0.263	6.4	1.000

### 6.3.2 Time-history Analysis – Elastomeric Bearing Stiffness

The time-history analysis results verify the conclusions from the modal analysis. The vertical and transverse displacements from the ground motions were nearly identical. This is because lateral translation for both the hinge and abutment bearings was fully restricted. It was assumed that the shear keys at both locations were effectively preventing lateral translation.

Superstructure displacements along the longitudinal axis demonstrated noticeable changes because of editing the bearing stiffnesses (Figure 6.10). Specifically, Frame 3 of the  $G = 1.38$  MPa variant experienced an average 8.3% decrease in longitudinal displacement. Increasing the stiffness of the bearings increased the interactions between the frames of the Galena Creek Bridge. As the bearing stiffness increased, the high stiffness of Frame 2 would limit the displacements of Frames 1 and 3.

Note that Frame 2 demonstrates nearly identical behavior among all the cases considered for this variable. The maximum lateral displacements of Frame 2 diverge the most from those of the other analyses near Hinge 1. This is likely a result of the fixed Abutment 1 located only 90 m from Hinge 1. Although the envelope longitudinal displacements of Frames 1 and 3 show greater discrepancies between the models than Frame 2, the results are inconclusive. The free bearing model variant showed increased longitudinal displacements throughout Frame 1. However, the maximum positive longitudinal displacement along Frame 3 was an average of 15.1% lower than the two models with bearing stiffnesses assigned. This is likely a consequence of the specific ground motion. Further research on the influence of bearing properties could consider

various ground motions to develop more substantial correlations. Another option could be to apply symmetrical ground motions, such as a sine wave, about both directions of the desired axes.

The results suggest that the bearing boundary conditions limiting translation and rotation are more important than the actual calculated stiffness values. Although increasing the bearing stiffness from  $G = 0.90$  MPa to 1.38 MPa increased the stiffness of the model, the difference in the modal analyses and time-history responses was negligible. The more significant changes to the modal behavior and dynamic response resulted from adding fixities to the bearing definitions to model them as rigid. These conclusions mirror those found in previous research conducted at the Georgia Institute of Technology (Wang, 2010). Wang found that the stiffness values assigned to elastomeric bearings did not influence the load bearing capacity of the bridges.

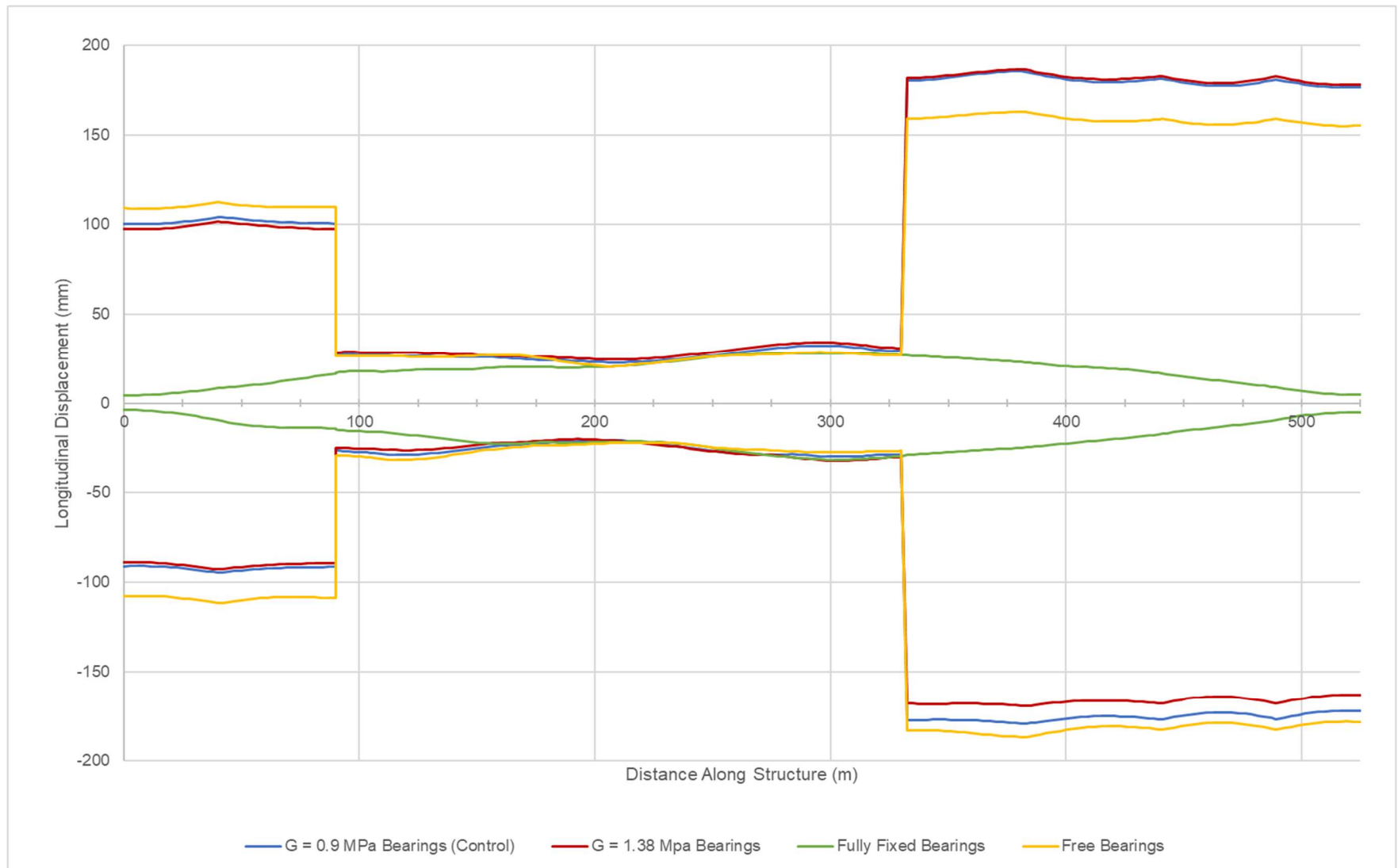


**Figure 6.10: Maximum longitudinal displacement of superstructures from bearing analyses**

## 6.4 Effective Moment of Inertia of Substructure

As cracks propagate, reinforced concrete elements suffer from a reduction in flexural rigidity. ACI suggests that when performing linear-elastic analyses, concrete cracking can be accounted for by applying a reduction factor to the moment of inertia (MOI) of the concrete member. ACI-14 Table 6.6.3.1.1 recommends reducing the MOI of a column to 70% to provide conservative estimates during the design process. Note that the gross cross-sectional area does not need additional factors when using this method. While conservative assumptions aid in the safe design of structures, they do not typically represent the physical in-service behavior. To better understand how variations in the moment of inertia influence the model, scaling factors for the moment of inertia were investigated between 100% and 50% in 5% increments.

A typical rectangular box column section of the Galena Creek Bridge has a gross MOI of  $11.59 \text{ m}^4$  about the transverse axis and  $44.57 \text{ m}^4$  about the longitudinal axis. The typical arch section has gross MOIs of  $14.22 \text{ m}^4$  and  $33.50 \text{ m}^4$  about the transverse and longitudinal axes, respectively. The MOI scaling factor was applied to the elements in CSiBridge by accessing the section properties of the arch and column cross sections under the Components Tab, as can be seen in Figure 6.11. For these set of trials, the same constant was applied to both the Pier Column and the Arch Typical. sections.

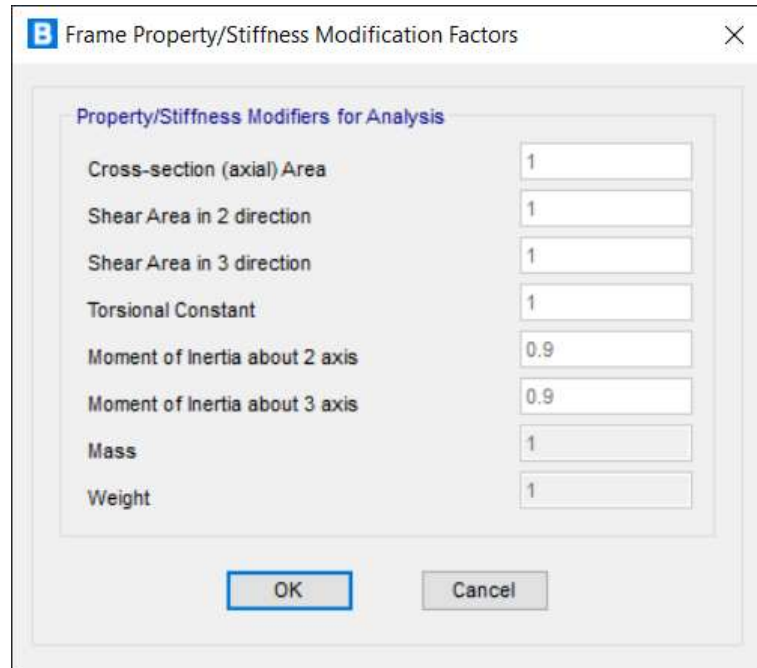


**Figure 6.11: Example of MOI reduction factor applied in CSiBridge**

#### 6.4.1 Modal Analysis – Effective Column Moment of Inertia

A total of 10 variant models were analyzed, excluding the control model. Tables 6.8 – 6.10 display the partial results from performing modal analyses; they show 10% increments as opposed to 5% for the purposes of presenting the findings in a clear format. The side-by-side comparison of the changes in period and participation factors reveal an inverse correlation between effective MOI and modal periods. The periods for the longitudinal and transverse modes considered increased as the effective MOI of the substructure elements decreased: the longitudinal modes increased up to 33.2% and the transverse modes increased up to 24.3%. This validates the assumption that increasing the flexibility would decrease the natural frequencies. The vertical modal data only exhibited minor changes between the analyses, suggesting that the substructure flexibility has minimal influence on the vertical behavior of the bridge.



**Table 6.8: Comparison of top longitudinal modes for MOI variant models**

100% MOI (Control Model)				90% MOI				80% MOI			
Mode	Period, $T_{control}$ (s)	Modal Part. Factor (%)		Mode	Period, $T$ (s)	Modal Part. Factor (%)	$T/T_{control}$	Mode	Period, $T$ (s)	Modal Part. Factor (%)	$T/T_{control}$
2	1.342	12.3		2	1.391	12.4	1.037	2	1.411	12.5	1.051
5	0.976	15.1		5	1.007	15	1.032	5	1.043	14.9	1.069
12	0.669	9.2		12	0.682	10.2	1.019	12	0.696	11.9	1.040
15	0.621	9.6		15	0.635	9.5	1.023	15	0.649	8.2	1.045
42	0.284	10.3		42	0.286	13.7	1.007	43	0.286	13.8	1.007
70% MOI				60% MOI				50% MOI			
Mode	Period, $T$ (s)	Modal Part. Factor (%)	$T/T_{control}$	Mode	Period, $T$ (s)	Modal Part. Factor (%)	$T/T_{control}$	Mode	Period, $T$ (s)	Modal Part. Factor (%)	$T/T_{control}$
2	1.452	12.7	1.082	2	1.501	12.9	1.118	2	1.559	13.3	1.162
5	1.086	14.9	1.113	5	1.139	14.7	1.167	5	1.206	14.5	1.236
7	0.824	6.7	1.232	7	0.854	6.9	1.277	6	0.891	6.5	1.332
12	0.713	13.7	1.148	12	0.735	16.3	1.184	12	0.765	19.6	1.232
43	0.288	16.3	1.014	44	0.29	18.1	1.021	44	0.293	19.2	1.032

**Table 6.9: Comparison of top transverse modes for MOI variant models**

100% MOI (Control Model)				90% MOI				80% MOI			
Mode	Period, $T_{control}$ (s)	Modal Part. Factor (%)		Mode	Period, $T$ (s)	Modal Part. Factor (%)	$T/T_{control}$	Mode	Period, $T$ (s)	Modal Part. Factor (%)	$T/T_{control}$
1	1.739	52.4		1	1.804	52.9	1.037	1	1.865	53.6	1.072
4	1.027	3.3		4	1.057	3.5	1.029	4	1.089	3.6	1.060
6	0.788	3.6		6	0.801	3.7	1.016	6	0.816	3.8	1.036
9	0.717	4.2		9	0.735	4.3	1.025	9	0.755	4.1	1.053
21	0.504	7.2		21	0.523	7.2	1.038	20	0.546	6.8	1.083
70% MOI				60% MOI				50% MOI			
Mode	Period, $T$ (s)	Modal Part. Factor (%)	$T/T_{control}$	Mode	Period, $T$ (s)	Modal Part. Factor (%)	$T/T_{control}$	Mode	Period, $T$ (s)	Modal Part. Factor (%)	$T/T_{control}$
1	1.945	54.3	1.118	1	2.041	55.1	1.174	1	2.162	56.1	1.243
4	1.128	3.8	1.098	4	1.173	3.9	1.142	4	1.23	3.9	1.198
6	0.835	3.9	1.060	6	0.859	4.0	1.090	7	0.889	4.0	1.128
9	0.776	3.6	1.082	9	0.8	3.0	1.116	9	0.827	5.3	1.153
20	0.571	6.7	1.133	20	0.601	6.3	1.192	18	0.64	3.8	1.270

**Table 6.10: Comparison of top vertical modes for MOI variant models**

100% MOI (Control Model)				90% MOI				80% MOI			
Mode	Period, $T_{control}$ (s)	Modal Part. Factor (%)		Mode	Period, $T$ (s)	Modal Part. Factor (%)	$T/T_{control}$	Mode	Period, $T$ (s)	Modal Part. Factor (%)	$T/T_{control}$
10	0.711	6.8		10	0.723	6.5	1.017	10	0.733	5.5	1.031
19	0.559	3.8		22	0.509	5.8	0.911	22	0.514	6.3	0.919
22	0.502	5.6		24	0.474	4.2	0.944	24	0.479	4.1	0.954
24	0.468	4.4		25	0.464	3.4	0.991	25	0.470	3.6	1.004
48	0.263	5.8		47	0.268	6.6	1.019	47	0.270	5.1	1.027
70% MOI				60% MOI				50% MOI			
Mode	Period, $T$ (s)	Modal Part. Factor (%)	$T/T_{control}$	Mode	Period, $T$ (s)	Modal Part. Factor (%)	$T/T_{control}$	Mode	Period, $T$ (s)	Modal Part. Factor (%)	$T/T_{control}$
10	0.748	4.6	1.052	16	0.627	3.7	0.882	13	0.741	5.3	1.042
22	0.522	6	0.934	22	0.532	4	0.952	22	0.545	3.7	0.975
24	0.480	4.2	0.956	24	0.493	4.8	0.982	24	0.503	6.1	1.002
25	0.477	3.9	1.019	25	0.485	3.9	1.036	45	0.288	3.7	0.615
46	0.275	7.9	1.046	46	0.28	9.3	1.065	46	0.284	6.3	1.080

#### 6.4.2 Time-history Analysis – Effective Column Moment of Inertia

The results from the time-history analyses corroborate the data from the modal analyses; decreasing the effective MOI of the substructure elements increases the deflection across the superstructure. Figure 6.12 shows that the structure experiences the greatest changes in deflection at Span 3 as the abutments restrict transverse displacement. To better view the influence of the effective MOI on maximum displacement, Figure 6.13 plots the envelope transverse displacement at the midspan of Span 3. The graph clearly shows that the increments between model variants increase as the effective MOI decreases. Reducing the factor from 100% to 90% results in a 11 mm increase in displacement at this

location; however, reducing the factor from 70% to 60% resulted in an increase of up to 121 mm at the crown of the arch.

It was noted in Figure 6.12 that the transverse displacements of Spans 6 and 7 did not follow the typical pattern exhibited by the rest of the structure. For Spans 1 through 5, decreasing the effective MOI of the substructure elements would increase the transverse displacement, as expected. Spans 6 and 7 demonstrate relatively congruent behavior between 100% and 70% effective MOI. Additionally, the 60% MOI analysis demonstrated less displacement than the control model between 425 m and 525 m along the structure. This is likely due to extreme deflections at Span 3 and the abutment boundary condition. The inverse curvature of Frame 3 of the structure is a result of connecting the displacements at Hinge 2 to Abutment 2, which restricts transverse translation. It is also likely that the atypical behavior might be a result of the specific ground motion applied. Performing further time-history analyses using various ground motions would reveal whether the behavior by Spans 6 and 7 is typical of the FEA model.

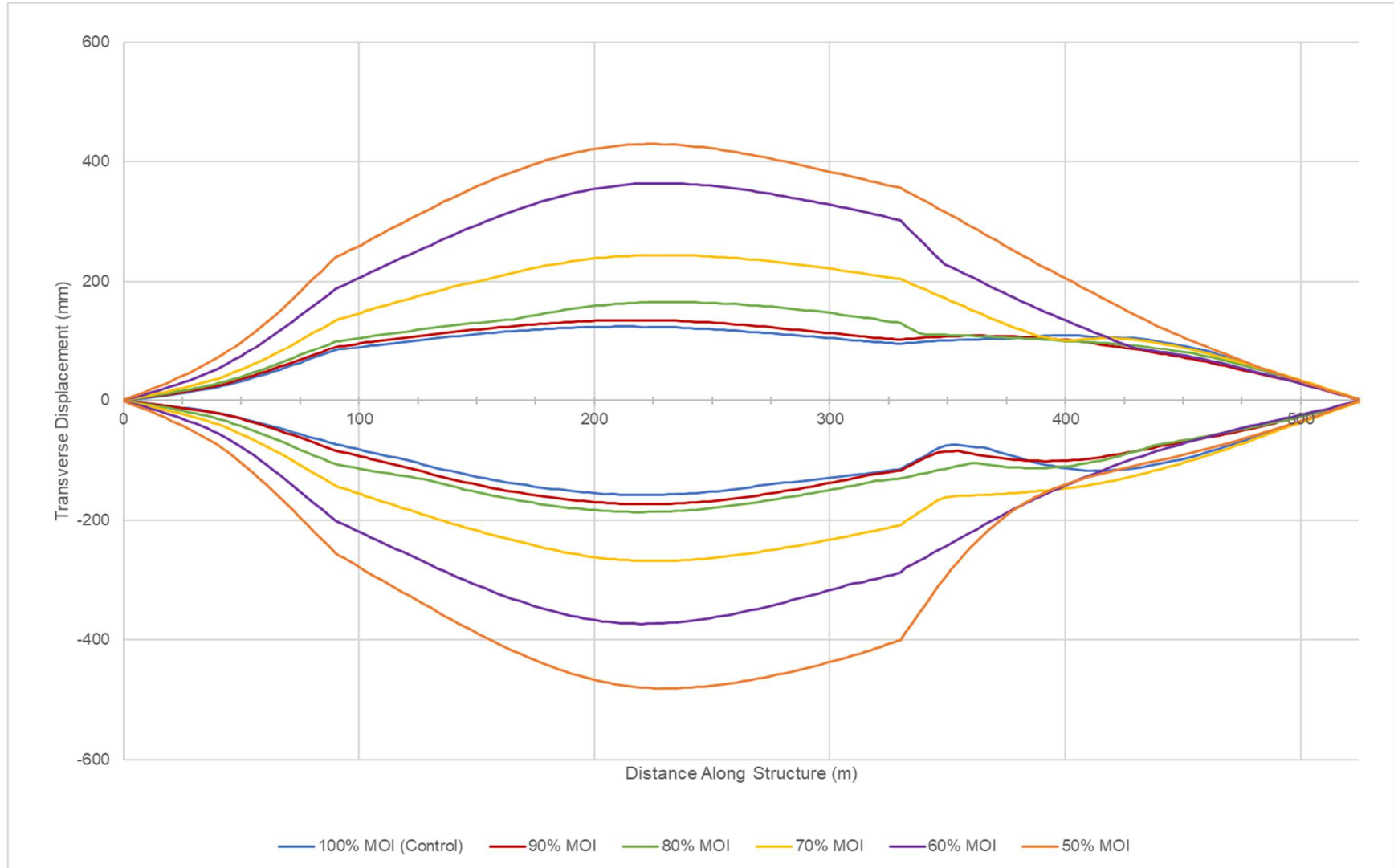


**Figure 6.12: Maximum transverse displacement of superstructures for substructure effective MOI analyses**

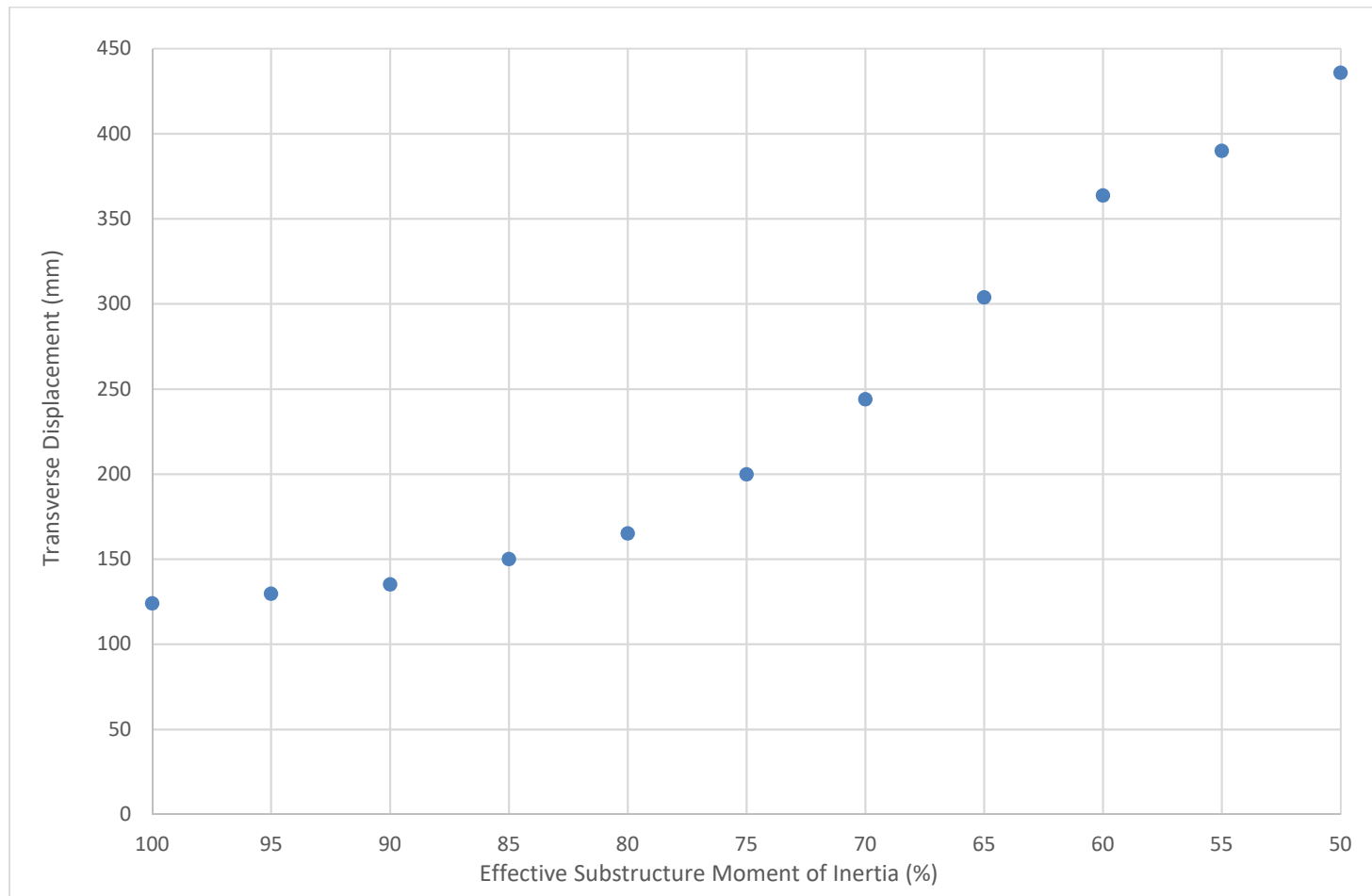


**Figure 6.13: Maximum transverse displacement at midspan of Span 3**

Applying a universal MOI reduction factor is not a practical representation of the Galena Creek Bridge. The time-history analysis of the control model reveals that the columns of the bridge experience different internal stresses and deformations. Substructure components that attract larger forces, such as Pier 1, develop deeper cracks than members that are not subject to as severe bending moments, resulting in different effective MOI factors. To further pursue this avenue of research would require tracking the moments in individual substructure elements. From there, the applied MOI reduction factor for each column would increase proportionally to the bending moments experienced based on reasonably assumed crack lengths. Finally, this parametric study only performed linear time-history analyses. Excessive reduction in the effective MOI of the substructure would likely result in the element failing before reaching the displacements noted in this evaluation.

## **6.5 Link Slab**

A 0.2 m thick link slab connects the northbound and southbound structures along the length of Frame 2. As the primary component connecting the northbound and southbound superstructures, the link slab provides significant resistance to lateral loads. The link slab is considered to be integral with the adjacent bridge decks due to the sufficient steel reinforcing between the aforementioned components. As the Galena Creek Bridge is most vulnerable to lateral loads, accurately modeling the link slab is crucial to calibrating the FEM to in-service behavior.

The bridge object superstructure is comprised of shell elements that are up to 3 m in length, as set by the user through the Update feature in CSiBridge. The nodes used to define

the rectangular link slab shells for the control model are attached to every other node of the superstructure; as such, the link slab shell elements are up to 6 m long. Two additional modeling methods were considered for simulating the link slab. The first variant considered decreasing the interval size of the link slab elements. All boundary conditions remain fixed and the maximum length for the link slab shell elements was reduced to 3 m. The second approach was to use a single shell element to connect Frame 2 of the northbound and southbound bridges. CSiBridge permits users to define nodes for a 2D shell element about a single plane. As the deck of both superstructures follow the same -1.25% grade, a single shell element was modeled by using each node at the ends of the bridge deck. The singular shell element was modeled by using each node at the ends of the bridge deck. The singular shell, comprising of 176 edge nodes, was used to mitigate interactions between numerous shell elements. A color coordinated representation is demonstrated by Figure 6.15 with the northbound and southbound superstructures highlighted in white and pink, respectively. Figure 6.15 demonstrates the single shell element, highlighted in teal, used to connect the northbound and southbound structures.

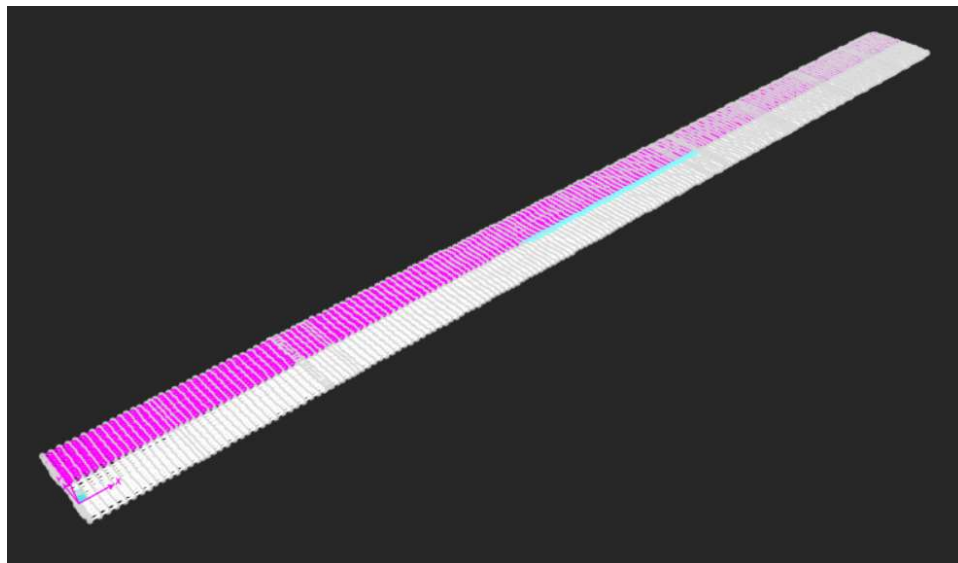


**Figure 6.14: Northbound (white) and southbound (pink) superstructures highlighted by color**



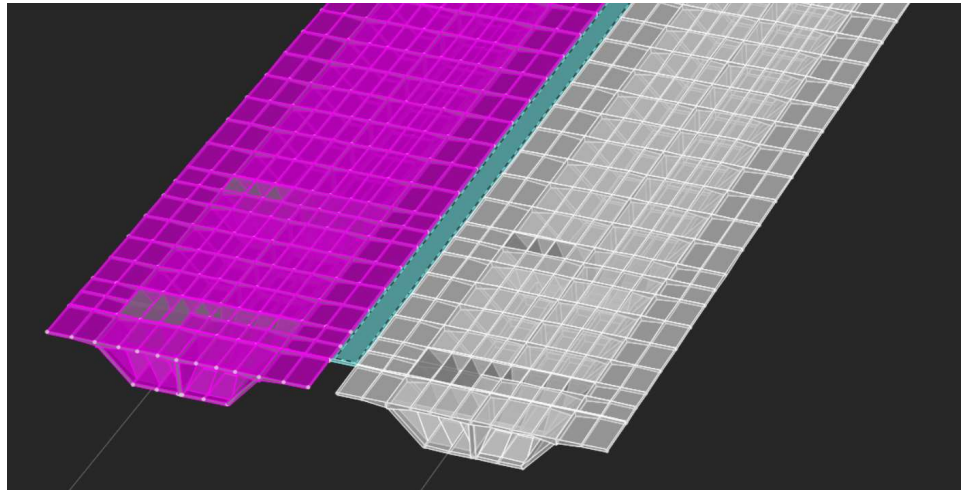


**Figure 6.15: Single shell element (teal) connecting northbound (white) and southbound (pink) structures**

#### 6.5.1 Modal Analysis – Link Slab

The results of the modal analyses of the control model and both link slab variants are displayed in Tables 6.11 – 6.13 the modal periods between the three FEMs compared are nearly identical. As the link slab is intended to be a component that resists lateral loadings, it was expected that the transverse modes would demonstrate the greatest variation between models. However, all changes between subsequent model were less than 0.5%.

**Table 6.11: Top five modes in the longitudinal direction (X-axis)**

6 m Link Slab Intervals (Control Model)			3 m Link Slab Intervals				Single Link Slab Shell Element			
Mode	Period, $T_{control}$ (s)	Modal Part. Factor (%)	Mode	Period, $T$ (s)	Modal Part. Factor (%)	$T/T_{control}$	Mode	Period, $T$ (s)	Modal Part. Factor (%)	$T/T_{control}$
2	1.342	12.3	2	1.342	12.3	1.000	2	1.342	12.3	1.000
4	0.976	15.1	4	0.977	15.1	1.001	4	0.977	15.1	1.001
9	0.671	9.2	9	0.671	9.3	1.000	9	0.671	9.2	1.000
11	0.627	9.8	11	0.627	9.8	1.000	11	0.627	9.8	1.000
39	0.284	9.3	39	0.284	9.5	1.000	39	0.284	9.1	1.000

**Table 6.12: Top five modes in the transverse direction (Y-axis)**

6 m Link Slab Intervals (Control Model)			3 m Link Slab Intervals				Single Link Slab Shell Element			
Mode	Period, $T_{control}$ (s)	Modal Part. Factor (%)	Mode	Period, $T$ (s)	Modal Part. Factor (%)	$T/T_{control}$	Mode	Period, $T$ (s)	Modal Part. Factor (%)	$T/T_{control}$
1	1.688	55	1	1.688	55	1.000	1	1.688	55	1.000
5	0.819	9.5	5	0.819	9.5	1.000	5	0.819	9.5	1.000
17	0.513	7	17	0.513	7	1.000	17	0.513	7	1.000
24	0.386	1.9	24	0.387	1.9	1.003	24	0.387	1.9	1.003
51	0.24	1.2	51	0.24	1.1	1.000	51	0.24	1.1	1.000

**Table 6.13: Top five modes in the vertical direction (Z-axis)**

6 m Link Slab Intervals (Control Model)			3 m Link Slab Intervals				Single Link Slab Shell Element			
Mode	Period, $T_{control}$ (s)	Modal Part. Factor (%)	Mode	Period, $T$ (s)	Modal Part. Factor (%)	$T/T_{control}$	Mode	Period, $T$ (s)	Modal Part. Factor (%)	$T/T_{control}$
7	0.721	5.8	7	0.712	5.8	0.998	7	0.712	5.8	0.988
15	0.56	3.9	15	0.56	3.9	1.000	15	0.56	3.9	1.000
18	0.505	4.1	18	0.506	4.1	1.002	18	0.506	4	1.002
20	0.469	3.9	20	0.469	4	1.000	20	0.469	4	1.000
44	0.263	6.1	44	0.263	6	1.000	44	0.263	6	1.000

### 6.5.2 Time-history Analysis – Link Slab

The results of the time-history analyses confirm the data presented by the modal analyses. Both the stresses and the displacements of the superstructure are congruent, with variations of less than 0.1%. The variations in results are minimal such that Figure 6.16 and 6.17 appear to display results from a single analysis. The analyses suggest that the number of elements and nodes when modeling the link slab for a linear analysis does not

impact the dynamic behavior of the model as long as the boundary conditions for the shell elements are consistent.

Although the results between the control model and the additional link slab modeling variants suggest that shell interval size is irrelevant, note that the scope of this study focused on linear time-history analyses. Linear analysis assumes a direct correlation between applied forces and resulting displacements and stresses. A nonlinear time-history analysis would account for material nonlinearity as the concrete cracks and the steel yields. Increasing the number of intervals and elements in a nonlinear analysis typically provides more accurate results.

The design plans intended for the link slab to be integral with the deck. This initial assumption is a crucial factor when calibrating the FEM to actual dynamic behavior. The 2018 Bridge Inspection Report did not note any significant cracking in the link slab, likely confirming that the components are behaving as intended (NDOT, 2018). Damage from routine service loads or extreme seismic activity could result in the inefficient transfer of forces between the link slab and bridge decks. To replicate such behavior, shell boundary conditions at locations of interest would have to be released accordingly.

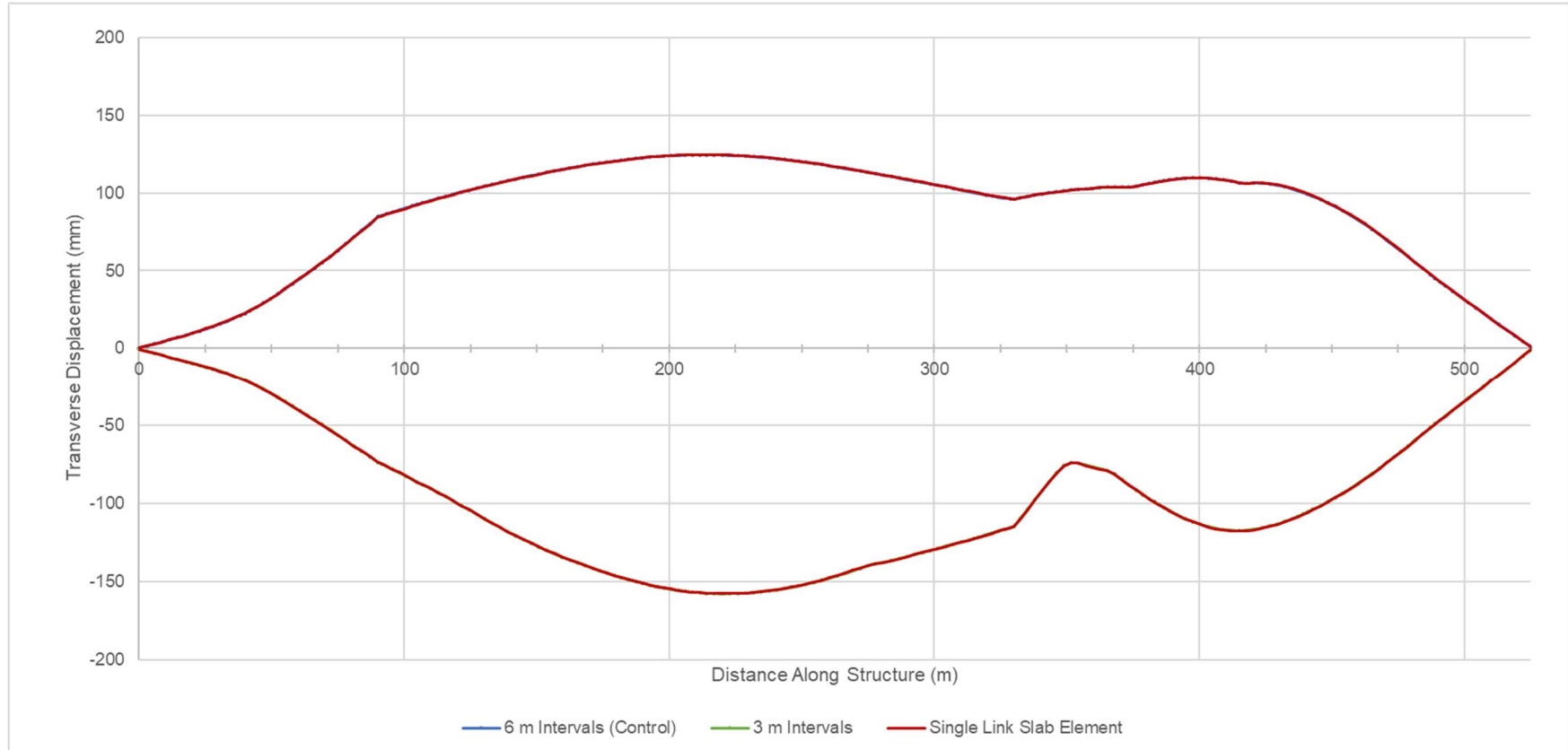


**Figure 6.16: Maximum transverse displacement of superstructures for link slab analyses**

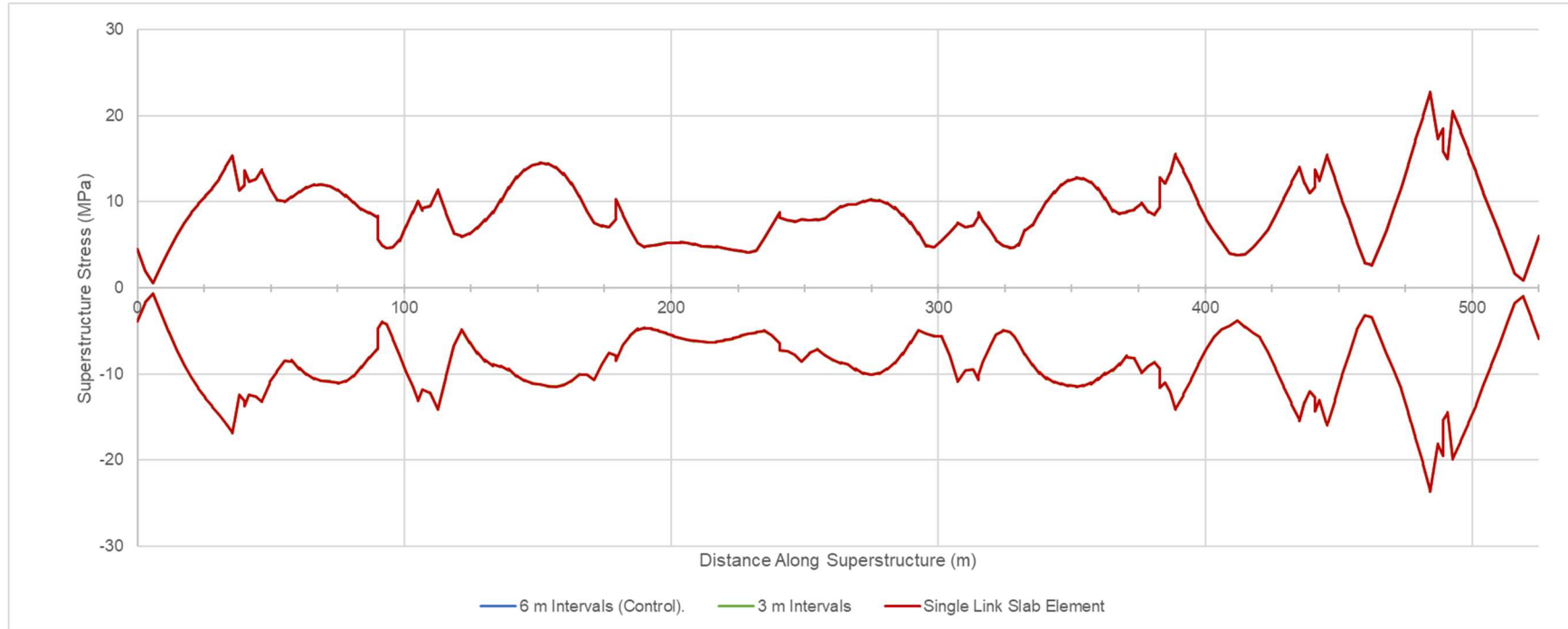


**Figure 6.17: Maximum superstructures stresses for link slab analyses**

## 6.6 Superstructure Modeling Approach

The control model defined the superstructure as an assembly of shell elements. The shell approach was selected to provide computationally efficient, yet reasonable results. Specifically, modeling the superstructure as shell elements would provide more accurate results than a spine frame structure. Further, the approach would yield similar results to a solid model at faster computational times. This study investigated these assumptions by defining the superstructure as using each modeling approach.

In addition to comparing the results to the control model, the spine frame model analyses results were compared to the 2013 study on the Galena Creek Bridge. The work performed by Carr and Sanders developed a SAP2000 FEA model to estimate modal properties. SAP2000 was limited to defining the superstructure as a series of frame elements. When using frame elements, the 3D representation of the model exists solely for visual purposes; as such, nodes are not generated at the edge of the deck (i.e., where the link slab connects to the box girder superstructure). The previous study simulated the connection between the northbound and southbound structures, which are spaced 20.92 m apart, using a combination of rigid links and shell elements. The rigid link elements extend from the superstructure spine, marking the centerline of the box girder, 9.45 m towards the adjacent structure, leaving a 2.02 m gap between the end nodes. The link slab shell elements then connect on either side to the rigid links, as can be seen in Figure 6.18. It should be noted that the spacing of the rigid links is not uniform, as can be seen in Figure 6.19. Based on a comparison of the model to the bridge plans, it is assumed this approach was taken to account for the additional reinforcing bars used at key locations in the structure (e.g., the arch-superstructure merge region and the hinge and pier diaphragms).

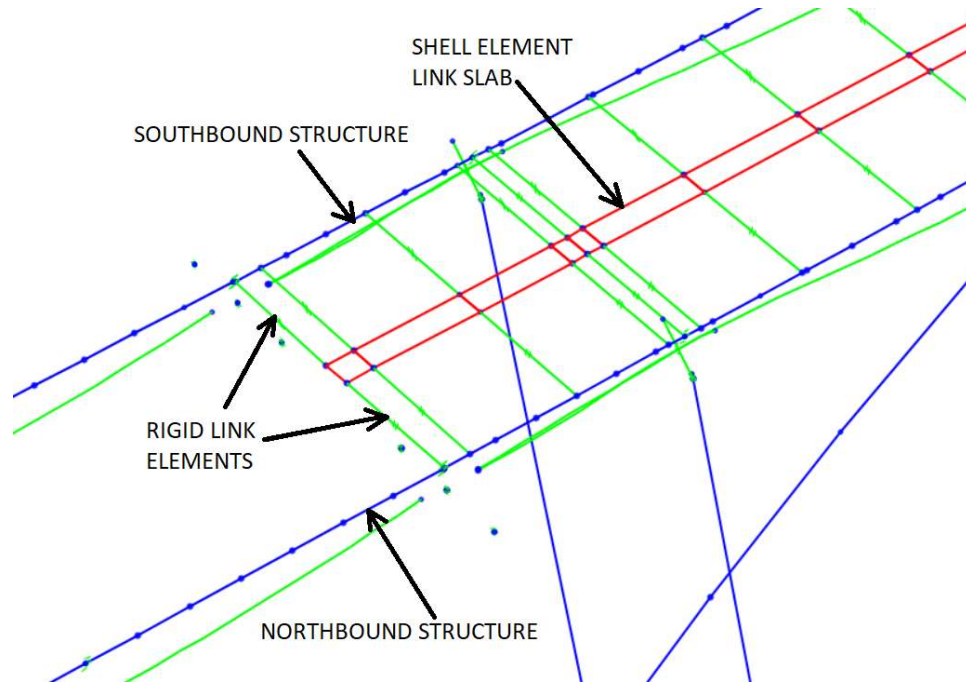


**Figure 6.18: Example of frame spine model using rigid links that extend to link slab shell**

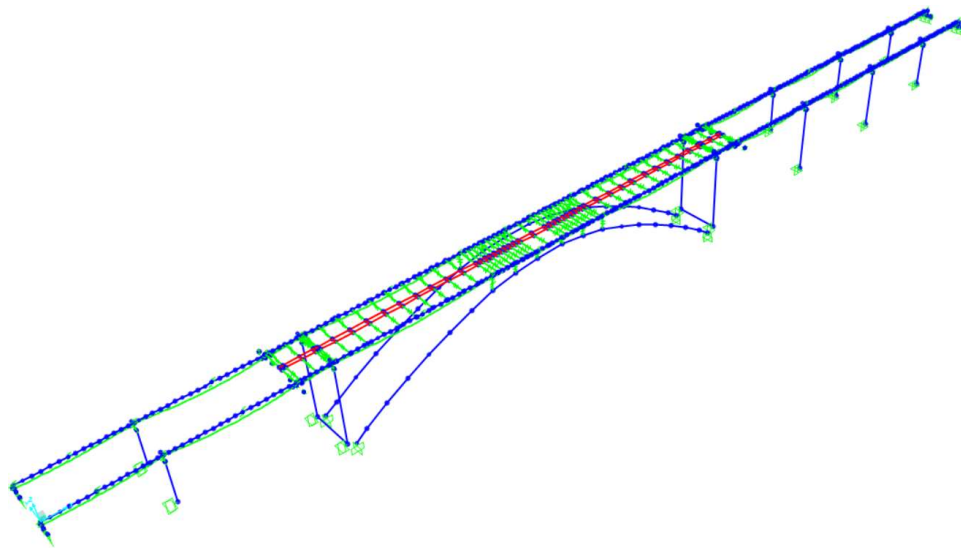


**Figure 6.19: Frame spine superstructure model to replicate the 2013 UNR SAP2000 model**

This evaluation also considered defining the superstructure using solid elements. In FEA, solid elements are a direct 3D representation of the component being modeled. Analyses are performed by modeling the desired material between the defined nodes of the 3D component. In contrast, shell elements are a 2D representation of 3D elements. When

3D features are simplified into 2D elements, the analysis is also subsequently simplified. Shell elements were initially used to define the control model to reduce computational times for the various variant models analyzed. A superstructure consisting of solid elements was expected to be a more accurate representation of the Galena Creek Bridge.

As stated in Section 5.5.8, Update feature under the Bridge Tab controls the modeling method used to develop the bridge object superstructure. Note that redefining the bridge using the Update feature only accounts for definitions from the Components Tab. After generating the spine frame model, the connection between the superstructure and arch had to be redefined. Like the control model, six vertical rigid link elements were used between the fillet diaphragms to simulate the merge between the arch and the superstructure

#### *6.6.1 Modal Analysis*

The use of rigid link elements to simulate the bridge deck resulted in additional stiffness when compared to the control model. Most of the modes considered in Table 6.14 – 6.16 exhibited decreased periods in relation to the control model. The most notable difference was the 20% decrease in modal period of primary transverse mode (Mode 1). It was noted that several of the modes considered in the transverse and vertical directions demonstrated increases compared to those of the control model. This is likely a result of the non-uniform spacing of the link elements along the length of the structure. The less stiff areas of Frame 2, such as between the arch crown and Pier 2, would be prone to higher distortions under loading.



In contrast, the modal analyses of the solid superstructure model remained relatively like that of the control model. The top five modes about all three degrees of freedom experienced an average variation of 1.5%. The most significant increase was a 36% increase (0.086 seconds) in Mode 51, suggesting that the shell model slightly underpredicted the lateral excitation of the bridge system.

**Table 6.14: Comparison of top long. modes for superstructure modeling analyses (X-axis)**

Shell Element Superstructure (Control)			Spine Frame Superstructure				Solid Element Superstructure			
Mode	Period, $T_{control}$ (s)	Modal Part. Factor (%)	Mode	Period, $T$ (s)	Modal Part. Factor (%)	$T/T_{control}$	Mode	Period, $T$ (s)	Modal Part. Factor (%)	$T/T_{control}$
2	1.342	12.3	2	1.315	12.3	0.979	2	1.343	12.4	1.001
4	0.976	15.1	3	0.932	14.8	0.954	4	0.999	14.7	1.023
9	0.671	9.2	9	0.613	9.5	0.913	10	0.667	11.3	0.994
11	0.627	9.8	10	0.590	7.7	0.942	12	0.631	10.0	1.008
39	0.284	9.3	32	0.274	16.1	0.966	39	0.283	16.6	0.995

**Table 6.15: Comparison of top transverse modes for shell vs frame superstructure (Y-axis)**

Shell Element Superstructure (Control)			Spine Frame Superstructure				Solid Element Superstructure			
Mode	Period, $T_{control}$ (s)	Modal Part. Factor (%)	Mode	Period, $T$ (s)	Modal Part. Factor (%)	$T/T_{control}$	Mode	Period, $T$ (s)	Modal Part. Factor (%)	$T/T_{control}$
1	1.688	55.0	1	1.349	52.2	0.799	1	1.678	31.5	0.994
5	0.819	9.5	5	0.784	8.6	0.958	5	0.808	5.8	0.987
17	0.513	7.0	8	0.621	3.1	1.210	18	0.502	4.0	0.979
24	0.386	1.9	13	0.500	8.8	1.293	22	0.427	0.6	1.106
51	0.240	1.2	33	0.272	2.2	1.134	34	0.326	1.0	1.359

**Table 6.16: Comparison of top vertical modes for shell vs frame superstructure (Z-axis)**

Shell Element Superstructure (Control)			Spine Frame Superstructure				Solid Element Superstructure			
Mode	Period, $T_{control}$ (s)	Modal Part. Factor (%)	Mode	Period, $T$ (s)	Modal Part. Factor (%)	$T/T_{control}$	Mode	Period, $T$ (s)	Modal Part. Factor (%)	$T/T_{control}$
7	0.721	5.8	7	0.657	8.2	0.922	9	0.709	0.2	0.995
15	0.56	3.9	10	0.590	5.2	1.054	15	0.562	0.3	1.004
18	0.505	4.1	14	0.475	7.9	0.939	17	0.508	0.3	1.004
20	0.469	3.9	16	0.433	7.6	0.923	20	0.469	0.2	0.999
44	0.263	6.1	38	0.242	8.0	0.918	43	0.261	0.4	0.990

The modal analysis of the spine frame model was dissimilar to the modal information documented from the 2013 study performed by Carr and Sanders. As seen in Table 6.17, the spine frame variant was considerably stiffer than the 2013 SAP2000 model, with the modal periods of the top transverse modes of the spine frame model an average of 23.3% lower than those of the SAP2000 model. These discrepancies can be explained by the fact the SAP2000 model assumed a decreased cracked MOI for the columns whereas the CSiBridge models were defined using the gross MOI.

**Table 6.17: Comparison of top transverse modes between 2013 SAP2000 model vs spine frame**

2013 SAP2000 Model (Carr and Sanders)			Frame Spine Superstructure			
Mode	Period, $T_{control}$ (s)	Modal Part. Factor (%)	Mode	Period, $T$ (s)	Modal Part. Factor (%)	$T/T_{control}$
1	1.650	38.9	1	1.349	52.2	0.817
5	0.990	4.1	5	0.784	8.6	0.792
10	0.720	5.5	8	0.621	3.1	0.862
11	0.670	0.9	13	0.500	8.8	0.746
32	0.320	1.1	33	0.272	2.2	0.851

### 6.6.2 Time-History Analysis

The results of the time-history analysis revealed that the spine frame model demonstrated increased transverse displacement at Frames 1 and 2 of the model, but significantly decreased displacements at Frame 3 (Figure 6.21). The midspan of the arch experienced the greatest increase in transverse displacement of up to 60%. In contrast, Span 4 of the frame spine model experienced up to 22% less transverse displacement than the control model. As the most significant changes in transverse deflection were at Frame 2, it is likely that the variations are a result of the means of modeling the link slab as opposed to the superstructure itself. It was noted in Section 6.5 that the shell intervals for modeling the link slab was not a factor on the modal properties of the FEM. The continuous fixed connection between the edges of the link slab and superstructure shell elements provided a fluid transfer of stresses between the adjacent elements, regardless of the number of shell segments used. When the link slab is supported by an intermittent series

of rigid links, it behaves similar to a one-way slab and loses stiffness. This loss of stiffness resulted in the sharp increase in deformations in Frame 2 of the variant model.

It is likely that decreasing the interval size between rigid links would not yield more reliable results. The rigid links attached to the resulted in a sharp decrease in the modal periods of the top transverse modes. The inclusion of additional link elements would further decrease the modal periods without realistically simulating the flow of stresses between the superstructure and link slab. Unfortunately, redefining the superstructure as a spine frame inevitably changes the modeling method for the link slab, meaning this modeling method cannot be tested as an independent variable. Although the influence of a spine frame model is inconclusive, these results show that the rigid link element approach was not an appropriate method of modeling the connection between the northbound and southbound structures.

The results of subjecting the solid superstructure model to the El Centro earthquake ground motions corroborate the information from the modal analyses. Figures 6.20 – 6.22 show that the envelope displacements about all three axes are nearly identical. As noted in previous section, the most notable change was an increase in transverse participation factor of Mode 51. Spans 6 and 7 reflect this change in modal behavior by exhibiting a slight increase in maximum lateral displacement of up to 5 mm from the control model.

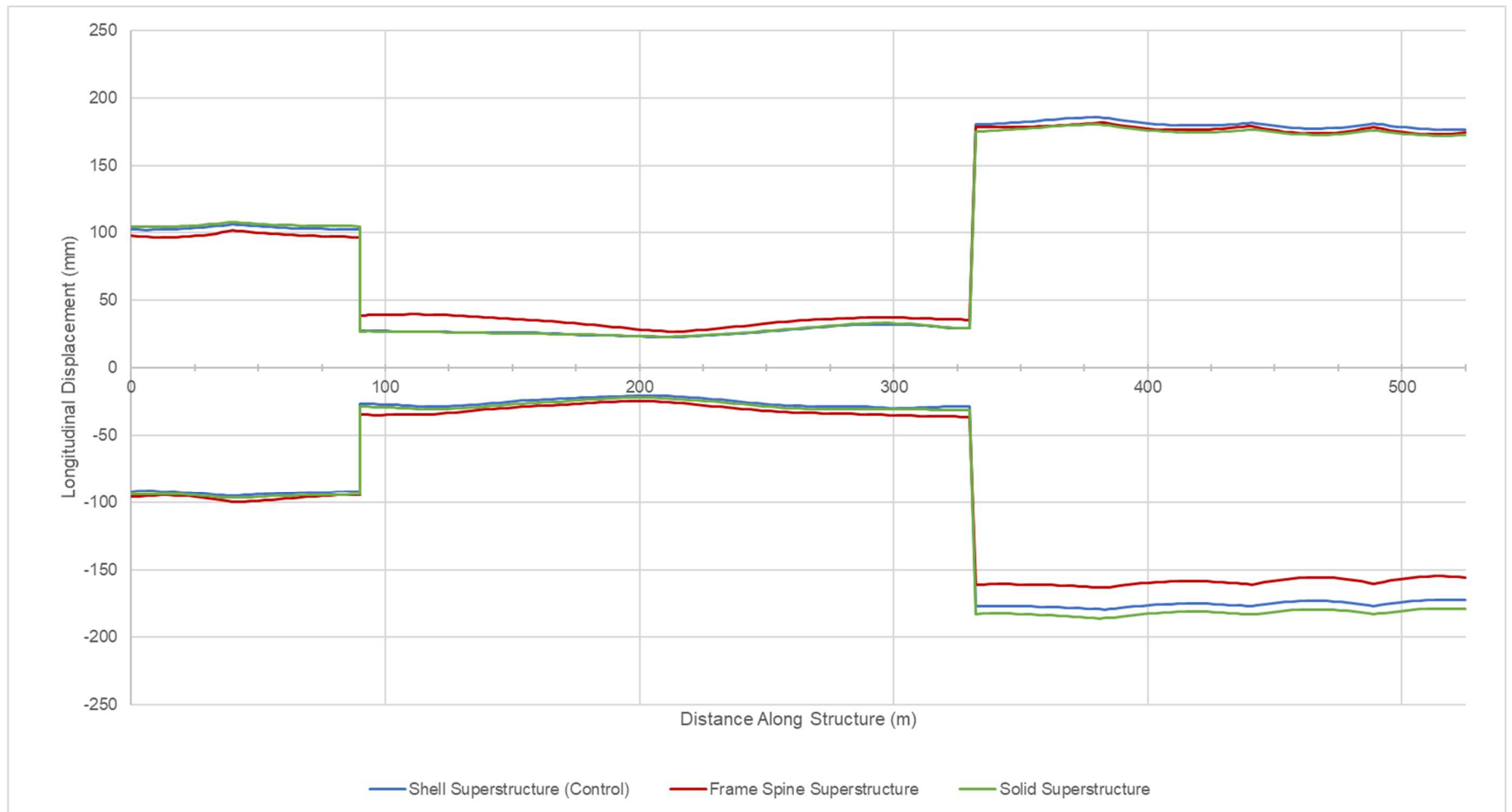


**Figure 6.20: Envelope of longitudinal displacement of superstructures for shell vs solid superstructure analyses (X-axis)**

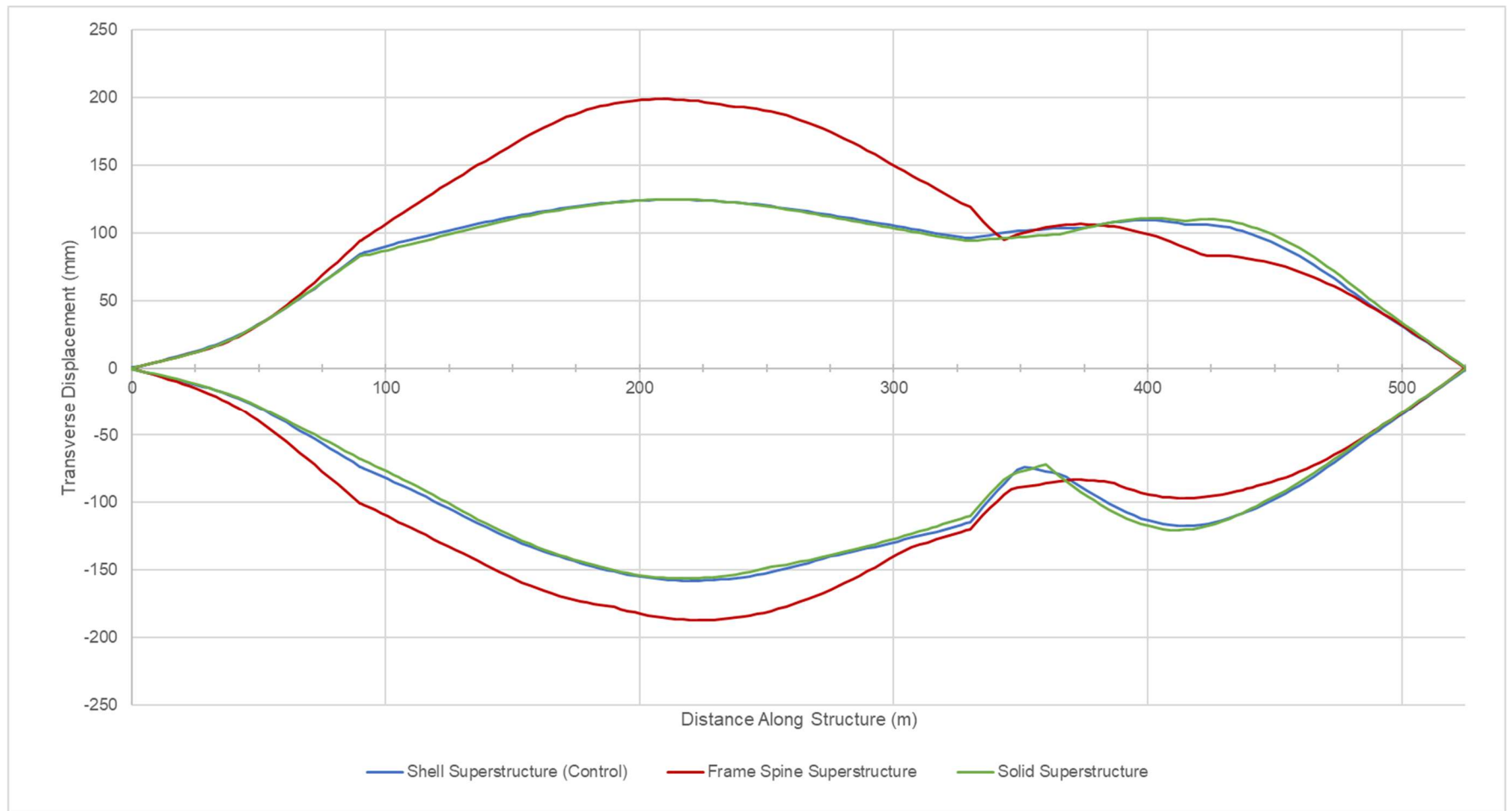


**Figure 6.21: Envelope of transverse displacement of superstructures for shell vs solid superstructure analyses (Y-axis)**

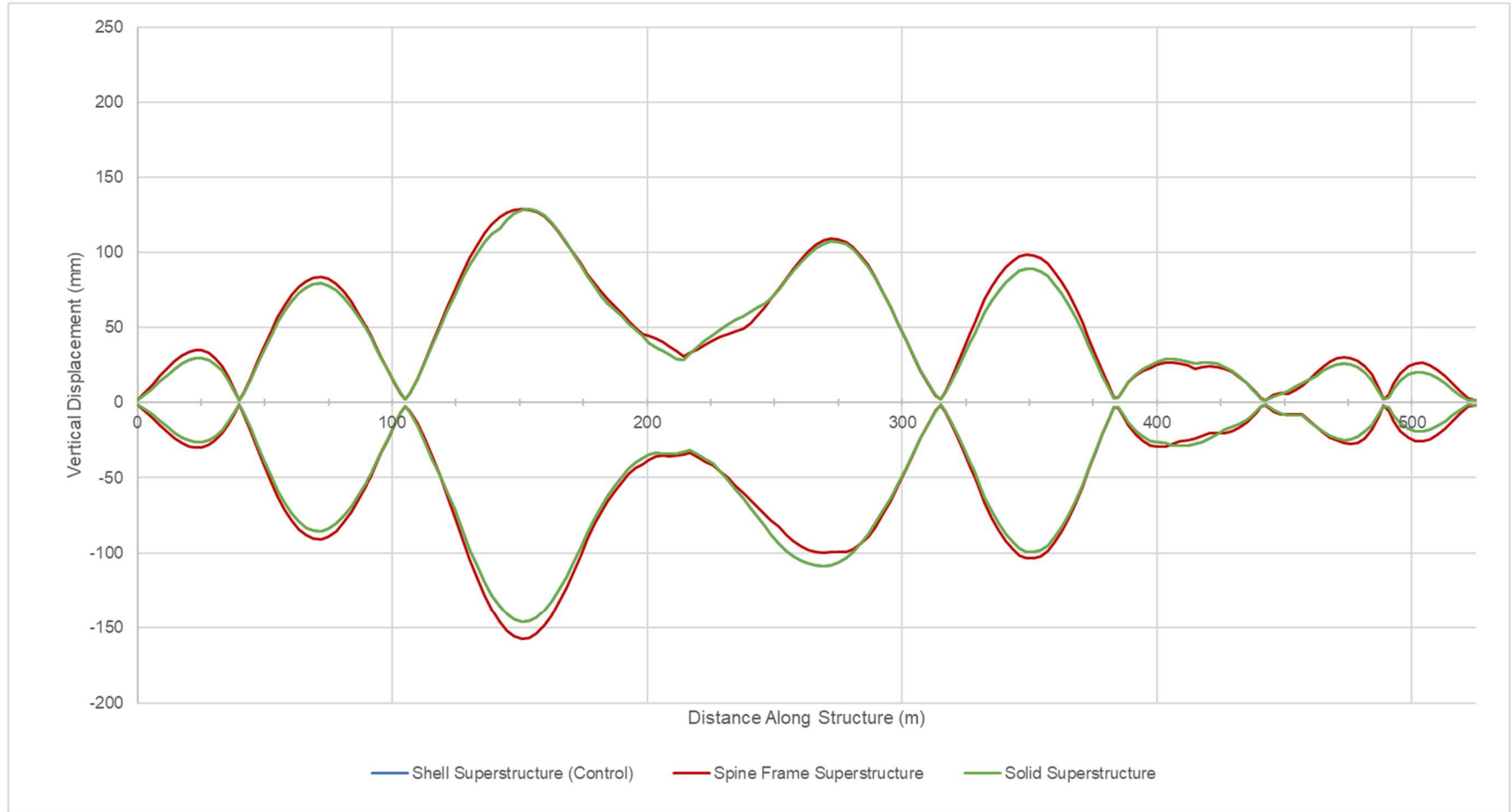


**Figure 6.22: Envelope of vertical displacement of superstructures for shell vs solid superstructure analyses (Z-axis)**

The conclusion drawn from performing the modal and time-history analyses suggests that the shell superstructure used in the control model definitions was an effective approach to modeling. As previously mentioned, shell elements are a means to simplify 3D structures using a 2D model. From a visual standpoint, the concrete box girder is a compilation of simple, thin geometric shapes. The geometric shapes range from a thickness of 0.2 – 0.6 m. As such, these relatively thin components allowed for shell elements to be an effective means of modeling the superstructure, as seen in Figure 6.23. The trivial discrepancies are likely a result of the increased number of mesh intervals used for analyzing solid elements as compared to shell elements.

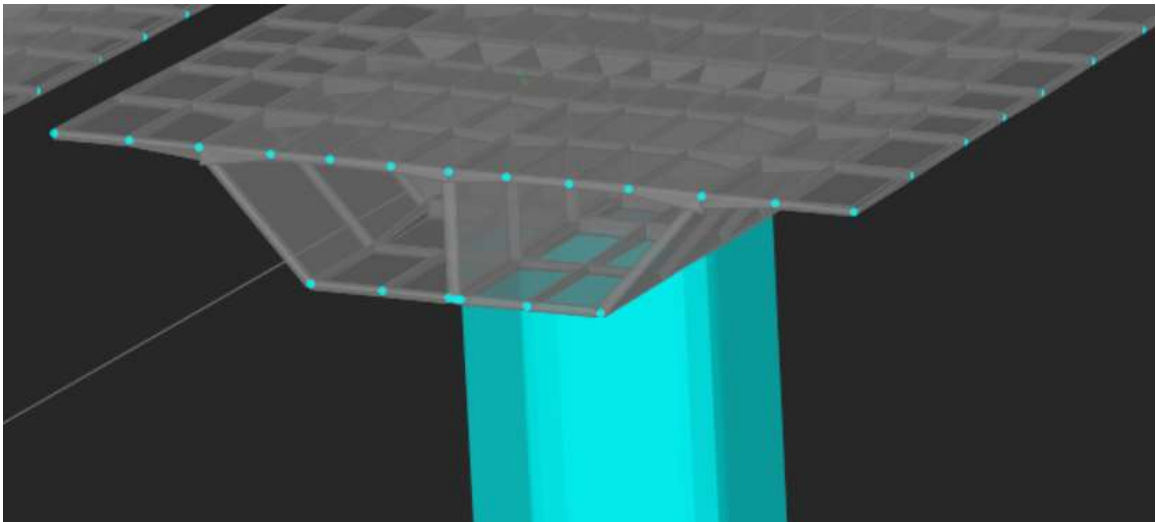


**Figure 6.23: Superstructure of control model made up of shell elements**



## 6.7 Barrier Rail Modeling

As mentioned in Section 2.1.3 of the Literature Review, parapets are not typically considered structural elements for bridge design. While this leads to conservative calculations for load bearing capacity, it does not accurately reflect the stiffness and dynamic properties of in-service structures. The control model considers the weight of the barrier rail as a line load applied at the edges of the bridge deck. The line loads are defined as a mass for modal analyses and, subsequently, time-history analyses. To determine the possible influence of the secondary structural elements, a custom frame element was defined and modeled along the edge of the deck to represent the barrier rail (i.e., the lighter teal colored element at edge of deck in Figure 6.24). For this modeling approach, the barrier rail line load was removed from the deck definition portion of the Components Tab and from the mass source definition of the Advanced Tab.

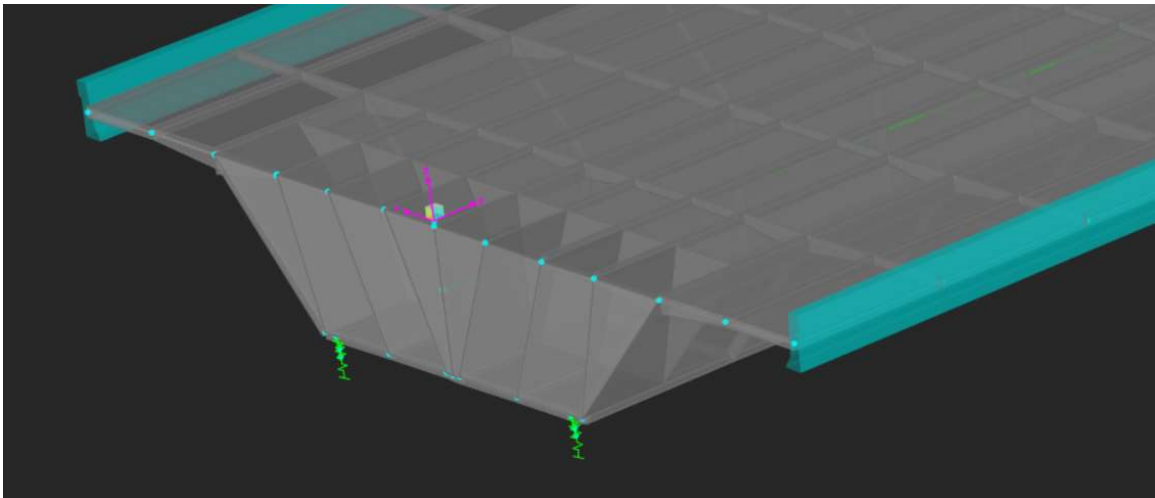


**Figure 6.24: Barrier rail frame elements drawn along deck edges**

The barrier rail frame was a user defined component created in the Section Designer tool under the Components Tab, as seen in Figure 6.25. The barrier rails were modeled along the edge of the 2D bridge deck shell elements using the Draw Frame tool under the Advanced Tab. It was assumed that the 20 mm chamfers used to blunt the top edges of the barrier had negligible impact on the stiffness and dead load of the superstructure and were not modeled when defining the parapet shape. Note that linear frame elements model the component around the center of gravity of the cross section, which was automatically defined by the Section Designer tool, as can be seen in Figure 6.24. Adding the barrier rail as additional frame elements would not model them as perfectly integral with the deck. To best simulate this connection, the frame elements were drawn along every node of the superstructure deck shell elements. The existing barrier rail of the Galena Creek Bridge has expansion joints intermittently located along the length of the structure. The initial modeling approach assumed a continuous parapet with no expansion joints; therefore, all the connections between the elements were modeled as rigid joints. This method was applied to provide an upper limit on the additional stiffness a barrier could provide, while the control model represented the designed condition of no additional stiffness from the barrier.

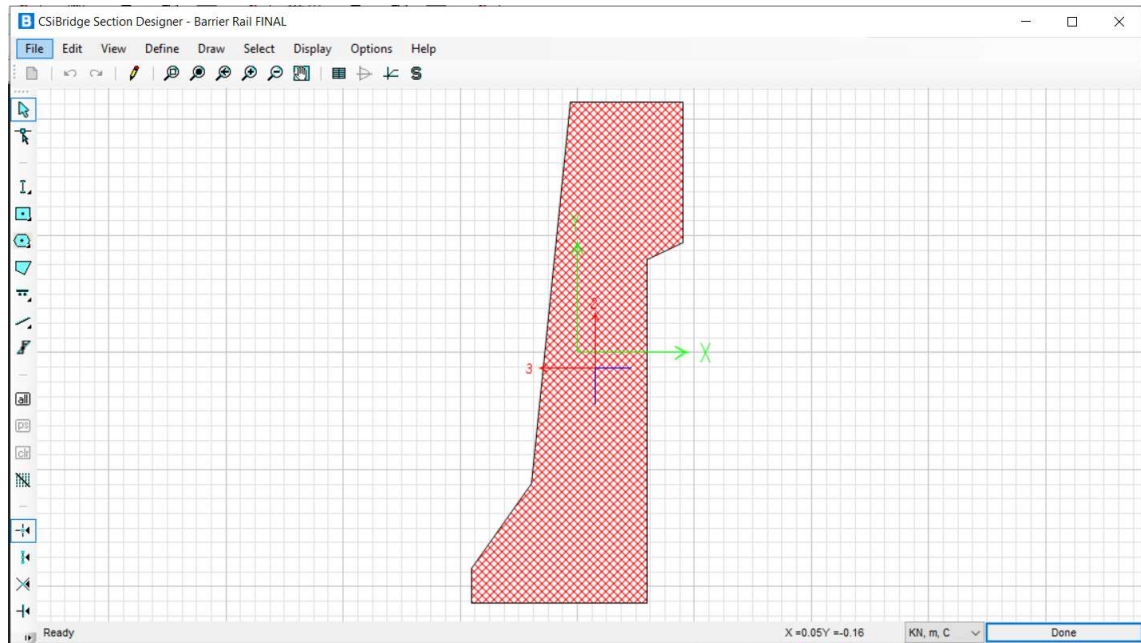


**Figure 6.25: Barrier rail cross section defined using section designer in CSiBridge**

#### 6.7.1 Modal Analysis – Barrier Rail Modelled as Frame Elements

The inclusion of the barrier rail as a frame element to the model was expected to increase the superstructure stiffness and reduce deflection, specifically in the vertical and transverse axes. It was anticipated that the barrier rail frame elements would act similar to flanges when resisting moments about the vertical axis and subsequently decrease translation. Additionally, the vertical orientation of the barrier rails would resist moments about the global y-axis and reduce vertical displacements. The general increase in stiffness to the superstructure from the frame elements was expected to reduce the modal periods about all three degrees of freedom.

The modal analyses suggested that modeling the barrier rail as a frame element had a negligible impact on the dynamic properties of the FEM. Although 13 of the 15 modes considered in Tables 6.18 – 6.20 decreased in modal periods, the average reduction was incremental (less than 0.7%). It was noted in Chapter 2 that the influence of barrier rails on

load bearing capacity of a bridge diminished as the size and complexity of the structure increased (Akinci, Liu and Bowman, 2008). The 525 m long, seven span, cathedral arch Galena Creek Bridge is far larger and more complex than any of those considered by studies from the Literature Review. As such, it is logical to assume that the impact of from the barrier rail on the dynamic properties is negligible.

**Table 6.18: Comparison of top longitudinal modes for control vs frame barrier rail (X-axis)**

Barrier Rail Line Load (Control Model)			Barrier Rail as Frame Element			
Mode	Period, $T_{control}$ (s)	Modal Part. Factor (%)	Mode	Period, $T$ (s)	Modal Part. Factor (%)	$T/T_{control}$
2	1.342	12.3%	2	1.335	12.3%	0.995
4	0.977	15.1%	4	0.977	15.1%	1.001
9	0.671	9.4%	9	0.669	9.3%	0.997
11	0.627	9.8%	11	0.625	10.3%	0.997
39	0.284	9.7%	39	0.283	12.3%	0.997

**Table 6.19: Comparison of top transverse modes for control vs frame barrier rail (Y-axis)**

Barrier Rail Line Load (Control Model)			Barrier Rail as Frame Element			
Mode	Period, $T_{control}$ (s)	Modal Part. Factor (%)	Mode	Period, $T$ (s)	Modal Part. Factor (%)	$T/T_{control}$
1	1.688	55.0%	1	1.665	55.7%	0.986
5	0.819	9.5%	5	0.802	9.3%	0.979
17	0.513	7.0%	17	0.509	6.5%	0.992
24	0.386	1.9%	24	0.386	2.0%	0.999
51	0.240	1.2%	51	0.242	1.8%	1.008

**Table 6.20: Comparison of top vertical modes for control vs frame barrier rail (Z-axis)**

Barrier Rail Line Load (Control Model)			Barrier Rail as Frame Element			
Mode	Period, $T_{control}$ (s)	Modal Part. Factor (%)	Mode	Period, $T$ (s)	Modal Part. Factor (%)	$T/T_{control}$
7	0.713	5.8%	7	0.709	7.0%	0.995
15	0.560	3.9%	15	0.557	3.8%	0.995
18	0.506	4.1%	18	0.502	4.1%	0.992
20	0.469	3.9%	20	0.466	4.2%	0.993
44	0.263	6.1%	44	0.262	5.3%	0.997

### 6.7.2 Time-history Analysis – Barrier Rail Modelled using Frame Elements

The results from the time-history analyses corroborate the results of the modal analyses; incorporating barrier rails as frame elements did not decrease superstructure displacements and stresses as expected. Prior sections have revealed that the longitudinal behavior is controlled by the substructure and bearings. This behavior is further confirmed by Figure 6.28 which shows that modeling barrier rails had no notable impact on the longitudinal displacements. Rather than provide resistance to vertical displacements, several locations along the structure actually experienced greater displacements. Figure 6.26 shows that the superstructure of the variant model experienced up to 11 mm more vertical displacement at Span 3 and up to 14 mm at Span 1 than the control model. The transverse displacement of the superstructure, shown in Figure 6.27, reveals up to an 8 mm reduction in offset along Frame 2. However, this behavior is not consistent along the length of the structure as displacements at both Span 1 and Span 4 of the variant model are greater than that of the control model by up to 14 mm.

Previous research on the influence of barrier rails as secondary structural elements observed changes in girder moment distribution factors, and thus internal stresses, as opposed to displacement. Figure 6.29 compares the stresses in the superstructure between the control model and the barrier rail variant. Rather than the expected decrease in internal stresses, the variant model showed identical internal stresses to the control model. At several sections of Frames 1 and 3, the variant model experienced marginally greater stresses of up to 2.5 MPa. Frames 1 and 3 of the bridge are supported by shorter columns than Frame 2 and, as a result, are stiffer. It is likely that this approach to modeling the barrier rail caused a greater increase in stresses at locations of the superstructure that were already relatively stiff. This behavior contradicts the expected decrease in girder stresses when modeling the barrier rail.

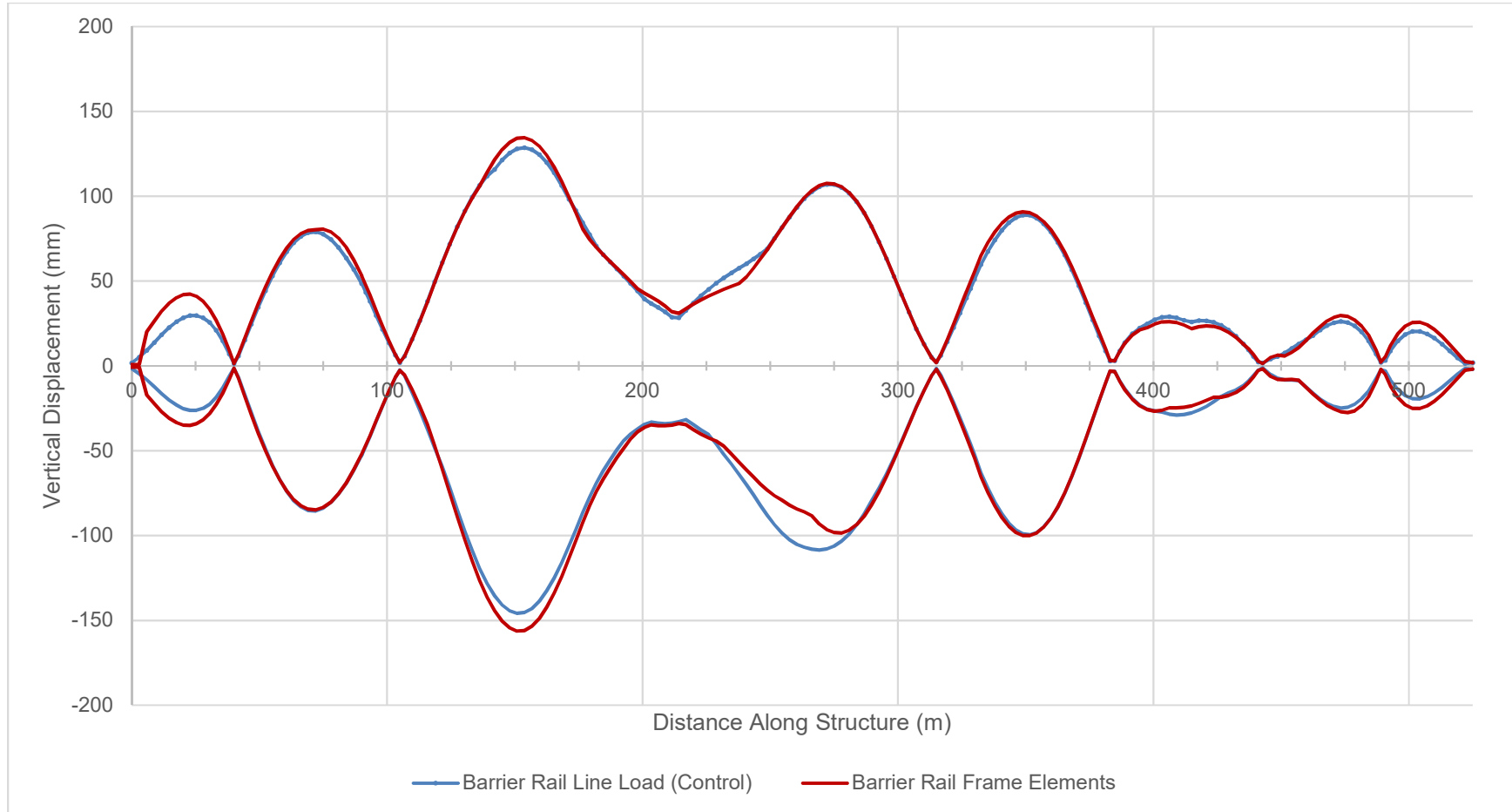


**Figure 6.26: Envelope of maximum vertical displacement of superstructures for parapet analyses**

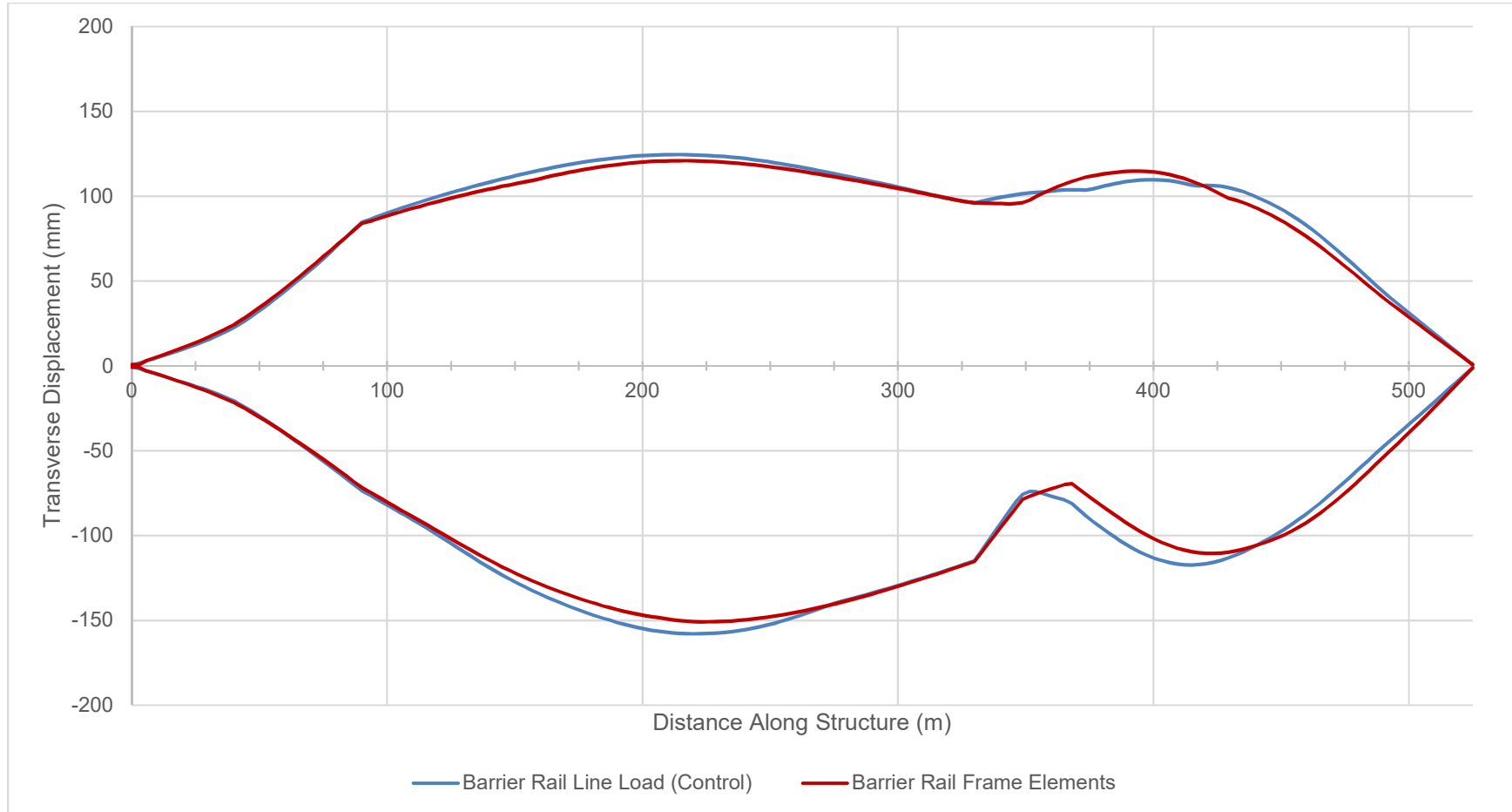


**Figure 6.27: Envelope maximum transverse displacement of superstructures for parapet analyses**



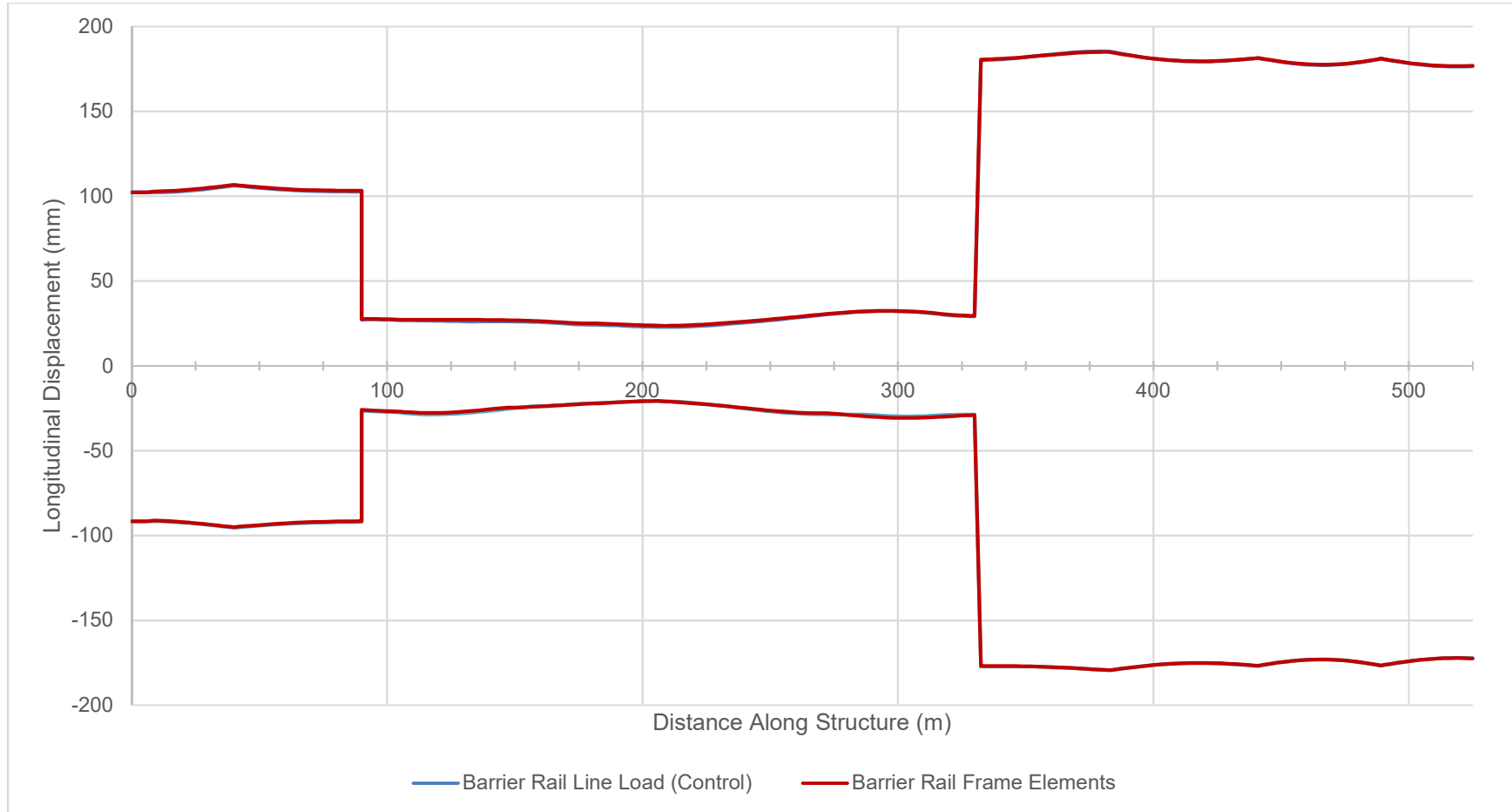


**Figure 6.28: Envelope maximum longitudinal displacement of superstructures for parapet analyses**

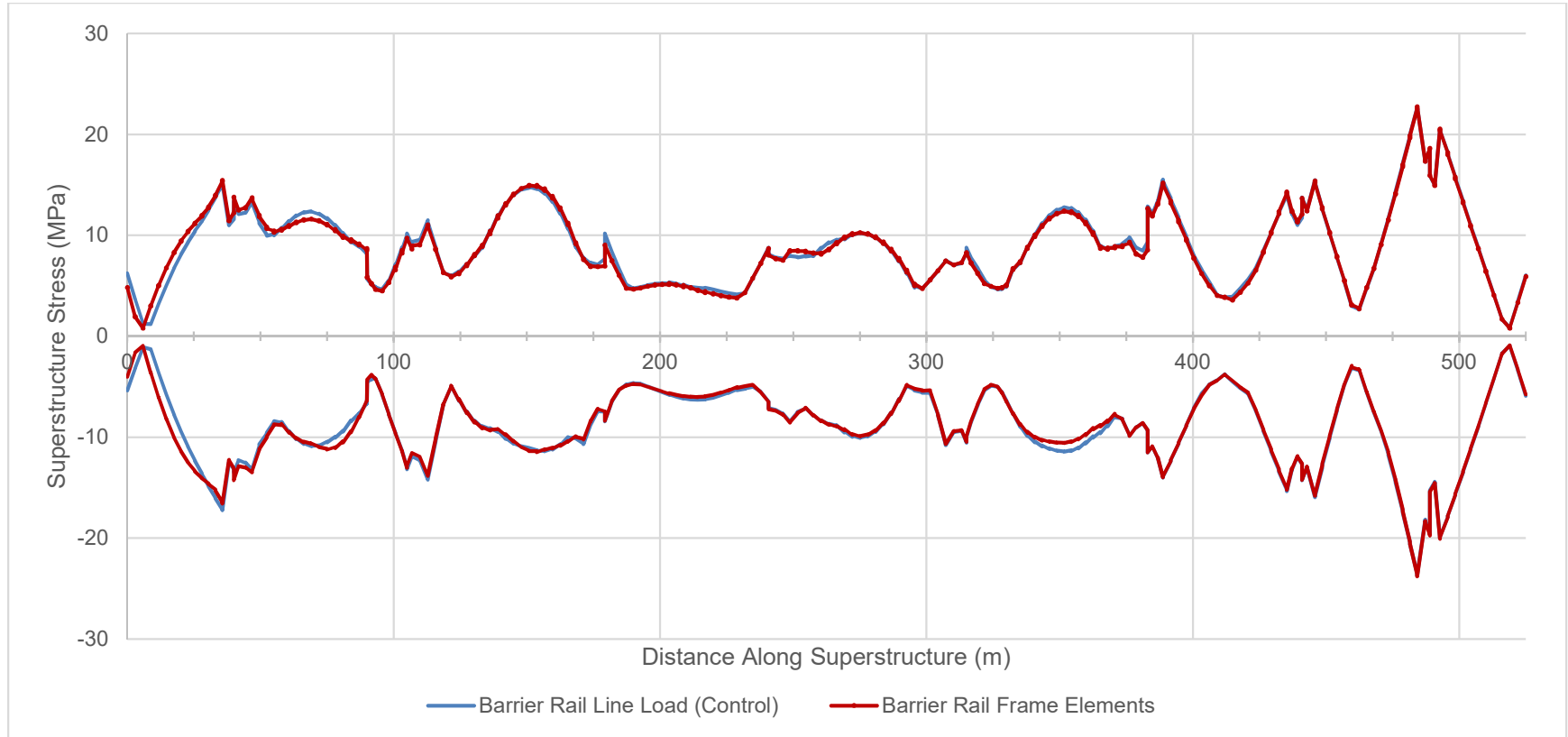


**Figure 6.29: Envelope maximum stresses in superstructure for parapet analyses**

Modeling the barrier rail as frame elements did not produce the expected results typical of their influence as secondary structural elements. One of the primary assumptions for this modeling approach was the transfer of shear flow between the parapet and the deck due to the substantial transverse reinforcing connecting the elements. It appears likely that modeling them in intervals along the nodes of the superstructure did not replicate the behavior of a continuous connection, in spite of their common degrees of freedoms at the nodes.

Additionally, previous research indicates that discontinuities in the barrier rail resulted in stress concentrations in both areas of positive and negative moment (Akinci, 2008). Further examination of the influence of barrier rails on the Galena Creek Bridge would require replicating the expansion joints and discontinuities in the barrier rail along the length of the bridge. Leaving gaps between the frame elements at joint locations would simulate this behavior. Another option would be to simply release the rotational boundary constraints of the 2D frame elements at joint locations. Note that most barrier rail segments measured between 11.7 m and 18.4 m between expansion joints. As the continuous barrier rail addition had a nominal impact on the dynamic properties of the Galena Creek Bridge FEM, it is assumed that incorporating the expansion joints, rather than resulting in stress concentrations, would further mitigate the impact of this method of modeling the barrier rail.

## **CHAPTER 7. REFINED FINAL MODEL**

A refined CSiBridge model was developed using the results from the parametric study. The final model is intended to be a platform upon which to further calibrate, based on the measured data. As noted in the 2013 study performed by Carr and Sanders, using generic ground motion data for time-history analyses is an effective means to estimate dynamic response. However, appropriate ground motions recorded from the local area are required to accurately calibrate the model to emulate actual response. In the absence of the measured data, several modifications were incorporated to the control model in preparation for final tuning with measured data.

Several of the variables examined through the parametric study resulted in trivial solutions, meaning the influence of these factors on the dynamic properties of the bridge were negligible. Specifically, the link slab shell intervals, bearing stiffness, and superstructure modeling techniques were found to be adequate in the control model. However, the structural damping, substructure effective moment of inertia, and material stiffness parameters were found to need additional refinement for the proposed model. The following sections detail the trivial solutions and refined parameters.

### **7.1 Trivial Solutions**

The link slab of the control model used shell element increments of up to 6 m long to simulate connection between the northbound and southbound structures. The parametric study evaluated the best way of modeling the connection between the two bridges by editing the length of the shell element intervals. Neither increasing the number of intervals

nor replacing the intervals with a single element resulted in noticeable changes, typically under 0.5%. Unless a non-linear time-history analyses is required to accurately capture the measured response, it was recommended that the approach to modeling the link slab remain consistent to that of the control model.

The shear modulus ( $G$ ) of the elastomer influences the stiffness of the bearing pads. The control model uses the lowest value for  $G = 0.90$  MPa, as recommended by AASHTO. A model variant using the highest recommended value ( $G = 1.38$  MPa) resulted in a maximum longitudinal displacement reduction of 9 mm. Further, the vertical and transverse displacement data between the control model and stiff bearing variant were identical. As such, it was concluded that the bearing stiffness did not have a significant impact on the dynamic response of the bridge; therefore, the bearing stiffness values remained based on  $G = 0.90$  MPa.

Several modeling techniques were also considered for defining the superstructure. The control model employs shell elements to generate the superstructure, whereas the variant models considered the superstructure as a spine frame and solid elements. The modal results between the control model and solid element superstructure variant had minor discrepancies in lower modes, and the results from the time-history analyses were generally parallel. The vertical and longitudinal modes considered exhibited less than a 0.8% difference between the control model and the solid superstructure model. Performing a linear-time history analysis indicated that lateral excitation of the solid superstructure model demonstrated an average difference of 1.1% from the control model.

Results from both the modal and time-history analyses for the spine frame model were not analogous to any of the other models. Due to the complexities of modeling the link slab with frame element superstructures, this approach to modeling the Galena Creek Bridge was determined to be unsuitable. Based on the agreement between the shell and solid elements, as well as computational efficiency of the shell element approach, it is recommended to model the superstructure using shell elements.

## **7.2 Structural Damping**

At the submission of this document, the most current bridge inspection report (NDOT, 2018) noted minor cracking on the observable area of the bridge, likely as a result of thermal expansion and contraction. Literature on damping properties of pristine concrete structures suggests that the damping likely ranges from 2% – 3% (Chopra, 2012). As the concrete elements sustain more damage, the damping ratio increases. Therefore, the initial assumption of 2% damping applied uniformly throughout the CSiBridge model may not be an accurate representation of the in-service structure.

Previous experiments conducted on the Galena Creek Bridge performed both vertical and lateral excitation tests (Carr and Sanders, 2013). It was noted during these experiments that the calculated damping values for the horizontal and vertical tests were different. When applying lateral excitation using an eccentric mass shaker, damping values between 2.6% and 3.4% were recorded. Alternatively, applying vertical excitation using a large construction vehicle resulted in damping between 1.8% and 2.5%. As such, using different damping ratios for various material definitions would result in a more accurate final model. As previously noted, the development of minor cracking suggests that the

assigned values should be higher than the idealized 2% – 3% from literature. For the recommended model, the upper limits of the damping recorded during the 2013 study were considered: 3.4% damping would be applied to transverse and longitudinal directions and 2.5% damping would be applied in the vertical direction.

For this approach, different vertical and lateral damping ratios were applied. The results of the time-history analyses conducted during the parametric study proposed that the substructure components were the controlling elements for longitudinal and transverse behavior. This was best demonstrated in the relatively large changes in transverse displacement noted during the effective moment of inertia study. Conversely, the superstructure definition was the primary factor in vertical excitation, best exemplified in the application of various strength concretes along Spans 2 – 4. The conclusion was that applying one damping ratio to the substructure materials and another damping ratio to the superstructure and link slab materials would be the best approach to simulate the structural behavior. The box girder, barrier rails, and link slab are composed of 31 MPa concrete, with 40 MPa material used at select sections. The pier columns and arches are made of 28 MPa and 35 MPa concrete, respectively. The final model was updated by assigning damping values of 2.5% to the 31 MPa material and 3.4% to the 35 MPa and 28 MPa materials.

### **7.3 Effective Moment of Inertia of Substructure Elements**

As cracks propagate and grow, reinforced concrete elements suffer from a reduction in flexural rigidity. ACI suggests that when performing linear-elastic analyses, concrete cracking can be accounted for by applying a reduction factor to the moment of inertia

(MOI) of the concrete member. ACI recommends reducing the MOI of a column to 70% to provide conservative estimates during the design process. While this conservative assumption aids in the safe design of structures, it does not represent the physical behavior of in-service structures.

Scaling factors were applied to the MOI of the substructure elements of the FEA model to better understand how substructure stiffness influenced the dynamic response. MOI scaling factors between 100% and 50% were investigated in 5% increments, where 100% MOI defined the control model. Once a range of behavior had been established, the next step was to determine the extent of damage to the substructure of the existing bridge. The 2018 NDOT bridge inspection report noted the columns and arches typically demonstrated minor hairline cracking characteristic of routine service loads, with cracks up to 8 mm wide and spalling up to 27 mm deep. Cracking, however minor, adversely affects the effective MOI of the substructure components. The effective MOI of the arch and column frame elements was reduced to 95% to account for the minor cracking that was documented while providing a more realistic value than the conservative assumption of 70% proposed by ACI.

#### **7.4 Material Stiffness**

The modulus of elasticity of the various elements of the Galena Creek Bridge were calculated as a function of the compressive strength of each material, with higher strength concretes having increased stiffness. This feature was used to evaluate the stiffness of the superstructure in Section CHAPTER 6. Although CSiBridge currently does not offer means for the user to assign multiple material properties to a concrete box girder definition,



the various models analyzed showed the influence of material stiffness on the dynamic response of the structure. As previously mentioned, the concrete strengths specified in the design plans are minimum requirements and it is highly likely that the actual material strengths of the Galena Creek Bridge are higher. To account for the compressive strength above the design value, the compressive strength and modulus of elasticity of the concrete materials used for the CSiBridge model were increased by a factor of 10%, as seen in Table 7.1. Note that this is an estimated value based typical data. Confirmation of this assumption would require access to the 28-day cylinder compression tests performed during the construction of the Galena Creek Bridge.

**Table 7.1: Final model concrete material propeties**

Concrete Design Strength (MPa)	Factored Strength (MPa)	Factored Modulus of Elasticity (MPa)
28	30.8	27,357
31	34.1	28,785
35	38.5	30,586

## 7.5 Final Proposed Modal Analysis

As noted in Section 6.2, classical damping was assumed for the CSiBridge model. As such, edits to the damping ratios would not impact the modal analysis. The material stiffness and substructure moment of inertia controlled the changes in modal results between the control model and final proposed model. The parametric study noted that decreasing the effective MOI of the substructure frame elements would predominantly result in an increase in transverse modal periods and participation factors. The longitudinal and vertical excitations were also influenced, but to a nominal degree (less than 1% among

the top modes considered). Conversely, increasing the material stiffness of both the superstructure and substructure elements would result in lower modal periods about all three degrees of freedom. Comparing the top five modes about each axis in Tables 7.2 – 7.4 confirms these assumptions. The modal periods of the final model decreased along all three axes, with the exception of a single transverse mode. This is likely a result of decreasing the effective MOI of the substructure frame elements.

**Table 7.2: Comparison of top longitudinal modes for control vs final model (X-axis)**

Control Model			Final Model			
Mode	Period, $T_{control}$ (s)	Modal Part. Factor (%)	Mode	Period, $T$ (s)	Modal Part. Factor (%)	$T/T_{control}$
2	1.342	12.3	2	1.300	12.3	0.969
4	0.976	15.1	4	0.950	15.1	0.973
9	0.671	9.2	9	0.647	10.4	0.964
11	0.627	9.8	11	0.604	9.8	0.963
39	0.284	9.3	39	0.272	10.0	0.957

**Table 7.3: Comparison of top transverse modes for control vs final model (Y-axis)**

Control Model			Final Model			
Mode	Period, $T_{control}$ (s)	Modal Part. Factor (%)	Mode	Period, $T$ (s)	Modal Part. Factor (%)	$T/T_{control}$
1	1.688	55.0	1	1.635	55.3	0.969
5	0.819	9.5	5	0.794	9.4	0.970
17	0.513	7.0	17	0.498	7.0	0.971
24	0.386	1.9	24	0.372	2.0	0.962
51	0.24	1.2	36	0.293	1.1	1.222

**Table 7.4: Comparison of top vertical modes for control vs final model (Z-axis)**

Control Model			Final Model			
Mode	Period, $T_{control}$ (s)	Modal Part. Factor (%)	Mode	Period, $T$ (s)	Modal Part. Factor (%)	$T/T_{control}$
7	0.721	5.8	7	0.685	5.1	0.950
15	0.56	3.9	18	0.486	4.2	0.869
18	0.505	4.1	20	0.450	4.0	0.891
20	0.469	3.9	21	0.441	3.6	0.940
44	0.263	6.1	44	0.253	6.1	0.962

The modal analyses from the final model were also compared to the study conducted by Carr and Sanders (2013) (see Table 7.5). As the Galena Creek Bridge is most vulnerable to lateral forces, the top transverse modes were used as the benchmark to compare the model. The final model demonstrated marginally lower modal periods than those resulting from the lateral excitation experiments. This is likely because the Carr and Sanders (2013) studies were performed within months of the completion of the bridge construction. The concrete of the Galena Creek Bridge has had almost an additional decade to cure; therefore, additional strength and stiffness gains would be expected. Further, despite being in service for eight years, the 2018 NDOT bridge inspection report did not note substantial deterioration that would result in significant loss of stiffness.

**Table 7.5: Comparison of top transverse modes for Carr & Sanders vs final model (Y-axis)**

Carr and Sanders Model			Final Model			
Mode	Period, $T_{control}$ (s)	Modal Part. Factor (%)	Mode	Period, $T$ (s)	Modal Part. Factor (%)	$T/T_{control}$
1	1.650	38.9	1	1.635	55.3	0.991
5	0.990	4.1	5	0.794	9.4	0.802
10	0.720	5.5	17	0.498	7.0	0.692
11	0.670	0.9	24	0.372	2.0	0.554
32	0.320	1.1	36	0.293	1.1	0.916

## 7.6 Final Proposed Model Time-History Analysis

The envelope displacements from the time-history analysis are analogous to the results from the modal analysis. The final model demonstrated more moderate envelope displacements than the control model from the same ground motions. Interestingly, the decreases in superstructure vertical displacements (Figure 7.1) are greater in areas of unbraced lengths, such as between Pier 2 and the arch crown. Conversely, shorter spans such as Spans 1 and 3 show greater vertical displacements than those of the control model.

Notably in Figure 7.2, increasing the material stiffness reduced the maximum transverse displacement along the entire length of the structure. However, decreasing the effective MOI of the substructure increases the curvature of the envelope displacement curves, as seen in Figure 6.12. This behavior exhibited again in Figure 7.2; decreasing the substructure stiffness to 95% increased the curvature of the graph despite the additional material stiffness. Figure 7.3 shows that the modifications made for the final model

decreased the longitudinal displacements of Frame 1 by an average of 8.8 mm and Frame 3 by 19.5 mm, whereas Frame 2 experienced almost no net change.

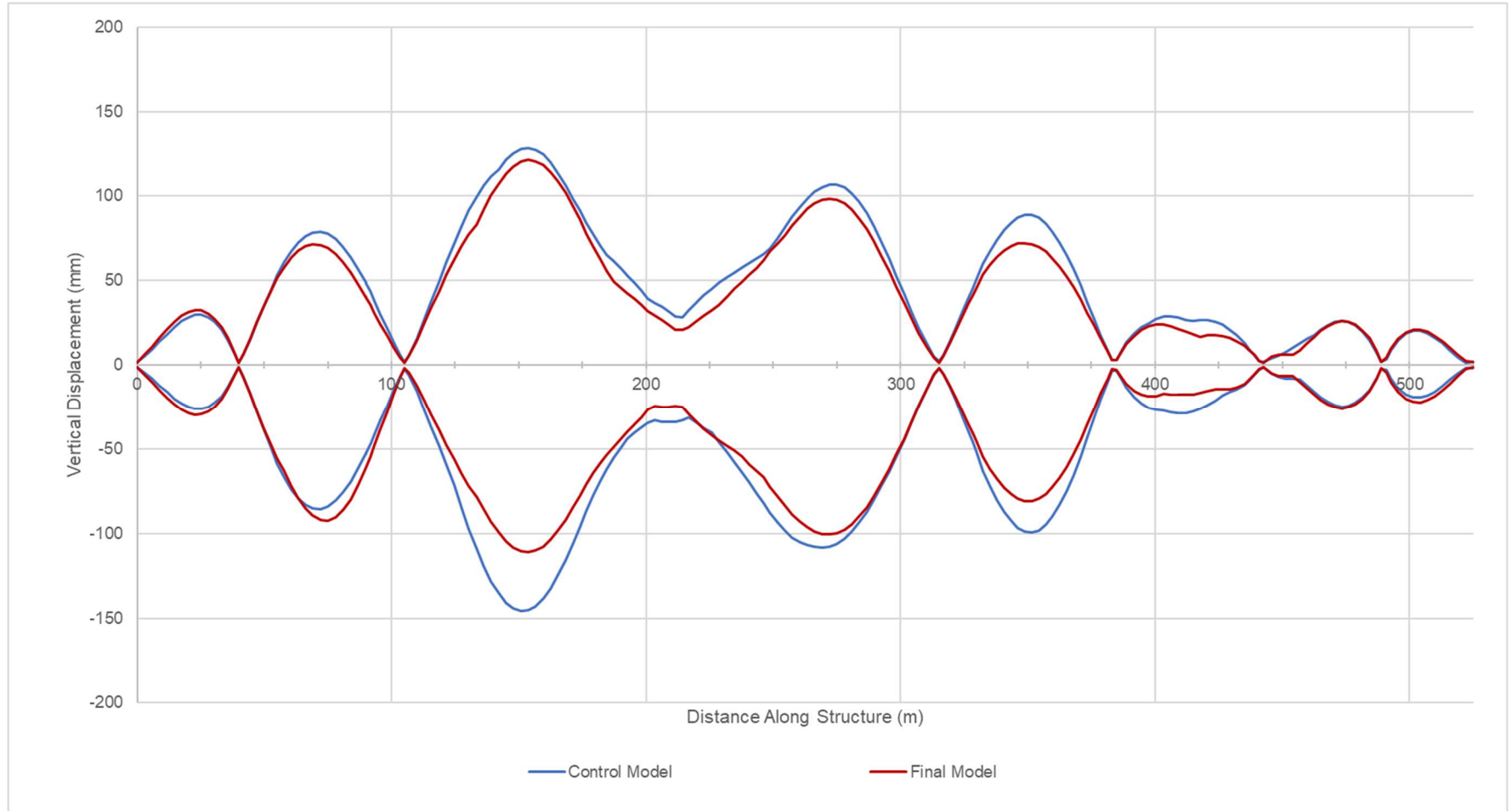


**Figure 7.1: Envelope of vertical displacements of northbound superstructure for control vs final models**

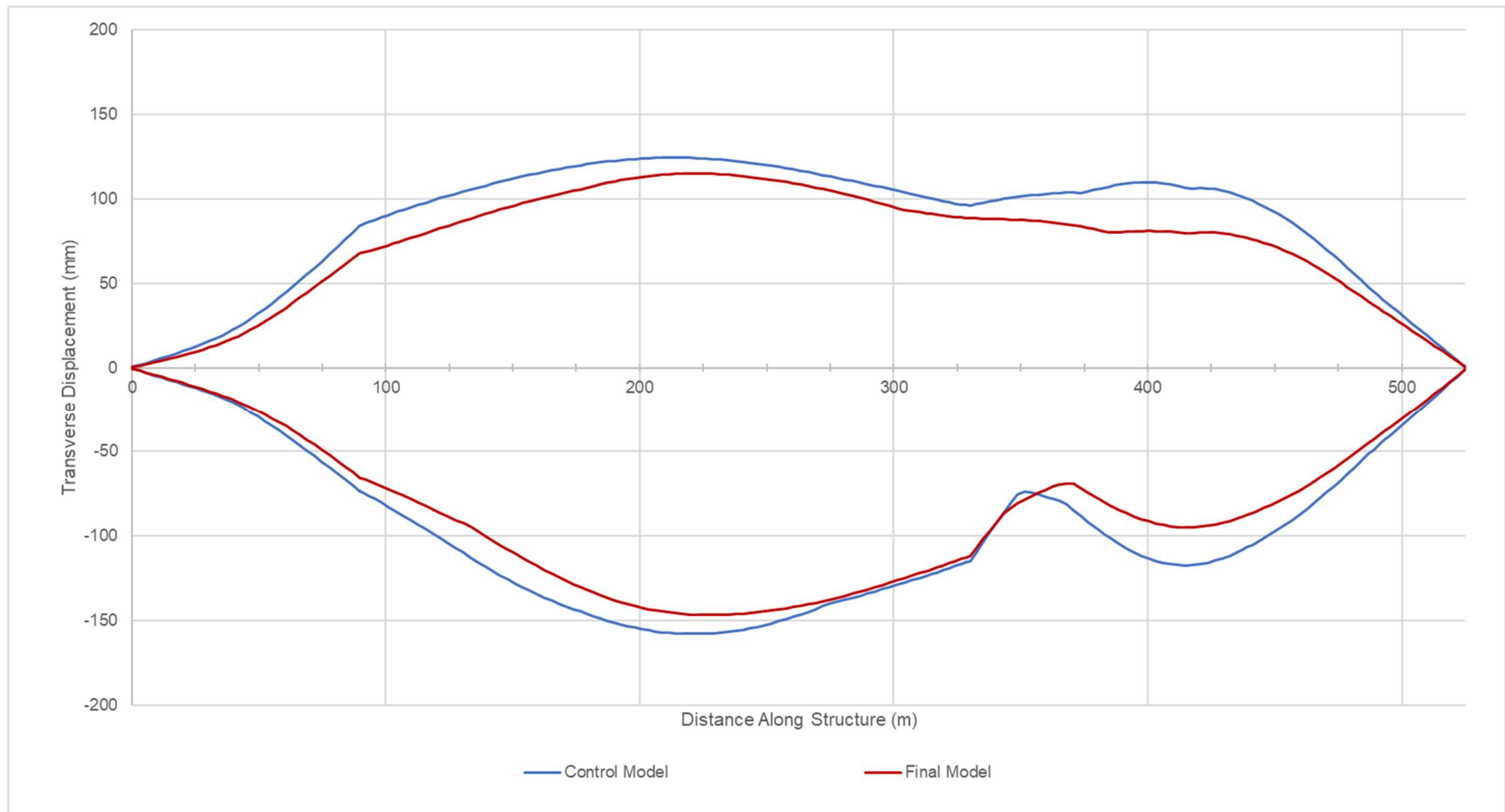


**Figure 7.2: Envelope of transverse displacement of northbound superstructure for control vs final models**

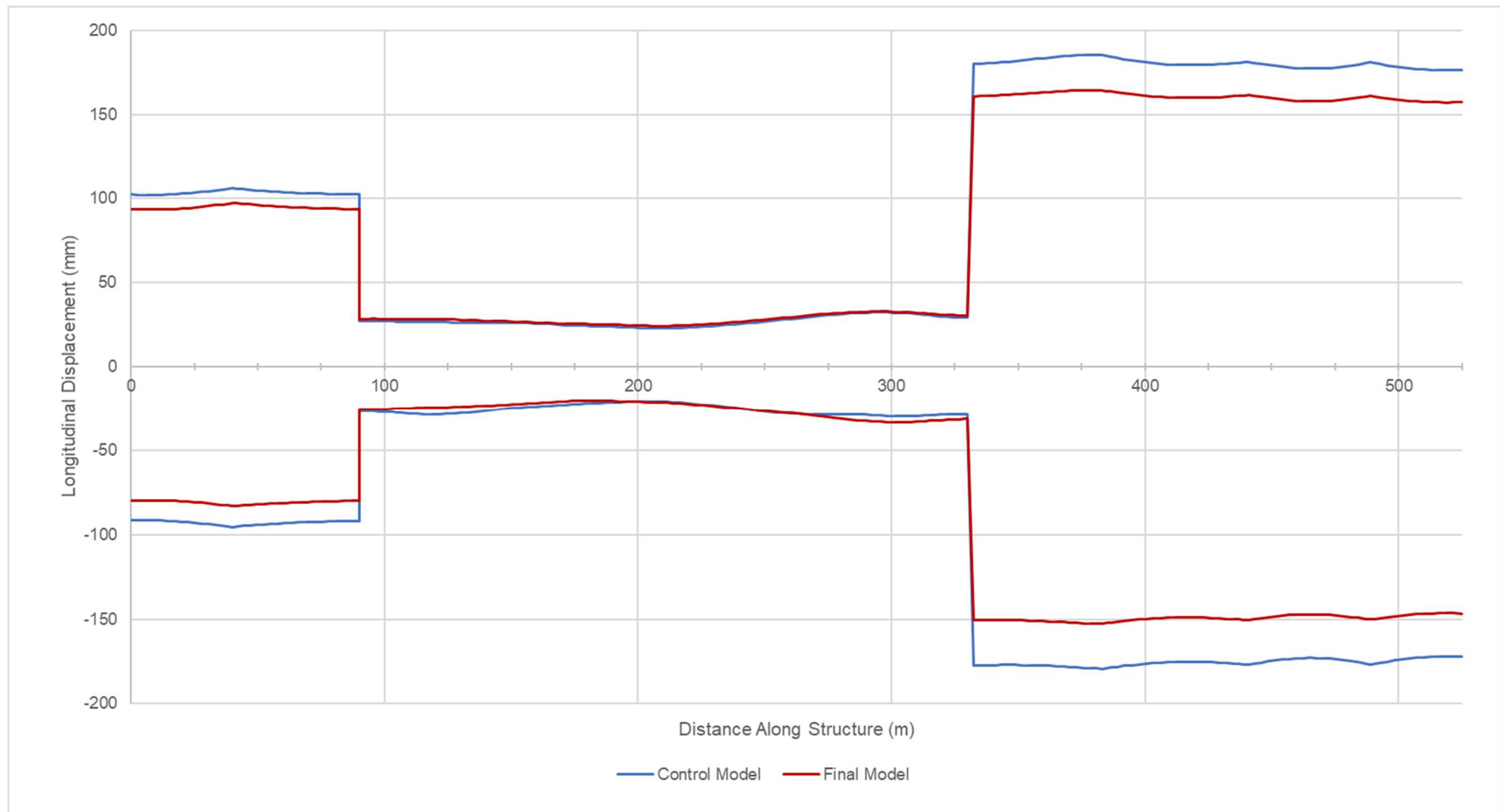


**Figure 7.3: Envelope of longitudinal displacement of northbound superstructure for control vs final models**



## **CHAPTER 8. CONCLUSIONS AND FUTURE WORK**

### **8.1 Conclusions**

As the largest cathedral arch bridge in the United States, the Galena Creek Bridge was the focus of a study to adapt a structural health monitoring system for applications on bridges. Two new, permanent SHM systems were installed on the northbound structure to enhance the understanding of the dynamic and in-service response of the bridge. The primary SHM system was composed of 33 uniaxial accelerometers located at key points along the superstructure and substructure. The secondary SHM system consisting of potentiometers, inclinometers, temperature gauges, and anemometers, served to further expand the capabilities of the primary system by recording displacement, tilt, temperature, and wind conditions. Together, the SHM systems continuously monitor bridge behavior during routine service loads, such as traffic, wind, and thermal expansion, as well as extreme events, such as seismic events.

In addition to the SHM systems installed on the structure, an FEA model of the Galena Creek Bridge was developed using CSiBridge. A parametric study was conducted to evaluate changes in the structural response relative to a defined set of parameters. The parametric study concluded that the methods of modeling the superstructure, barrier rail, link slab, and expansion joint bearings for the control model were sufficient. Additional variables considered in the study, such as the effective moment of inertia of the substructure elements, structural damping ratios, and material stiffnesses, were modified to reflect the behavior of bridge more accurately. Data recorded by the SHM systems will be used in

future studies to further calibrate the results of time-history analyses of the analytical model to the measured dynamic response of the Galena Creek Bridge.

At the submission of this document, no significant ground motions have been recorded. To properly evaluate the capabilities of the SHM systems, the seismic loading on the bridge must exceed the typical noise resulting from routine service loads. Once the functionality of both the seismic and exploratory systems are confirmed, data will be used to compare and calibrate the CSiBridge model. Once the FEA model of the Galena Creek Bridge is tuned to accurately reflect the in-service response, it will be used as an additional means to evaluate the structural integrity of the bridge. Furthermore, the CSiBridge model could be used to predict response and potential damage of the bridge to more extreme seismic excitation before high magnitude ground motions occur.

## **8.2 Proposal for Future Work**

### *8.2.1 Verification of Structural Health Monitoring Systems*

A central objective of the secondary health monitoring system was to further expand the capabilities of the primary system. The accelerometer-based seismic system was proven as an effective means to evaluate building structural integrity following seismic events by the United States Geological Survey during their Strong Ground Motion Project. The inclusion of additional sensors for this study was to adapt the seismic system for bridges and to gather data on additional response characteristics. Future research on the Galena Creek Bridge could consider additional instrumentation to further expand the capabilities of the SHM systems installed for this study.

One of the key factors in the dynamic response is the reliable behavior of the abutments and expansion joints. Predictable behavior between the frames of the bridge is crucial for the longevity of the structure. As such, additional string potentiometers added at Hinge 2 and Abutment 2 would ensure any irregularities in Frame 3 are captured. As Frame 1 has the shortest columns, both the superstructure and substructure experience the greatest internal stresses. Conversely, Frame 2 has the tallest columns and longest spans, resulting in the greatest vertical and transverse displacements. The addition of displacement sensors at the elastomeric bearing locations bookending Frame 3 would confirm the intended longitudinal translation between Frames 2 and 3.

Although the instrumentation locations were selected with the explicit intent of providing an understanding of dynamic behavior, the connection between the northbound and southbound structures remains an underexplored area of study. As noted in Section 6.3, the expansion joint boundary conditions control the longitudinal behavior of the bridge. Likewise, the connection between the northbound and southbound structures are a defining characteristic of the transverse behavior. Instrumentation to monitor the integrity and condition of the link slab could provide valuable insights on the bridge performance. The addition of weather-resistant strain gages along the length of the link slab would provide information on the component response as well as signify potential damage as it occurs.

#### *8.2.2 CSiBridge Finite Element Model*

The ultimate goal of the CSiBridge FEA model was to calibrate the model to the physical dynamic response of the Galena Creek Bridge. The parametric study explored several variables that influence the modal and dynamic behavior of the model. Although

the results of the parametric evaluation led to the development of a final proposed CSiBridge model, the dynamic response of the model has yet to be verified by comparing to measured data. Calibration of the model will be conducted by comparing the excitation experienced by nodes of the model to the sensors at each of the 15 locations. Table 8.1 lists each of the sensor locations with the corresponding node designation to aid with future calibration attempts.

**Table 8.1: Final model node numbers corresponding with sensor locations**

<b>Sensor Location</b>	<b>CSiBridge Node Number</b>
Top of Pier 1	4200
Bottom of Pier 1	4199
Midspan of Span 2	775
Top of Pier 2	4202
Bottom of Pier 2	4201
Midspan between Pier 2 and south merge	1415
South arch/superstructure merge	1574
Crown of Arch at Span 3	1795
North arch/superstructure merge	2014
Midspan between Pier 3 and north merge	2175
Top of Pier 3	4204
Bottom of Pier 3	4203
Midspan of Span 4	2874
Top of Pier 4	4206
Bottom of Pier 4	4205

There are several other factors that must be considered when calibrating the CSiBridge model to in-service behavior. One of the initial assumptions was that live loads did not influence the dynamic response. Additionally, the bearings were assumed to only permit rotation about the vertical direction. Further research can consider releasing the

rotational fixities of the elastomeric bearing about the horizontal axes. The scope of this study was limited to linear time-history analyses. The bridge will likely exhibit linear behavior for a majority of minor ground motions; however, the influence of an extreme seismic activity may require a non-linear time-history analyses. This more complex method of analysis will also require reevaluating the approach to modeling components such as the columns and link slab. Evaluating these advanced parameters will yield a FEM that will consistently predict the dynamic response of the Galena Creek Bridge to seismic activity. The complete model would then serve alongside the seismic and exploratory SHM systems to monitor the integrity of the structure throughout the service life.

## **APPENDIX A**

### **CALCULATIONS**



## Galena Creek Bridge Dead Load Calculations

$$\rho_{conc} := 150 \frac{\text{lb}}{\text{ft}^3}$$

Density of Concrete

$$L := 525 \text{ m}$$

Length of Bridge

### Barrier Rails

$$A_{box} := 0.45 \text{ m} \cdot 1.07 \text{ m}$$

$$cut_1 := 0.1675 \text{ m} \cdot 0.815 \text{ m}$$

$$cut_2 := 0.77 \text{ m} \cdot 0.075 \text{ m}$$

$$cut_3 := 0.18 \text{ m} \cdot 0.125 \text{ m} \cdot 0.5$$

$$A_{barrier\_rail} := A_{box} - cut_1 - cut_2 - cut_3 = 0.276 \text{ m}^2$$

$$line\_load := A_{barrier\_rail} \cdot \rho_{conc} = 6.503 \frac{\text{kN}}{\text{m}}$$

$$W_{barrier\_rail} := 4 \cdot L \cdot line\_load = 13.657 \text{ MN}$$

The cross sectional area of the barrier rail was taken by taking the full 450 mm x 1070 mm area and subtracting areas where there is no concrete.

Multiplied by a factor of 4. The NB structure and SB structure both have two barrier rails.

### Future Wearing Surface

Assume 3 in thick hot mix asphalt as wearing surface

$$area\_load := 3 \text{ in} \cdot \rho_{conc} = 1.796 \frac{\text{kN}}{\text{m}^2}$$

$$lane\_width := 18 \text{ m}$$

$$W_{FWS} := 2 \cdot L \cdot lane\_width \cdot area\_load = 33.935 \text{ MN}$$

$$W_{loads} := W_{FWS} + W_{barrier\_rail} = 47.592 \text{ MN}$$

## Superstructure

### Box Girder

Cross sectional area computed by CSi Bridge

$$A_{box\_girder} := 8.4664 \text{ m}^2$$

$$W_{box\_girder} := A_{box\_girder} \cdot \rho_{conc} \cdot 525 \text{ m} \cdot 2$$

$$W_{box\_girder} = 209.47 \text{ MN}$$

### Diaphragms

$$A_{diaph} := \frac{3.192 \text{ m} + 5.283 \text{ m}}{2} \cdot 2.6 \text{ m} \cdot 2$$

Diaphragm Thicknesses

$$t_{intermediate} := 0.25 \text{ m}$$

$$t_{hinge} := 5.8 \text{ m}$$

$$t_{abut} := 1.6 \text{ m}$$

$$t_{fillet} := 0.5 \text{ m}$$

$$t_{crown} := 0.3 \text{ m}$$

$$t_{total} := 2 \cdot (2 \cdot t_{hinge} + 2 \cdot t_{fillet} + 2 \cdot t_{crown} + 7 \cdot t_{abut} + 8 \cdot t_{intermediate}) = 52.8 \text{ m}$$

$$W_{diaph} := 2 \cdot A_{diaph} \cdot t_{total} \cdot \rho_{conc} = 54.829 \text{ MN}$$

### Link Slab

$$V_{link\_slab} := 0.2 \text{ m} \cdot 2.02 \text{ m} \cdot 240 \text{ m}$$

$$W_{link\_slab} := \rho_{conc} \cdot V_{link\_slab} = 2.285 \text{ MN}$$

$$W_{superstructure} := W_{box\_girder} + W_{diaph} + W_{link\_slab} = 266.583 \text{ MN}$$

Properties	
Base Material 4500Psi (31MPa) v	
A	8.4664
J	24.581
I33	10.7151
I22	176.3352
I23	0.
AS2	3.0022
AS3	6.5324
S33(+face)	10.6375
S33(-face)	5.3772
S22(+face)	18.6598
S22(-face)	18.6598
Z33	7.567
Z22	31.8184
r33	1.125
r22	4.5637
Xcg	9.45
Ycg	1.9927
Xpna	9.45
Ypna	2.7437
OK	





## Substructure

### Columns

$$A_{column} := 6 \text{ m} \cdot 3 \text{ m} - 1.8 \text{ m} \cdot 4 \text{ m} + 2 \cdot 0.15 \text{ m} \cdot 0.15 \text{ m}$$

$$W_{NB\_col\_1} := \rho_{conc} \cdot A_{column} \cdot 19.2 \text{ m}$$

$$W_{SB\_col\_1} := \rho_{conc} \cdot A_{column} \cdot 16.6 \text{ m}$$

$$W_{NB\_col\_2} := \rho_{conc} \cdot A_{column} \cdot 38.0 \text{ m}$$

$$W_{SB\_col\_2} := \rho_{conc} \cdot A_{column} \cdot 38.0 \text{ m}$$

$$W_{NB\_col\_3} := \rho_{conc} \cdot A_{column} \cdot 38.8 \text{ m}$$

$$W_{SB\_col\_3} := \rho_{conc} \cdot A_{column} \cdot 38.8 \text{ m}$$

$$W_{NB\_col\_4} := \rho_{conc} \cdot A_{column} \cdot 34.4 \text{ m}$$

$$W_{SB\_col\_4} := \rho_{conc} \cdot A_{column} \cdot 22.0 \text{ m}$$

$$W_{NB\_col\_5} := \rho_{conc} \cdot A_{column} \cdot 31.3 \text{ m}$$

$$W_{SB\_col\_5} := \rho_{conc} \cdot A_{column} \cdot 22.2 \text{ m}$$

$$W_{NB\_col\_6} := \rho_{conc} \cdot A_{column} \cdot 23.9 \text{ m}$$

$$W_{SB\_col\_6} := \rho_{conc} \cdot A_{column} \cdot 16.5 \text{ m}$$

$$W_{NB\_columns} := W_{NB\_col\_1} + W_{NB\_col\_2} + W_{NB\_col\_3} + W_{NB\_col\_4} + W_{NB\_col\_5} + W_{NB\_col\_6}$$

$$W_{SB\_columns} := W_{SB\_col\_1} + W_{SB\_col\_2} + W_{SB\_col\_3} + W_{SB\_col\_4} + W_{SB\_col\_5} + W_{SB\_col\_6}$$

$$W_{columns} := W_{NB\_columns} + W_{SB\_columns} = 86.808 \text{ MN}$$

### Link Beams

$$V_{link\_beam} := 4 \text{ m} \cdot 6 \text{ m} \cdot 13.92 \text{ m}$$

$$W_{link\_beams} := 2 \cdot V_{link\_beam} \cdot \rho_{conc} = 15.744 \text{ MN}$$

Thust blocks were not taken into consideration when computing self weight of structure.

### Arch

$$A_{arch} := 6 \text{ m} \cdot 3.6 \text{ m} - 5.2 \text{ m} \cdot 2.8 \text{ m} + 2 \cdot 0.35 \text{ m} \cdot 0.35 \text{ m}$$

$$W_{arch} := 2 \cdot \rho_{conc} \cdot A_{arch} \cdot (74.911 \text{ m} + 79.615 \text{ m} + 76.119 \text{ m}) = 79.184 \text{ MN}$$

$$W_{arch\_diaph} := 2 \cdot \rho_{conc} \cdot 5.2 \text{ m} \cdot 2.8 \text{ m} \cdot (6.731 \text{ m} + 7.827 \text{ m}) = 9.989 \text{ MN}$$

$$W_{substructure} := W_{columns} + W_{link\_beams} + W_{arch} + W_{arch\_diaph} = 191.724 \text{ MN}$$

### Comparison to Leo's Calculations

$$W_{total} := W_{loads} + W_{superstructure} + W_{substructure} = 505.899 \text{ MN}$$

$$W_{Leo} := 499.0 \text{ MN}$$

Value for Leo's calculations taken from page 70 of his thesis

$$Difference_{Leo} := \frac{W_{Leo} - W_{total}}{W_{total}} = -1.364\%$$

Note: I assume my calculations were a little higher because I took the chamfered fillets into account for the pier columns and arches.

### Comparison to CSI Bridge Values

$$W_{CSI} := 151711 \text{ kip} + W_{loads} = 722.436 \text{ MN}$$

Note: the current DEAD load case in CSI Bridge does not take into account the barrier rails or future wearing surface.

$$Difference_{CSI} := \frac{W_{CSI} - W_{total}}{W_{total}} = 42.802\%$$

### Additional substructure loads

$$W_{footings} := 8 \cdot \rho_{conc} \cdot 2.75 \text{ m} \cdot 14 \text{ m} \cdot 13.42 \text{ m} = 97.395 \text{ MN}$$

$$W_{thrust\_blocks} := 4 \cdot \rho_{conc} \cdot 12 \text{ m} \cdot 13.4 \text{ m} \cdot 5.7 \text{ m} = 86.388 \text{ MN}$$

$$W_{GCB} := W_{total} + W_{thrust\_blocks} + W_{footings} = 689.682 \text{ MN}$$

$$Difference_{CSI} := \frac{W_{CSI} - W_{GCB}}{W_{GCB}} = 4.749\%$$

Note: the values I calculated were slightly under the values reported by CSI Bridge. I assume the difference is attributed to the change in superstructure depth and soffit thickness in the CSI model, which are not accounted for in this report.

### Column Height Calculations (meters)

Column heights were evaluated by calculating the difference between the elevation of the bottom of the box girder and the top of the footing at the centeline of the respective pier. All values are in meters unless specified otherwise

SB Pier 1	$1593.072 - 1576.45 = 16.622$	NB Pier 1	$1593.539 - 1574.35 = 19.189$
SB Pier 2	$1592.308 - 1554.259 = 38.049$	NB Pier 2	$1592.727 - 1554.68 = 38.047$
SB Pier 3	$1589.683 - 1550.914 = 38.769$	NB Pier 3	$1590.102 - 1551.333 = 38.769$
SB Pier 4	$1588.833 - 1568.85 = 19.983$	NB Pier 4	$1589.252 - 1554.85 = 34.402$
SB Pier 5	$1588.108 - 1565.95 = 22.158$	NB Pier 5	$1588.527 - 1557.25 = 31.277$
SB Pier 6	$1587.508 - 1571.05 = 16.458$	NB Pier 6	$1587.885 - 1563.95 = 23.935$



### Elastomeric Bearing Stiffness Calculations

$$G := 1.06 \text{ MPa}$$

Section Modulus of 60 Durometer Elastomer

$$E := 4.4 \text{ MPa}$$

Modulus of Elasticity of 60 Durometer Elastomer

#### Abutment Bearings

$$b := 640 \text{ mm}$$

Elastomer Length

$$w := 640 \text{ mm}$$

Elastomer Width

$$A := b \cdot w = 0.41 \text{ m}^2$$

Gross Plan Area of Elastomer

$$I := \frac{b \cdot w^3}{12} = 0.014 \text{ m}^4$$

Elastomer Moment of Inertia

$$H_r := 12 \text{ mm} + 7 \cdot 13 \text{ mm}$$

Total Elastomer Thickness

$$H := 119 \text{ mm}$$

Total Bearing Height

$$K_H := \frac{G \cdot A}{H_r} = 4215.301 \frac{\text{kN}}{\text{m}}$$

Lateral Stiffness

$$K_V := \frac{E \cdot A}{H_r} = 17497.476 \frac{\text{kN}}{\text{m}}$$

Vertical Stiffness

$$K_\theta := \frac{E \cdot I}{H} = 516.945 \text{ kN} \cdot \text{m}$$

Rotational Stiffness

## Hinge Bearings

$$b := 710 \text{ mm}$$

Elastomer Length

$$w := 760 \text{ mm}$$

Elastomer Width

$$A := b \cdot w = 0.54 \text{ m}^2$$

Gross Plan Area of Elastomer

$$I := \frac{b \cdot w^3}{12} = 0.026 \text{ m}^4$$

Elastomer Moment of Inertia

$$H_r := 12 \text{ mm} + 13 \cdot 19 \text{ mm}$$

Total Elastomer Thickness

$$H := 287 \text{ mm}$$

Bearing Height

CSiBridge accepts a single input for bearing info at hinges. Multiply values by 3 to determine bearing properties for the three bearings at each hinge.

$$K_H := \frac{3 \cdot G \cdot A}{H_r} = 6625.205 \frac{\text{kN}}{\text{m}}$$

Lateral Stiffness

$$K_V := \frac{3 \cdot E \cdot A}{H_r} = 27500.849 \frac{\text{kN}}{\text{m}}$$

Vertical Stiffness

$$K_\theta := \frac{3 \cdot E \cdot I}{H} = 1194.565 \text{ kN} \cdot \text{m}$$

Rotational Stiffness

## **APPENDIX B**

### **INSTRUMENTATION SPECIFICATIONS**

# ES-U2

## Uniaxial Force Balance Accelerometer

### For use in a variety of applications

The EpiSensor ES-U2 force balance accelerometer is a uniaxial surface package designed primarily for structural engineering applications. However, it can be used in a variety of applications for measuring accelerations up to  $\pm 4g$  and down to the ambient noise level. With full-scale recording ranges of  $\pm 0.25$  to  $\pm 4g$  (user selectable) the ES-U2 provides on-scale recording of earthquake motions even at near-fault locations and in a wide variety of structure types.

Because the ES-U2 is extremely low-noise, it can detect motions of the ambient vibration field at most urban sites and civil structures from 1 Hz to 200A Hz. This makes the ES-U2 a unique sensor at a great price. The output of the ES-U2 is an amplified, conditioned signal—it requires no external electronics other than a data acquisition system.

The significantly improved bandwidth of DC to 200 Hz allows engineers and scientists to study motions at higher frequencies while maintaining the very important DC response that allows simple field calibration and reduces processing confusion.

Output circuitry is also significantly enhanced. Four types of outputs can be field-selected by the user:  $\pm 2.5V$  single-ended,  $\pm 10V$  single-ended,  $\pm 5V$  differential or  $\pm 20V$  differential.

The sensor has a number of full scale outputs to match the traditional Kinemetrix earthquake recording instruments, as well as the most modern Kinemetrix' Rock+ series and Quanterra's Q330 series of dataloggers.

EpiSensor force balance accelerometers are also available in triaxial surface and borehole (the FBA ES-SB shallow and FBA ES-DH deep) packages.



### FEATURES

- Low noise
- Extended bandwidth - DC to 200Hz
- User-selectable full-scale range
- Calibration coil (standard)
- Single-end or differential output (user selectable)



## SPECIFICATIONS

<b>Dynamic range:</b>	155 dB+
<b>Bandwidth:</b>	DC to 200Hz
<b>Calibration coil:</b>	Standard
<b>Full-scale range:</b>	User selectable at $\pm 0.25g$ , $\pm 0.5g$ , $\pm 1g$ , $\pm 2g$ or $\pm 4g$
<b>Outputs:</b>	User selectable at: $\pm 2.5V$ single-ended $\pm 10V$ single-ended $\pm 5V$ differential $\pm 20V$ differential
<b>Zero adjust:</b>	User-friendly access holes for simple, safe, efficient adjustment
<b>Linearity:</b>	$< 1000 \mu g/g^2$
<b>Hysteresis:</b>	$< 0.1\%$ of full scale
<b>Cross-axis sensitivity:</b>	$< 1\%$ (including misalignment)
<b>Zero point thermal drift:</b>	$< 500 \mu g/^{\circ}C$ (1g sensor)
<b>Power consumption:</b>	Quiescent current $< 9 mA$ from $\pm 12V$
<b>Mounting:</b>	Dual bolt for horizontal or vertical mounting
<b>Operating Temperature:</b>	$-20^{\circ}$ to $70^{\circ}C$ ( $0^{\circ}$ to $160^{\circ}F$ )
<b>Housing:</b>	EMI/RFI Watertight enclosure 55x65x97mm (2.2"x2.6"x3.8")
<b>Weight:</b>	0.35kg (0.77 pounds)



# HX-P510 SERIES

## 0 to 5, 0 to 10, $\pm 5$ , $\pm 10$ VDC ANALOG OUTPUT



The UniMeasure HX-P510 Series transducer offers a voltage output with wide adjustability to give a 0 to 5, 0 to 10,  $\pm 5$  or  $\pm 10$  VDC output. The device may be powered with an unregulated voltage in the range of 4.9 to 30 VDC. Zero and span adjustment potentiometers are readily accessible. With the zero position set anywhere within the first 30% of total travel, the span may be adjusted to give a full 0 to 5 or 0 to 10 VDC output with the span set anywhere within the last 20% of travel. Alternatively, the zero position may be set anywhere between 10% and 90% of full travel to give an output of  $\pm 5$  or  $\pm 10$  VDC with the span set between 50% to 100% of the longest travel from the zero position.



### SPECIFICATIONS

#### GENERAL

Available Measurement Ranges .....See Supplemental Data<sup>[1]</sup>, Table 12  
Sensing Device .....Precision Potentiometer  
Connector .....MS3102E-14S-6P  
Mating Connector (included) .....MS3106E-14S-6S

#### PERFORMANCE

Linearity  
2", 3", 4", 5" & 6" Ranges ..... $\pm 0.30\%$  Full Scale  
10", 15", 20" & 25" Ranges ..... $\pm 0.20\%$  Full Scale  
All other ranges ..... $\pm 0.15\%$  Full Scale  
Repeatability ..... $\pm 0.015\%$  Full Scale  
Resolution .....Essentially Infinite

#### ENVIRONMENTAL

Operating temperature .....-40°C to +85°C  
Storage Temperature .....-55° to +100°C  
Operating humidity .....100%  
Vibration .....15 G's 0.1 ms max.  
Shock .....50 G's 0.1 ms max.

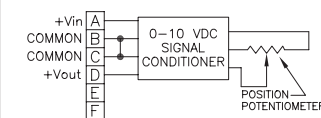
#### INGRESS PROTECTION (Exclusive of Wire Rope Area)

Standard .....IP-65 (NEMA 4)  
Optional .....IP-68 (NEMA 6)

#### ELECTRICAL

Output .....0 to 5 or 10 VDC,  $\pm 5$  or  $\pm 10$  VDC  
Excitation Voltage .....4.9 to 30 VDC  
Excitation Current .....25 mA max.  
Output Impedance .....10 $\Omega$  max.  
Output Load .....5K $\Omega$  min.  
**ADJUSTMENT RANGE-0 to 5 or 0 to 10 VDC**  
Zero .....0 to 30% of Range  
Span .....80% to 100% of Range  
**ADJUSTMENT RANGE- $\pm 5$  or  $\pm 10$  VDC**  
Zero .....10% to 90% of Range  
Span .....50% to 100% of Longest Possible Travel from Zero Position  
Protection .....Reversed Polarity  
Temperature Stability .....0.02%/°C of Span

#### CONNECTION DIAGRAM



#### FOOTNOTES TO SPECIFICATIONS

1. Supplemental Data section located at end of HX Series pages.

### MODEL NUMBER CONFIGURATION

**HX-P510-** 0 1 2 3 4 5 6 7 8 9

#### BASIC CONFIGURATION (FOR ALL RANGES)

**HX-P510-50-S10-N0S-1BC**

**0 RANGE**  
Select Measurement Range From Supplemental Data Table 12<sup>p</sup> 12 (next page), Insert Corresponding Measurement Range Designator

**1 WIRE ROPE**  
S ..... Stainless Steel  
(See Supplemental Data, Table 12)  
N .....  $\varnothing 0.018$  (0.45 mm)  
Nylon Jacketed Stainless Steel  
Ranges to 80" (2m) only. (formerly NJC)  
J .....  $\varnothing 0.037$  (0.94 mm)  
Nylon Jacketed Stainless Steel  
Ranges 100" (2.5m) to 500" (12.7m) only.

**2 WIRE ROPE TENSION**  
1 ..... Standard  
2 ..... Reduced (Ranges to 80" only)

**3 WIRE ROPE EXIT DIRECTION**  
Use Number designators shown  
RANGES TO 80" (2000 mm)  
  
RANGES 100" TO 2000" (2.5 m TO 50 M)

**4 N** ..... Required Designator  
**5 0** ..... Required Designator  
**6 ELECTRICAL OUTPUT POLARITY**  
S ..... Standard (increasing output as wire rope is extended)  
R ..... Reversed (decreasing output as wire rope is extended)

#### NOTES FOR OPTION BOXES 7, 8, and 9

**IP-65 (NEMA 4):** Transducer equipped with body mounted connector and with or without mating connector. Mating connector with electrical cable available separately as part number 10119-xM where 'x' is length of electrical cable in meters.

**IP-68 (NEMA 6):** Transducer equipped with bulkhead fitting and length of electrical cable. Remote end of electrical cable may be outfitted with water proof connector. Mating connector with electrical cable available separately as part number 10424-xM where 'x' is length of electrical cable in meters.

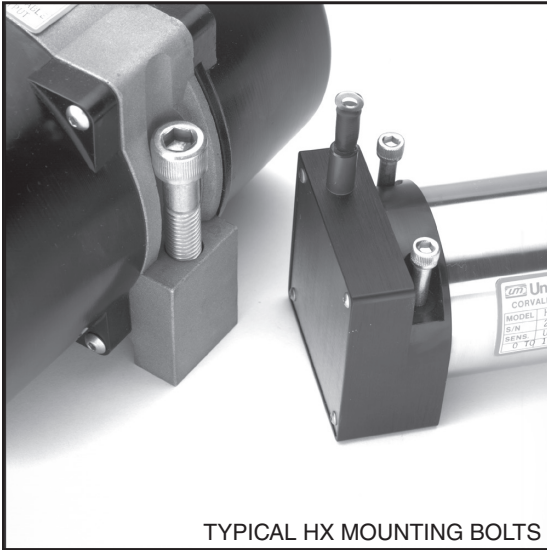
**7 INGRESS PROTECTION**  
1 ..... IP-65 (NEMA 4)  
2 ..... IP-68 (NEMA 6)  
3 ..... IP-68 (NEMA 6) Corrosion Resistant Construction

**8 IP-65-NEMA 4 CONNECTOR**  
B ..... 6 Pin 3102E Body Mounted Connector  
**IP-68-NEMA 6 ELECTRICAL CABLE**  
P ..... Bulkhead Fitting w/ 0.3m (12") Electrical Cable  
3 ..... Bulkhead Fitting w/ 3m (10') Electrical Cable  
4 ..... Bulkhead Fitting w/ 4m (13.5') Electrical Cable  
5 ..... Bulkhead Fitting w/ 5m (16.5') Electrical Cable  
6 ..... Bulkhead Fitting w/ 6m (20') Electrical Cable  
7 ..... Bulkhead Fitting w/ 7m (23') Electrical Cable

**9 IP-65-NEMA 4 MATING CONNECTOR**  
C ..... IP-65 Mating Connector Included  
K ..... IP-65 Mating Connector Omitted\*  
\*Electrical cable with mating connector may be ordered separately as part number 10119-xM where 'x' is the length required in meters.

**IP-68-NEMA 6 CABLE MOUNTED CONNECTOR**  
N ..... No connector on end of electrical cable  
K ..... IP-68 Cable to cable connector with **NO** mating connector\*\*  
\*\*Electrical cable with mating connector may be ordered separately as part number 10424-xM where 'x' is the length required in meters. Mating connector alone unavailable.

### MECHANICAL SPECIFICATIONS



TYPICAL HX MOUNTING BOLTS

**AVAILABLE MEASUREMENT RANGES** .... See Table 12

#### CONSTRUCTION

Ranges 80" (2 m) and under .....	Anodized Aluminum Mounting Base
	Stainless Steel & Anodized Aluminum Housing
Ranges 100" (2.5 m) and greater .....	Stainless Steel Mounting Base
	High Impact, Corrosion Resistant
	Thermoplastic Housings
Wire Rope Tension.....	See Table 12
Wire Rope Diameter .....	See Table 12
Weight .....	See Table 12
Connector .....	MS3102A-14S-6P
Mating Connector .....	MS3106E-14S-6S
Optional NEMA 6 Capability.....	Bulkhead fitting with shielded twisted pair cable

#### Life<sup>(1)</sup>

Ranges 2" to 6" .....	5,000,000 full stroke cycles
Ranges 10" to 25" .....	500,000 full stroke cycles
Ranges 30" to 400" .....	250,000 full stroke cycles
Ranges 500" to 2000" .....	200x10 <sup>6</sup> lineal inches

#### NOTES:

1. With 1K ohm potentiometer, wire rope misalignment 2° maximum at full stroke, relatively dust free environment, nylon jacketed wire rope on units with ranges 80" and less.

Use value from this column to indicate overall measurement range



Check mark indicates available measurement range

## TABLE 12

MEASUREMENT RANGE DESIGNATOR	STANDARD MEASUREMENT RANGES (in) (mm)		APPLICABLE SERIES			WIRE ROPE TENSION (NOMINAL) (oz) (N)		WIRE ROPE DIAMETER (in) (mm)		TRANSDUCER WEIGHT (lb) (Kg)		Product Photo
			HX-PA HX-PB HX-P420 HX-P510	HX-EP	HX-V HX-VP							
2	2	50	✓	-	✓	34	9.4	.016	0.4	2	0.9	
3	3	75	✓	-	✓	24	6.7	.016	0.4	2	0.9	
4	4	100	✓	-	✓	24	6.7	.016	0.4	2	0.9	
5	5	125	✓	-	✓	19	5.3	.016	0.4	2	0.9	
6	6	150	✓	-	✓	24	6.7	.016	0.4	2	0.9	
10	10	250	✓	✓	✓	34	9.4	.016	0.4	2	0.9	
15	15	390	✓	-	✓	24	6.7	.016	0.4	2	0.9	
20	20	500	✓	-	✓	24	6.7	.016	0.4	2	0.9	
25	25	640	✓	✓	✓	19	5.3	.016	0.4	2	0.9	
30	30	750	✓	-	✓	24	6.7	.016	0.4	2	0.9	
40	40	1000	✓	-	✓	24	6.7	.016	0.4	2	0.9	
50	50	1250	✓	✓	✓	19	5.3	.016	0.4	2	0.9	
60	60	1500	✓	✓	✓	24	6.7	.016	0.4	2	0.9	
80	80	2.0m	✓	✓	✓	21	5.8	.016	0.4	2	0.9	
100	100	2.5m	✓	✓	✓	36	10.0	.024	0.6	6.8	3.1	
120	120	3.0m	✓	✓	✓	36	10.0	.024	0.6	6.8	3.1	
150	150	3.8m	✓	✓	✓	36	10.0	.024	0.6	6.8	3.1	
200	200	5.0m	✓	✓	✓	36	10.0	.024	0.6	6.8	3.1	
250	250	6.3m	✓	✓	✓	36	10.0	.024	0.6	6.8	3.1	
300	300	7.5m	✓	✓	✓	36	10.0	.024	0.6	6.8	3.1	
350	350	8.8m	✓	✓	✓	36	10.0	.024	0.6	6.8	3.1	
400	400	10.0m	✓	✓	✓	36	10.0	.024	0.6	6.8	3.1	
500	500	12.5m	✓	✓	✓	36	10.0	.024	0.6	8.6	3.9	
600	600	15.2m	✓	✓	✓	36	10.0	.024	0.6	8.6	3.9	
800	800	20.3m	✓	✓	✓	36	10.0	.024	0.6	8.6	3.9	
1000	1000	25.4m	✓	✓	-	36	10.0	.024	0.6	12.0	5.4	
1200	1200	30.4m	✓	✓	-	36	10.0	.024	0.6	12.3	5.6	
1600	1600	40.6m	✓	✓	-	36	10.0	.024	0.6	14.1	6.4	
1800	1800	45.7m	✓	✓	-	36	10.0	.021	0.6	15.9	7.2	
2000	2000	50.8m	✓	✓	-	36	10.0	.021	0.5	16.3	7.4	

Specifications subject to change without notice

### OPTION DESCRIPTIONS

OPTION	OPTION DESIGNATOR	DESCRIPTION																												
NYLON JACKETED WIRE ROPE <u>RANGES TO 80" ONLY</u>	N	Replaces standard stainless steel wire rope with Ø.018 nylon jacketed wire rope. This option increases wire rope life dramatically but may increase non-linearity by as much as ±.05% of full scale.																												
NYLON JACKETED WIRE ROPE <u>RANGES 100" TO 500" ONLY</u>	J	Replaces standard stainless steel wire rope with Ø.037 nylon jacketed wire rope.																												
ALTERNATE WIRE ROPE EXIT <u>RANGES TO 80" (2.0 m)</u>	1, 2, 3	<div><div><div><div>1</div><div></div></div><div><div>2</div><div></div></div><div><div>3</div><div></div></div></div><div><p>MOUNTING SURFACE MOUNTING HOLES</p><table><tr><th>RANGE</th><th>"A"</th><th>"B"</th><th>"C"</th></tr><tr><td>2", 10"</td><td>1.12 (28.4)</td><td>1.79 (45.5)</td><td>1.21 (30.7)</td></tr><tr><td>3", 15", 30"</td><td>.96(24.4)</td><td>1.95 (49.5)</td><td>1.37 (34.8)</td></tr><tr><td>4", 20", 40"</td><td>.80 (20.3)</td><td>2.11 (53.6)</td><td>1.53 (38.9)</td></tr><tr><td>5", 25", 50"</td><td>.64 (16.3)</td><td>2.27 (57.7)</td><td>1.69 (42.9)</td></tr><tr><td>6", 60"</td><td>.49 (12.4)</td><td>2.42 (61.5)</td><td>1.84 (46.7)</td></tr><tr><td>80"</td><td>.25 (6.4)</td><td>2.66 (67.6)</td><td>2.08 (52.8)</td></tr></table><p>Dimensions in brackets are millimeters</p></div></div>	RANGE	"A"	"B"	"C"	2", 10"	1.12 (28.4)	1.79 (45.5)	1.21 (30.7)	3", 15", 30"	.96(24.4)	1.95 (49.5)	1.37 (34.8)	4", 20", 40"	.80 (20.3)	2.11 (53.6)	1.53 (38.9)	5", 25", 50"	.64 (16.3)	2.27 (57.7)	1.69 (42.9)	6", 60"	.49 (12.4)	2.42 (61.5)	1.84 (46.7)	80"	.25 (6.4)	2.66 (67.6)	2.08 (52.8)
RANGE	"A"	"B"	"C"																											
2", 10"	1.12 (28.4)	1.79 (45.5)	1.21 (30.7)																											
3", 15", 30"	.96(24.4)	1.95 (49.5)	1.37 (34.8)																											
4", 20", 40"	.80 (20.3)	2.11 (53.6)	1.53 (38.9)																											
5", 25", 50"	.64 (16.3)	2.27 (57.7)	1.69 (42.9)																											
6", 60"	.49 (12.4)	2.42 (61.5)	1.84 (46.7)																											
80"	.25 (6.4)	2.66 (67.6)	2.08 (52.8)																											
ALTERNATE WIRE ROPE EXIT <u>RANGES 100" (2.5 m) and GREATER</u>	1, 2, 3	<div><div><div><div>1</div><div></div></div><div><div>2</div><div></div></div><div><div>3</div><div></div></div></div><div><p>Dimensions in brackets are millimeters</p></div></div>																												
NON-STANDARD POTENTIOMETER <u>APPLIES TO HX-PA &amp; HX-VPA ONLY</u>	3, 4	<p>Non-standard potentiometer linearity is as follows:</p> <table><tr><th>RANGE</th><th>LINEARITY</th></tr><tr><td>5" and Below</td><td>±1.00% of full scale</td></tr><tr><td>10" to 25"</td><td>±0.50% of full scale</td></tr><tr><td>30" and above</td><td>±0.25% of full scale</td></tr></table> <p><b>Note:</b> This option is subject to potentiometer availability.</p>	RANGE	LINEARITY	5" and Below	±1.00% of full scale	10" to 25"	±0.50% of full scale	30" and above	±0.25% of full scale																				
RANGE	LINEARITY																													
5" and Below	±1.00% of full scale																													
10" to 25"	±0.50% of full scale																													
30" and above	±0.25% of full scale																													
REVERSED OUTPUT	R	Output is at a maximum when wire rope is fully retracted. Output decreases as wire rope is extended. Does not apply to velocity signal.																												
IP-68, (NEMA 6) CAPABILITY	2	<div><p>Connector is replaced with a bulkhead fitting and a designated length of urethane jacketed, shielded, twisted pair cable. Retraction mechanism and electrical components are sealed to IP-68, (NEMA 6) capability.</p></div>																												
CORROSION RESISTANT CONSTRUCTION	3	<p>All external anodized aluminum parts of transducer are replaced with stainless steel and corrosion resistant plastic. Transducer is sealed to IP-68 (NEMA 6) capability. Urethane jacketed, shielded, twisted pair cable exits unit. No connector on unit.</p> <div></div>																												

### DIMENSIONAL INFORMATION

#### HX SERIES – RANGES TO 80" (2 m)

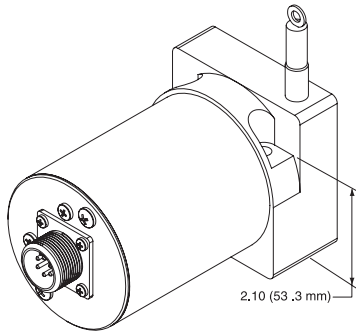
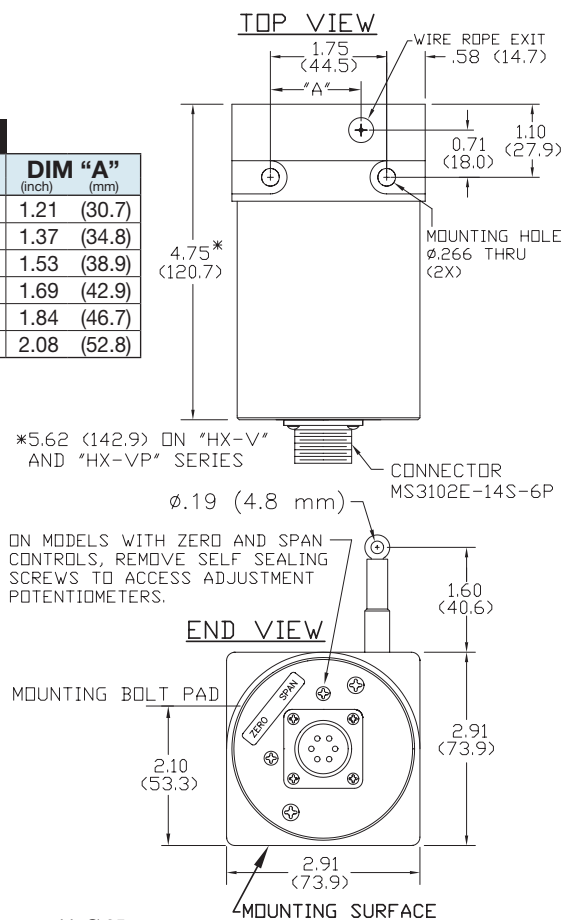


**FIG. 1**

**TABLE 13**

RANGE	DIM "A"	DIM "A"
(inch)	(mm)	(mm)
2", 10"	1.21	(30.7)
3", 15", 30"	1.37	(34.8)
4", 20", 40"	1.53	(38.9)
5", 25", 50"	1.69	(42.9)
6", 60"	1.84	(46.7)
80"	2.08	(52.8)



**NOTES:**

1. Transducer mounts with Ø.25 or M6 Socket head cap bolts.

Dimensions in brackets are millimeters

**TABLE 14**

RANGE	DIM "A"	DIM "B"
(inch)	(mm)	(mm)
Ranges to 800"	7.70 (196)	3.80 (97)
1000" to 2000"	11.0 (280)	5.60 (142)

**NOTES:**

1. Transducer mounts with Ø.50 or M12 socket head cap bolts.
2. Dimension "C" is the cable offset that occurs as the cable is extended from the transducer. For "C" in inches,  $C = .0016 \times E$  where E = extension in inches. For "C" in millimeters,  $C = .0016 \times E$  where E = extension in mm.

#### HX SERIES – RANGES GREATER THAN 80" (2 m)

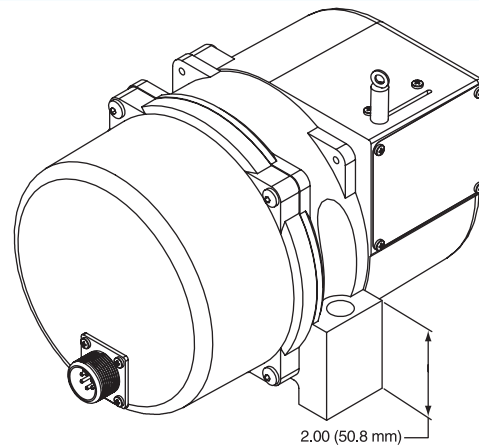
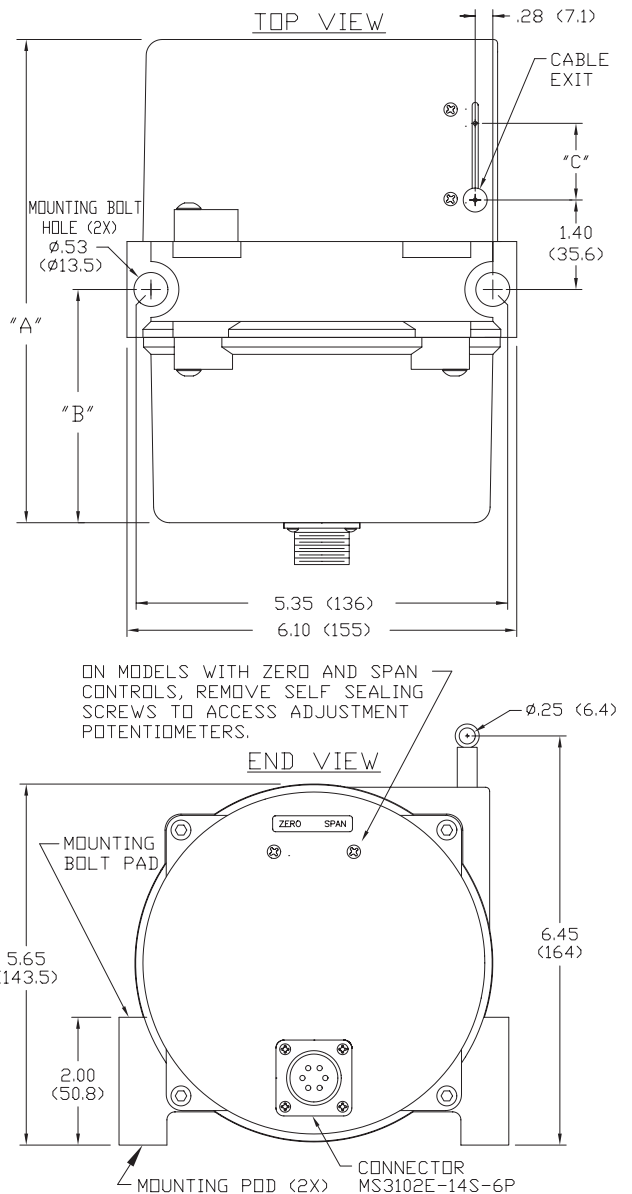


**FIG. 2**



Dimensions in brackets are millimeters



## Accurate, User-Configurable, All-in-One Inclinometer

### DESCRIPTION

The H6 inclinometer provides highly accurate, dual axis inclination sensing in a rugged environmentally protected housing. This unit incorporates MEMS sensing elements referenced to gravity with integrated temperature compensation over the entire industrial operating range of  $-40^{\circ}$  to  $+85^{\circ}\text{C}$ .

The H6 provides two continuous and fully configurable analog outputs. These outputs can be individually set to current, voltage or open collector switch modes. The voltage output can be set to any value between 0V and 10V, the current output can be set to any value between 0mA and 24mA - either to any angle range between  $\pm 180^{\circ}$ . The current and voltage outputs are linear with respect to the input angle directly.

The open collector switch output connects to signal common and can be set to trip above, below, between, or outside any angle threshold or window range. The transistor output can be used directly or to drive an external relay (up to 250mA drive capability)

The H6 also includes a polled, half-duplex (2-wire), RS-485 digital interface for angle measurements and configuration. Also available upon request, the H6 has CAN bus hardware available for customer specified protocols (including J1939 and CanOPEN).

All analog output parameters can be configured via the RS-485 interface at the factory to meet your specifications or through the Flex Series Development Kit and software allowing the end customer to modify the sensor as needed right from a PC - providing full flexibility for R&D and OEM production lines.

Used as integrated devices by original equipment manufacturers (OEMs) or as standalone sensors for test and measurement, the H6 is made for applications where high accuracy and long-term stability are required in noisy and wide temperature changing environments. For use with most applications including commercial, industrial, and military applications.



### FEATURES

- Dual Axis
- Horizontal and Vertical Mount
- Scalable Angle Range up to  $\pm 180^{\circ}$
- Fully Temperature Compensated
- Multiple, Simultaneous, Configurable Outputs
  - Current
  - Voltage
  - Open Collector Switch
  - RS-485
  - CAN bus
  - Optional Logging to SD Card
- Daisy-chain Multiple Sensors
- Vibration and shock resistant
- Environmentally sealed IP68
- Rugged Aluminum housing
  - Optional Stainless Steel 316
- EMC protected to 100V/m
- Reverse Polarity Protection
- Overvoltage/overcurrent protection
- $-40^{\circ}$  to  $+85^{\circ}\text{C}$  Operating Temperature
- CE Certified

### INDUSTRIES

- Aerospace & Defense
- Construction
- Mining
- Offshore
- Transportation

**Rieker Rugged. Rieker Reliable.™**

RIEKER INC • 34 MOUNT PLEASANT ROAD • ASTON • PA • 19014 • USA

610-500-2000

fax: 610-500-2002

[inquiry@riekerinc.com](mailto:inquiry@riekerinc.com)

[www.riekerinc.com](http://www.riekerinc.com)

**TABLE 1: H6 SENSOR SPECIFICATIONS**

INPUT PARAMETERS			
SUPPLY VOLTAGE	+11..36 VDC Non-Regulated		
SUPPLY CURRENT <sup>1</sup>	22mA @ 24VDC (Digital Output only)		
	30mA nominal @ 24VDC (Analog Output - no load)		
	75mA max @ 24VDC (Analog and Digital Outputs enabled)		
	85mA max @ 12VDC (Analog and Digital Outputs enabled)		
ANALOG MEASURING RANGE	Scalable within 360°		
DIGITAL MEASURING RANGE	±180°		
INPUT PROTECTION	Reverse Polarity, ESD & Surge Protected		
ABSOLUTE ACCURACY OVER FULL OPERATING TEMPERATURE			
RANGE: ±180°	±0.1° typical, ±0.2° absolute max		
RESOLUTION	0.05°		
RESPONSE TIME	6 user-configurable options from 4Hz to 0.3Hz		
ANALOG CURRENT & VOLTAGE OUTPUT PARAMETERS			
OUTPUT RANGES	Current	4..20 mA, 0..20 mA (Configurable within 0..24mA)	$R_{sense} \leq \frac{V_{supply} - 2.5}{0.020 - R_{wire}}$
	Voltage	0..5 V, 0..10V (Configurable within 0..10V)	1kΩ load min.
SENSITIVITY <sup>2</sup>	Relative to Scaled Range		
NULL (0°)	Fully Configurable		
SWITCH OUTPUT PARAMETERS			
OUTPUT MODE	Open Collector Switch to Signal Common		
TRIP MODES	Fully Configurable (Window, Threshold, etc.)		
SWITCH CAPABILITY	250mA @ 36V max		
DIGITAL OUTPUT PARAMETERS			
OUTPUT TYPE	RS-485 Half Duplex (2-wire)		
INCLINATION OUTPUT	32-Bit IEEE Packetized Float		
BAUD RATE	125K Default (Configurable from 9600 to 250K)		
BYTE FORMAT	8 Data Bits, No Parity, 1-stop Bit, No Flow Control		
PACKET FORMAT	See Installation Manual for Packet Details and Commands		
INFORMATION RATE	Polled (up to 20 times/sec)		
LOGGING CAPABILITY (OPTIONAL)			
SUPPLY CURRENT	Additional 20mA @24VDC		
LOGGING RESOLUTION	Configurable in one minute increments		
CARD TYPE	μSD		

**Rieker Rugged. Rieker Reliable.™**

RIEKER INC • 34 MOUNT PLEASANT ROAD • ASTON • PA • 19014 • USA

610-500-2000

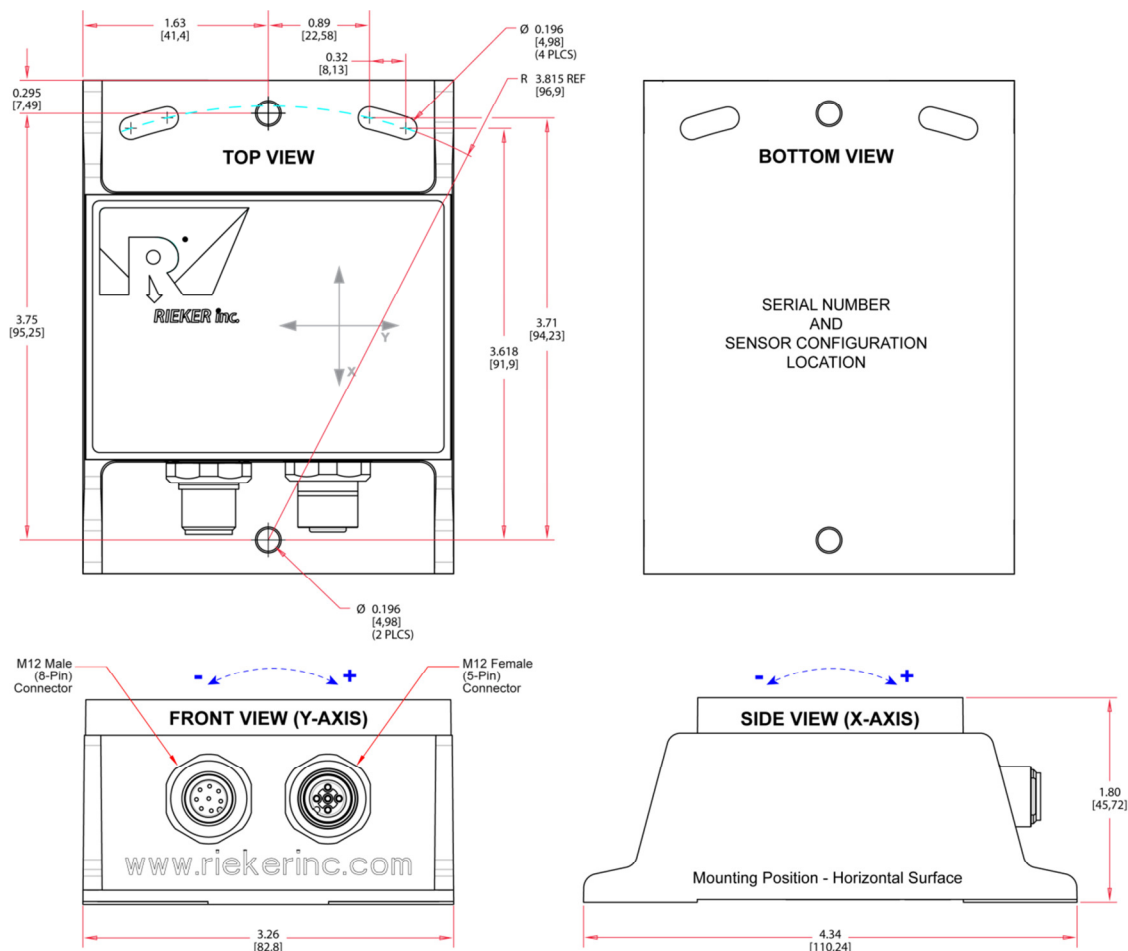
fax: 610-500-2002

[inquiry@riekerinc.com](mailto:inquiry@riekerinc.com)

[www.riekerinc.com](http://www.riekerinc.com)

TEMPERATURE RANGES	
OPERATING TEMPERATURE	-40°F..+185°F (-40°C..+85°C)
STORAGE TEMPERATURE	-49°F..+194°F (-45°C..+90°C)
MECHANICAL CHARACTERISTICS	
HOUSING	Aluminum, IP68, All-weather, Submersible
WEIGHT	18.6 oz. (525 Grams)
MOUNTING HOLES	Accept #8 or M4.5 screws (See Dimensional Drawing)
MOUNTING PLANE	Flat Horizontal Surface (Factory Configurable for Vertical Mount)
OUTLINE DIMENSIONS	4.34" x 3.26" x 1.8" [110mm x 82.8mm x 45.7mm]
ELECTRICAL CONNECTION	See Electrical Connection Drawing
<b>Notes:</b> 1. Supply Current varies depending on outputs connected. Digital output only assumes analog output section is always active however current loop is not connected. 2. Sensitivity defined as (max analog output range) / (sensor input angle range). Ex, A current range set to 4..20mA with a $\pm 30^\circ$ input range will have a corresponding sensitivity of 16mA/60° or 0.267mA/°.	

**FIGURE 1: Dimensions (inches [mm])**



**Rieker Rugged. Rieker Reliable.™**

RIEKER INC • 34 MOUNT PLEASANT ROAD • ASTON • PA • 19014 • USA

610-500-2000

fax: 610-500-2002

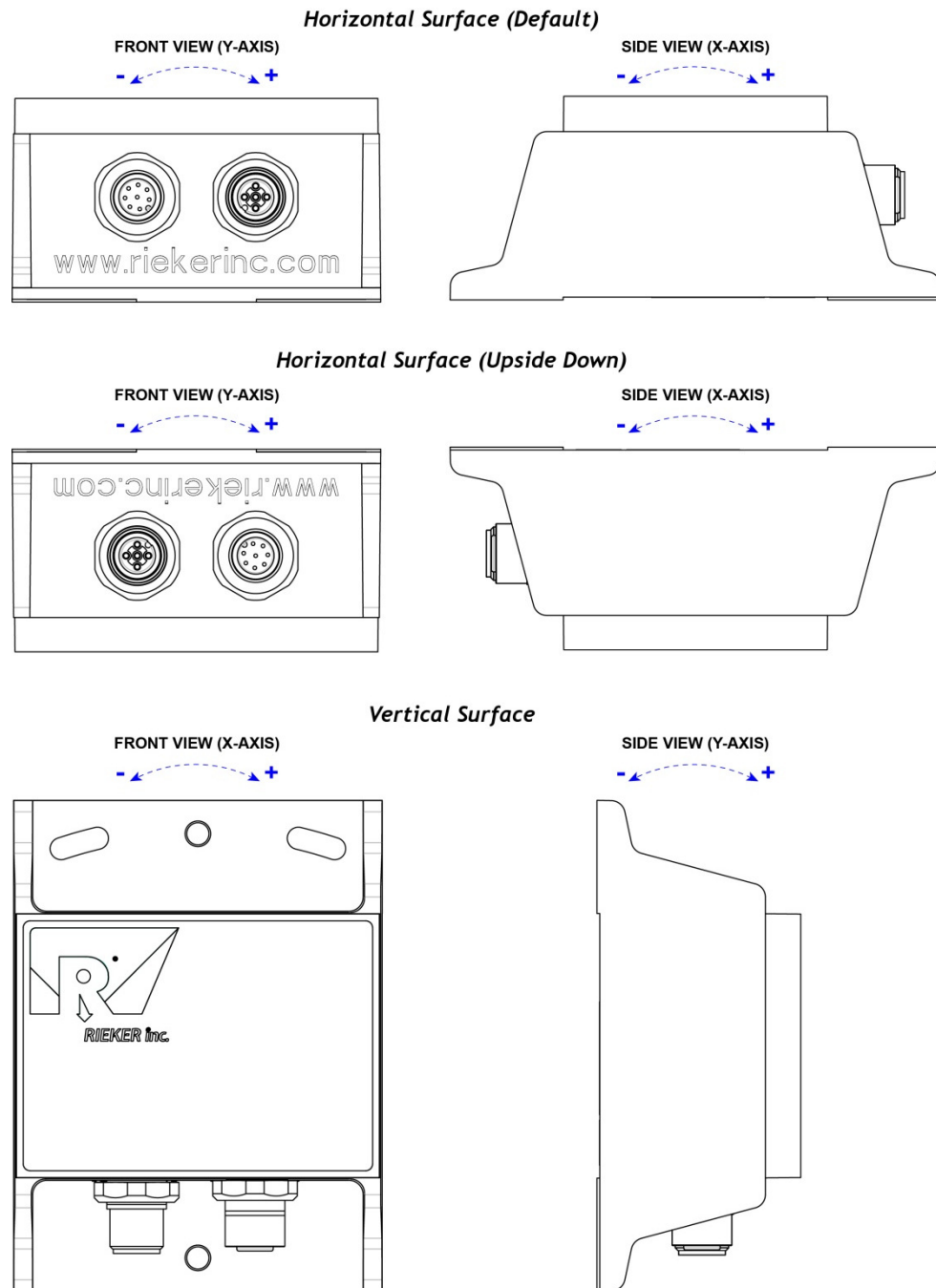
[inquiry@riekerinc.com](mailto:inquiry@riekerinc.com)

[www.riekerinc.com](http://www.riekerinc.com)

### FIGURE 2: Mounting Positions

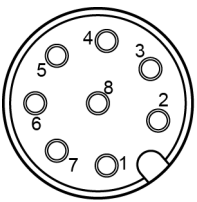
**Note:** The factory default settings for mounting position (either horizontal or vertical) must be selected at time of order. Default output polarity shown is configurable at the factory (defined at time of order) or by the end user via the Flex Dev Kit that includes Rieker Flexware app, sold separately.

- Special H6MM Multi-Mount model (available exclusively through Digi-Key) allows the end user to select between horizontal and vertical mounting positions via a special Flex Dev Kit that includes Rieker Flexware app, also sold separately through Digi-key.





**TABLE 2: MALE 8-PIN INPUT CONNECTOR**

PIN	FUNCTION	 <p>M12 (male 8-pin) Pin Assignment FRONT VIEW</p>
1	SUPPLY VOLTAGE +11...+36VDC	
2	POWER / SIGNAL COMMON	
3	RS485 D+ OR CAN HI	
4	RS485 D- OR CAN LO	
5	NO CONNECTION OR CAN SHIELD	
6	ANALOG OUTPUT 1 (DEFAULT: X-AXIS)	
7	ANALOG OUTPUT 2 (DEFAULT: Y-AXIS)	
8	NO CONNECTION	



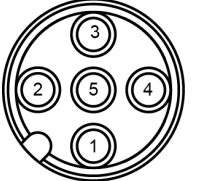


**TABLE 3: FEMALE 5-PIN DIGITAL OUTPUT DAISY CHAIN CONNECTOR**

PIN	FUNCTION	 <p>M12 (female 5-pin) Pin Assignment FRONT VIEW</p>
1	CAN SHIELD	
2	SUPPLY VOLTAGE +11...+36VDC	
3	POWER COMMON	
4	RS485 D+ OR CAN HI	
5	RS485 D- OR CAN LO	

**TABLE 4: CURRENT SENSE**

<p>Rsense is dependent upon supply voltage and cable/wire resistance. Ensure the following equation is met:</p> $R_{sense} \leq \frac{V_{supply} - 2.5}{0.020} - R_{wire}$	QUICK REFERENCE	
	SUPPLY VOLTAGE	SENSE RESISTOR
	12V	200-350 OHMS
	24V	200-1000 OHMS
	28V	200-1000 OHMS

**TABLE 5: ACCESSORIES (SOLD SEPARATELY)**

	<p><b>Flex Series Configurator Kit</b></p> <ul style="list-style-type: none"> <li>Flexware™ Toolkit Applications</li> <li>USB Interface Cable from Sensor to PC</li> <li>Also available through Digi-Key (pn Dev-Kit-C)</li> </ul>
	<p><b>Input / Output Interface &amp; Daisy-chain Cables</b></p> <ul style="list-style-type: none"> <li>I/O Cable, mating connector to sensor, varying cable lengths w/ pigtail leads for input power and output.</li> <li>Daisy-chain cable, M12 8-pin to M12 5-pin, varying cable length for sensor to sensor connection.</li> </ul>
	<p><b>Termination Resistor for Daisy-Chain Configuration</b></p> <ul style="list-style-type: none"> <li>Terminating Resistor M12 5-pin male</li> </ul>
	<p><b>Display Box</b></p> <ul style="list-style-type: none"> <li>Single or Dual Line LCD</li> <li>0.1° Resolution</li> <li>Battery or 12...24VDC input supply</li> </ul>

**Rieker Rugged. Rieker Reliable.™**

RIEKER INC • 34 MOUNT PLEASANT ROAD • ASTON • PA • 19014 • USA

610-500-2000

fax: 610-500-2002

[inquiry@riekerinc.com](mailto:inquiry@riekerinc.com)

[www.riekerinc.com](http://www.riekerinc.com)



# METEOROLOGICAL INSTRUMENTS

## INSTRUCTIONS

### ULTRASONIC ANEMOMETER MODEL 86000



# OPERATING INSTRUCTIONS

Model 86000 Ultrasonic Anemometer

---

## Contents

SECTION	DESCRIPTION	PAGE
1.0	<b>SPECIFICATIONS</b>	1
2.0	<b>INTRODUCTION</b>	1
3.0	<b>BEFORE INSTALLATION</b>	1
4.0	<b>INSTALLATION</b>	2
4.1	Placement	2
4.2	Mounting and Alignment	2
4.3	Wiring Connections	2
5.0	<b>OPERATION</b>	2
5.1	Analog Outputs	2
5.2	With YOUNG Wind Tracker Display	2
5.3	Serial Output Formats and Protocols	2
5.4	Low Power Operation	3
6.0	<b>SETTING SERIAL OUTPUTS AND OPERATING PARAMETERS</b>	
6.1	Setup using YOUNG 86SETUP program	3
6.2	Setup using terminal program	3
6.3	Command Overview	3
6.4	Command Details	4
7.0	<b>EXAMPLE SETTINGS</b>	5
8.0	<b>EMC COMPLIANCE</b>	5
9.0	<b>WARRANTY</b>	5
<b>APPENDIX</b>		
A	<b>WIRING CONNECTIONS</b>	6
B	<b>SENSOR ORIENTATION AND DIMENSIONS</b>	9



## MODEL 86000 ULTRASONIC ANEMOMETER



### 1.0 SPECIFICATIONS

#### WIND SPEED

Range: 0-75 m/s (156 mph)  
Resolution: 0.01 m/s  
Accuracy: 0 to 30 m/s  $\pm 2\%$  or 0.1 m/s  
30 to 75 m/s  $\pm 3\%$

#### WIND DIRECTION

Azimuth Range: 0-360 degrees  
Resolution: 0.1 degree  
Accuracy:  $\pm 2$  degrees

#### SERIAL OUTPUT (Selectable)

Interface Type: RS-232 or RS-485/422  
Formats: ASCII Text (polled and continuous)  
RMYT (YOUNG Wind Tracker)  
NMEA  
Baud Rates: 1200, 4800, 9600, 19200 and 38400

#### ANALOG OUTPUT (Selectable)

Polar Speed: 0-5000mV or 4-20 mA (0 to 100 m/s)  
Polar Direction: 0-5000mV or 4-20 mA (0 to 360° or 0 to 540°)  
Cartesian UV: 0-5000mV or 4-20 mA (-100 m/s to +100 m/s)

#### GENERAL

Output rate: 0.1-20 Hz, 1 Hz typical  
Power Supply: 10 to 30 VDC,  
20 mA typical, 85 mA max  
Protection Class: IP65  
EMC Compliance: FCC Class A digital device  
IEC standard 61326-1  
Dimensions: 29 cm high x 11 cm wide  
Weight: 0.4 kg (0.9 lb)  
Shipping Weight: 1.6 kg (3.5 lb)  
Operating Temperature: -40 to +60°C

### 2.0 INTRODUCTION

The YOUNG 86000 Ultrasonic Anemometer is a 2-axis, no-moving-parts wind sensor. It is ideal for general meteorological applications requiring accurate and reliable measurement. The sensor features wide operating range, compact size, easy installation and low power operation.

The 86000 measures wind speed and direction based on the transit time of ultrasonic pulses between three transducers.

Measurement results are available as calibrated analog output signals, or serial data using RS-232 or RS-485. Continuous serial output or polled operation may be used. Serial format options include direct connection to YOUNG Wind Tracker displays, marine NMEA systems, data loggers, or other compatible serial communication devices.

Operating parameters are easily set using the 86SETUP program provided. All 86000 parameter settings are stored internally in non-volatile memory.

The sensor is constructed using ultraviolet-stabilized thermoplastic for superior environmental resistance. It is easily mounted on standard 1 inch (IPS) pipe. An orientation ring preserves mounting position when the sensor is removed.

### 3.0 BEFORE INSTALLATION

The 86000 arrives fully calibrated and ready to use. Unless otherwise specified, the sensor is configured as follows:

#### FACTORY DEFAULT CONFIGURATION

##### Analog Voltage Outputs:

- Channel V11: Wind Speed  
0-5000 mV = 0-100 m/sec
- Channel V12: Wind Direction  
0-5000mV = 0-360 Deg

If using the sensor with a datalogger or other device requiring 0-5000 mV outputs, no further action is required. Simply connect the device as shown in Appendix A, figure A1.

If using the sensor with a YOUNG Wind Tracker, jumpers must be moved as shown in figure A5. The sensor will then provide RS485 serial output in RMYT format.

Other options are described in APPENDIX A. These are accomplished using various jumper combinations and configuring settings using the 86SETUP program available at [www.youngusa.com](http://www.youngusa.com).

**Note: Always connect and bench test a complex system before installation in the field.**

## 4.0 INSTALLATION

### 4.1 PLACEMENT

Proper instrument placement is important. Eddies from buildings, trees, or other structures can influence measurements. For most applications, locate the sensor well above or upwind of obstructions. As a general rule, air flow around a structure is disturbed to 2 times the height of the structure upwind, 6 times the height downwind, and up to 2 times the height of the structure above ground.

### 4.2 MOUNTING AND ALIGNMENT

Mount the sensor to standard 1-inch (IPS) pipe that has an outside diameter of 1.34 inches (34 mm).

Most applications require aligning the sensor to geographic north (0 degrees). In this orientation the sensor junction box faces SOUTH (180 degrees). See the diagram in APPENDIX B.

- 4.2.1 Place orientation ring over pipe with guide pin up.
- 4.2.2 Place sensor mounting post over pipe.
- 4.2.3 Using the transducers as a sighting aid, align the sensor with a feature on the horizon that represents the proper orientation. After alignment, tighten the mounting post band clamp to secure the position. DO NOT OVER-TIGHTEN.
- 4.2.4 Slide the orientation ring up so its guide pin is fully engaged in the sensor mounting post notch. Tighten the orientation ring band clamp to secure its position. DO NOT OVER-TIGHTEN.

If the sensor needs to be removed later, leave the orientation ring on the pipe to preserve sensor alignment.

### 4.3 WIRING CONNECTIONS

With long cable lengths, resistance in the power supply wires reduces the available voltage at the sensor. Power at the sensor must be in the range of 10 to 30 VDC when the sensor is operating. See WIRING DIAGRAMS in APPENDIX A.

## 5.0 OPERATION

### 5.1 ANALOG OUTPUTS

As supplied, the sensor is configured for VOLTAGE OUTPUT, Wind Speed and Wind Direction. The sensor may also be set up for 4-20 mA CURRENT output by changing internal settings. Details are in section 6.0.

Analog VOLTAGE or 4-20mA CURRENT outputs may be connected to a datalogger or other device such as a YOUNG 26800 Meteorological Translator. See APPENDIX A for connection details.

Analog outputs may be used simultaneously with RS-232 serial connection. RS-485 serial output may not be used simultaneously with analog outputs since they share connection terminals in the junction box.

Analog outputs may be configured for either Polar (speed and direction) or Cartesian (UV) output format.

For voltage output with cable lengths greater than 3m (10 ft.), measure the signal differentially. Current output signals may be measured single-ended.

### 5.2 USE WITH YOUNG WIND TRACKER DISPLAY

The factory default serial output format is RMYT which is compatible with the YOUNG Model 06201 Wind Tracker display. Set the Wind Tracker input to 'INP 09' and connect as shown in the Wiring diagram, Fig A5, Appendix A. Note that jumpers need to be moved so the RS-485 output is available at the connection terminals. Wind speed and direction measurements appear on the Wind Tracker display. See the Wind Tracker manual for display options and other details.

### 5.3 SERIAL OUTPUT FORMATS

Available serial output formats include RMYT, ASCII, ASCII polled, and NMEA. The factory default format is RMYT for use with the YOUNG Wind Tracker display. Other formats may be selected using the 86SETUP program described in Section 6.0.

#### 5.3.1 RMYT

RMYT is a 6-byte binary data format sent at 9600 baud using RS-485 OUTPUT ONLY mode. This is the factory default serial format for use with the YOUNG Model 06201 Wind Tracker.

#### 5.3.2 ASCII

ASCII output format provides continuous wind measurement data in text format at any of the available baud rates.

ASCII output appears either in POLAR (default) or CARTESIAN UV format. With POLAR format, the wind speed threshold, wind speed units, and resolution are user-selectable. With CARTESIAN the wind threshold is ignored and wind speed units are always meters per second (m/s).

#### ASCII POLAR FORMAT

```
a www.w ddd ss*cc<CR>      Low resolution
a www.ww ddd.d ss*cc<CR>    High resolution
```

#### where

a	= Sensor address
www.ww	= Wind speed
ddd.d	= Wind direction
ss	= Status code
*	= Asterisk (ASCII 42)
cc	= Checksum
<CR>	= Carriage return (ASCII 13)

#### ASCII CARTESIAN (UV) FORMAT

```
a uu.uu vv.vv ss*cc<CR>
```

#### where

a	= Sensor address
±uu.uu	= U-axis wind speed (m/s)
±vv.vv	= V-axis wind speed (m/s)
ss	= Status code
*	= Asterisk (ASCII 42)
cc	= Checksum
<CR>	= Carriage return (ASCII 13)

CHECKSUM is a two-character hexadecimal value (in printable ASCII format) generated by taking the exclusive-or of all characters up to the asterisk. STATUS CODE shows a non-zero value when the sensor cannot acquire sufficient samples or a measurement error has occurred.

#### 5.3.3 ASCII POLLED

ASCII POLLED is like ASCII format described above except just one serial output string is sent for each polling command received. The polling command is Ma! where 'a' is the sensor address (valid characters: 0-9, A-Z, a-z). The default address is '0' (ASCII 48).

### 5.3.4 NMEA

NMEA format provides continuous wind measurements in standard NMEA marine sentences at 4800 baud. Use RS-485 OUTPUT ONLY serial output mode with YOUNG Model 06206 Marine Wind Tracker or other NMEA-capable device.

#### NMEA FORMAT

\$WIMWV, ddd, R, www.w, N, A\*cc<CR><LF>

where

ddd = Wind direction (degrees)

www.w = Wind speed (knots)

\* = Asterisk (ASCII 42)

cc = Checksum

<CR><LF> = Carriage return, line feed (ASCII 13, 10)

CHECKSUM is the two-character printable hexadecimal value generated by taking the exclusive-or of all characters between '\$' and '\*'. .

### 5.4 LOW POWER OPERATION

Average current consumption with default settings is about 20 mA. This configuration uses minimal power and enables all features even though they may not be used. This is suitable for many low power applications.

To reduce current consumption further, additional strategies include disabling unused outputs, using polled serial operation, increasing the output interval, and limiting the sample count to the minimum optimal number. Faster baud rates also reduce power by limiting transmit duration.

## 6.0 SETTING OUTPUTS AND OPERATING PARAMETERS

### 6.1 SENSOR CONFIGURATION WITH 86SETUP PROGRAM (RECOMMENDED)

The YOUNG 86SETUP program is available from the factory web site at [www.youngusa.com](http://www.youngusa.com). It provides an easy method for checking and configuring sensor operation. Install the program on a Windows PC and follow instructions that appear on the program screen to retrieve current sensor settings or send new settings.

### 6.2 SENSOR CONFIGURATION USING A GENERAL-PURPOSE COMMUNICATIONS PROGRAM

A general purpose text-based serial communications program like HyperTerminal may be used to manually configure the sensor by sending simple text commands.

The YOUNG sensor and communication program must operate at the same baud rate and be properly connected. Sensor RS-232 mode must be enabled. See the RS-232 Wiring diagram, Fig A3, in Appendix A.

Factory default sensor baud rate is 9600, but may be set to 1200, 4800, 19200 or 38400. Configure the serial communications program for NO handshaking and 1 start, 8 data, 1 stop bit.

The sensor must be in COMMAND MODE in order to set parameters. Enter COMMAND MODE by sending three ESC characters (ASCII 27) in quick succession while the sensor is running. When the sensor is in COMMAND MODE, it sends a '>' prompt character indicated that it is ready to accept commands.

If the prompt does not appear after sending three ESC characters, re-check wiring and communication program setup. If the sensor baud rate is unknown, try sending the ESC characters at each of the five available baud rates (1200, 4800, 9600, 19200 and 38400). It is also possible that sensor parameters have been purposely configured to disable RS-232 mode. If this the case, the following method must be used.

In order to provide access under all conditions, the sensor always begins operation at power up with serial communications set to 38400 baud and RS-232 connections enabled. Immediately after power up, there is a short time window in which to send the ESC characters and enter COMMAND MODE.

To use this feature, set your serial communication program baud rate to 38400. Remove power then wait 5 seconds. Re-apply power to the sensor. The sensor will transmit four asterisks immediately after power up. After the asterisks appear, send three ESC characters. The COMMAND MODE '>' prompt should appear.

### 6.3 COMMAND OVERVIEW

After the '>' prompt appears, send '??' to display a list of available commands. Send 'RPTV' to report current settings. (Note that some values in the report are for factory settings cannot be changed by the user.)

Commands are case sensitive and the exact format must be used. For example, the SET01nn command requires two digits for the serial format code. If you send SET014 instead of SET0104 the sensor will reject the command and indicate an error. End all commands with a carriage return (ASCII 13). In HyperTerminal, do this by pressing the ENTER key.

After receiving the carriage return, the sensor will evaluate the command. Valid commands will be executed. Current settings can be evaluated at any time by sending RPTV to get a new report.

#### IMPORTANT NOTE:

The YOUNG 86SETUP program automatically saves all settings to flash memory when they are sent to the sensor. Settings that are changed manually must be saved to flash with the SET77 command.

## 6.4 COMMAND DETAILS

COMMAND	DESCRIPTION
SET01nn	Set OUTPUT MODE
01	Enable voltage output
03	Enable current output
04	Enable RS-232
08	Enable RS-485 output only
16	Enable RS-485 half duplex
24	Enable RS-485 full duplex
SET02n	Set OUTPUT FORMAT
1	RMYT
2	ASCII
3	ASCII POLLED
4	NMEA
SET03nn	Set BAUD RATE
12	1200
48	4800
96	9600
19	19200
38	38400
SET04n	Set ASCII WS UNITS
1	MPH
2	KNOTS
3	KMPH
4	M/S
SET05c	ASCII character sensor address (0-9, A-Z, a-z)
SET06nnnn	Wind speed threshold for polar output (cm/s)
SET07nnnnnn	Wind speed scale (nnnnn/10000)
SET08nnnnnn	Direction offset (±nnnnn degrees x 10)
SET09nn	Damping factor
SET10nnnnn	Output interval (0-9999 milliseconds)
SET11nn	Direction VOUT (36=0-360, 54=0-540 degrees)
SET12nnnn	Sample count (3 to 200)
SET13n	Wind output format (0/1=Polar/UV)
SET14n	Analog error code (1/2/3=None/Lo/Hi)
SET15n	ASCII serial resolution(0/1=Lo/Hi)
SET16n	Force analog out (0/1/2=Lo/Mid/Hi)
SET77	SAVE SETTINGS
XX	Go to OPERATE MODE
RPT	Report parameter settings
??	Command Help list

### 6.4.1 SET01nn SET OUTPUT MODE

This enables and disables 0-5000 mV output, 4-20 mA current output, RS-232, and RS-485. Only one of the two analog output types (voltage or current) may be enabled at one time. Both RS-232 and RS-485 can be enabled at the same time but only one serial output may be used.

Add together values shown in 6.4 COMMANDS SET01 to configure multiple compatible modes. For example, to enable voltage output and RS-232, add the code for each one: 01 + 04 = 05, SET0105. To enable only RS-232, SET0104.

To conserve power, enable only those modes that are needed

### 6.4.2 SET02n OUTPUT FORMAT

This parameter determines the serial output format.

### 6.4.3 SET03nn BAUD RATE

Sets the baud rate for RS-232 and RS-485 serial communication. Make sure this baud rate is the same as the connected device.

### 6.4.4 SET04n ASCII and NMEA WIND SPEED UNITS

Sets wind speed units for polar ASCII, ASCII POLLED, and NMEA serial outputs.

### 6.4.5 SET05c POLL ADDRESS CHARACTER

Sets the sensor address for ASCII POLLED serial format. The default is '0' (ASCII 48). This is the address recognized when the 'Ma' polling command is received ('a' is the address character). Valid address characters include 0-9, A-Z, and a-z.

### 6.4.6 SET06nn WIND SPEED THRESHOLD

Sets the wind speed threshold for polar outputs (wind speed and direction) to minimize erratic wind direction indications at very low wind speeds. This allows the sensor output to mimic a mechanical wind vane that retains its orientation when there is no wind.

Wind below the threshold is reported as zero, while the wind direction angle is held at the last value when wind speed was above threshold. Set threshold in centimeters per second (m/s x 100). The default setting is 25 cm/s (0.25 m/s, 0.56 mph).

### 6.4.7 SET07nnnnn WIND SPEED MULTIPLIER

All wind speed measurements are multiplied by this parameter. The default value is 10000 for a multiplier of 1.0000.

### 6.4.8 SET08nnnnn WIND DIRECTION OFFSET

Use this parameter to add or subtract a wind direction offset. Value is degrees x 10 and may be positive or negative. Wind direction is always re-scaled to a 0-360 range after offset is applied. The default value is 00000.

### 6.4.9 SET09nn DAMPING FACTOR

Wind measurement outputs are damped using the following formula:

$$S_{\text{damped}} = [(d-1) * S_{\text{damped}} + S_{\text{sample}}] / d$$

where:

$S_{\text{damped}}$	= New or last damped wind speed
$S_{\text{sample}}$	= New wind speed speed
d	= Damping factor

The default value is 00. This means no damping is applied. High damping values at long output intervals can slow the rate at which indicated wind values change.

### 6.4.10 SET10nnnnn OUTPUT INTERVAL

Sets the time interval between measurements in one millisecond increments. Lower values increase power consumption when continuous measurements are taken.

### 6.4.11 SET11nn ANALOG DIRECTION SCALE

Sets wind direction analog output scale to 0-360 or 0-540 degrees. Use the 0-540 scale whenever possible to avoid full-scale analog output swings between 0 and 360 in variable north wind. (Data loggers or display systems may otherwise obtain samples midpoint during these transitions causing erroneous readings.)

Logged data in 0-540 form may be re-scaled to 0-360 by subtracting 360 degrees from any value greater than or equal to 360. The default parameter setting is 0-360 for systems that cannot re-scale the 0-540 output.

### 6.4.12 SET12nnn SAMPLE COUNT

The rate at which the sensor internally takes complete sonic wind samples is greater than 200 times per second. This command sets the number of internal samples used to calculate the median measurement result.

More internal samples consume more power while providing greater immunity to conditions like turbulent high-speed wind. Fewer samples consume less power while providing less immunity to disruptive conditions.

This command interacts with the OUTPUT INTERVAL setting. More samples may require a longer output interval.

#### 6.4.13 SET13n ASCII and ANALOG OUTPUT FORMAT

This setting determines whether ASCII and ASCII POLLED serial outputs and analog outputs provide wind data in either Polar (speed and direction) or Cartesian (UV) form.

#### 6.4.14 SET14n ANALOG OUTPUT STATUS

Serial ASCII and ASCII POLLED formats report a STATUS CODE where non-zero values indicate insufficient samples or measurement error. SET14n determines how the STATUS CODE is indicated by the analog output.

#### 6.4.15 SET15n ASCII RESOLUTION

Sets low or high wind speed and direction resolution.

#### 6.4.16 SET16n FORCE ANALOG OUTPUT

This command forces both analog output channels to LO, MID, or HI scale. This may be used to calibrate or check the operation of externally connected analog measurement devices.

#### 6.4.17 SET77 SAVE SETTINGS

Use this command to save current parameter settings to non-volatile memory. Any settings which have not been saved will be lost when power is removed. Saved settings are loaded at power up. This command may be used any time the sensor is in COMMAND MODE.

#### 6.4.16 XX, RPTV, and ??

XX Returns the sensor to OPERATE MODE.  
RPT Reports the current parameter settings.  
?? Shows a list of commands.

## 7.0 EXAMPLE SETTINGS

Suggested settings. Not all possible setting combinations are shown. Using YOUNG 86SETUP program for changing parameters is recommended. See wiring diagrams for jumper settings.

### 7.1 FACTORY DEFAULT

RS-232	Enabled
RS-485 Output Only	Enabled
Voltage Output:	Enabled
Current Output:	Disabled
Serial Output Format:	RMYT
Output Interval	250
Sample Count:	16

### 7.2 MINIMUM POWER

RS-232	Enabled
RS-485	Disabled
Voltage Output:	Disabled
Current Output:	Disabled
Serial Output Format:	ASCII
Output Interval	1000
Sample Count:	16

### 7.3 4-20 mA OUTPUT

RS-232	Enabled
RS-485	Disabled
Voltage Output:	Disabled
Current Output:	Enabled
Output Interval	1000
Sample Count:	50

### 7.4 RS-485 POLLED ASCII OUTPUT

RS-232	Enabled
RS-485 (Full Duplex)	Enabled
Voltage Output:	Disabled
Current Output:	Disabled
Serial Output Format:	ASCII POLLED
Sample Count:	50

### 7.5 HIGH WINDS

Output Delay:	1000
Sample Count:	200

## 8.0 EMC COMPLIANCE

This sensor complies with limits for a Class A digital device, pursuant to part 15 of the FCC Rules, and IEC standard 61326-1. This sensor generates, uses, and can radiate radio frequency energy and, if not installed and used in accordance with the instruction manual, may cause harmful interference to radio communications. Sensor operation may be temporarily affected by radio frequency and transient interference sources, but will revert to proper operation when the source of interference is removed.

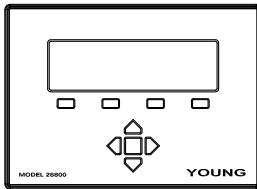
## 9.0 WARRANTY

This product is warranted to be free of defects in materials and construction for a period of 12 months from date of initial purchase. Liability is limited to repair or replacement of the defective item. A copy of the warranty policy may be obtained from R. M. Young Company.



## APPENDIX A: WIRING CONNECTIONS

Fig. A1: VOLTAGE OUTPUT



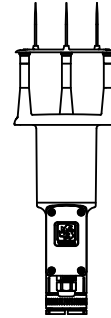
Model 26800 Translator, Datalogger,  
or other voltage measuring device

### SETTINGS

Output Mode: VOUT  
WD Output Scale: 0-360 or 0-540 degrees  
Wind Format: Polar or UV  
Analog Output Error Code: None, Low, or High

CALIBRATION: 0 to 5000 mV  
Polar Wind Speed: 0 to 100 m/s  
Wind Direction: 0 to 360° or 0 to 540°  
U or V: -100 m/s to +100 m/s

For best accuracy measure output voltage differentially as shown. Use shielded cable. Connect cable shield to earth ground as shown.



Model 86000 / 86106  
Ultrasonic Anemometer

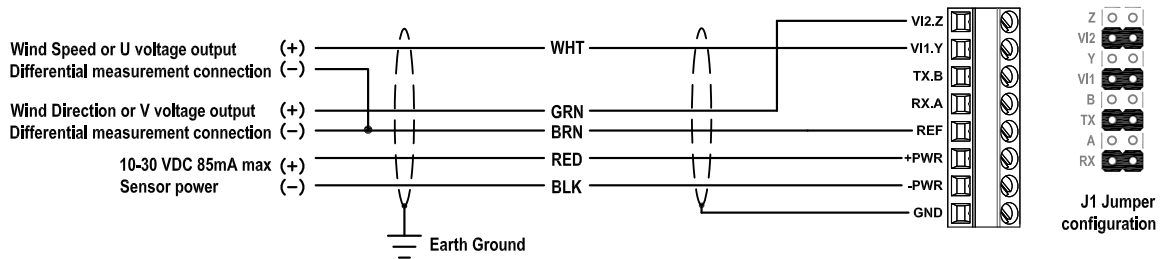
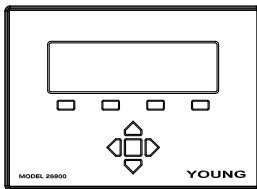


Fig. A2: 4-20 mA CURRENT OUTPUT



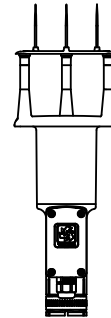
Model 26800 Translator, Datalogger,  
or other current measuring device

### SETTINGS

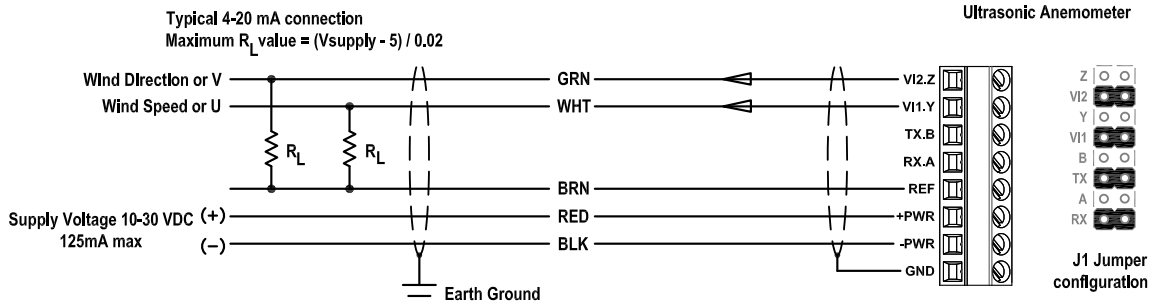
Output Mode: IOUT  
WD Output Scale: 0-360 or 0-540 degrees  
Wind Format: Polar or UV  
Analog Output Error code: None, Low, or High

CALIBRATION: 4.00 to 20.00 mA  
Polar Wind Speed: 0 to 100 m/s  
Wind Direction: 0 to 360° or 0 to 540°  
U or V: -100 m/s to +100 m/s

Use shielded cable. Connect cable shield to earth ground as shown.

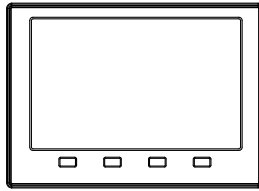


Model 86000 / 86106  
Ultrasonic Anemometer



## APPENDIX A: WIRING CONNECTIONS

Fig. A3: RS-232 SERIAL CONNECTION



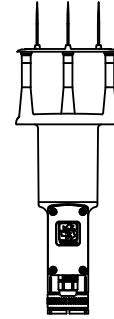
Serial Device

### SETTINGS

Output Mode: RS-232  
Output Format: ASCII, ASCII POLLED, NMEA, or RMYT  
Baud Rate: 1200, 4800, 9600, 19200 or 38400

Set connected serial device baud rate to match sensor.  
1 start bit, 8 data bits, no parity, 1 stop bit, no flow control.

Use shielded cable. Connect cable shield to earth ground as shown.



Model 86000 / 86106  
Ultrasonic Anemometer

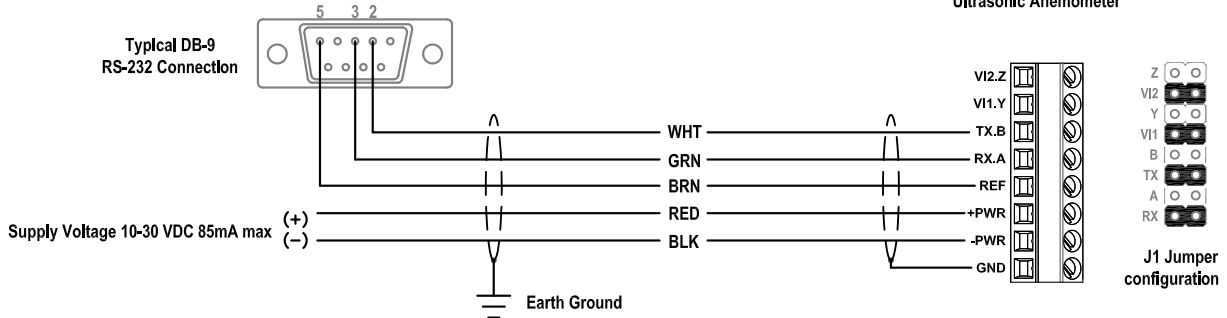
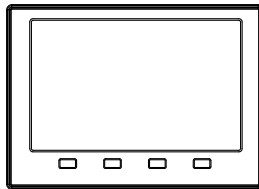


Fig. A4: RS-485 SERIAL CONNECTION



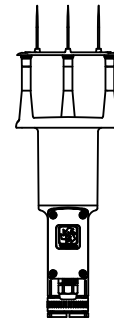
Serial Device

### SETTINGS

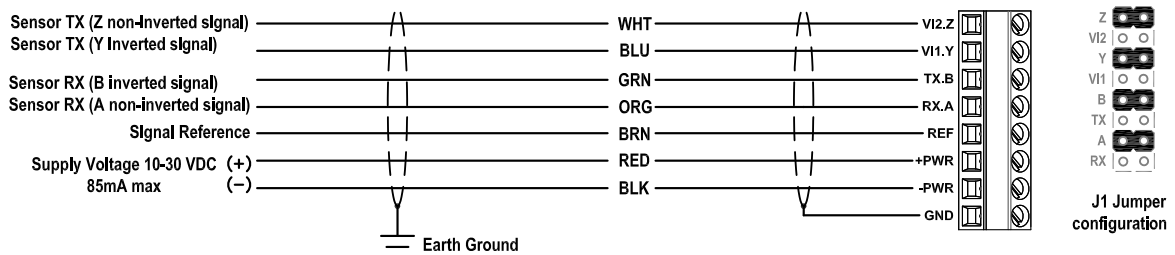
Output Mode: RS-485 Full Duplex  
Output Format: ASCII, ASCII POLLED\*, NMEA, or RMYT  
Baud Rate: 1200, 4800, 9600, 19200 or 38400

Set connected device baud rate to match sensor.  
1 start bit, 8 data bits, no parity, 1 stop bit, no flow control.

Use shielded cable. Connect cable shield to earth ground as shown.

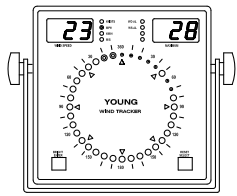


Model 86000 / 86106  
Ultrasonic Anemometer



## APPENDIX A: WIRING CONNECTIONS

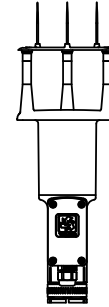
Fig. A5: 06201 WIND TRACKER



Model 06201  
Wind Tracker

SETTINGS:  
Output Mode: RS-485 Output Only  
Output Format: RMYT  
Baud Rate: 9600

These are the default sensor settings as shipped unless otherwise requested. Use shielded cable. Connect earth ground as shown.



Model 86000 / 86106  
Ultrasonic Anemometer

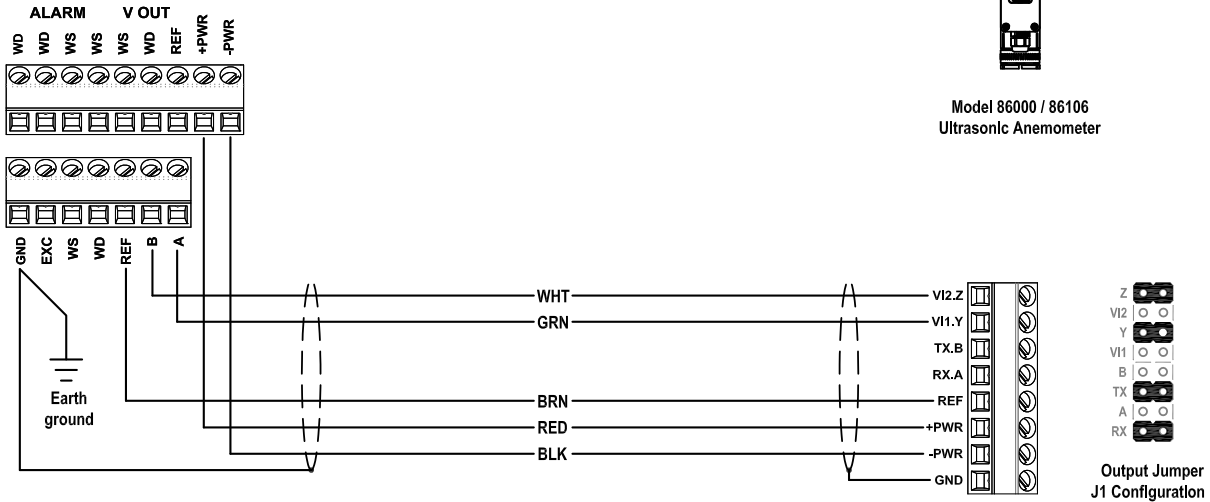
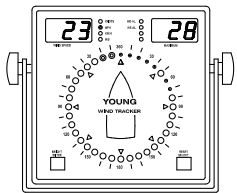


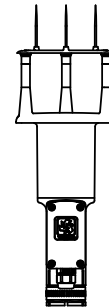
Fig. A6: 06206 MARINE WIND TRACKER



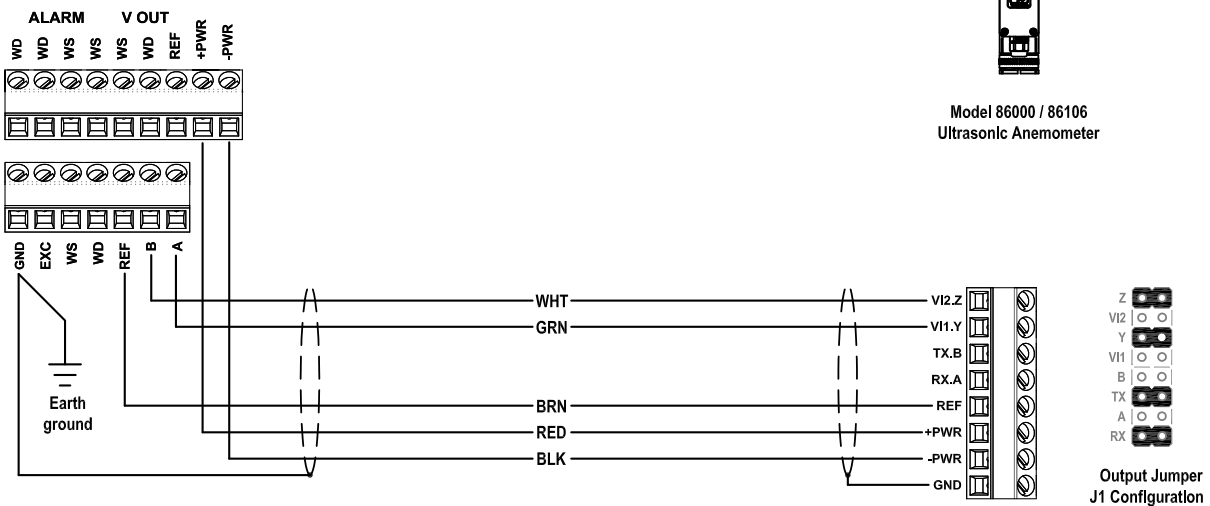
Model 06206  
Wind Tracker

SETTINGS:  
Output Mode: RS-485 Output Only  
Output Format: NMEA  
Baud Rate: 4800

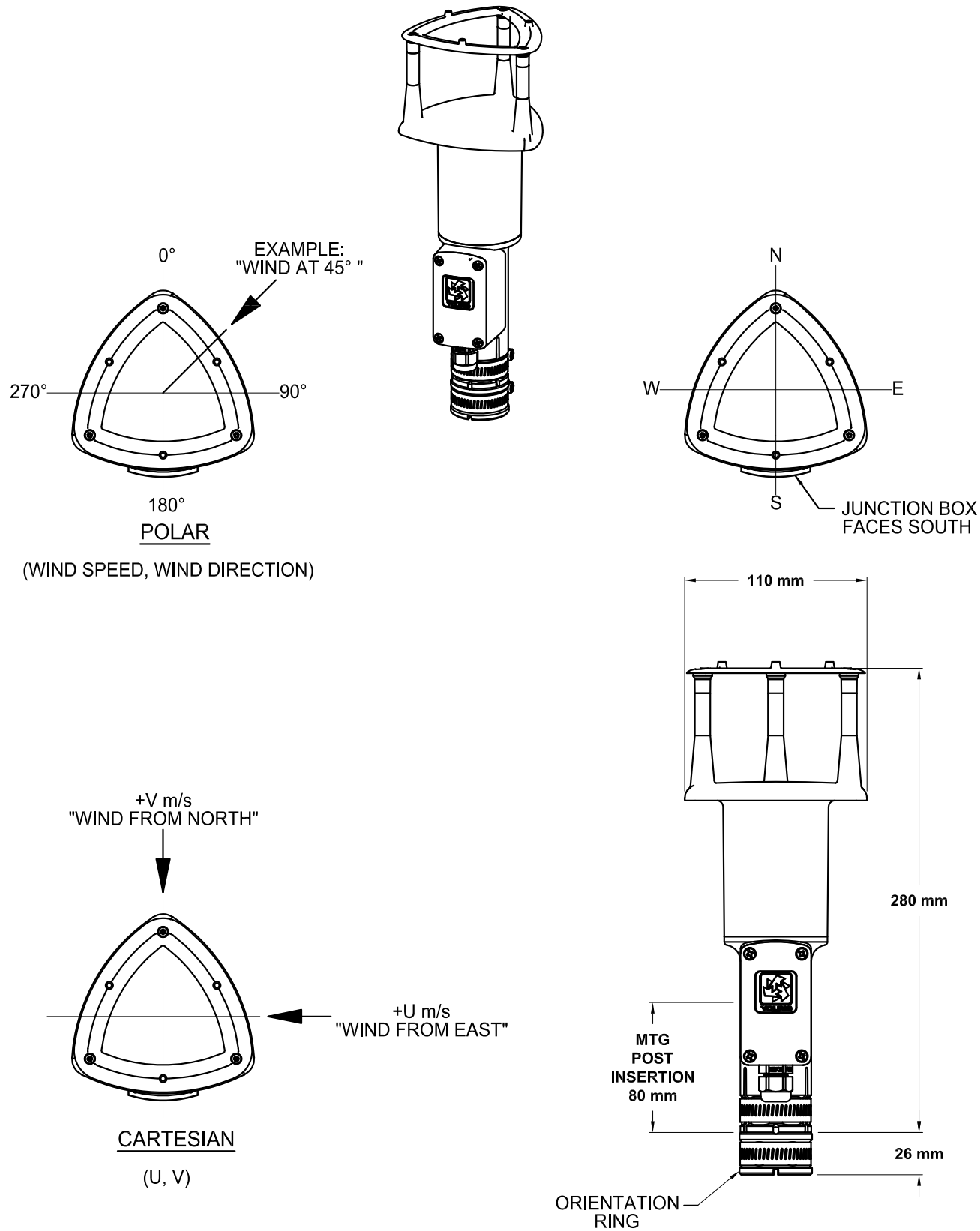
Use shielded cable. Connect earth ground as shown.



Model 86000 / 86106  
Ultrasonic Anemometer



**APPENDIX B: SENSOR ORIENTATION AND DIMENSIONS**



## Obsidian 4X/8X/12X/24X/36X

### Next Generation of Web Based, High Dynamic Range, GPS/PTP Ready, Multi-Channel Recorders

Ready for the *right tool* for the job?

The **Obsidian 4X/8X** is Kinemetrix's NEW seismic recorder and a new paradigm in *open-architecture* seismic data acquisition systems defining the *World's Next Generation* of seismic products. It is designed to give you the flexibility required by *the earthquake monitoring solutions of tomorrow*, being the *most versatile* seismic recorder of today. No more and no less than you need.

You expect outstanding data fidelity and spectral purity. High accuracy data timing is of course required. But it goes beyond that. There are several standard recorded data formats to select from, or you can add your own. On the fly processing of parametric data using your algorithms. Interface to major data center software packages using *their* protocols. For timing use GPS where it makes sense and/or PTP when several units are connected via Ethernet along with DC power.

And when you're ready to get into Earthquake Early Warning Systems (EEWS), the **Obsidian 4X/8X** is ready too. Balance communications bandwidth and data latency with not one but two mechanisms to deliver *ultra-low* latency data.

Why struggle with limited keypads and hard to read displays when you're usually not there anyway? Access the system using your favorite web browser remotely or locally and wirelessly. Where it makes sense to retrieve data locally, do it with a simple thumb drive without commands or buttons.

And for those whose job it is to maintain the station we developed Streamlined Station Maintenance (SSM) that allows you to use your browser to log maintenance activities such as software updates, site inspections, or battery replacements right on the unit. These logs can be automatically uploaded to your data center for archiving, reducing paper work in the field.

Choose from a suite of built-in Kinemetrix features, add-on packages from trusted providers or expand the capabilities of the system yourself. It's the *open-architecture* seismic data acquisition system!

Quanterra and Kinemetrix data acquisition products provide *data availability* of over 99% in several large networks year after year. Our users will tell you so.



## FEATURES

- 3 + 1 sensor channels recorder (Obsidian 4X) or 2 x (3+1) sensor channels recorder (Obsidian 8X)
- 24-bit Delta Sigma converter, one per channel
- Built-in GPS/GNSS, built-in PTP
- Record and communicate multiple sample rates
- Multiple data formats and telemetry protocols
- Ultra-Low latency data for Earthquake Early Warning Systems
  - \* 0.1sec data packet
  - \* 0.01sec DFS at 100sps
- Streamlined Station Maintenance (SSM)
- Data offloaded automatically to removable thumb drives connected to a USB host port. Parallel recording (mirroring) data on an external USB thumb drive.
- Wireless communications via USB based Wi-Fi
- Extensive state-of-health monitoring, including input and system voltages, internal temperature, humidity, communication link diagnostics
- Application Programming Interface (API) to develop your own add-on software modules. You can customize real-time data processing, file formats, stream data using your own protocol, shape data with a custom filter, and so on.
- IP Security through SSH and SSL
- Optional Terminal strips for easy sensor connection
- Transient and EMI/RFI protection on all connections
- System Status LEDs
- Rugged aluminum extruded case designed for 1m drop and 1m temporary immersion (IP67)
- Designed for RoHS Compliance and easy re-cycling
- Designed for the lowest Total Cost of Ownership (TCO)



## SPECIFICATIONS

### Channels

Number: 4, 8, 12, 24 and 36  
Input level: 5Vpp, 10Vpp, 40Vpp Differential Input

### Data Acquisition

Type: Individual 24-bit Delta Sigma converter per channel bandwidth-optimized 32-bit data path  
Anti-alias filter: Double Precision FIR Filter Causal/Acausal;  
>140 dB attenuation at output Nyquist  
Dynamic range: 200 sps ~127 dB (RMS clip to RMS noise - Typical)  
100 sps ~130 dB (RMS clip to RMS noise - Typical)  
Frequency response: DC to 80 Hz @ 200 sps  
Sampling rates: 1, 10, 20, 50, 100, 200, 250, 500, 1000, 2000, 5000 sps  
Channel skew: None – simultaneous sampling of all channels  
Acquisition modes: Continuous, triggered, time windows  
Output data format: 24 bit signed (3 bytes) in user selectable format  
Parameter calculations: Calculations of key parameters in real-time, including JMA intensity  
Real time digital output: Ethernet or RS-232 output of digital stream

### Trigger

Type: IIR bandpass filter (three types available)  
Trigger selection: Independently selected for each channel  
Threshold trigger: Selectable from 0.01% to 100% of full scale  
Trigger voting: Internal, external and network trigger votes with arithmetic combination  
Additional trigger: STA/LTA, Time Window

### Timing

Type: Oscillator digitally locked to GPS/GNSS or PTP:  
Integrates completely with system, providing timing, internal oscillator correction and position information.  
Shared timing: 3 Ports for shared timing for multiple local units

Accuracy: <1 microseconds of UTC with GPS/GNSS or PTP

### Storage

Data slot: Internal SDHC Card Slot, standard 32 GB  
System slot: Internal SDHC Card Slot, 4 GB  
Recording capacity: Approximately 42 kB per channel per minute on Memory Card of 24-bit data @ 200 sps.  
(33 days of 4x200sps recording on 8GB Data card)  
SDHC Format: Linux EXT4  
Data: Offloaded automatically to removable thumb drives connected to a USB host port. Parallel recording (mirroring) data on an external USB thumb drive.  
USB drives format: FAT32

### Communications

Ethernet interface: Real Time Telemetry (Multiple destinations TCP/IP Protocol), Parameter set up, and event retrieval (FTP/SFTP)  
RS-232 interface: Real Time Telemetry (over modem, radio, etc.), Parameter set up, and event retrieval  
Modem: Built in modem, Remote access, initiated by user or by the Obsidian  
Telemetry: Real-time data via DFS, SEEDLink, Earthworm, Antelope compatible ORB server, or Altus SDS protocols.

### Instrument Software

Type: Multi-tasking operating system supports simultaneous acquisition and interrogation; allows remote and automatic firmware upgrades  
Security: Supports SSH and SSL  
System control: Configure sample rate, filter type, trigger type and voting, maintains communications and event storage  
File formats: Kinemetrix EVT, MiniSEED, SAC, COSMOS, MATLAB, SUDS, SEISAN, ASCII, others  
Intelligent alerting: Initiate communications when an event is detected or if an auto-diagnostic failure occurs  
Auto-diagnostics: Continuously check system voltages, temperature, humidity, and timing system integrity  
Rapid setup: Can be configured from a parameter file  
System timing: Supports PTP Slave and PTP Master timing (Using Internal GPS as Master clock), NTP and External 1PPS

### I/O and Display

Power input: Mil-style connector for DC power input, external battery connection, Power over Ethernet (Option)  
Interfaces: 10/100 BaseT Ethernet Port  
(M12 connectors) 3 x USB 2.0 Host Ports  
USB 2.0 Device  
3 x RS-232  
DFS Port (RS232)  
Linux Console (RS232)  
POTS Modem  
3 x Time/Power Ports (1PPS In/Out, Switched Power)  
GPS Antenna (TNC)  
EMI/RFI protection: All I/O lines EMI/RFI and transient protected  
LED: System, power and event status, Ethernet Link & Data



## SPECIFICATIONS

### Power Supply

Type:	Internal high efficiency switched power supply and battery charger system with extensive SOH outputs
DC input:	9-28 VDC (>15.5VDC for Battery Charger Operation)
External AC/DC:	Universal Input 100-250 VAC 50/60 Hz
Power module:	Output 15.5 VDC
Internal battery charger:	Digitally temperature compensated output for External Valve Regulated Lead Acid (VRLA) batteries with reverse protection and deep discharge recovery.
Fuses:	None. Uses resettable Polyswitch protection
Current drain:	180ma @12V (Obsidian 4X w/o sensors)

### Environment

Operating temp: -20° to 70°C Operation  
 Humidity: 0-100% RH (Non-condensing)

### Physical

Size: Obsidian 4X: 14" (L) x 5.5" (D) x 6.8" (H)  
 Obsidian 8X: 19" (L) x 7.5" (D) x 6.8" (H)  
 Enclosure rating: IP67 Equivalent  
 Environmental: RoHS Compliant Unit

### Support Software

File Viewer*:	Multiplatform program for rapid review of waveforms and event information.
Antelope:	Comprehensive commercial network operational and management system for medium and large networks
Earthworm:	Comprehensive public domain network operational and management system for medium and large networks
Rock Monitor Professional:	Rock network operation and monitoring tool
Rockhound:	Commercial open architecture user-extensible real-time data collection and processing software that runs on a variety of computers
PSD:	Commercial Pseudo Spectral Density software for earthquake data analysis
SMA:	Commercial Strong Motion Analyst software for earthquake data analysis and processing
K2COSMOS*:	Conversion software from Altus EVT file format to COSMOS v1.20 format (COSMOS format can also be produced natively from the Obsidian)
Miscellaneous:	Format converters to ASCII and other formats. Web Server for command and control, Optional Software Development Kit and Compilers. Contact Kinemetrix for other options. *No charge

Specifications subject to change without notice



## ETNA 2

### Next Generation of Web Based, Cost Effective, Strong Motion Accelerographs

Kinemetrics' **ETNA** accelerograph established the world's standard for strong motion recording for almost two decades with more than 6000 installations worldwide. The **ETNA 2** represents the next generation of ETNA-class accelerographs offering NEW and cost effective, web based monitoring capabilities paired with another Kinemetrics' established world standard, the exemplary **EpiSensor** accelerometer.

The ETNA 2 is easy to use since it was designed around the Rockhound application software first implemented on the Basalt instruments and continued now on the new Obsidian instruments.

ETNA 2 offers the most essential accelerograph features supporting a wide range of earthquake monitoring applications in a small, lightweight, and simple to use package. If you are interested in Earthquake Early Warning, in structural monitoring, in aftershocks surveys or even in induced earthquake monitoring related to oil and gas, and geothermal fluid injection activities, the ETNA 2 is the right product for you.

And for those whose job it is to maintain large number of stations, we implemented Streamlined Station Maintenance (SSM) that allows you to use your browser to log maintenance activities such as software updates, site inspections, or battery replacements right on the unit. These logs can be automatically uploaded to your data center for archiving, reducing paper work in the field, and eliminating human error.



## FEATURES

- 3 sensor channels with an internal EpiSensor triaxial deck
- 24-bit Delta Sigma converter, one per channel
- Matched to Kinemetrics outstanding EpiSensor accelerometer performance
- Built-in GPS/GNSS and PTP timing options
- Record and communicate multiple sample rates
- Earthquake Early Warning low latency 0.1s packets ready
- Multiple telemetry protocols: ORB natively or public domain Earthworm and SeedLink
- Streamlined Station Maintenance (SSM)
- Data offloaded automatically to removable thumb drive connected to the USB host port. Parallel recording (mirroring) data on an external USB thumb drive.
- Wireless communications via USB based Wi-Fi or cellular modem
- State-of-health monitoring, including input and system voltages, internal temperature, communication link diagnostics, available storage
- IP Security through SSH and SSL
- Reverse voltage protection and self resettable fuses
- System Status LEDs
- Surviving temporary immersion at 1 m depth (rated IP67)
- Designed for RoHS Compliance and easy re-cycling
- Designed for the lowest Total Cost of Ownership (TCO)





## SPECIFICATIONS

### Sensor

Type: Triaxial EpiSensor force balance accelerometers, orthogonally oriented, internal  
Full scale range: User selectable at  $\pm 1g$ ,  $\pm 2g$  or  $\pm 4g$   
Bandwidth: DC to 200 Hz  
Dynamic range: 155 dB+  
Offset: Factory set, software re-zeroing

### Digitizer

Channels: 3 24-bit sensor channels for the internal sensors  
bandwidth-optimized 32-bit data path  
Dynamic range: ~130 dB at 100 sps (defined as RMS clip to RMS  
shorted- input noise) or  
~139 dB at 100 sps (defined as full scale peak to peak  
to RMS shorted-input noise)  
Primary sample rates: 1, 10, 20, 50, 100, 200, 250, 500 sps  
Secondary sample rates: A second lower sample rate can be  
selected from the primary sample rates  
above

Acquisition modes: Continuous (ring buffer) and triggered  
Calibration & test: Pulse and Sensor Response Test

### Trigger

Trigger selection: Independently selected for each channel Internal  
Trigger: Threshold, selectable from 0.01% to 100%  
of full scale or STA/LTA algorithm  
Trigger voting: Internal and network trigger votes with  
arithmetic combination

### Timing

Type: Oscillator digitally locked to GPS/GNSS or to PTP master  
Accuracy: <1 microseconds of UTC with GPS locked

### Storage

Data storage: Internal SDHC Card, 32 GB  
System storage: Internal SDHC Card, 4 GB  
Data: Offloaded automatically to removable thumb drive  
connected to the USB host port. Parallel recording  
(mirroring) data on an external USB thumb drive.  
File formats: MiniSEED, EVT, and ASCII  
USB drive file system: FAT32

### Interfaces and Digital Control

Interfaces: 1 x Ethernet 10/100BaseT  
(M12 connectors) 1 x USB 2.0 Device Port for data access  
1 x USB 2.0 Host Port for peripherals  
1 x RS-232 for factory use only  
Relays: 2 x SPDT relays, software configurable  
LEDs: System, power and event status, Ethernet Link

### Communications

Ethernet interface: Real Time Telemetry (Multiple destinations TCP/IP  
Protocol), web server for parameter setup, event  
retrieval via FTP/SFTP; supports Point of Contact  
(POC) name service  
Modem: External, cellular or POTS, connected via the  
USB 2.0 Host interface; consult factory for details  
Protocols: Real-time data streaming via Antelope compatible ORB  
server or via public domain SEEDLink and Earthworm  
protocols  
State-Of-Health: Input voltage, Super Capacitor voltage, Time  
synchronization, internal temperature, available storage  
Low latency: 1s and 0.1s data packets i.e. for EEWS applications  
Data visualization: Waveform Viewer for continuous waveform display  
and File Viewer for triggered event display;  
consult factory for other support software

### Power Requirements

Consumption: <3W operational  
Voltage range: 9-28 VDC  
Protections: Reverse voltage, over/under voltage, self resettable fuses

### Physical

Mounting: Central bolt, 3 adjustable feet, air bubble leveling  
Dimensions: 6" x 6" x 3" (15cm x 15 cm x 7.5cm)  
Volume: 1.6 liters  
Weight: 3.3 lbs. (1.5 kg)

### Environmental

Temperature range: -20° to 70°C operational  
Humidity: 0-100% RH (non-condensing)  
Enclosure rating: IP67

Specifications subject to change without notice

## BIBLIOGRAPHY

- Akinci, N. O., Liu, J. and Bowman, M. D. (2008) ‘Parapet Strength and Contribution to Live-Load Response for Superload Passages’, *Journal of Bridge Engineering*, 13(1), pp. 55–63. doi: 10.1061/(asce)1084-0702(2008)13:1(55).
- Akogul, C. and Celik, O. (2008) ‘Effect of Elastomeric Bearing Modeling Parameters on the Seismic Design of RC Highway Bridges with Precast Concrete Girders’, *The 14th World Conference on ....* Available at: <ftp://jetty.ecn.purdue.edu/spujol/Andres/files/05-02-0036.PDF>.
- Annamdas, V. G. M., Bhalla, S. and Soh, C. K. (2017) ‘Applications of Structural Health Monitoring Technology in Asia’, *Structural Health Monitoring*, 16(3), pp. 324–346. doi: 10.1177/1475921716653278.
- Briggs, R. W. and Hammond, W. C. (2011) *Evaluation of Geodetic and Geologic Datasets in the Northern Walker Lane*.
- Carr, T. M. and Sanders, D. H. (2013) *Instrumentation and Dynamic Characterization of the Galena Creek Bridge*. University of Nevada, Reno.
- Conner, S. and Huo, X. S. (2006) ‘Influence of Parapets and Aspect Ratio on Live-Load Distribution’, *Journal of Bridge Engineering*, 11(2), pp. 188–196. doi: 10.1061/(asce)1084-0702(2006)11:2(188).
- Eamon, C. D. and Nowak, A. S. (2002) ‘Effects of Edge-Stiffening Elements and Diaphragms on Bridge Resistance and Load Distribution’, *Journal of Bridge Engineering*, 7(5), pp. 258–266. doi: 10.1061/(asce)1084-0702(2002)7:5(258).
- Eddine, W. N., Tarhini, K. and Mabsout, M. (2020) ‘Influence of railing stiffness on single-span two-lane steel girder bridges’, *International Journal of GEOMATE*, 19(73), pp. 33–40. doi: 10.21660/2020.73.9353.
- Falkensammer, L. H. (2018) *Galena Creek Bridge Structural Health Monitoring Instrumentation and Modeling*. University of Nevada, Las Vegas. doi: 10.1017/CBO9781107415324.004.
- Feng, Y., Kaya, Y. and Ventura, C. (2016) ‘Finite Element Model Updating of Portage Creek Bridge’, in Li, D. and Li, X. (eds). Vancouver: Society for Experimental Mechanics, Inc., pp. 247–253. doi: 10.1007/978-3-319-29751-4.
- FHWA (2013) ‘Post-Tensioning Tendon Installation and Grouting Manual’, p. 184.
- FHWA (2016) ‘Post-Tensioned Box Girder Design Manual’. Washington, DC: Federal Highway Administration, p. 389. Available at: <https://www.fhwa.dot.gov/bridge/concrete/hif15016.pdf>.

Fujino, Y. and Siringoringo, D. M. (2011) ‘Bridge Monitoring in Japan: The Needs and Strategies’, *Structure and Infrastructure Engineering*, 7(7–8), pp. 597–611. doi: 10.1080/15732479.2010.498282.

Gunes, B. and Gunes, O. (2021) ‘Vibration-Based Damage Evaluation of a Reinforced Concrete Frame Subjected to Cyclic Pushover Testing’, *Shock and Vibration*, 2021, pp. 1–16. doi: 10.1155/2021/6666702.

Hu, M. *et al.* (2017) ‘Seismic Collapse Analysis of RC Highway Bridges Based on a Simplified Multiscale FE Modeling Approach’, *Shock and Vibration*, 2017. Available at: <https://doi.org/10.1155/2017/5124767>.

NDOT (2019) *Galena Creek Bridge Northbound Routine Inspection Report*.

Qiang, H. *et al.* (2009) ‘Seismic Damage of Highway Bridges during the 2008 Wenchuan Earthquake’, *Earthquake Engineering and Engineering Vibration*, 8(2), pp. 263–273. doi: 10.1007/s11803-009-8162-0.

Sakai, J. and Unjoh, S. (2006) ‘Earthquake simulation test of circular reinforced concrete bridge column under multidirectional seismic excitation’, *Earthquake Engineering and Engineering Vibration*, 5(1).

Taylor, M. S. and Sanders, D. H. (2008) *Seismic Time History Analysis and Instrumentation of the Galena Creek Bridge*. University of Nevada, Reno. doi: 10.1017/CBO9781107415324.004.

Wang, N. (2010) *Reliability-Based Condition Assessment of Existing Highway Bridges*. Georgia Institute of Technology.

Wolterbeek, M. (2020) *How the burgeoning Walker Lane may split the American West, University of Nevada at Reno*. Available at: <https://www.unr.edu/nevada-today/stories/walker-lane>.

Xu, Y. L. and Xia, Y. (2012) *Structural Health Monitoring of Long-Span Suspension Bridges, Structural Health Monitoring of Long-Span Suspension Bridges*. Taylor & Francis Group. doi: 10.1201/b13182.